

MINISTRY OF EDUCATION AND TRAINING
UNIVERSITY OF TECHNOLOGY AND EDUCATION
HO CHI MINH CITY

DO VAN HIEN

**ISOGOMETRIC FINITE ELEMENT METHOD
FOR LIMIT AND SHAKEDOWN ANALYSIS OF
STRUCTURES**

DOCTORAL THESIS

MAJOR: ENGINEERING MECHANICS

Ho Chi Minh City, June 16, 2020

Declaration

I, Do Van Hien, declare that this thesis entitled, "Isogeometric finite element method for limit and shakedown analysis of structures" is a presentation of my original research work. I confirm that:

- Wherever contributions of others are involved, every effort is made to indicate this clearly, with due reference to the literature, and acknowledgement of collaborative research and discussions.
- The work was done under the guidance of Prof. Nguyen Xuan Hung at the Ho Chi Minh City University of Technology and Education.

Acknowledgements

This thesis summarizes my research carried out during the past five years at the Doctoral Program "Engineering Mechanics" at Ho Chi Minh City University of Technology and Education in Ho Chi Minh City. This thesis would not have been possible without help of many, and I would like to acknowledge their kind efforts and assistance.

First of all I would like to express my deep gratitude to my supervisor Prof. Nguyen Xuan Hung, for his guidance, support and encouragement during the past five years. I appreciate that he left a lot of freedom for me to pursue my own ideas, set the right direction when it was necessary and contributed valuable advice.

I am also very grateful to Assoc.Prof. Van Huu Think, who has been my second advisor at HCMUTE for many years.

I am indebted to Prof. Timon Rabczuk for giving me the chance to spend a one-year research visit at the Bauhaus-Universität Weimar, and I also want to thank Prof. Tom Lahmer and Prof. Xiaoying Zhuang for the fruitful discussions and their support.

I also would like to thank the research group members at GACES (at HCMUTE), CIRTECH (at HUTECH) and ISM (at Bauhaus-Universität Weimar, Germany) for their helpful supports.

I would like to thank from the bottom of my heart to Assoc.Prof. Nguyen Hoai Son, Assoc.Prof Nguyen Trung Kien, Assoc.Prof Chau Dinh Thanh and other colleagues at HCMUTE for their kind supports and advice.

I am immensely indebted to my father Do Tang, my mother Pham Thi Nghe and my parents in-law who have been the source of love and discipline for their inspiration and encouragement throughout the course of my education including this Doctoral Program.

Last but not least, I am extremely grateful to my wife Mrs. Nguyen Thi Nhu Lan who has been the source of love, companionship and encouragement, to my sons, Do Quang Khai and Do Minh Nhat, who has been the source of joy and love.

Abstract

The structural safety such as nuclear power plants, chemical industry, pressure vessel industry and so on can commonly be evaluated with the help of limit and shakedown analysis. Nowadays, the limit and shakedown analysis plays a well-known role in not only assessing the safety of engineering structures but also designing of the engineering structures. The limit load multipliers can be determined by using lower or upper bound method. In order to utilize the limit and shakedown analysis in many practical engineering areas, the development of numerical tools which are sufficiently efficient and robust is a necessary of current research in the field of limit and shakedown analysis. The numerical tools involve the two steps: finite element discretisation strategy and constrained optimization.

In this research, the isogeometric finite element method is used to discretise the displacement domain of structures in the first step. The primal-dual algorithm based upon the von Mises yield criterion and a Newton-like iteration is used in the second step to solve optimization problem. Mathematically, the shakedown problem is considered as a nonlinear programming problem. Starting from upper bound theorem, shakedown bound is the minimum of the plastic dissipation function, which is based on von Mises yield criterion, subjected to compatibility, incompressibility and normalized constraints. This constraint nonlinear optimization problem is solved by combined penalty function and Lagrange multiplier methods.

The isogeometric analysis (IGA) uses NURBS basis functions for both the representation of the geometry and the approximation of solutions. The main aim of the IGA was to integrate Finite Element Analysis (FEA) into NURBS based Computer Aid Design (CAD) design tools. The Bézier and Lagrange extraction of NURBS was used in the analysis due to The computational aspects of the NURBS function increase the question of how to implement efficiently the NURBS function in the existing FEM codes due to a significant differences between the NURBS basis function and the Lagrange function. The Bézier extraction is founded on the NURBS basis functions in terms of C^0 Bernstein polynomials. Lagrange extraction is similar to Bézier extraction but it sets up a direct connection between NURBS and Lagrange polynomial basis functions instead

of using C^0 Bernstein polynomials as a new shape function in the Bézier extraction. Numerical results of structure problems are compared with analytical or other available solutions to prove the reliability and efficiency of these approaches.

Pressure vessel which is designed to hold liquids or gases contains various parts such as thin walled vessels, thick walled cylinders, nozzle, head, nozzle head, skirt support and so on. Two types of defects, axial and circumferential cracks, are commonly found in pressure vessel and piping. The application of shakedown analysis in pressure vessel engineering is illustrated in this study.

Table of Contents

| <i>Contents</i> | <i>Page</i> |
|---|-------------|
| Acknowledgments | iii |
| Abstract | v |
| List of Figures | viii |
| List of Tables | xii |
| Notations | xii |
| 1 INTRODUCTION | 1 |
| 1.1 General introduction | 1 |
| 1.2 Motivation of the thesis | 3 |
| 1.3 Objectives and Scope of study | 4 |
| 1.4 Outline of the thesis | 6 |
| 1.5 Original contributions of the thesis | 6 |
| 1.6 List of Publications | 7 |
| 2 FUNDAMENTALS | 9 |
| 2.1 Material model | 9 |
| 2.1.1 Elastic perfectly plastic and rigid perfectly plastic material models | 9 |
| 2.1.2 Drucker's stability postulate | 12 |
| 2.1.3 Normal rule | 12 |
| 2.2 Yield condition | 13 |
| 2.2.1 Plastic dissipation function | 16 |
| 2.2.2 Variational principles | 16 |
| 2.3 Shakedown analysis | 17 |
| 2.3.1 Introduction | 17 |
| 2.3.2 Fundamental of shakedown analysis | 19 |
| 2.4 Summary | 27 |

| | | |
|----------|--|-----------|
| 2.5 | Primal-dual interior point methods | 28 |
| 3 | ISOGEOMETRIC FINITE ELEMENT METHOD | 30 |
| 3.1 | Introduction | 30 |
| 3.2 | NURBS | 34 |
| 3.2.1 | B-Splines basis functions | 34 |
| 3.2.2 | B-Spline Curves | 37 |
| 3.2.3 | B-Spline Surfaces | 38 |
| 3.2.4 | B-Spline Solids | 38 |
| 3.2.5 | Refinement techniques | 38 |
| 3.2.6 | NURBS | 42 |
| 3.3 | NURBS-based isogeometric analysis | 44 |
| 3.3.1 | Elements | 47 |
| 3.3.2 | Mesh refinement | 48 |
| 3.3.3 | Stiffness matrix | 48 |
| 3.4 | A brief of NURBS based on Bézier extraction | 49 |
| 3.4.1 | Bézier decomposition | 49 |
| 3.4.2 | Bézier extraction of NURBS | 50 |
| 3.5 | A brief review on Lagrange extraction of smooth splines | 54 |
| 3.5.1 | Lagrange decomposition | 54 |
| 3.5.2 | The Lagrange extraction operator | 56 |
| 3.5.3 | Rational Lagrange basis functions and control points | 57 |
| 3.5.4 | Using Lagrange extraction operators in a finite element code | 60 |
| 4 | THE ISOGEOMETRIC FINITE ELEMENT METHOD APPROACH TO LIMIT AND SHAKEDOWN ANALYSIS | 61 |
| 4.1 | Introduction | 61 |
| 4.2 | Isogeometric FEM discretizations | 62 |
| 4.2.1 | Discretization formulation of lower bound | 62 |
| 4.2.2 | Discretization formulation of upper bound and upper bound algorithm | 65 |
| 4.3 | Dual relationship between lower bound and upper bound and dual algorithm | 76 |
| 5 | NUMERICAL APPLICATIONS | 85 |
| 5.1 | Introduction | 85 |
| 5.2 | Limit and shakedown analysis of two dimensional structures | 85 |
| 5.2.1 | Square plate with a central circular hole | 85 |
| 5.2.2 | Grooved rectangular plate subjected to varying tension | 94 |

| | | |
|----------|--|------------|
| 5.3 | Limit and shakedown analysis of 3D structures | 99 |
| 5.3.1 | Thin square slabs with two different cutout subjected to tension | 99 |
| 5.3.2 | 2D and 3D symmetric continuous beam | 104 |
| 5.3.3 | Thin-walled pipe subjected to internal pressure and axial force | 109 |
| 5.4 | Limit and shakedown analysis of pressure vessel components | 113 |
| 5.4.1 | Pressure vessel support skirt | 113 |
| 5.4.2 | Reinforced Axisymmetric Nozzle | 119 |
| 5.5 | Limit analysis of crack structures | 123 |
| 6 | CONCLUSIONS AND FURTHER STUDIES | 128 |
| 6.1 | Conclusions | 128 |
| 6.2 | Limitations and Further studies | 129 |
| | References | 131 |

List of Figures

| | | |
|------|---|----|
| 2.1 | Structure model | 9 |
| 2.2 | Material models: (a) Elastic perfectly plastic; (b) Rigid perfectly plastic | 10 |
| 2.3 | Elastic perfectly plastic material model | 11 |
| 2.4 | Stable (a) and unstable (b, c) materials | 12 |
| 2.5 | Normality rule | 13 |
| 2.6 | von Mises and Tresca yield conditions in biaxial stress states | 15 |
| 2.7 | Interaction diagram (Bree diagram) | 18 |
| 2.8 | Load domain with two variable loads | 20 |
| 2.9 | Critical cycles of load for shakedown analysis [72; 84; 89] | 24 |
| 3.1 | Estimation of the relative time costs | 31 |
| 3.2 | The workchart of a design-through-analysis process | 32 |
| 3.3 | The concept of mesh in IGA | 33 |
| 3.4 | The concept of IGA: | 33 |
| 3.5 | Different types of B-Spline basis functions on the same distinct knot vector | 35 |
| 3.6 | The cubic B-Spline functions $N_i^3(\xi)$ and its first and second derivatives | 36 |
| 3.7 | Knot insertion. Control points are denoted by red circular \bullet | 39 |
| 3.8 | Knot insertion. Control points are denoted by red circular \bullet . The knots, which define a mesh by partitioning the curve into elements, are denoted by green square \blacksquare | 40 |
| 3.9 | Comparison of refinement strategies: p -refinement and k -refinement . . | 41 |
| 3.10 | A circle as a NURBS curve | 43 |
| 3.11 | Bent pipe modeled with a single NURBS patch. (a) Geometry. (b) NURBS mesh with control points. (c) Geometry with 32 NURBS elements | 44 |
| 3.12 | Flowchart of a classical finite element code | 45 |
| 3.13 | Flowchart of a multi-patch isogeometric analysis code | 46 |
| 3.14 | Isogeometric elements. The basis functions extend over a series of elements | 48 |
| 3.15 | Bézier decomposition of $\Xi = [0, 0, 0, 0.25, 0.5, 0.75, 1, 1, 1]$ | 50 |
| 3.16 | The Bernstein polynomials for polynomial degree $p = 1, 2, 3$ and 4. . . | 52 |

| | | |
|------|--|-----|
| 3.17 | Smooth C^2 -continuous curve represented by a B-spline basis | 54 |
| 3.18 | Smooth C^2 -continuous curve represented by a nodal Lagrange basis | 55 |
| 3.19 | Demonstration of the Lagrange extraction operators in 1D case and their inverse for the transformation of B-spline, Lagrange on an element level. The second B-Splines element of the example curve is shown in Fig 3.17 | 57 |
| 3.20 | Demonstration of the Lagrange extraction operators in 2D case and their inverse for the transformation of NURBS and Lagrange on an element level. The first NURBS element of 2D case example is shown in Fig. 3.20(a) | 59 |
| 4.1 | Flow chart for the upper bound algorithm for shakedown analysis | 75 |
| 4.2 | Flow chart for the primal-dual algorithm for shakedown analysis | 84 |
| 5.1 | Square plate with a central hole: Full (a) and symmetric geometry (b). | 86 |
| 5.2 | Square plate with central circular hole: Quadratic NURBS mesh with 32 elements and control net. | 86 |
| 5.3 | The convergence of the IGA compared with those of different methods for limit analysis (with $P_2 = 0$) of the square plate with a central circular hole. | 87 |
| 5.4 | The limit load domain of the square plate with a central circular hole using the IGA compared with those of other numerical methods. | 88 |
| 5.5 | Limit and shakedown load factors for square plate with a central hole | 89 |
| 5.6 | Influency parameter of ε, c and τ | 92 |
| 5.7 | Full geometry and applied load of grooved rectangular plate. | 93 |
| 5.8 | A symmetry of the grooved rectangular plate: a) A symmetric model including applied loads and boundary conditions; b) 2D control point net and 40 NURBS quadratic elements. | 94 |
| 5.9 | Limit load factors of the plate with tension of a strip with semi-circular notches. | 95 |
| 5.10 | Limit and shakedown load factors for the grooved rectangular plate subjected to both tension and bending loads. | 97 |
| 5.11 | Influency parameter of ε, c and τ | 98 |
| 5.12 | The 2D view geometry of thin square slabs with two different cutouts subjected to biaxial loading. | 100 |
| 5.13 | The 3D geometry of thin square slabs with two different cutouts subjected to biaxial loading. | 100 |

| | | |
|------|--|-----|
| 5.14 | The 3D quadrant NURBS meshes of thin square slabs with two different cutouts: (a)-Circular cutout and (b)-Square cutout | 100 |
| 5.15 | Finite element discretization using quartic NURBS elements for thin square slabs with two different cutouts. | 101 |
| 5.16 | Convergence of limit load factors using the IGA solution in comparison with those of other methods for thin square slabs with two different cutouts: a) circular; b) square. | 102 |
| 5.17 | Influency parameter of ε, c and τ for 3D circular cutout. | 103 |
| 5.18 | Geometry and loading of the continuous beam | 104 |
| 5.19 | Continuous beam: (a) 2D NURBS mesh and (b) 3D NURBS mesh. | 105 |
| 5.20 | 2D Continuous beam: Convergence of limit and shakedown load factors in comparison with those of two other methods. | 107 |
| 5.21 | Influency parameter of ε, c and τ | 109 |
| 5.22 | A thin-walled pipe subjected to internal pressure and axial force: a) Full model subjected to internal pressure and axial uniform loads; b) Cubic mesh and control net; c) a quarter of the model with symmetric conditions imposed on the oxz, oyz and oxy surface. | 110 |
| 5.23 | The limit load domain of the IGA compared with exact solution for thin-walled pipe problem. | 111 |
| 5.24 | The limit load domain of the IGA compared with exact solution for thin-walled pipe problem: a) Limit Analysis; b) Shakedown analysis. | 112 |
| 5.25 | Influency parameter of ε, c and τ | 112 |
| 5.26 | The pressure vessel skirt: Three quarter of full 3D model. | 113 |
| 5.27 | Axisymmetric model of the pressure vessel skirt | 114 |
| 5.28 | Limit analysis: Convergence of limit load factors for the pressure vessel skirt. | 115 |
| 5.29 | Shakedown analysis: Convergence of shakedown load factors for the pressure vessel skirt. | 115 |
| 5.30 | Influency parameter of ε, c and τ | 116 |
| 5.31 | The reinforced nozzle model and geometry: Three quarter of full 3D model. | 117 |
| 5.32 | The reinforced nozzle model and geometry: Geometry of the axisymmetric model | 118 |
| 5.33 | The NURBS mesh of the reinforced axisymmetric nozzle | 119 |
| 5.34 | Convergence of limit load factors for the reinforced axisymmetric nozzle. | 121 |
| 5.35 | Convergence of shakedown load factors for the reinforced axisymmetric nozzle. | 121 |
| 5.36 | Influency parameter of ε, c and τ | 122 |

| | |
|--|-----|
| 5.37 Full geometrical and dimensional model | 123 |
| 5.38 The half model of the cylinder with longitudinal crack subjected to internal pressure | 124 |
| 5.39 NURBS mesh of the half model for the cylinder subjected to internal pressure with a longitudinal crack | 124 |
| 5.40 Limit load factors of the cylinder with a longitudinal crack under internal pressure | 127 |

List of Tables

| | | |
|------|--|-----|
| 5.1 | Collapse load multiplier for square plate | 90 |
| 5.2 | Influence of parameter ε , ($c = 10^{10}$ and $\tau = 0.9$) | 91 |
| 5.3 | Influence of parameter c , ($\varepsilon = 10^{-10}$ and $\tau = 0.9$). | 91 |
| 5.4 | Influence of parameter τ , ($\varepsilon = 10^{-10}$ and $c = 10^{10}$) | 93 |
| 5.5 | Collapse multiplier for the grooved rectangular plate subjected to constant pure tension: Comparison of limit load multipliers for different approaches. | 96 |
| 5.6 | Elastic shakedown analysis load multiplier for the grooved rectangular plate subjected to both tension p_N and bending p_M with the defined load domains $p_N \in [0 \ \sigma_y]$ and $p_M \in [0 \ \sigma_y]$ | 96 |
| 5.7 | Influence of parameter ε , ($c = 10^{10}$ and $\tau = 0.9$) | 98 |
| 5.8 | Influence of parameter c , ($\varepsilon = 10^{-10}$ and $\tau = 0.9$) | 99 |
| 5.9 | Influence of parameter τ , ($\varepsilon = 10^{-10}$ and $c = 10^{10}$) | 99 |
| 5.10 | The limit load factor of the IGA in comparison with those of other methods for thin square slabs with two different cutouts. | 101 |
| 5.11 | Shakedown load factor of the symmetric continuous beam with various load domains | 105 |
| 5.12 | Influence of parameter ε^2 , ($c = 10^{10}$ and $\tau = 0.9$) | 106 |
| 5.13 | Influence of parameter c , ($\varepsilon = 10^{-10}$ and $\tau = 0.9$). | 108 |
| 5.14 | Influence of parameter τ , ($\varepsilon = 10^{-10}$ and $c = 10^{10}$) | 108 |
| 5.15 | Collapse multiplier for the vessel pressure skirt: Comparison of limit load multipliers for different approaches | 117 |
| 5.16 | Collapse multiplier for the reinforced axisymmetric nozzle: Comparison of limit load multipliers for different approaches | 120 |
| 5.17 | Collapse multiplier for the cracked cylinder subjected to internal pressure: Comparison of limit load multipliers for different approaches | 126 |

Notations

Ω : volume of the body.

Γ_u, Γ_t : boundary regions.

t : thickness.

IGA: Isogeometric Analysis

NURBS: Non-Uniform Rational Basis Spline.

ξ_i : a knot value.

Ξ : a knot vector.

p : polynomial degree.

\mathbf{N} : B-Splines basis function matrix.

N : B-Splines basis functions.

\mathbf{R} : NURBS basis function matrix.

R : NURBS basis functions.

\mathbf{P} : a set of control points.

\mathbf{P}^b : a set of Bézier control points.

\mathbf{P}^l : a set of Lagrange control points.

\mathbf{W}_b : the Bézier weights

$\mathbf{C}(\xi)$: B-spline curve.

$\mathbf{S}(\xi, \eta)$: B-spline surface.

$\mathbf{V}(\xi, \eta)$: B-spline solid.

-
- \mathbf{K} : global stiffness matrix.
- \mathbf{K}^e : element stiffness matrix.
- \mathbf{B}^e : element deformation matrix.
- \mathbf{f} : body force in Ω .
- \mathbf{f}_t : traction on Γ_t .
- J : Jacobian matrix.
- E : constitutive matrix of elastic stiffnesses.
- C^e : the Bézier extraction operator.
- D^e : the Lagrange extraction operator.
- \mathbf{e}_{ik} : the new strain rate vector.
- \mathbf{t}_{ik} : the new fictitious elastic stress vector.
- $\hat{\mathbf{B}}_{ik}$: the new deformation matrix.
- F_P : the penalty function.
- F_{PL} : the Lagrange function.
- E : Youngth's modulus.
- ν : Poisson ratio.
- $\boldsymbol{\sigma}$: general stress.
- $\sigma_x, \sigma_y, \sigma_z, \tau_{xy}, \tau_{yz}, \tau_{zx}$: stress components.
- $\sigma_1, \sigma_2, \sigma_3$: principal normal stress.
- f : Yield function.
- $\boldsymbol{\rho}$: residual stress field.
- $\boldsymbol{\epsilon}$: General strain.
- $\dot{\boldsymbol{\epsilon}}^p$: plastic strain rate.

1

INTRODUCTION

1.1 General introduction

Plastic analysis plays a significant role in safety assessment and structure design, especially in nuclear power plants, chemical industry, metal forming and civil engineering. Plastic collapse takes place when the structure is converted into a mechanism by development of suitable number and disposition of plastic hinges. The most important outcomes of a plastic structural analysis is a plastic collapse factor. It is useful for the reliable and economical safety assessment and design of ductile structures.

Based on the elastic-perfectly plastic model of material, the theory of limit and shakedown have been developed since the early twentieth century. Review of early contributions to the development of limit analysis theory should include the works of Kazincky [1] in 1914 and Kist [2] in 1917. The first complete formulation of the lower and upper theorems was introduced by Drucker *et al.* [3] in 1952. Contributions of Prager [4] and Martin [5] can be found in their works in 1972 and 1975, respectively. The application of limit analysis theory in computational mechanics have been widely reported since then, among publications concerning the problem are the application of limit analysis structural engineering by Hodge [6–8] in 1959, 1961 and 1963 respectively, Chakrabarty [9] in 1998, Lubliner [10] in 1990. Pham [11–14] proposed the powerful shakedown theorems which can be constructed for certain classes of elastic plastic materials.

Although there exist analytical solutions to deal with the problems of limit and shakedown analysis [15; 16], they are limited in solving simple cases and are not available for general problems in practical application [3; 17]. Traditionally, limit and shakedown

load multipliers can be obtained using upper bound and lower bound methods. The first method based on Koiter's kinematic theorem [15] uses displacement rates as main variables and leads to a minimization problem. The second method, which uses stresses as main variables, is based on Melan's static theorem [16]. This procedure leads to a maximization problem. The numerical solutions of limit analysis can be divided into two steps called discretizing problem fields and solving optimizations. The first step can be done by many numerical approaches such as finite element methods [18–36], boundary element methods [37–47], meshfree methods [48–53] and isogeometric analysis (IGA) [40–47; 54–67]. The second step involves to solve optimization problems which become either linear or non-linear programming to obtain a solution. In order to solve optimization problems for limit analysis problems, many approaches can be listed such as basic reduction technique [24], interior-point method [27; 68], linear matching method (LMM) [69–71], second order cone programming (SOCP) [48; 51; 55]. However, the duality of the kinematic upper bound and static lower bound is not practically applied in numerical simulations. For one thing, the upper bound approach deals with problems caused by the incompressibility. For the other, the lower bound approach solves a large system of nonlinear inequalities. In order to get over the difficulty, the primal-dual interior-point method was developed by Andersen *et al.* [25; 26] and these algorithms are the optimization tool which is very effective for limit analysis of structures [27]. In addition, it was proved that the primal-dual interior-point algorithm associated with the Newton iteration yields correct results in limit and shakedown analysis [28; 72].

Although a lot of numerical methods has been developed over many years, a better numerical method is still needed in engineering practice. In recent years, the isogeometric analysis (IGA) is introduced by Hughes *et al.* [73; 74]. This method allows us integrate the computer aided geometric design (CAGD) representations directly into the element finite formulation. The isogeometric finite element formulation uses Non-uniform rational basis spline (NURBS) instead of the Lagrange interpolation in the FEM. The NURBS can provide higher continuity of derivatives in comparison with Lagrange interpolation functions. In addition, the order of the NURBS function can be easily elevated without changing the geometry or its parameterization. The computational aspects of the NURBS function increase the question of how to implement efficiently the NURBS function in the existing FEM codes due to a significant differences between the NURBS basis function and the Lagrange function. The first attempt to answer this question is Bézier extraction. To ease the integration of NURBS in an existing finite element context, Borden *et al.* [75], Scott *et al.* [76] developed FE data structures based on Bézier extraction of NURBS and T-splines. The Bézier extraction operator decomposes the NURBS based elements to C^0 continuous Bézier elements which bear

a close resemblance to the Lagrange elements. The global smoothness of NURBS is localized to an element level similar to FEA, making isogeometric analysis compatible with existing FE codes while still utilizing the excellent properties of the spline basis functions as a basis for modelling and analysis. Isogeometric data structures based on Bézier extraction are therefore one of the most promising steps towards integration of CAD and FEA. A Bézier extraction operator can be established for each element that casts the relation between the vector of smooth basis functions and the vector of Bernstein polynomials concisely in matrix form. Bézier projection is a technique for obtaining an approximate L^2 projection of a function onto the smooth spline basis that uses only local element-level operations. This significantly decreases computational cost as compared to global projection (which requires the formation and solution of a global system of equations), but still converges optimally and leads to results that are virtually indistinguishable from global projection. More recently, Dominik Schillinger and co-worker has been introduced Lagrange extraction [77] which is similar to Bézier extraction but it sets up a direct connection between NURBS and Lagrange polynomial basis functions instead of using C^0 Bernstein polynomials as a new shape function in the Bézier extraction. In addition, it is very simple and compact to establish the algorithms compared with Bézier extraction. As a result, it was shown that algorithmic simplifications adopt isogeometric capabilities in the standard FEA codes.

In attempts to enhance the accuracy of the limit and shakedown analysis solution, adaptive mesh refinement becomes rather important. It is known that localized plastic deformations cause the slow convergence of the numerical approaches [78]. Therewith, the mesh should be automatically refined along plastic zones. Theoretically, the error-based indicator has to be known to conduct adaptive mesh refinement. Then, several alternative indicators related to the plastic dissipation and both the static and kinematic bound problems are studied in Refs [64; 73; 79; 80]. This research direction is also studied by many reseachers in literature.

Based on the foregoing discussion, it can be seen that an efficient method which is called "NURBS based on Bézier or Lagrange extraction in combination with primal-dual algorithm" to estimate simultaneously upper bound and quasi-lower bound limit load factor based on the von Mises yield criterion for structures in practical engineering is desirable in this research.

1.2 Motivation of the thesis

There are two approaches existing in literature to estimate the limit load factor of structures in the problems of limit and shakedown analysis such as analytical methods

and numerical methods. The former is limited in solving simple problems and is not suitable for general problems in practical application. The later has two methods called step by step method and direct method. The step by step method also called incremental methods is based on incremental evaluations of the nonlinear stress-strain relations of flow theory. However, incremental methods may be computationally expensive because of the need to perform an analysis in an iterative manner. The direct method directly computes the shakedown load factor without intermediate steps by combining a finite element discretisation and constrained optimization. The practical application of limit and shakedown analysis is widely used in the realistic engineering structures by the direct method. Although both theoretical and numerical investigations on limit and shakedown analysis reported in the literature are studied by many researchers, a better robustness and efficiency method are still needed in engineering practice. There are some approaches to solve optimization problems using in the direct method such as basic reduction technique [24], interior-point method [27; 68], linear matching method (LMM) [69–71], second order cone programming (SOCP) [48; 51; 55]. The lower or upper bound load multiplier can be obtained based on following static theorem or kinematic theorem to discretise problem, respectively.

Current research in the field of limit and shakedown analysis is focussing on the development of numerical tools which are sufficiently efficient and robust to be of use to engineers working in practice. Based on mathematical algorithms and numerical tools, there are many approaches to solve limit and shakedown problems such as: different numerical methods, finite elements [18–36], boundary element methods [37–47], smoothed finite elements [81; 82] and meshfree methods [48–51]. These methods are based on lower or upper bound approaches. However, simultaneously solving of the lower or upper bound methods is very difficult in practical engineering simulations. The difficulty of the lower bound method deals with problems caused by a large system of nonlinear inequalities while the difficulty of the upper bound method solves problems of the incompressibility.

The research motivation of the thesis is to develop an Isogeometric Finite element method based on efficient dual algorithm for limit and shakedown analysis of structures made of elastic perfectly plastic material with von Mises yield criterion.

1.3 Objectives and Scope of study

The aim of this research is to contribute to the development of robust and efficient algorithms for the limit and shakedown analyses of structures. As mentioned in Section 1.2, limit and shakedown analysis are involved the discretization method and

mathematical optimization. The work will focus on the two problems researched in this area.

- The first aim of the research is to develop so-called "*Isogeometric Finite Element Method*", which have been developed in recent years to change paradigm in Finite Element Analysis, for limit and shakedown analyses of structures. IGA has been applied successfully a lot of mechanics problems in the literature [43; 61–63; 66; 67; 73; 76; 77; 83] and so on. The IGA allows both CAD and FEA to use the same basis NURBS-based functions. Although IGA becomes an effective numerical method due to some advantages such as an exact geometry description with fewer control points, high-order continuity, and high accuracy, this method also exists some disadvantages. One of these advantages is that the high-order basis functions in IGA are not confined to one element. This property makes the programming task difficult, and more importantly they cannot be straightforwardly embedded into the existing FEM framework. The concept of Bézier extraction, which was introduced in detail by Borden *et al.* [76], has proved a milestone in this regard and has revolutionized the way IGA capabilities are implemented. The structure of Bézier elements allows the integration of IGA in existing standard FEA codes, which are typically built around element subroutines. Through this extraction operator, a set of NURBS basis functions can be decomposed into linear combinations of Bernstein polynomials. This significantly decreases computational cost as compared to global projection (which requires the formation and solution of a global system of equations), but still converges optimally and leads to results that are virtually indistinguishable. More recently, Dominik Schillinger and co-worker has been introduced Lagrange extraction [77] which is similar to Bézier extraction but it sets up a direct connection between NURBS and Lagrange polynomial basis functions instead of using C^0 Bernstein polynomials as a new shape function in the Bézier extraction.

- The second aim of the research is to solve the nonlinear optimization problem with constraints. There are many approaches to efficiently solve optimization problem for limit and shakedown analysis problems such as basic reduction technique [24], interior-point method [27; 68], linear matching method (LMM) [69–71], second order cone programming (SOCP) [48; 51; 55].

In order to archive the specific aims of this research, the following tasks will be undertaken:

- Develop a kinematic limit and shakedown formulation based on the Isogeometric Finite Element Method.

- Investigate a complete solution procedure for the discretization formulation of lower bound and upper bound using the IGA based on Bézier extraction of NURBS in combination with the primal-dual algorithm.
- Investigate a complete solution procedure for the discretization formulation of lower bound and upper bound using Lagrange extraction for NURBS basis function in combination with the primal-dual algorithm.

1.4 Outline of the thesis

This research deals with limit and shakedown analyses of engineering structures. It consists of six chapters, including the general introduction. Two of these (chapters 4 and 5) are presented as self-contained in papers which have been published in the scientific journal. As a result, minor overlaps of the contents in the papers may occur here. The contents of each chapter are briefly described as follows.

Chapter 2 present the two fundamental of limit and shakedown theories, the static and kinematic theorems which proposed by Melan and Koiter. The fundamental relations governing elastic, limit and shakedown analysis are given, based on the books by Martin [5], König [84] and Kazinczy [1]. The assumptions in limit and shakedown analysis within the static and kinematic approaches are briefly explained.

Chapter 3 is to review the theory of isogeometric analysis. A summary of the main ideas behind isogeometric analysis and isogeometric finite element discretizations is given such as B-Splines, NURBS objects, their definition and basic properties. The isogeometric analysis based on Bézier extraction and Lagrange extraction are also presented in this chapter.

Chapter 4 considers the discretization of static and kinematic limit and shakedown analysis with the help of isogeometric finite element method. Dual theorems in discretized forms are presented together with kinematic and dual algorithms.

Some various typical examples of limit and shakedown analysis are illustrated to show and validate the present approach in *Chapter 5*. Numerical results are tested and compared with analytical solutions or available solutions in literature.

Finally, *Chapter 6* contains some main conclusions and future studies.

1.5 Original contributions of the thesis

According to the author's knowledge, the original contributions of the thesis are:

- Development of a kinematic limit and shakedown analysis formulation based on isogeometric analysis by Bézier extraction extraction NURBS.

- Development of a kinematic limit and shakedown analysis formulation based on isogeometric analysis by Lagrange of extraction NURBS.
- Development of a novel numerical approach for evaluating limit and shakedown load factors of 2D, 3D structures and pressure vessel components for application in piping engineering.
- Improvement of the efficiency of the proposed limit analysis and shakedown procedures by integration of some advantages of the IGA in terms of flexibility in refinement, exact geometry that lead the more accurate solutions in comparison with other available.
- Investigation of the isogeometric analysis based on Bézier extraction and Lagrange extraction which can integrate IGA into the existing FEM codes in combination with primal-dual algorithm in computation of limit and shakedown load factors.

1.6 List of Publications

Some of the materials reported in this research have been published in international journals and presented in conferences. These papers are:

1. **Hien V. Do**, H. Nguyen-Xuan, Limit and shakedown isogeometric analysis of structures based on Bezier extraction, *European Journal of Mechanics- A/Solids*, 63, 149-164, 2017.
2. **Hien V. Do**, H. Nguyen-Xuan, Computation of limit and shakedown loads for pressure vessel components using isogeometric analysis based on Lagrange extraction, *International Journal of Pressure Vessels and Piping*, 169, 57-70, 2019.
3. H. Nguyen-Xuan, **Hien V. Do**, Khanh N. Chau, An adaptive strategy based on conforming quadtree meshes for kinematic limit analysis, *Computer Methods in Applied Mechanics and Engineering*, 341, 485-516, 2018.
4. **Hien V. Do**, H. Nguyen-Xuan, Isogeometric analysis of plane curved beam, *The National Conference on Engineering Mechanics*, at the Da Nang University, Da Nang.
5. **Hien V. Do**, H. Nguyen-Xuan, Application of Isogeometric analysis to free vibration of Truss structures, *The 12th National Conference on Solid Mechanics at the Duy Tan University*.

6. **Do Van Hien**, Ho Ngoc Bon, Van Huu Thinh, Limit analysis for plane stress problem by using NURBS based on Be1zier extraction in combination with second order cone program, Journal of Technical Education Science, 52, 17-24, 2019.

2

FUNDAMENTALS

In this chapter, a fundamental of shakedown analysis theory in many of previous works [3; 6; 10; 15; 28; 72], which is necessary for the developments in the subsequent chapters, is overviewed. Firstly, an overview introduction of material model and yield condition are presented. Then, shakedown analysis formulation based on classical shakedown theorems is established and discussed.

2.1 Material model

2.1.1 Elastic perfectly plastic and rigid perfectly plastic material models

A structural model used is a bounded domain Ω occupied by a rigid or elastic perfectly-plastic material continuum as shown in Fig 2.1

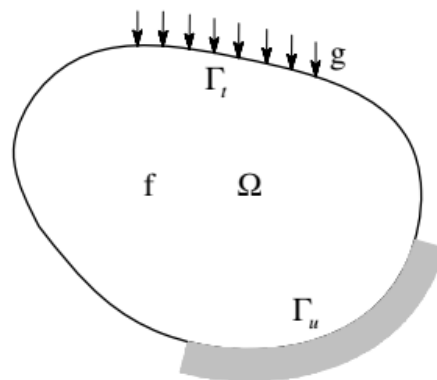


Figure 2.1: Structure model

The boundary of the body consists of two regions Γ_u and Γ_t . On Γ_u , the boundary is fixed so that $\dot{\mathbf{u}} = 0$, where $\dot{\mathbf{u}} = \dot{\mathbf{u}}(\mathbf{x})$ represents the plastic displacement rates at \mathbf{x} point in Ω . Applied forces to model include surface forces \mathbf{g} on Γ_t and body forces \mathbf{f} on Ω . There are some material models applied in continuum mechanics to describe the response of real materials to various loading conditions to model actual stress-strain relations: linear elastic, rigid perfectly plastic, rigid hardening, linear elastic perfectly-plastic and linear elastic-plastic hardening. In our work, the material models rigid perfectly plastic and linear elastic perfectly-plastic as shown in Fig 2.2 (a and b) are assumed throughout.

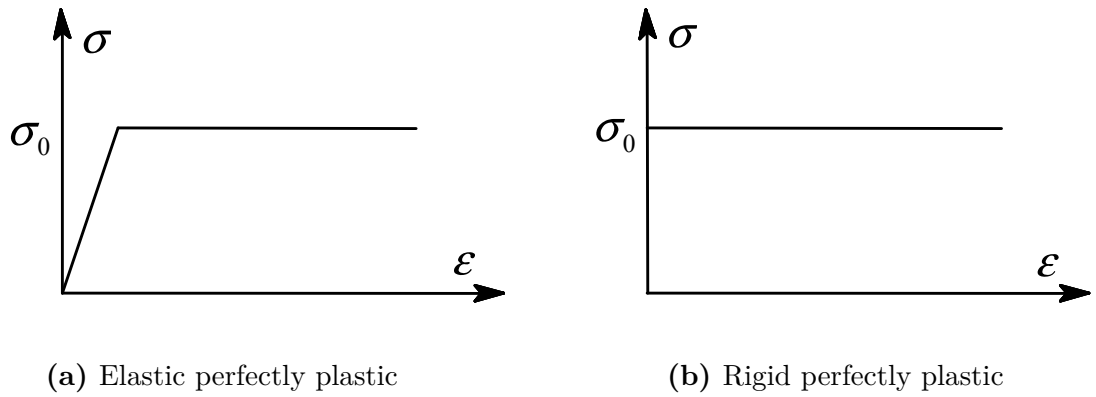


Figure 2.2: Material models: (a) Elastic perfectly plastic; (b) Rigid perfectly plastic

Elastic perfectly plastic is the simplest elasto-plastic model of material. The properties of this model are summarized:

- Material behaves elastically below the yield stress and obeys the Hook's law of linear elasticity as

$$\varepsilon_{ij}^e = C_{ijkl}^{-1} \sigma_{kl} \quad (2.1)$$

where C_{ijkl} is a fourth-rank tensor. For an isotropic material, this tensor is expressed in the form below

$$C_{ijkl} = \frac{\nu E}{(1 + \nu)(1 - 2\nu)} \delta_{ij} \delta_{kl} + \frac{E}{2(1 + \nu)} (\delta_{ik} \delta_{jl} + \delta_{il} \delta_{jk}) \quad (2.2)$$

where E denotes the Young's modulus, ν is the Poisson ratio, and δ_{**} is the Kronecker delta. The inverse relationship of Eq. 2.1 can be written as

$$\sigma_{ij} = 2G\varepsilon_{ij}^e + \frac{2\nu}{(1 - 2\nu)} G \delta_{ij} \varepsilon_{ij}^e \quad (2.3)$$

where $G = \frac{E}{2(1+\nu)}$ is the shear modulus of elasticity.

- When the stress reaches the yield value σ_o , unlimited plastic flow may be observed in the material under constant stress σ . During this flow, there is no stress increment. The plastic strain increment $d\varepsilon^p$ must have the same sign as the stress so as

$$\sigma d\varepsilon^p \geq 0 \quad (2.4)$$

- The material behaves purely elastically during the unloading process. The deformation in this case is illustrated in Fig 2.3 by a straight line 2-3 parallel with the initial line 0-1. The relation between stress and strain also follows the Hook's law

$$d\sigma = C d\varepsilon^e \quad (2.5)$$

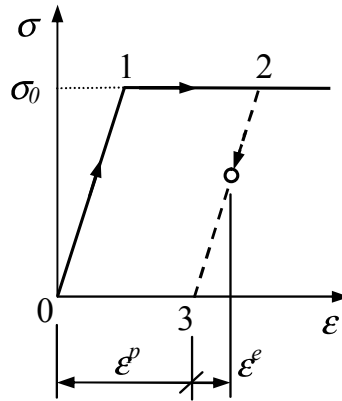


Figure 2.3: Elastic perfectly plastic material model

- During a certain loading process, the total strain in the material can be expressed by the sum of elastic strain ε^e and plastic strain ε^p

$$\varepsilon = \varepsilon^e + \varepsilon^p \quad (2.6)$$

and the total strain rates can be also written by sum of elastic strain rate and plastic strain rate as

$$\dot{\varepsilon} = \dot{\varepsilon}^e + \dot{\varepsilon}^p \quad (2.7)$$

2.1.2 Drucker's stability postulate

Material are also assumed to be stable in Drucker's sense during a complete cycle of loading and unloading. Drucker accordingly defines a plastic material if the two following conditions hold true:

- + The work done during incremental loading is positive

$$\dot{\sigma}_{ij}\dot{\varepsilon}_{ij} > 0 \quad (2.8)$$

- + The work done in the loading and unloading cycle is non-negative

$$\oint (\sigma_{ij} - \sigma_{ij}^o) d\varepsilon_{ij} \geq 0 \quad (2.9)$$

where \oint sign is the integral taken over the complete cycle of loading and unloading. σ_{ij} is the stress tensor on the yield surface satisfying the yield condition $f(\sigma_{ij}) = 0$ and σ_{ij}^o is the plastically admissible stress tensor, lying inside or on the yield surface satisfying $f(\sigma_{ij}) \leq 0$. The stability postulate is shown graphically in Fig 2.4.

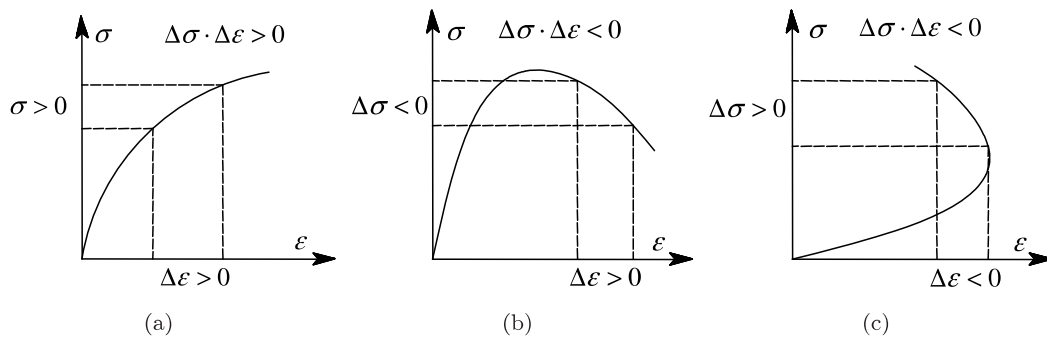


Figure 2.4: Stable (a) and unstable (b, c) materials

2.1.3 Normal rule

As we known, the outward-pointing normal to a surface called $f(\mathbf{x})$ at a point x_i is a vector perpendicular to its tangent plane. The gradient of f , $\frac{\partial f}{\partial x_i}$ at point x_i is in the direction normal to this surface. The normality rule must be enforced at any stress point in plasticity. The strain rate tensor $\dot{\varepsilon}^p$ must be normal to the yield surface at a smooth point or lie between the adjacent normals at non-smooth point (see Fig. 2.5). This rule may be represented as:

$$\dot{\varepsilon}_{ij}^p = \lambda \frac{\partial f}{\partial \sigma_{ij}} \quad (2.10)$$

When n differentiable surfaces intersect at a singular point, the relationship Eq 2.10 should be represented by:

$$\dot{\epsilon}_{ij}^p = \sum_{k=1}^n \dot{\lambda}_k \frac{\partial f_k}{\partial \sigma_{ij}} \dot{\sigma}_{ij} \quad (2.11)$$

where $\dot{\lambda}$ is non-negative plastic factor.

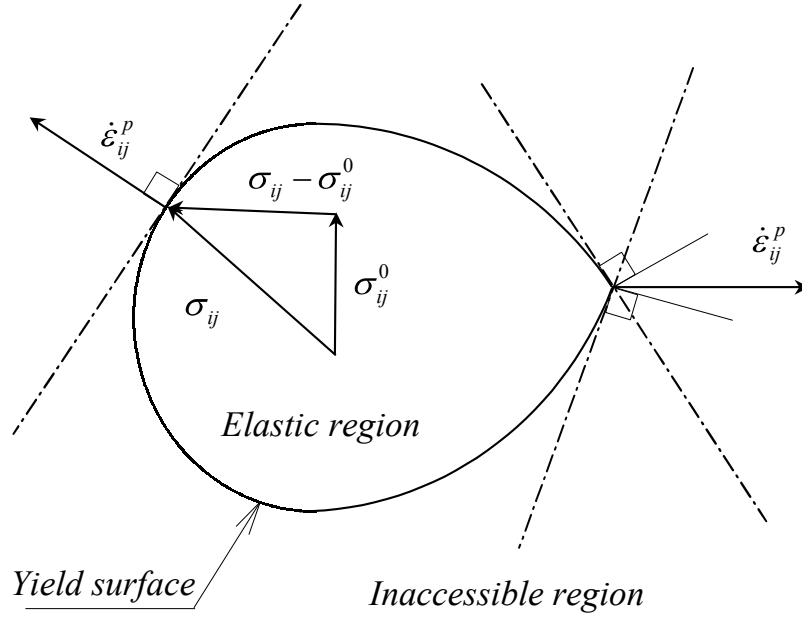


Figure 2.5: Normality rule

Materials that obey Drucker's stability postulate must have their plastic yield function $f(\sigma_{ij})$ convex in the stress space σ_{ij} . The convexity of the yield surface has a very important role in plasticity. It allows the use of convex programming tools in limit and shakedown analysis.

2.2 Yield condition

The yield conditions are used to define the valid range of Hook's law and the constitutive equations in the presence of plastic deformations. An assumption exists a yield function $f(\sigma_{ij})$ which has a following properties:

- $f(\sigma_{ij}) < 0$ corresponds to the elastic behavior
- $f(\sigma_{ij}) = 0$ corresponds to the appearance of plastic deformation
- $f(\sigma_{ij}) > 0$ is inaccessible region

Based on the properties of the yield function, the stress point can not move outside the yield surface. Plastic flow occurs only when stress point is on yield surface and the additional loading σ_{ij} move along the tangent direction. The yield function is simplified by a set of assumptions which makes it simpler and easier to use. Firstly, the body is typically considered to be homogeneous and the material temperature and time independent. Consequently, the yield function is independent of the coordinate x , the stress rate, the strain rate, the temperature T and the time t . Secondly, the material properties are assumed to be independent of any historical elastic or plastic deformations, i.e. path-independent. As a result, the yield function can be represented by only the instantaneous stress state in the body and the material property so that

$$f = f(\sigma_{ij}, \kappa), \quad (2.12)$$

where κ is a constant representing the plastic property of the material.

Furthermore, the yield function can be simplified by the assumption that it is an isotropic material, which states that the material properties are not dependent on the transformation of coordinates. In practical engineering plasticity, the von Mises yield condition and the Tresca yield condition are the most widely used for metals. They are reviewed in the following.

2.2.1 The von Mises yield criterion

Dated in 1913, the von Mises yield criterion states that yielding will begin when octahedral shearing stress reaches a critical value κ_v such as

$$\frac{1}{\sqrt{3}\kappa_v} \sqrt{\frac{1}{2} \left[(\sigma_1 - \sigma_2)^2 + (\sigma_2 - \sigma_3)^2 + (\sigma_3 - \sigma_1)^2 \right]} = 1 \quad (2.13)$$

or written in term of stress invariant J_2 :

$$f(\sigma_{ij}) = J_2 - \kappa_v^2 = 0 \quad (2.14)$$

where $\kappa_v = \frac{\sigma_o}{\sqrt{3}}$, σ_o is the yield limit of the material. For perfectly plastic material, κ_v is a constant independent of strain history. J_2 is the second principle invariant of the stress deviator tensor σ_{ij} and in a form of principle stress

$$J_2 = \frac{1}{6} \left[(\sigma_1 - \sigma_2)^2 + (\sigma_2 - \sigma_3)^2 + (\sigma_3 - \sigma_1)^2 \right] \quad (2.15)$$

If material is subjected to a pure shear σ_{12} while all other stress components vanish ($\sigma_1 = \sigma_o; \sigma_2 = \sigma_3 = 0$), then $J_2 = \frac{\sigma_o^2}{3}$. From Eq. 2.14, The relation between yield stress in pure shear and yield stress in pure tension can be derived as $\kappa_v = \frac{\sigma_o}{\sqrt{3}}$.

2.2.2 The Tresca yield criterion

In 1864, Tresca suggested that yielding would occur when maximum shearing stress at a point in the material reaches a critical value κ_T . He proposed the yield criterion stipulating that the maximum shear stress has a constant value during plastic flow.

$$f(\sigma_{ij}) = \max \left(|\sigma_1 - \sigma_2|, |\sigma_2 - \sigma_3|, |\sigma_3 - \sigma_1| \right) - 2\kappa_T = 0 \quad (2.16)$$

In an uniaxial stress state ($\sigma_2 = \sigma_3 = 0$), the Tresca yield condition has a form:

$$f = \sigma_1 - 2\kappa_T = 0 \quad (2.17)$$

The relation between yield stress in pure shear and yield stress in pure tension can be written as: $\kappa_T = \frac{\sigma_o}{2}$.

2.2.3 Comparison between the two yield conditions

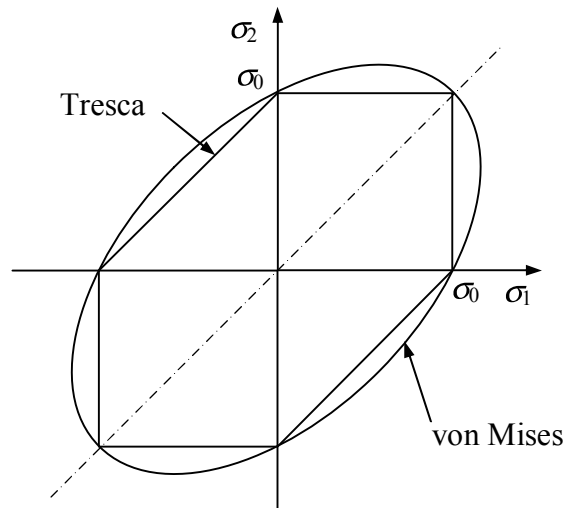


Figure 2.6: von Mises and Tresca yield conditions in biaxial stress states

The most distinctive difference between the von Mises and Tresca yield conditions is the fact that while in the former all three principal stresses have an equal "role", in the

latter the intermediate principal stresses have no effect on yielding. In the principal stress states, the von Mises yield condition is represented by a circular cylinder, and the Tresca by a regular hexagonal cylinder as illustrated in Fig 2.6. Fig 2.6 also shows the Tresca hexagon in circumscribed by von Mises ellipse.

2.2.1 Plastic dissipation function

The plastic dissipation function is defined by

$$D^p = \max (\sigma_{ij}^* \dot{\epsilon}_{ij}^p) = \sigma_{ij} \dot{\epsilon}_{ij}^p \quad (2.18)$$

where σ_{ij}^* is a plastically admissible stress tensor satisfying $f(\sigma_{ij}^*) \leq 0$. σ_{ij} is the stress tensor satisfying yield condition $f(\sigma_{ij}^*) = 0$. The plastic dissipation for the von Mises criterion and associated flow rule is given by Lubliner [10].

$$D^p = \sqrt{2} \kappa_v \sqrt{\dot{\epsilon}_{ij}^p \dot{\epsilon}_{ij}^p} \quad (2.19)$$

2.2.2 Variational principles

A structural model subjected to surface and body forces is considered as illustrated in Fig. 2.1. A statically admissible field and a kinematically admissible field are defined as follow:

1. Any stress field satisfying the equation of equilibrium and stress boundary condtion

$$-\nabla \sigma + g = 0 \quad \text{in} \quad \Omega \quad (2.20)$$

$$n\sigma = q \quad \text{on} \quad \Gamma_t \quad (2.21)$$

is called a statically admissible field.

2. A kinematically admissible strain rate and velocity fields are any deformation mode that satisfies the velocity boundary conditions, the strain rate and velocity compatible conditions:

$$\dot{\epsilon}_{ij} = \frac{1}{2} (\dot{u}_{i,j} + \dot{u}_{j,i}) \quad \text{in} \quad \Omega \quad (2.22)$$

$$\dot{u} = 0 \quad \text{on} \quad \Gamma_u \quad (2.23)$$

By using these definitions, variational principles can be stated as below:

2.2.2.1 Principle of virtual power

The principle of virtual work establishes the equilibrium state between the internal stress field and an external force field acting on the body. It states that "For an arbitrary set of infinitesimal virtual displacement variations δu_i that are kinematically admissible, the necessary and sufficient condition to make the stress tensor σ_{ij} equilibrium is to satisfy the following equation"

$$\int_{\Omega} \sigma_{ij} \delta \varepsilon_{ij} d\Omega = \int_{\Omega} g_i \delta u_i d\Omega + \int_{\Gamma_t} q \delta u d\Gamma_t \quad (2.24)$$

The principle of virtual power can be derived from the principle of the virtual work by replacing virtual strain $\delta \varepsilon$ and virtual displacement δu by kinematically admissible strain rate $\delta \dot{\varepsilon}$ and velocity $\delta \dot{u}$, respectively. The Eq. 2.24 becomes

$$\int_{\Omega} \sigma_{ij} \delta \dot{\varepsilon}_{ij} d\Omega = \int_{\Omega} g_i \delta \dot{u}_i d\Omega + \int_{\Gamma_t} q \delta \dot{u} d\Gamma_t \quad (2.25)$$

2.2.2.2 Principle of compliment virtual power

For an arbitrary set of infinitesimal virtual variations of the stress tensor $d\sigma_{ij}$ that statically admissible, the necessary and sufficient condition to make the strain tensor ε_{ij} and displacement u_i compatible is to satisfy the following equation

$$\int_{\Omega} \varepsilon_{ij} \delta \sigma_{ij} = \int_{\Gamma_t} n_j \delta \sigma_{ij} \bar{u}_i d\Gamma_t \quad (2.26)$$

The principle of compliment virtual power can be derived when expressing the works in the term of stress and force rates as:

$$\int_{\Omega} \dot{\varepsilon}_{ij} \delta \sigma_{ij} = \int_{\Gamma_t} n_j \delta \sigma_{ij} \dot{\bar{u}}_i d\Gamma_t \quad (2.27)$$

2.3 Shakedown analysis

2.3.1 Introduction

The loading in limit analysis considered above is simple and proportional. However, practical structures are often subjected to the action of varying loading. These loads may be repeated or varying arbitrarily in certain domain. In this case, different types of behavior may arise, depending on the magnitude of the loading. As a result, loads which are less than plastic collapse limit may cause the failure of the structure due to an excessive deformation or to a local break after a finite number of loading cycles. Let

us consider a structure made of perfectly plastic materials, subjected to cyclic loads may behave in one of the four ways which are presented in Bree-diagram by Bree [85] as shown in Fig 2.7, depending on the intensity and character of the applied loads.

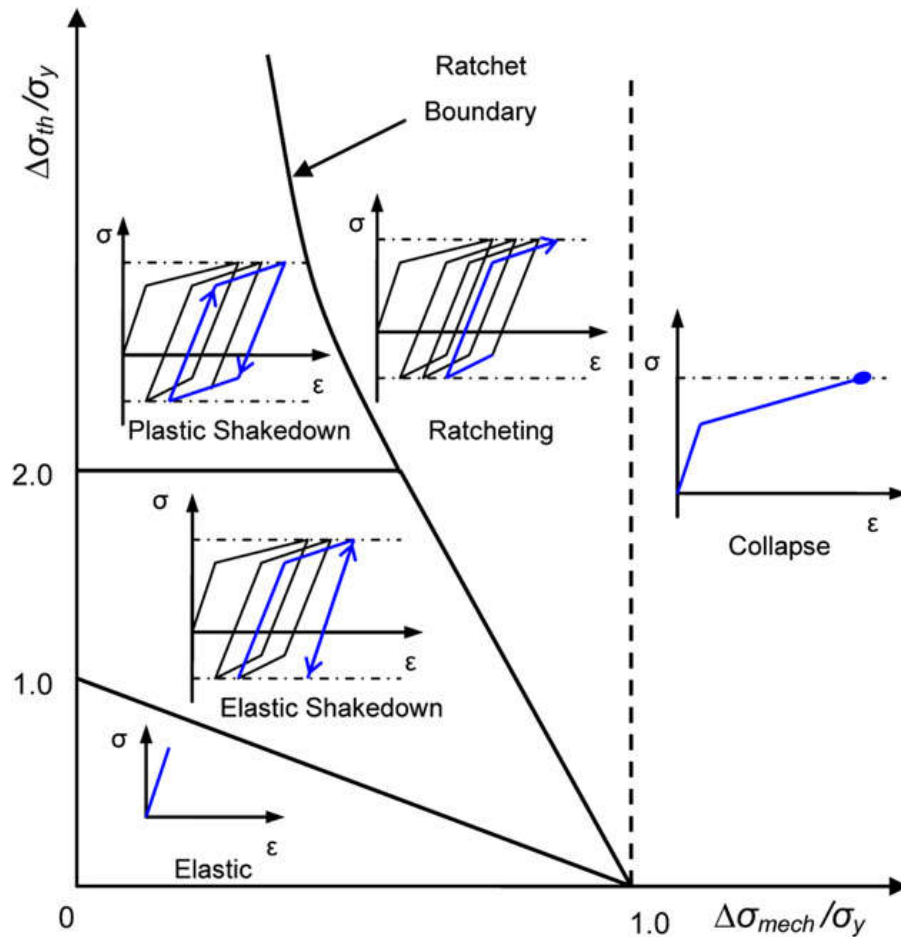


Figure 2.7: Interaction diagram (Bree diagram [85]) for thin-walled pipes for perfectly plastic material

1. *Elastic*: If the applied loads are sufficiently low, the structure response is *purely elastic*. The total stresses from all loads at any location in the component are less than the yield strength of material at all times (no plasticity).
2. *Elastic shakedown*: If the load intensities is higher than the elastic limit, but do not exceed a certain limit. Plastic deformation occurs initially and stops after some cycles. Within a few cycles, the deformations remain in the elastic range and the structure is dimensionally stabilized in purely elastic cycles.

3. *Plastic shakedown (alternating plasticity)*: After a small number of cycles the strain increments change sign at each half cycle and eventually cancel each other (summing to zero). Similar to elastic shakedown, the final response of the structure is dimensionally stable. However, the stabilized response involves plasticity during every cycle.
3. *Ratcheting (incremental collapse)*: If the cyclic loading is high enough, ratcheting will occur. Asymptotically, some dimension of the component will increase by a fixed increment with each cycle. As plastic strain increments are accumulated in some direction, strains can become so large that the structure loses its serviceability. Ratcheting also intensifies the fatigue damage; the cyclic strain-life curve will then underestimate the fatigue life of the component. Therefore, ratcheting is usually not an acceptable response in the design of a component.
4. *Collapse*: The magnitude of the applied primary load(s) is high enough that uncontained plastic flow occurs in the structure under one time load application.

The set of load combinations at the transition between shakedown and ratcheting will be called the ratchet boundary. Below the ratchet boundary, in the absence of ratcheting, the component can either shakedown to elastic or to plastic action, depending on the combination of cyclic and steady loads. The classical theorems in shakedown analysis are restricted to elastic shakedown in which the structure will only undergo elastic cycles after an initial period that may involve plasticity. It should be noted that in most of the literature the term “shakedown” (without qualifier) refers to elastic shakedown, since the upper and lower bound theorems exist presently only for elastic shakedown. The classical concepts in shakedown analysis allow the calculation of lower and upper bounds to the loads combination for which elastic shakedown can be guaranteed.

2.3.2 Fundamental of shakedown analysis

The main problem of shakedown theory is to study whether or not a structure made of certain material will shake down under prescribed loads. In general step by step approach are not applicable in solving such cumbersome task and therefore direct methods are preferred. Nevertheless even direct methods are useful in some loading conditions as well as for certain material models. Some assumptions are considered in shakedown analysis as below:

- Loading is quasi-static so that dynamic effects can be neglected.
- Material exhibits perfectly plastic with the associated flow rule without strain hardening or softening.

- Deformation and displacement are assumed to be sufficiently small so that changes in geometry can be neglected in the equilibrium equations and strain - displacement relations can be assumed in linear form:

$$\sigma_{ij,j} + f_i = 0 \quad \text{in} \quad \Omega \quad (2.28)$$

2.3.2.1 Load domain

In shakedown analysis, the applied loads may vary independently, so it is necessary to define the load domain L . This load domain contains all possible load histories. We study here the shakedown problem of a structure subjected to n time-dependent loads $\bar{P}_k^o(t)$ with time denoted by t , each of them can be vary independently within a given range

$$\bar{P}_k^o(t) \in I_k^o = [\bar{P}_k^-, \bar{P}_k^+] = [\mu_k^-, \mu_k^+] P_k^o, \quad k = 1 : n \quad (2.29)$$

These loads form a convex polyhedral domain L of n dimensions with $m = 2^n$ vertices in the load space as illustrated in Fig 2.8 for two variable loads. This load domain can be represented in the following linear form

$$P(t) = \sum_{k=1}^n \mu_k(t) P_k^o \quad (2.30)$$

where

$$\mu_k^- \leq \mu_k(t) \leq \mu_k^+, \quad k = 1 : n \quad (2.31)$$

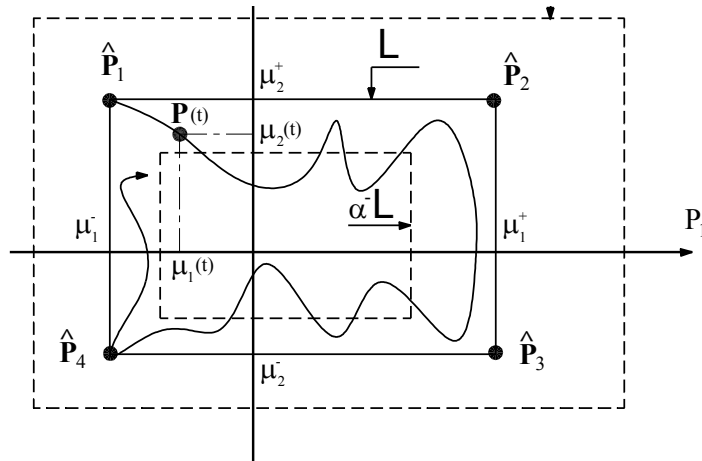


Figure 2.8: Load domain with two variable loads

In the case of limit and shakedown analysis, it is useful to describe this load domain L in the stress space. To this end, we use here the notion of a *fictitious infinitely elastic*

structure which has the same geometry as the actual one. The fictitious elastic response $\sigma_{ij}^E(\mathbf{x}, t)$ is defined as the response which would appear in the fictitious structure if this structure was subjected to the same loads as the actual one. This fictitious elastic response may be written in a form similar to Eq. 2.30:

$$\sigma_{ij}^E(\mathbf{x}, t) = \sum_{k=1}^n \mu_k(t) \sigma_{ij}^{Ek}(\mathbf{x}) \quad (2.32)$$

where $\sigma_{ij}^{Ek}(\mathbf{x})$ is the stress field in the reference (fictitious) structure when subjected to the unit load mode P_k^o .

2.3.2.2 Static or lower bound shakedown theorem (Melan)

Let $\sigma_{ij}^E(\mathbf{x}, t)$ denote the fictitious elastic stress response for all possible load combinations in the load domain L (see Eq. 2.32). If after some load cycles the structure has already shaken down, everywhere in the structure plastic deformation ceased to develop: $\varepsilon_{ij}^p = 0$. The actual stresses $\sigma_{ij}(\mathbf{x}, t)$ can be expressed by the sum of elastic stresses and another stress field $\bar{\rho}_{ij}(\mathbf{x})$ which is called the residual stress field as

$$\sigma_{ij}(\mathbf{x}, t) = \sigma_{ij}^E(\mathbf{x}, t) + \bar{\rho}_{ij}(\mathbf{x}) \quad (2.33)$$

does not anywhere violate the yield criterion

$$f(\sigma_{ij}(\mathbf{x}, t)) = f(\sigma_{ij}^E(\mathbf{x}, t) + \bar{\rho}_{ij}(\mathbf{x})) \leq 0 \quad (2.34)$$

The following theorem shows that this is the necessary and sufficient condition for a structure to shake down (for perfect plasticity see Koiter [15] in 1960):

Theorem 2.1:

1. Shakedown occurs if there exists a permanent residual stress field $\bar{\rho}_{ij}(\mathbf{x})$, statically admissible, such that:

$$f(\sigma_{ij}(\mathbf{x}, t)) = f(\sigma_{ij}^E(\mathbf{x}, t) + \bar{\rho}_{ij}(\mathbf{x})) < 0 \quad (2.35)$$

2. Shakedown will not occur if no $\bar{\rho}_{ij}(\mathbf{x})$ exists such that

$$f(\sigma_{ij}(\mathbf{x}, t)) = f(\sigma_{ij}^E(\mathbf{x}, t) + \bar{\rho}_{ij}(\mathbf{x})) \leq 0 \quad (2.36)$$

Based on the above static theorem, we can find a permanent statically admissible residual stress field in order to obtain a maximum load domain αL that guarantees that guarantees Eq. 2.36. The obtained shakedown load multiplier α^- is generally a lower bound. The shakedown problem can be seen as a maximization issue in nonlinear programming

$$\begin{aligned} \alpha^- &= \max \alpha & (a) \\ \text{subjected to:} & & (2.37) \\ \left\{ \begin{array}{ll} \partial_j \bar{\rho}_{ij}(\mathbf{x}) & = 0 \quad \text{in } \Omega & (b) \\ \bar{n}_j \bar{\rho}_{ij}(\mathbf{x}) & = 0 \quad \text{on } \Gamma_t & (c) \\ f(\alpha \sigma_{ij}^E(\mathbf{x}, t) + \bar{\rho}_{ij}(\mathbf{x})) & \leq 0 \quad \forall t & (d) \end{array} \right. \end{aligned}$$

2.3.2.3 Kinematic or upper bound shakedown theorem (Koiter)

Using plastic strain fields to formulate shakedown criterion, the kinematic shakedown theorem is the counterpart of the static one. The theorem was given by Koiter [15] in 1960 and some of its applications in analysis of incremental collapse were derived by Gokhfeld [86] in 1980, Sawczuk [87] in 1969. According to Koiter [15], an admissible cycle of the plastic strain field $\Delta \dot{\varepsilon}_{ij}^p$ is introduced, corresponding to a cycle of displacement field Δu_i . The plastic strain rate $\dot{\varepsilon}_{ij}^p$ may not necessarily be compatible at each instant during the time cycle T but the plastic strain accumulation over the cycle defined below

$$\Delta \varepsilon_{ij}^p = \int_0^T \dot{\varepsilon}_{ij}^p dt \quad (2.38)$$

must be compatible, such that

$$\Delta \varepsilon_{ij}^p = \frac{1}{2} \left(\frac{\partial \Delta u_i}{\partial x_j} + \frac{\partial \Delta u_j}{\partial x_i} \right) \quad \text{in } \Omega \quad (2.39)$$

$$\Delta u_i = 0 \quad \text{on } \Gamma_u \quad (2.40)$$

and

$$\int_{\Omega} \int_0^T \sigma_{ij}^E \dot{\varepsilon}_{ij}^p dt d\Omega > 0 \quad (2.41)$$

Theorem 2.2: [15]

1. Shakedown may happen if the following inequality is satisfied:

$$\int_0^T dt \left[\int_{\Omega} f_i \dot{u}_i d\Omega + \int_{\Gamma_t} \bar{t}_i \dot{u}_i d\Gamma_t \right] \leq \int_0^T dt \int_{\Omega} D^p(\dot{\varepsilon}_{ij}^p) d\Omega \quad (2.42)$$

2. Shakedown can not happen when the following inequality holds:

$$\int_0^T dt \left[\int_{\Omega} f_i \dot{u}_i d\Omega + \int_{\Gamma_t} \bar{t}_i \dot{u}_i d\Gamma_t \right] > \int_0^T dt \int_{\Omega} D^p(\dot{\varepsilon}_{ij}^p) d\Omega \quad (2.43)$$

Virtual power principle permits us to write Eq. 2.42 in more general form:

$$\int_0^T \int_{\Omega} \sigma_{ij}^E(\mathbf{x}, t) \dot{\varepsilon}_{ij}^p d\Omega dt \leq \int_0^T \int_{\Omega} D^p(\dot{\varepsilon}_{ij}^p) d\Omega \quad (2.44)$$

Based on the kinematic theorem, an upper bound of the shakedown limit load multiplier α^+ can be computed. The shakedown problem can be seen as a mathematical minimization problem in nonlinear programming

$$\alpha^+ = \min \frac{\int_0^T dt \int_{\Omega} D^p(\dot{\varepsilon}_{ij}^p) d\Omega}{\int_0^T dt \int_{\Omega} \sigma_{ij}^E(\mathbf{x}, t) \dot{\varepsilon}_{ij}^p d\Omega} \quad (a)$$

subjected to: (2.45)

$$\left\{ \begin{array}{l} \Delta \varepsilon_{ij}^p = \int_0^T \varepsilon_{ij}^p dt \quad \text{in } \Omega \quad (b) \\ \Delta \varepsilon_{ij}^p = \frac{1}{2} \left(\frac{\partial \Delta u_i}{\partial x_j} + \frac{\partial \Delta u_j}{\partial x_i} \right) \quad \text{in } \Omega \quad (c) \\ \Delta u_i = 0 \quad \text{on } \Gamma_u \quad (d) \end{array} \right.$$

In order to calculate the shakedown limit load multiplier, the two following methods can be applied: separated and unified methods. While the former analyses separately two different failure modes: incremental plasticity (ratchetting) and alternating plasticity, the latter analyses them simultaneously. Both methods deserve special attention due to their role in structural computation. In the following sections, unified shakedown limit is presented to find directly the shakedown limit defined by the minimum of incremental plasticity limit and alternating plasticity limit.

2.3.2.4 Unified shakedown limit

In practical computation, in most cases it is impossible to apply lower and upper theorems to find directly the shakedown limit defined by the minimum of incremental plasticity limit and alternating plasticity limit. The difficulty here is the presence of the time-dependent generalized stress field $\sigma_{ij}^E(\mathbf{x}, t)$ in Eqs. 2.35÷ 2.36. These obstacles can be overcome with the help of the following two convex-cycle theorems, introduced by König and Kleiber [84].

Theorem 2.3: [84]

"Shakedown will happen over a given load domain L if and only if it happens over the convex envelope of L ".

Theorem 2.4: [84]

"Shakedown will happen over any load path within a given load domain L if it happens over a cyclic load path containing all vertices of L ".

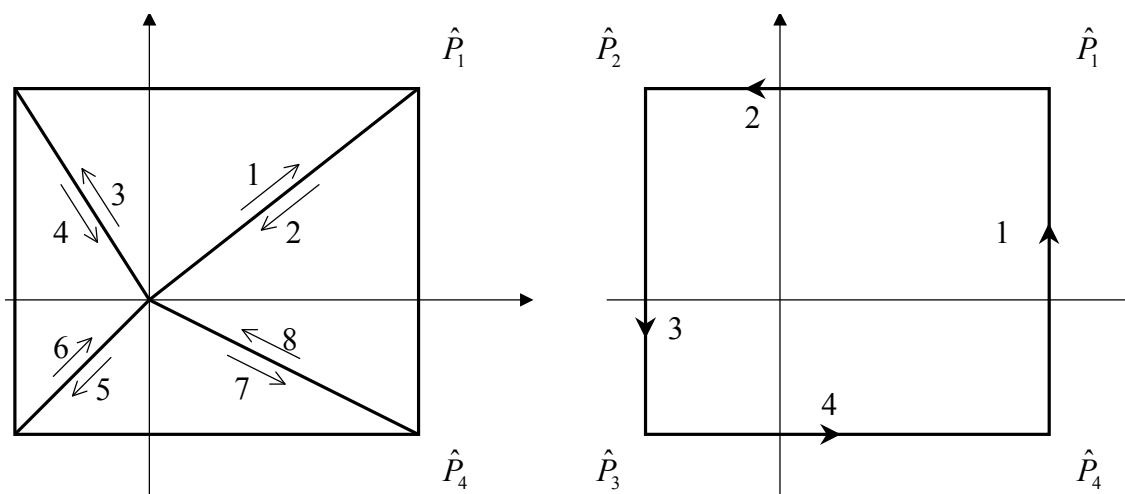


Figure 2.9: Critical cycles of load for shakedown analysis [72; 84; 89]

These theorems, which hold for convex load domains and convex yield surfaces, permit us to consider one cyclic load path instead of all loading history. They allow us to examine only the stress and strain rate fields at every vertex of the given load domain instead of computing an integration over the time cycle. Based on these theorems, König and Kleiber [84] suggested a load scheme as shown in Fig. 2.9 (a) for two independently varying loads. This scheme was applied in a simple step-by-step shakedown analysis by Borkowski and Kleiber [88] in 1980. Another scheme as shown in Fig 2.9 (b) was adopted later by Morelle [89] in 1984. Extensions and implementations of these theorems can

also be found in the works of Morelle and Nguyen [90], Polizzotto [91], Jospin [92], Yan [93] and so on.

Let us restrict ourselves to the case of a convex polyhedral load domain L . The question is how to apply the above theorems to eliminate time-dependent elastic generalized stress field $\sigma_{ij}^E(\mathbf{x}, t)$ and time integrations in the lower and upper shakedown theorems. In order to do so, let us consider a special load cycle $(0, T)$ passing through all vertices of the load domain L such as

$$\mathbf{P}(\mathbf{x}, t) = \sum_{k=1}^m \delta(t_k) \hat{\mathbf{P}}_k(\mathbf{x}) \quad (2.46)$$

where $m = 2^n$ is the total number of vertices of L , n is the total number of varying loads, $\delta(t_k)$ denote the Dirac function defined by:

$$\delta(t_k) = \begin{cases} 1 & \text{if } t = t_k \\ 0 & \text{if } t \neq t_k \end{cases} \quad (2.47)$$

Over this load path, the generalized strain at any instant t is represented by

$$\varepsilon_{ij}(t) = \sum_k \delta(t_k) \dot{\varepsilon}_{ij}^k \quad (2.48)$$

At each instant (or at each load vertex), the kinematical condition may not be satisfied, however the accumulated generalized strain over a load cycle

$$\Delta \varepsilon_{ij} = \sum_{k=1}^m \dot{\varepsilon}_{ij}^k \quad (2.49)$$

must be kinematically compatible.

Obviously, the Melan [16] condition required in the whole load domain will be satisfied if and only if it is satisfied at all vertices (or the above special loading cycle) of the domain due to the convex property of load domain and yield function. This remark permits us to replace the time-dependent generalized stress field $\sigma_{ij}^E(\mathbf{x}, t)$ by its values calculated only at load vertices. The following static shakedown theorem is presented as:

Theorem 2.5:

The necessary and sufficient condition for shakedown to occur is that there exists a

permanent residual generalized stress field $\bar{\rho}_{ij}(\mathbf{x})$, statically admissible, such that

$$f\left(\sigma_{ij}^E(\mathbf{x}, \hat{P}_k) + \bar{\rho}_{ij}(\mathbf{x})\right) \leq 0 \quad \forall k = \overline{1, m} \quad (2.50)$$

The application of loading cycle Eq. 2.46 also leads to the elimination of time integration in kinematic shakedown condition as stated in the theorem hereafter

Theorem 2.6:

The necessary and sufficient condition for shakedown to occur is that there exists a plastic accumulation mechanism $\dot{\varepsilon}_{ij}^k$ such that:

$$\left\{ \begin{array}{l} \sum_{k=1}^m \int_{\Omega} \sigma_{ij}^E(\mathbf{x}, \hat{P}_k) \dot{\varepsilon}_{ij}^k d\Omega \leq \sum_{k=1}^m \int_{\Omega} D^p(\dot{\varepsilon}_{ij}^k) d\Omega \\ \Delta \varepsilon_{ij} = \sum_{k=1}^m \dot{\varepsilon}_{ij}^k \\ \Delta \varepsilon_{ij} \text{ is kinematically admissible} \end{array} \right. \quad (2.51)$$

These shakedown theorems hold for convex yield functions, convex polyhedral load domains and can be further extended for much more realistic materials such as materials with temperature-dependent yield surface. This issue will be discussed in the later section.

The bounds of shakedown limit load multiplier Eq. 2.37 and 2.45 now can be reformulated in simpler forms corresponding to the static theorem Eq. 2.50 and the kinematic theorem 2.51:

1. The lower bound:

$$\alpha^- = \max \alpha \quad (a)$$

$$\text{subjected to:} \quad (2.52)$$

$$\left\{ \begin{array}{l} \partial_j \bar{\rho}_{ij}(\mathbf{x}) = 0 \quad \text{in } \Omega \quad (b) \end{array} \right.$$

$$\left\{ \begin{array}{l} \bar{n}_j \bar{\rho}_{ij}(\mathbf{x}) = 0 \quad \text{on } \Gamma_t \quad (c) \end{array} \right.$$

$$\left\{ \begin{array}{l} f\left(\alpha \sigma_{ij}^E(\mathbf{x}, \hat{P}_k) + \bar{\rho}_{ij}(\mathbf{x})\right) \leq 0 \quad \forall k = \overline{1, m} \quad (d) \end{array} \right.$$

2. The upper bound (in normalized form):

$$\alpha^- = \min \sum_{k=1}^m \int_{\Omega} D^p(\dot{\varepsilon}_{ij}^k) d\Omega \quad (a)$$

subjected to: (2.53)

$$\left\{ \begin{array}{l} \Delta \varepsilon_{ij} = \sum_{k=1}^m \dot{\varepsilon}_{ij}^k \quad (b) \\ \Delta \varepsilon_{ij} = \frac{1}{2} \left(\frac{\partial \Delta u_i}{\partial x_j} + \frac{\partial \Delta u_j}{\partial x_i} \right) \quad \text{in } \Omega \quad (c) \\ \Delta u_i = 0 \quad \text{on } \Gamma_u \quad (d) \\ \sum_{k=1}^m \int_{\Omega} \sigma_{ij}^E(\mathbf{x}, \hat{P}_k) \dot{\varepsilon}_{ij}^k d\Omega = 1 \quad (e) \end{array} \right.$$

Let us note that if there is only one load and this load does not vary then according to load domain definition Eq. 2.31, one has

$$\mu_1^- = \mu_1^+ \quad (2.54)$$

In this case it is easy to see that the above upper bound and lower bound reduce to the formulations of upper and lower bounds of limit load factor formulations. It is mentioned here that limit analysis can be considered as a special case of shakedown analysis when the number of load vertices is reduced to one.

2.4 Summary

In summary, both lower bound and upper bound approaches have advantages and disadvantages. Detail of advantages and disadvantages for lower bound approach are presented as below:

2.4.1 Disadvantages of lower bound approach

- Suffers from nonlinear inequality constraints.
- Finite element methods based on stress method are more difficult.
- It is difficult to present alternating limit and ratchetting limit separately.

2.4.2 Advantages of lower bound approach

- Avoids the non-differentiability of the objective function, which must be regularized via internal dissipation energy.
- There is no incompressibility constraint in the nonlinear programming problem.

The advantages and disadvantages of upper bound approach are the disadvantages and advantages of lower bound approach.

2.5 Primal-dual interior point methods

The primal-dual interior point algorithm to solve a general limit analysis in mechanics for linear programming was introduced by Karmarkar. It is now widely used in the engineering optimization problems to solve very large linear and non-linear optimization problems. The general form of the optimization problems is written as follow:

$$\begin{aligned} \min \quad & f(x) \\ \text{s.t.} \quad & Ax + s = b \\ & s \geq 0 \end{aligned} \tag{2.55}$$

According to Ref [25], the problem of minimizing a sum of Euclidean norms can be expressed as:

$$\begin{aligned} \min \quad & \sum_{i=1}^n \|z_i\| \\ \text{s.t.} \quad & \mathbf{A}_i^T \mathbf{y} + \mathbf{z}_i = \mathbf{c}_i, \quad i = 1, \dots, n \\ & \mathbf{y} \in \mathfrak{R}^m, \quad i = 1, \dots, n \\ & \mathbf{z}_i \in \mathfrak{R}^d, \quad i = 1, \dots, n \end{aligned} \tag{2.56}$$

where $\mathbf{A}_i \in \mathfrak{R}^{m \times d}$ and $\mathbf{c}_i \in \mathfrak{R}^d$, $i = 1, \dots, n$ are given. $d = 2$ or $d = 3$ is denoted for two or three dimensional Euclidean space.

By using min-max theory, the dual problem of the primal problem in Eq. 2.56 can be obtained as

$$\begin{aligned} \min_{\mathbf{A}_i^T \mathbf{y} + \mathbf{z}_i = \mathbf{c}_i} \sum_{i=1}^n \|z_i\| &= \min_{\mathbf{A}_i^T \mathbf{y} + \mathbf{z}_i = \mathbf{c}_i} \max_{\|\mathbf{x}_i\| \leq 1} \sum_{i=1}^n \mathbf{x}_i^T \mathbf{z}_i \\ &= \max_{\|\mathbf{x}_i\| \leq 1} \min_{\mathbf{A}_i^T \mathbf{y} + \mathbf{z}_i = \mathbf{c}_i} \sum_{i=1}^n \mathbf{x}_i^T \mathbf{z}_i \\ &= \max_{\|\mathbf{x}_i\| \leq 1} \min_{\mathbf{y}} \left(\sum_{i=1}^n \mathbf{c}_i^T \mathbf{x}_i - \mathbf{y}^T \sum_{i=1}^n \mathbf{A}_i \mathbf{x}_i \right) \\ &= \max \left\{ \sum_{i=1}^n \mathbf{c}_i^T \mathbf{x}_i : \|\mathbf{x}_i\| \leq 1; \sum_{i=1}^n \mathbf{A}_i \mathbf{x}_i = 0 \right\} \end{aligned}$$

where \mathbf{x}_i and \mathbf{y} ; \mathbf{z}_i refer to the primal variables and the dual variables, respectively. Finally, the dual problem of the primal problem can be expressed as

$$\begin{aligned}
 \max \quad & \sum_{i=1}^n \mathbf{c}_i^T \mathbf{x}_i \\
 \text{s.t.} \quad & \sum_{i=1}^n \mathbf{A}_i \mathbf{x}_i = 0 \\
 & \|\mathbf{x}_i\| \leq 1, \quad i = 1, \dots, n \\
 & \mathbf{x}_i \in \mathfrak{R}^d, \quad i = 1, \dots, n
 \end{aligned} \tag{2.57}$$

A specific method for solving the primal problem is presented by Andersen [25]. According to the method, the terms $\|\mathbf{z}_i\|$ are replaced by $\sqrt{\|\mathbf{z}_i\|^2 + \varepsilon^2}$, where $\varepsilon > 0$.

3

ISOGEOMETRIC FINITE ELEMENT METHOD

3.1 Introduction

Nowadays, numerical simulation using FEM which was introduced in the 1950s to 1960s to solve differential equations plays an important role in engineering design. Differential equations can be described a physical problem which is divided into certain region. The certain region is called elements. The physical problem is typically modelled in or imported into FEA software. However, the generation of numerical models from CAD geometries takes about 80% of overall analysis time. According to Sandia National Laboratories [74], mesh generation accounts for about 20% of overall analysis time, whereas creation of the analysis-suitable geometry requires about 60%. Detail estimation of the relative time costs is illustrated in Fig 3.1. The workchart of a design-through-analysis process in practical engineering is shown as Fig3.2. The first step in the workchart is a construction of geometrical model analysis. In CAD programs geometry is typically represented by spline curves and surfaces. The additional benefit of NURBS over B-Splines is the possibility to represent conic intersections exactly, which is very important for designing engineering shapes. The second step defines a functionally-suitable version of the geometry called neutral files due to the different CAD and CAE computer environments. The third step generates mesh for the imported model. The mesh is the set of Finite Elements (triangles, quadrilaterals, tetrahedra, hexahedra) that constitute the domain of the mathematical model. The next step

defines the elastic and inertial properties of the material. In case an assembly of components, we also define the relative positions and connections among the parts.

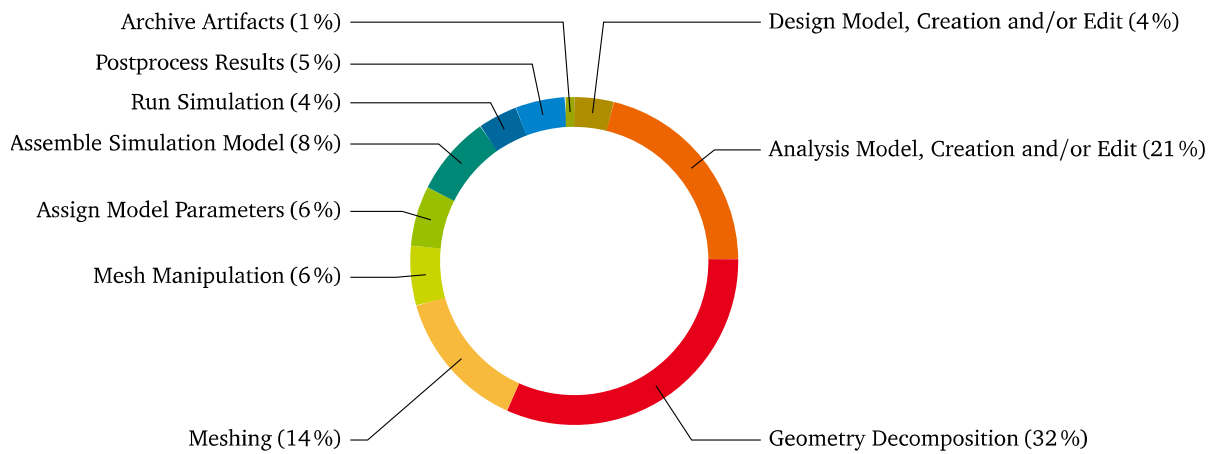


Figure 3.1: Estimation of the relative time costs of each component of the model generation and analysis process at Sandia National Laboratories [74]

The boundary conditions and applied loads to the structure are defined in the step 5. In order to find the value of the unknown variables, the system equation is solved in step 6 called the analysis step. The results of this step are displacement, temperature,... Post-processing includes three steps as 7, 8 and 9. Results in the step 7 are usually numbers arranged in vectors or matrices and are interpreted into graphs, charts or contours. These graphical plots in the step 7 are not enough information to check performances of product. Engineers have to clearly point out comments on the results in step 8 such as critical zones, prediction of possible issues to decide whether a product or a system meets the required performance specifications or not. Depending on the results in step 7 and comments in step 8, the product is confirmed the the required performance specifications or needed modifications. In the later case, a loop with the connection to the first step might be necessary, involving the need to modify the geometry and to follow all the steps of the workflow again. The transition from step 1 to step 3 is the most time-consuming. From the practical point of view, the drawback of CAD-CAE integration is the need of the development of new methods to allow a geometrical design and a mathematical model for simulation to work with the same data and, eventually, in a unique model. Isogeometric analysis (IGA) has been recently introduced by Hughes *et al* [73; 74].

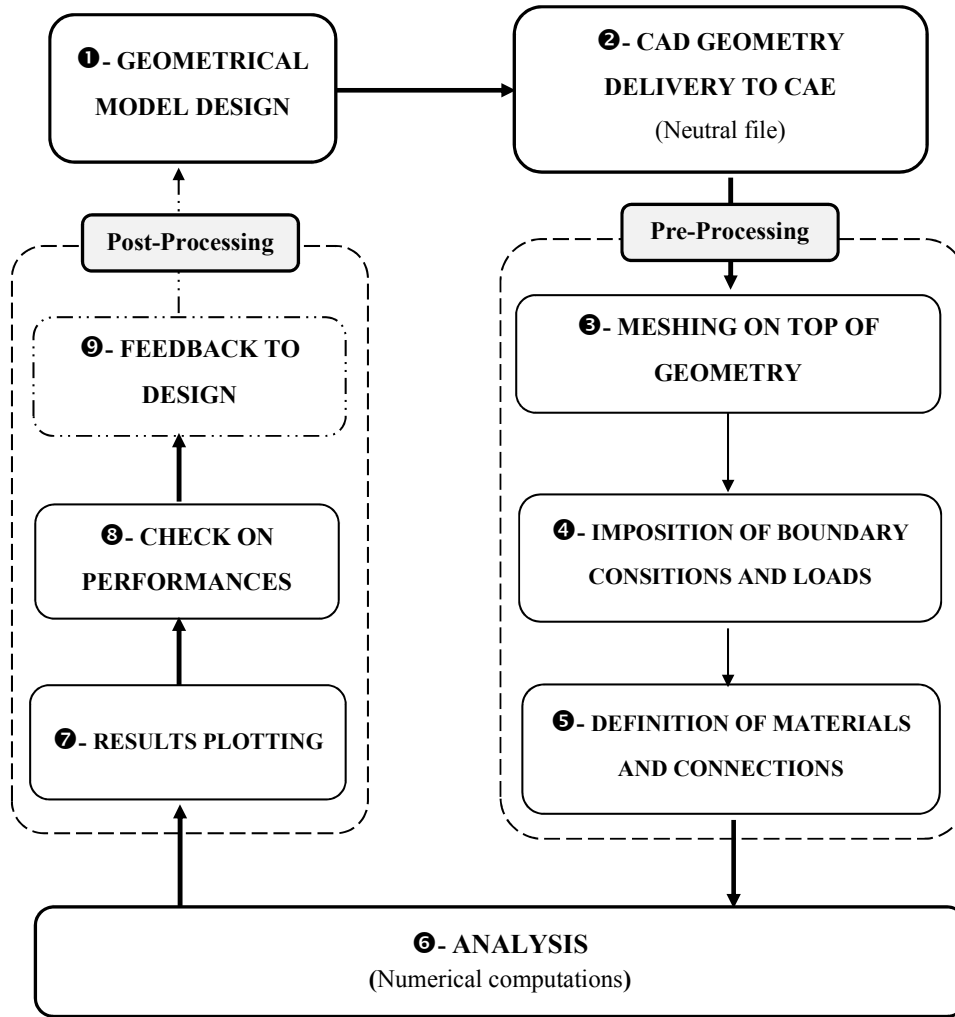


Figure 3.2: The workchart of a design-through-analysis process [74]

The idea of IGA is that the functions used for the geometry description in CAD are adopted by the analysis for the geometry and the solution field. By this, the whole process of meshing can be omitted and the two models for design and analysis merge into one. This chapter provides a basic introduction into the concepts of isogeometric analysis and isogeometric finite elements which are used for limit and shakedown analysis. Some terms are defined to understand NURBS-based on isogeometric analysis. There are 2 notions of meshes, the control mesh and the physical mesh as shown in Fig 3.3. The control mesh does not conform to the actual geometry. The control variables are the degree of freedom and located in control points. The physical mesh is a decomposition of actual geometry. There are two notions of elements in physical mesh, the patch and the knot span. The patch may be thought of as a macro-element or subdomain. Each patch has two representations, one in a parent domain and one in physical space. Each

patch can be decomposed into knot spans. Knot spans are convenient for numerical quadrature. They have presentations in both a parent domain and physical space.

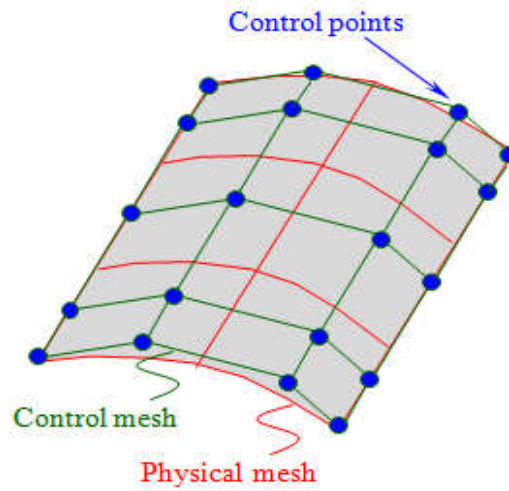


Figure 3.3: The concept of mesh in IGA: Physical mesh, control mesh and control points.

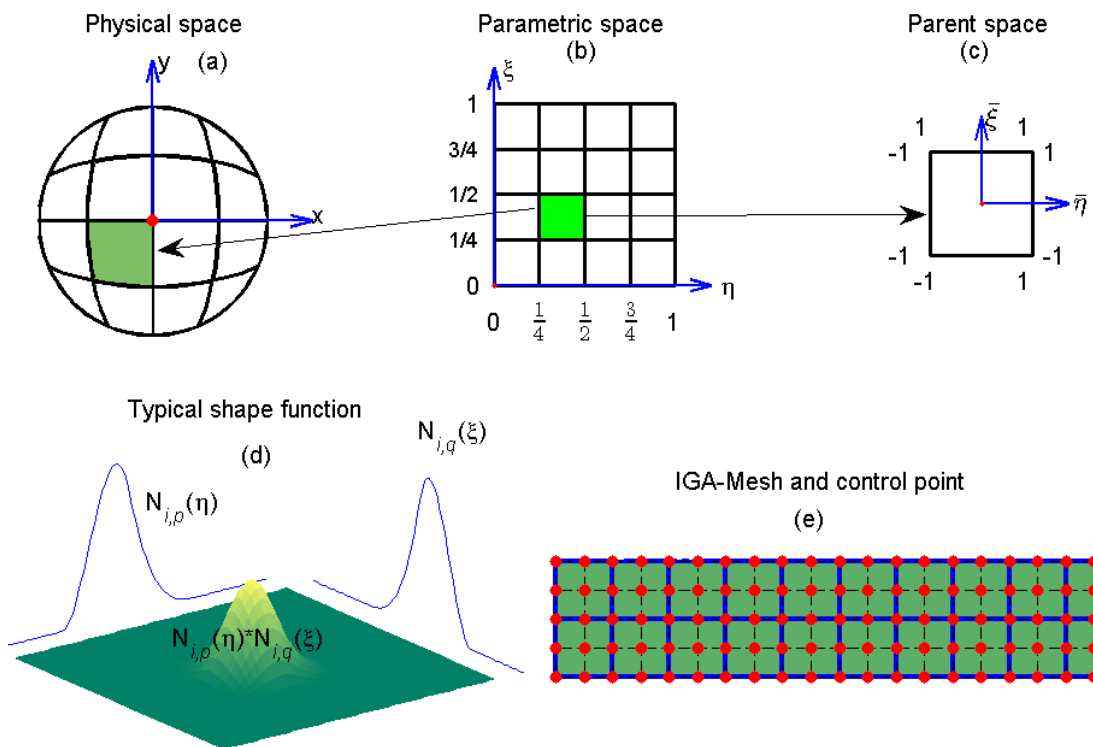


Figure 3.4: The concept of IGA: Physical space (a), parametric space (b), parent space (c) and typical basis functions (d). IGA mesh and control point, The red squares represent control points

NURBS functions are used as shape functions for modelling the geometry of the structure and are also used as shape functions in the analysis process. NURBS are the cornerstone of IGA. NURBS are built from B-splines. B-splines are dependent on the polynomial degree p and a knot vector ξ , which is defined in the parameter space. In the following, the definitions for isogeometric NURBS-elements are presented, as well as their consequences for analysis and the differences to classical finite element analysis.

3.2 NURBS

The NURBS basis functions are defined using the B-spline basis functions, and the former is actually a generalization of the latter. Thus, in order to use the NURBS basis functions, it is necessary to understand how the B-spline basis functions behave. This section is started by defining the B-spline basis functions and explore some of their most important properties.

3.2.1 B-Splines basis functions

In order to construct B-spline basis functions of degree p , we need a knot vector. The knot vector is defined as a set of parametric coordinates, called knot value ξ_i in non-descending sequence of numbers, written $\Xi = [\xi_1, \xi_2, \dots, \xi_m]$. The knot value ξ_i can appear more than once and is then called a multiple knot. The interval between two consecutive knots (ξ_i, ξ_{i+1}) is called knot span. Two types of knot vectors are used in computer-aided design, namely periodic and open knot vectors. In this thesis, the term “open” is used and the parameter space is used the interval $[0; 1]$. The open knot vector is always of the form:

$$\Xi = \left[\underbrace{\xi_a, \xi_a, \xi_a}_{p+1\text{-times}}, \dots, \xi_i, \dots, \underbrace{\xi_b, \xi_b, \xi_b}_{p+1\text{-times}} \right] \text{ where } \xi_a = 0 \ \& \ \xi_b = 1 \quad (3.1)$$

The most common knot vector used in CAD is the non-uniform open knot vector, which calls two properties in one: (1. non-uniform – the space between the knots is not equal; 2. open – the first and last knots are repeated $p + 1$ times). Based on the knot vector $\Xi = [\xi_1, \xi_2, \dots, \xi_m]$ and the polynomial degree p , the B-Spline basis functions are defined recursively by the *Cox-deBoor* recursion formula as follows, starting with $p = 0$

$$N_{i,0}(\xi) = \begin{cases} 1 & \xi_i \leq \xi < \xi_{i+1} \\ 0 & \text{otherwise,} \end{cases} \quad (3.2)$$

For $p \geq 1$

$$N_{i,p}(\xi) = \frac{\xi - \xi_i}{\xi_{i+p} - \xi_i} N_{i,p-1}(\xi) + \frac{\xi_{i+p+1} - \xi}{\xi_{i+p+1} - \xi_{i+1}} N_{i+1,p-1}(\xi) \quad (3.3)$$

The first derivative of a B-Spline basis function is computed by the following formula:

$$N'_{i,p}(\xi) = \frac{p}{\xi_{i+p} - \xi_i} N_{i,p-1}(\xi) - \frac{p}{\xi_{i+p+1} - \xi_{i+1}} N_{i+1,p-1}(\xi) \quad (3.4)$$

Similarly, higher order derivatives, $N_{i,p}^k$ are computed by following the same procedure:

$$N_{i,p}^k(\xi) = \frac{p}{\xi_{i+p} - \xi_i} N_{i,p-1}^{k-1}(\xi) - \frac{p}{\xi_{i+p+1} - \xi_{i+1}} N_{i+1,p-1}^{k-1}(\xi) \quad (3.5)$$

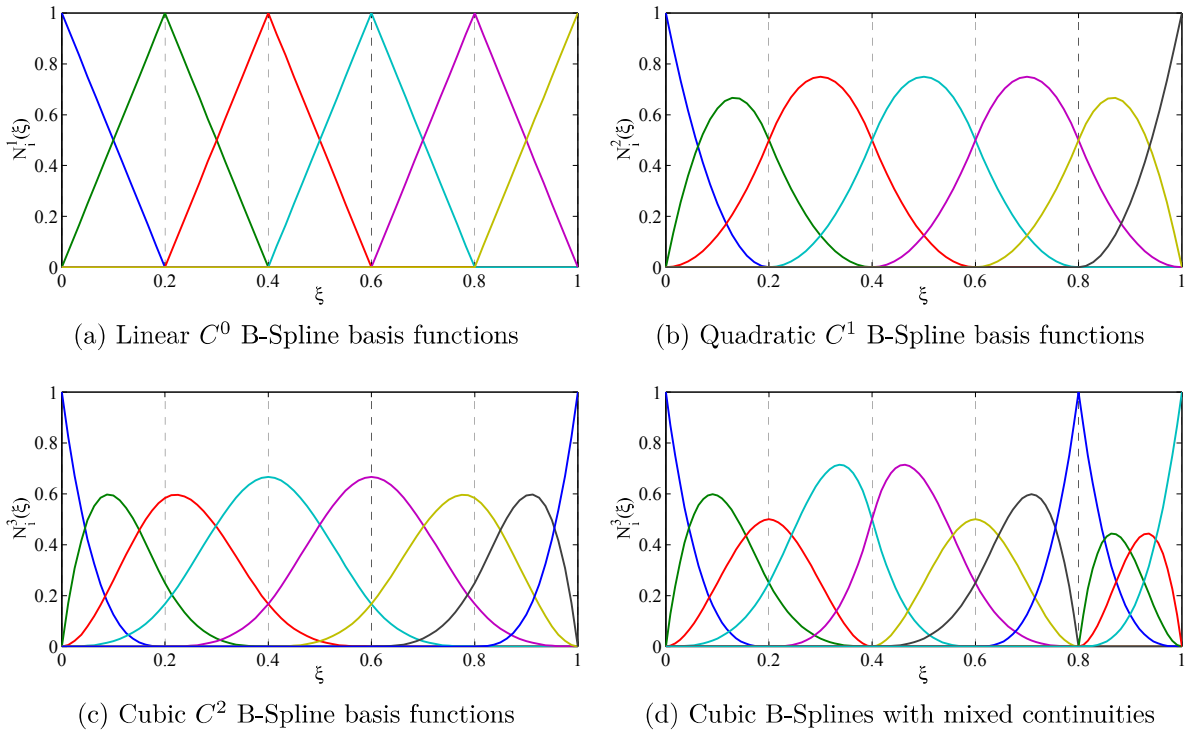


Figure 3.5: Different types of B-Spline basis functions on the same distinct knot vector

Example: Fig 3.5 shows an example of B-Spline basis functions with different degrees and continuities based on the same distinct knot vector $\Xi = [0, 0.2, 0.4, 0.6, 0.8, 1]$. Using knot vectors $\Xi_a = [0, 0, 0.2, 0.4, 0.6, 0.8, 1, 1]$, $\Xi_b = [0, 0, 0, 0.2, 0.4, 0.6, 0.8, 1, 1, 1]$, $\Xi_c = [0, 0, 0, 0, 0.2, 0.4, 0.6, 0.8, 1, 1, 1, 1]$ and $\Xi_d = [0, 0, 0, 0, 0.2, 0.2, 0.4, 0.6, 0.8, 0.8, 0.8, 1, 1, 1, 1]$, the linear B-Spline basis functions with C^0 -continuity are obtained quadratic with C^1 -continuity, cubic with C^2 -continuity and

cubic with C^1 -continuity at $\xi = 0.4$, C^0 -continuity at $\xi = 0.8$ and C^2 -continuity at all other knots, respectively. These functions are shown in Fig 3.5 (a,b,c and d).

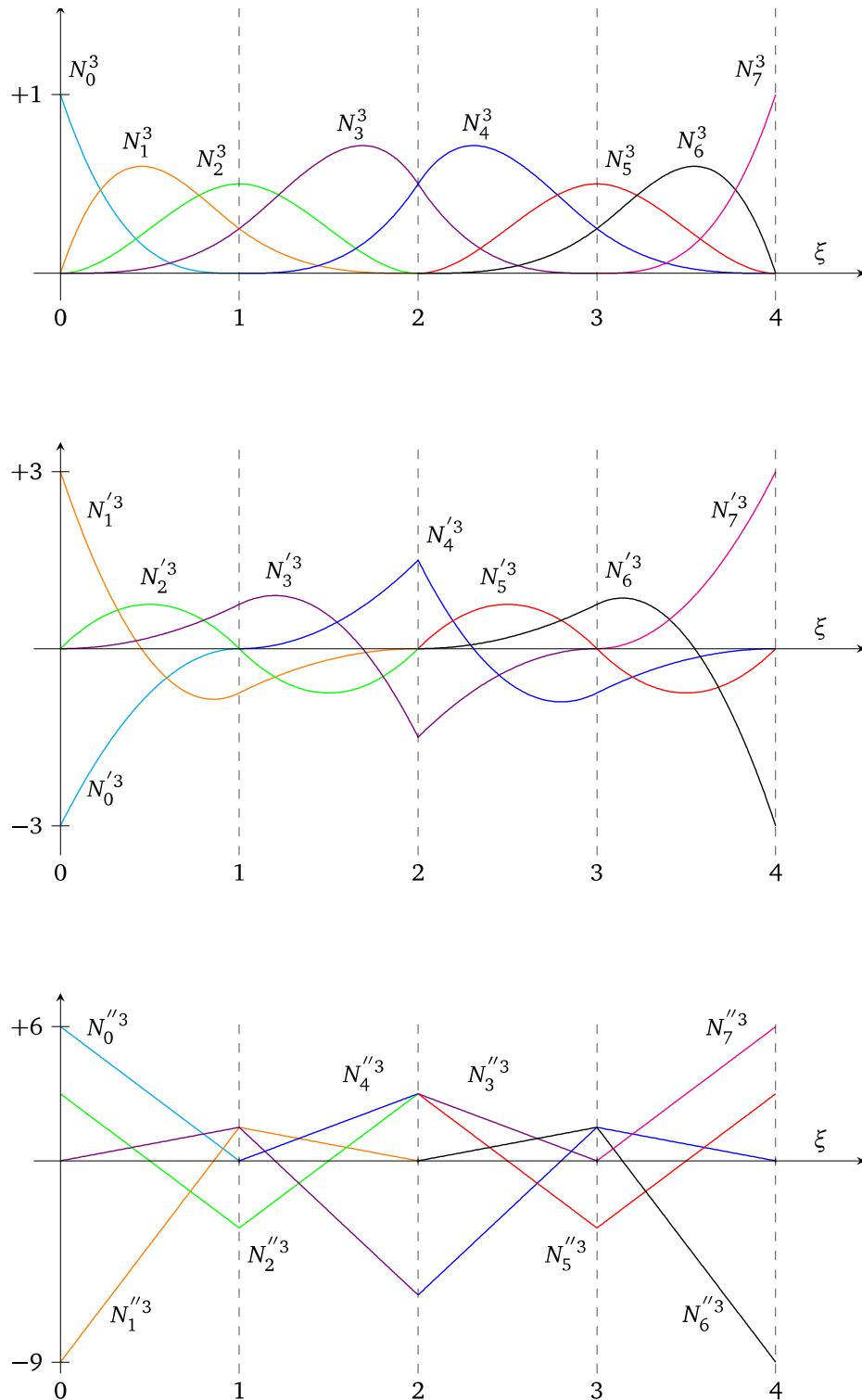


Figure 3.6: The cubic B-Spline functions $N_i^3(\xi)$ and its first and second derivatives on the domain defined by the knot vector $\Xi = [0, 0, 0, 0, 1, 2, 2, 3, 4, 4, 4, 4]$

Important properties of B-spline basis functions

B-spline basis functions have several important properties:

- + Local support: $N_{i,p}(\xi)$ is a polynomial function of degree p and non-zero only in the interval $[\xi_i, \xi_{i+p+1})$
- + Partition of unity: $\sum_{i=1}^n N_{i,p}(\xi) = 1$
- + Non-negativity: $N_{i,p}(\xi) \geq 0$
- + Linear independence: $\sum_{i=1}^n \alpha_i N_{i,p}(\xi) = 0 \Leftrightarrow \alpha_j = 0, j = 1, \dots, n$
- + Basis function $N_{i,p}(\xi)$ is C^{p-k} if a knot repeats k times. Thus, the continuity of the B-spline basis functions decrease by increasing the multiplicity of the knot.

The proofs can be found in Ref [94].

Fig 3.6 illustrates some of these properties for a set of cubic basis functions. The local support and the non-negativity of the basis functions can be readily observed, as well as the interpolative nature of the basis functions $N_i^3(\xi)$ at the boundaries of the domain.

3.2.2 B-Spline Curves

B-Spline curves are defined by a linear combination of control points and basis functions over a parametric space. A B-spline curve can be expressed as

$$\mathbf{C}(\xi) = \sum_{i=1}^n N_{i,p}(\xi) \mathbf{P}_i \quad (3.6)$$

where $\mathbf{C}(\xi)$ is the physical curve of interest,

Properties of B-splines

- + Convex Hull Property: A curve may lie within the convex hull of the control polygon.
- + Locality Properties: if a particular control point is moved, the curve is affected only in a local area. The control points have influence on maximum $p + 1$ sections.
- + For open knot vectors, the first and the last control point are interpolated and the curve is tangential to the control polygon at the start and the end of the curve.
- + The curve is C^∞ continuous between two knots and C^{p-k} continuous at a knot of multiplicity k .

3.2.3 B-Spline Surfaces

Given two knot vectors $\Xi = [\xi_1, \xi_2, \dots, \xi_n]$ and $H = [\eta_1, \eta_2, \dots, \eta_m]$, two polynomial degrees p and q and a set of $n \times m$ control points $\mathbf{P}_{i,j}$. Similarly to the case of a curve, the function for a B-Spline surface is computed as below:

$$\mathbf{S}(\xi, \eta) = \sum_{i=1}^n \sum_{j=1}^m N_{i,p}(\xi) M_{j,q}(\eta) \mathbf{P}_{i,j} \quad (3.7)$$

where $N_{i,p}$ and $M_{j,q}$ are B-Spline basis functions in two parametric dimensions ξ and η .

3.2.4 B-Spline Solids

Similar to surfaces, a B-Spline solid is obtained by the tensor product of B-Spline basis functions $N_{i,p}$, $M_{j,q}$ and $L_{k,r}$ in three parametric dimensions ξ , η and ζ with a set of $n \times m \times l$ control points $\mathbf{P}_{i,j,l}$ as below:

$$\mathbf{V}(\xi, \eta) = \sum_{i=1}^n \sum_{j=1}^m \sum_{k=1}^l N_{i,p}(\xi) M_{j,q}(\eta) \mathbf{P}_{i,j} \quad (3.8)$$

3.2.5 Refinement techniques

In order to increase the accuracy of the solution, we might have to be refined. Three types of refinement are operated in isogeometric analysis:

- Knot insertion (h -refinement)
- Degree elevation (p -refinement)
- k -refinement

3.2.5.1 Knot insertion (h -refinement)

The knot insertion method is called h -refinement. The new knot values will add between existing knots without changing the curve. Result of this technique increases number of elements and control points. Assumed that we have a knot vector $\Xi = [\xi_1, \xi_2, \dots, \xi_m]$. Inserting a new knot $\bar{\xi} \subset (\xi_k, \xi_{k+1})$ with $k > p$ into the original knot vector. Number of basis functions will increase one and will determine following Eq. 3.2 or 3.3. The $m = n + 1$ new control points $\{\bar{P}_i\}_1^m$ are formed from the original control points, $\{P_i\}_1^n$,

as follow:

$$\bar{\mathbf{P}}_i = \begin{cases} \mathbf{P}_1 & i = 1 \\ \alpha_i \mathbf{P}_i + (1 - \alpha_i) \mathbf{P}_{i-1} & 1 < i < m \\ \mathbf{P}_m & i = m \end{cases} \quad (3.9)$$

where

$$\alpha_i = \begin{cases} 1 & i \leq k - p \\ \frac{\bar{\xi} - \xi_i}{\xi_{p+i} - \xi_i} & k - p + 1 \leq i \leq k \\ 0 & \geq k + 1 \end{cases} \quad (3.10)$$

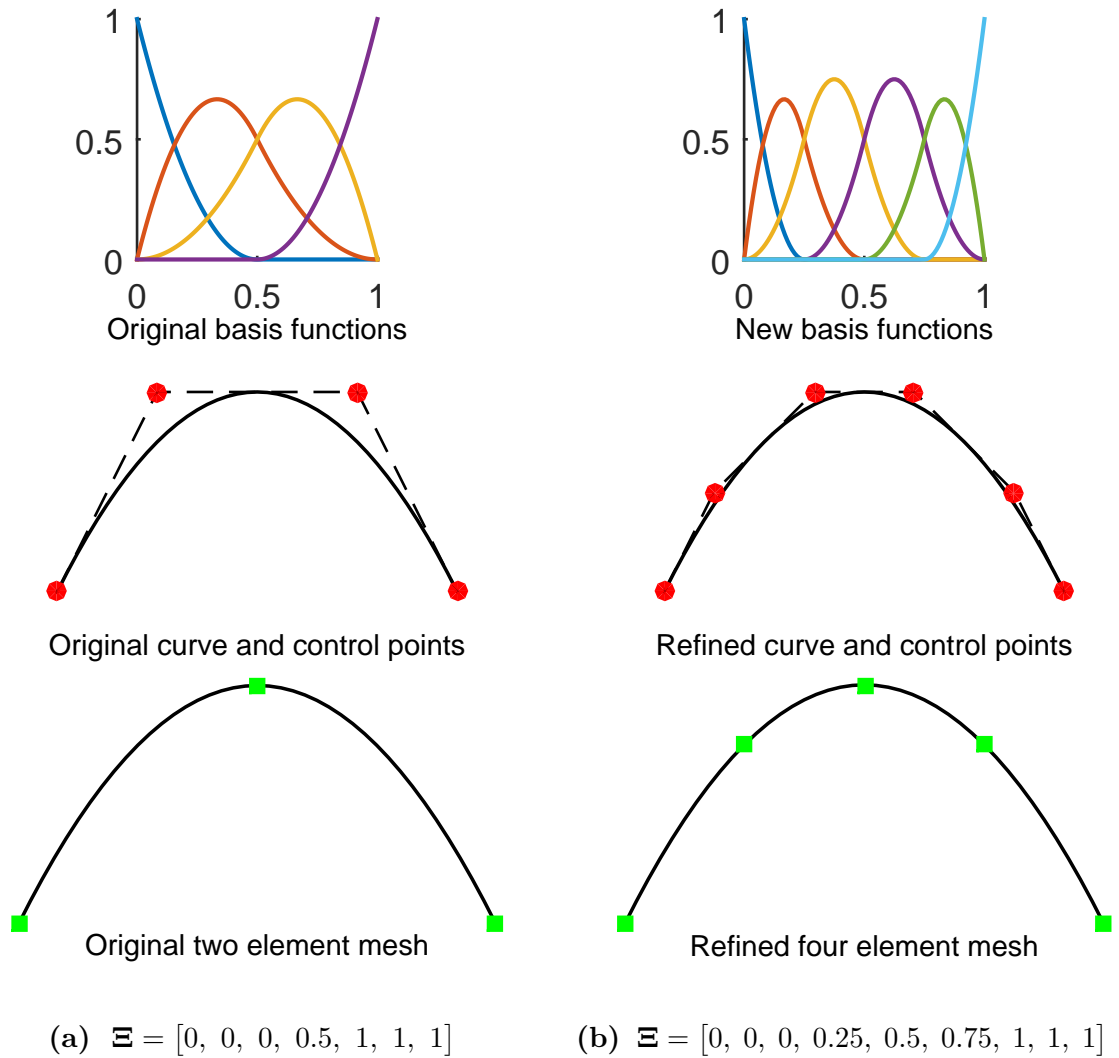


Figure 3.7: Knot insertion. Control points are denoted by red circular \bullet . The knots, which define a mesh by partitioning the curve into elements, are denoted by green square \blacksquare

Fig 3.7 shows an example h refinement with original knot vector $\Xi = [0, 0, 0, 0.5, 1, 1, 1]$ and new knot vector $\Xi = [0, 0, 0, 0.25, 0.5, 0.75, 1, 1, 1]$ after h -refinement.

3.2.5.2 Degree elevation (p -refinement)

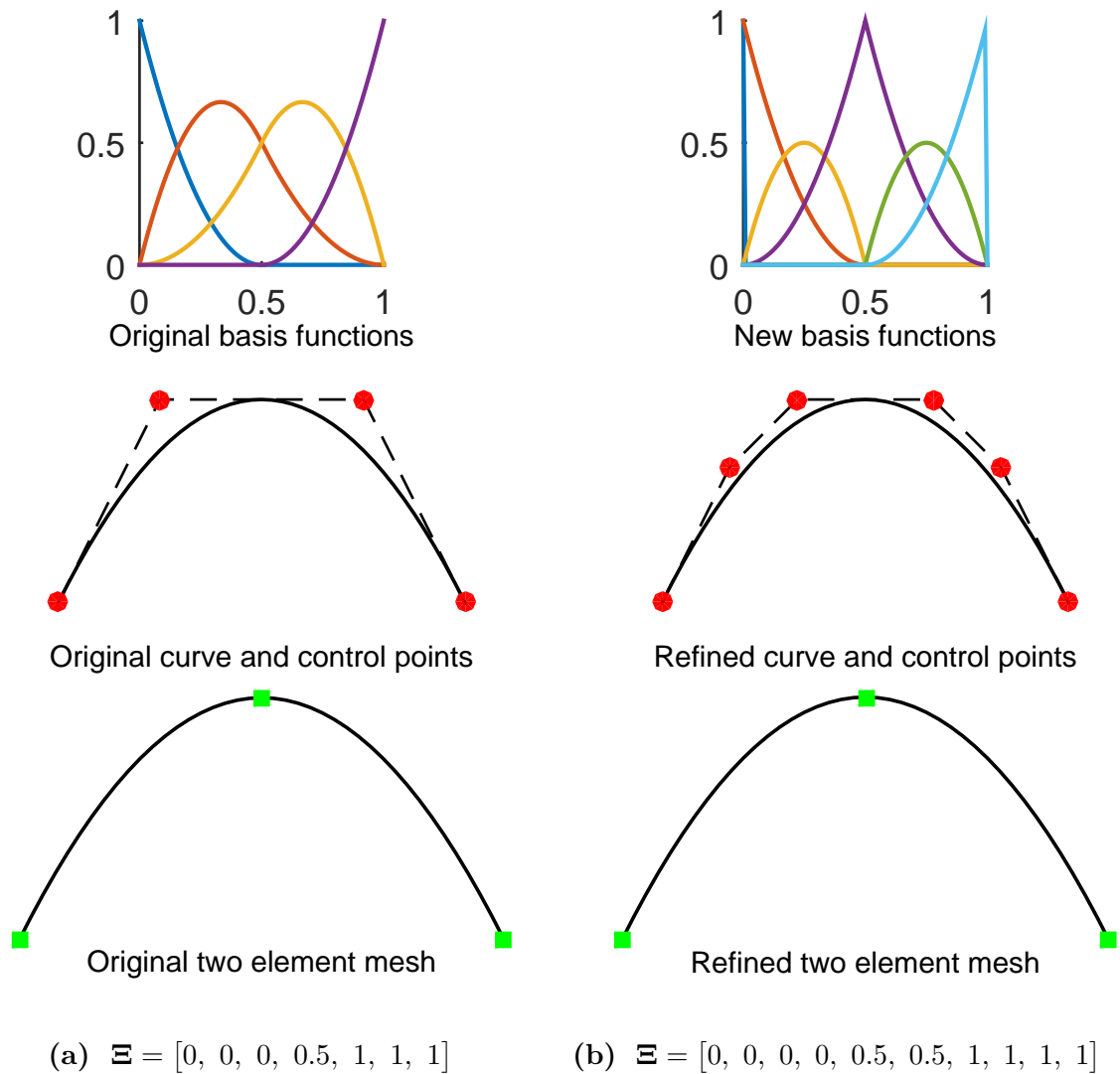


Figure 3.8: Knot insertion. Control points are denoted by red circular \bullet . The knots, which define a mesh by partitioning the curve into elements, are denoted by green square \blacksquare

This is technique used to rise a the polynomial order of the element or raise the polynomial degree of the basis functions. Order elevation involves increasing the multiplicity of each knot value by one. The geometry and the parametrization of the

physical curve are not changed, however the number of basis functions and control points increases. The number of elements remains the same because no new knot is added. The basis function C^{p-k} is continuous at the knots of multiplicity k . This process is illustrated in Fig 3.8.

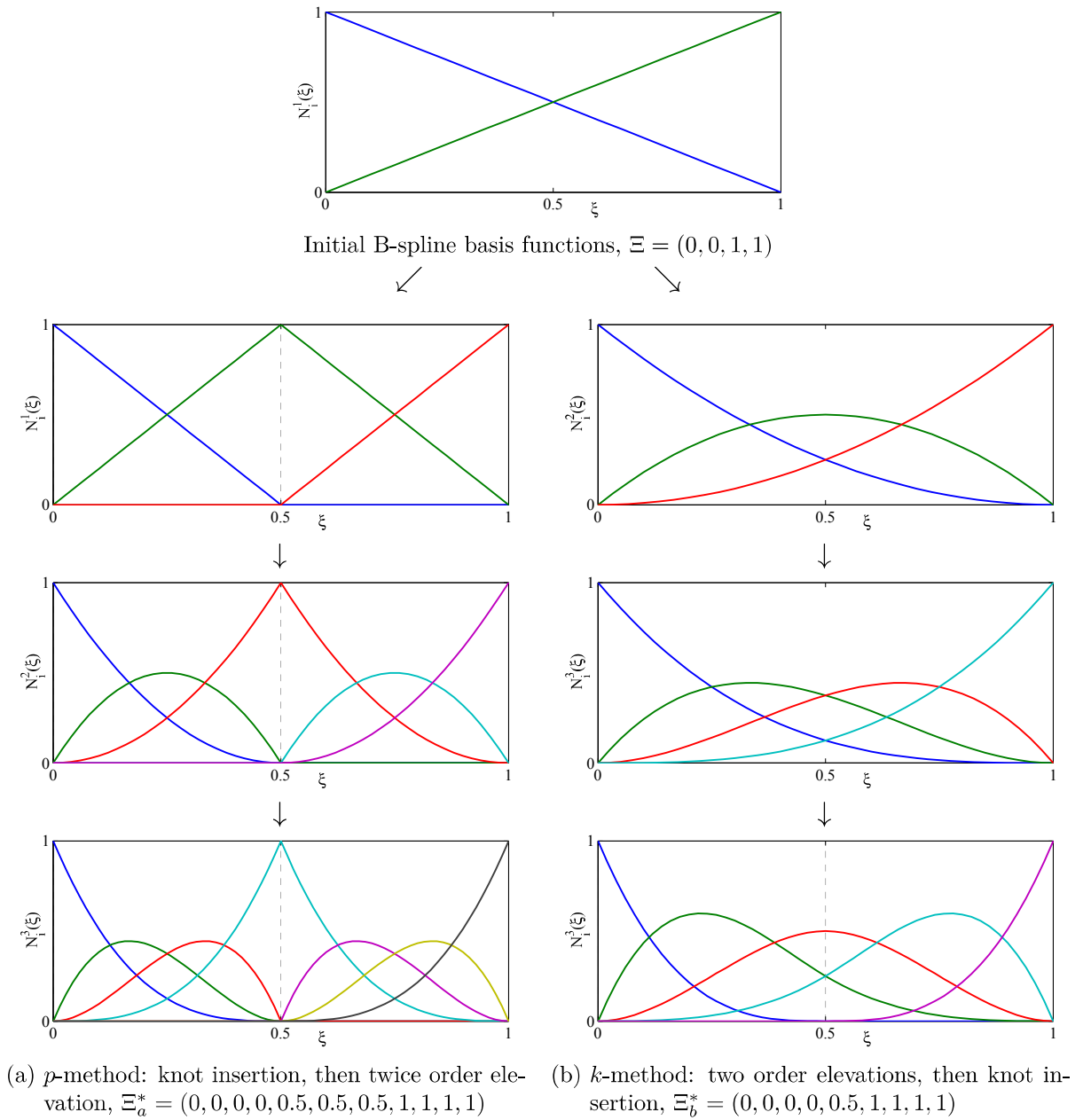


Figure 3.9: Comparison of refinement strategies: *p*-refinement and *k*-refinement

3.2.5.3 *k*-refinement

This technique is a combination of both order elevation and knot insertion. The idea is to increase both the order of the curve and also the continuity across knot values. This method can also be presented as starting with a knot vector with only first and last values, do order elevation as much as desired, and finally insert knots between first and last values. Hence combination of order elevation and knot insertion. The concept of *k* refinement is shown in Fig 3.9(b). Fig 3.9 also shows a comparison of two refinement method: *p*-refinement and *k*-refinement.

3.2.6 NURBS

Even though B-splines are widely used, they have the limitation that they cannot represent conics as circles and ellipses, exactly. In order to overcome this limitation, a rational form of B-splines was developed and this is the NURBS. It represents a transformation from a space in R^{d+1} to a space in R^d , where d is the number of physical spatial coordinates. Such a point $P_i(x_i, y_i, z_i, w_i)$ in R^3 space can be represented with homogeneous coordinates $P_i^w(w_i x_i, w_i y_i, w_i z_i, w_i)$ in a projective R^4 space. Given a set of positive weights $w_i, w_{i,j}$ and $w_{i,j,k} \in R$, where $i = 1, 2, \dots, n; j = 1, 2, \dots, m$ and $k = 1, 2, \dots, l$. NURBS basis functions are defined as:

1. 1D NURBS shape basis function

$$R_p^i(\xi) = \frac{N_{i,p}(\xi)w_i}{\sum_{\bar{i}=1}^n N_{\bar{i},p}(\xi)w_{\bar{i}}} = \frac{N_{i,p}(\xi)w_i}{W(\xi)} \quad (3.11)$$

2. 2D NURBS shape basis function

$$R_{p,q}^{i,j}(\xi, \eta) = \frac{N_{i,p}(\xi)M_{j,q}(\eta)w_{i,j}}{\sum_{\bar{i}=1}^n \sum_{\bar{j}=1}^m N_{\bar{i},p}(\xi)M_{\bar{j},q}(\eta)w_{\bar{i},\bar{j}}} = \frac{N_{i,p}(\xi)M_{j,q}(\eta)w_{i,j}}{W(\xi, \eta)} \quad (3.12)$$

3. 3D NURBS shape basis function

$$\begin{aligned}
 R_{p,q,l}^{i,j,k}(\xi, \eta, \zeta) &= \frac{N_{i,p}(\xi) M_{j,q}(\eta) L_{k,r}(\zeta) w_{i,j,k}}{\sum_{\bar{i}=1}^n \sum_{\bar{j}=1}^m \sum_{\bar{k}=1}^l N_{\bar{i},p}(\xi) M_{\bar{j},q}(\eta) L_{\bar{k},r}(\zeta) w_{\bar{i},\bar{j},\bar{k}}} \\
 &= \frac{N_{i,p}(\xi) M_{j,q}(\eta) L_{k,l}(\zeta) w_{i,j,k}}{W(\xi, \eta, \zeta)}
 \end{aligned} \tag{3.13}$$

where $N_{i,p}(\xi)$, $M_{j,q}(\eta)$ and $L_{k,r}(\zeta)$ are B-Spline basis functions in parametric dimension ξ , η and ζ respectively. Based on the 1D, 2D and 3D Nurbs basis functions above and a set of control points, we define the Nurbs curve, surface and solid as below:

1. NURBS curve is defined by three things: control points, the curve's order and a knot vector

$$\mathbf{C}(\xi) = \sum_{i=1}^n R_i^p(\xi) \mathbf{P}_i \tag{3.14}$$

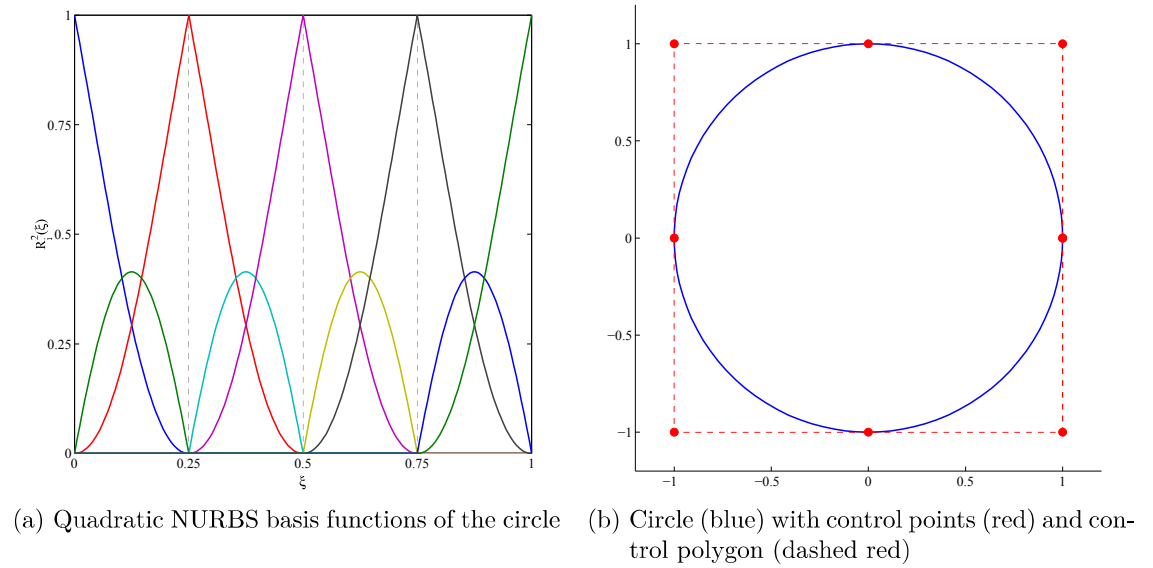


Figure 3.10: A circle as a NURBS curve

2. NURBS surface

$$\mathbf{S}(\xi, \eta) = \sum_{i=1}^n \sum_{j=1}^m R_{p,q}^{i,j}(\xi, \eta) \mathbf{P}_{i,j} \tag{3.15}$$

3. NURBS solid

$$\mathbf{V}(\xi, \eta, \zeta) = \sum_{i=1}^n \sum_{j=1}^m \sum_{k=1}^l R_{p,q,r}^{i,j,k}(\xi, \eta, \zeta) \mathbf{P}_{i,j,k} \quad (3.16)$$

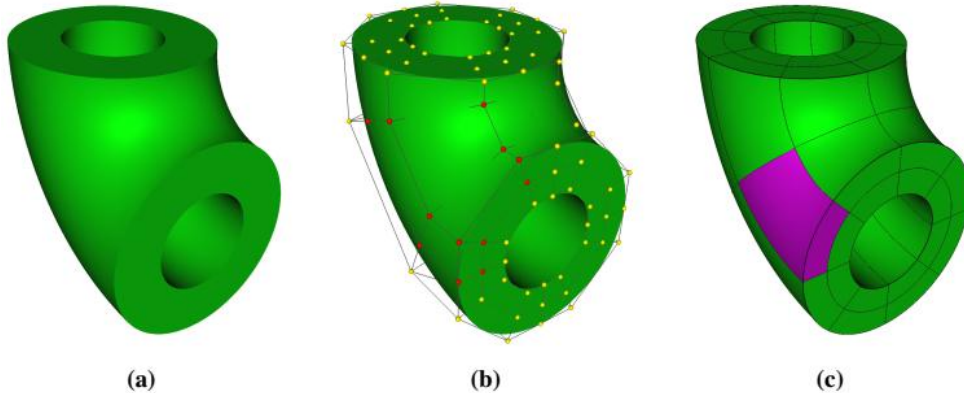


Figure 3.11: Bent pipe modeled with a single NURBS patch. (a) Geometry. (b) NURBS mesh with control points. (c) Geometry with 32 NURBS elements

3.3 NURBS-based isogeometric analysis

Similar to finite element analysis, isogeometric analysis works with elements. To obtain the system equation the principle of virtual work is presented in Eq. (2.24). The relationship that links the displacement of the system to the general displacement field is as follows:

$$\mathbf{u}(\mathbf{x}) = \mathbf{R}\mathbf{q} \quad (3.17)$$

where \mathbf{R} is the NURBS shape function, $\mathbf{u}(\mathbf{x})$ is displacement field and \mathbf{q} is displacement at control points. The strain can be written as

$$\boldsymbol{\varepsilon} = \frac{\partial \mathbf{u}}{\partial \mathbf{x}} = \frac{\partial \mathbf{R}}{\partial \mathbf{x}} \mathbf{q} = \mathbf{B}\mathbf{q} \quad (3.18)$$

where \mathbf{B} is the strain-displacement matrix, while the stress is obtained

$$\boldsymbol{\sigma} = \mathbf{D}\boldsymbol{\varepsilon} = \mathbf{D}\mathbf{B}\mathbf{q} \quad (3.19)$$

The virtual strains and displacements may be expressed as

$$\delta \mathbf{u}^T = \delta \mathbf{q}^T \mathbf{R}^T \quad (3.20)$$

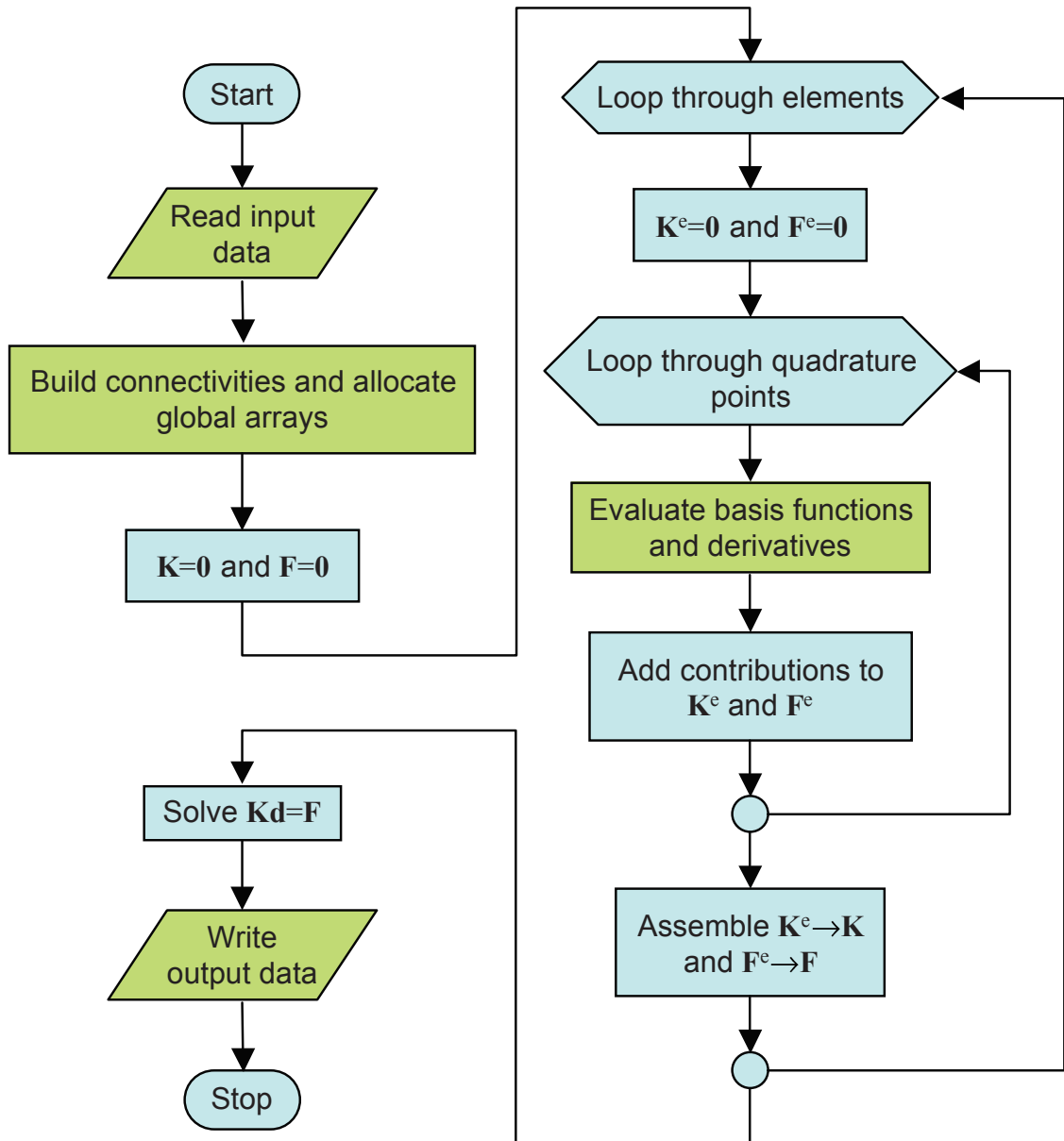


Figure 3.12: Flowchart of a classical finite element code. This figure is adopted in Prof. Hughes' book [74]

$$\delta \varepsilon^T = \delta \mathbf{q}^T \mathbf{B}^T \quad (3.21)$$

Insert Eq.3.20 and 3.21 into the principle of virtual work, we have

$$(\delta \mathbf{q}) \left(\int_{\Omega} \mathbf{B}^T \mathbf{D} \mathbf{B} d\Omega \mathbf{q} - \int_{\Omega} \mathbf{R}^T \mathbf{g} d\Omega - \int_{\Gamma_t} \mathbf{R}^T \mathbf{f} d\Gamma_t \right) = 0 \quad (3.22)$$

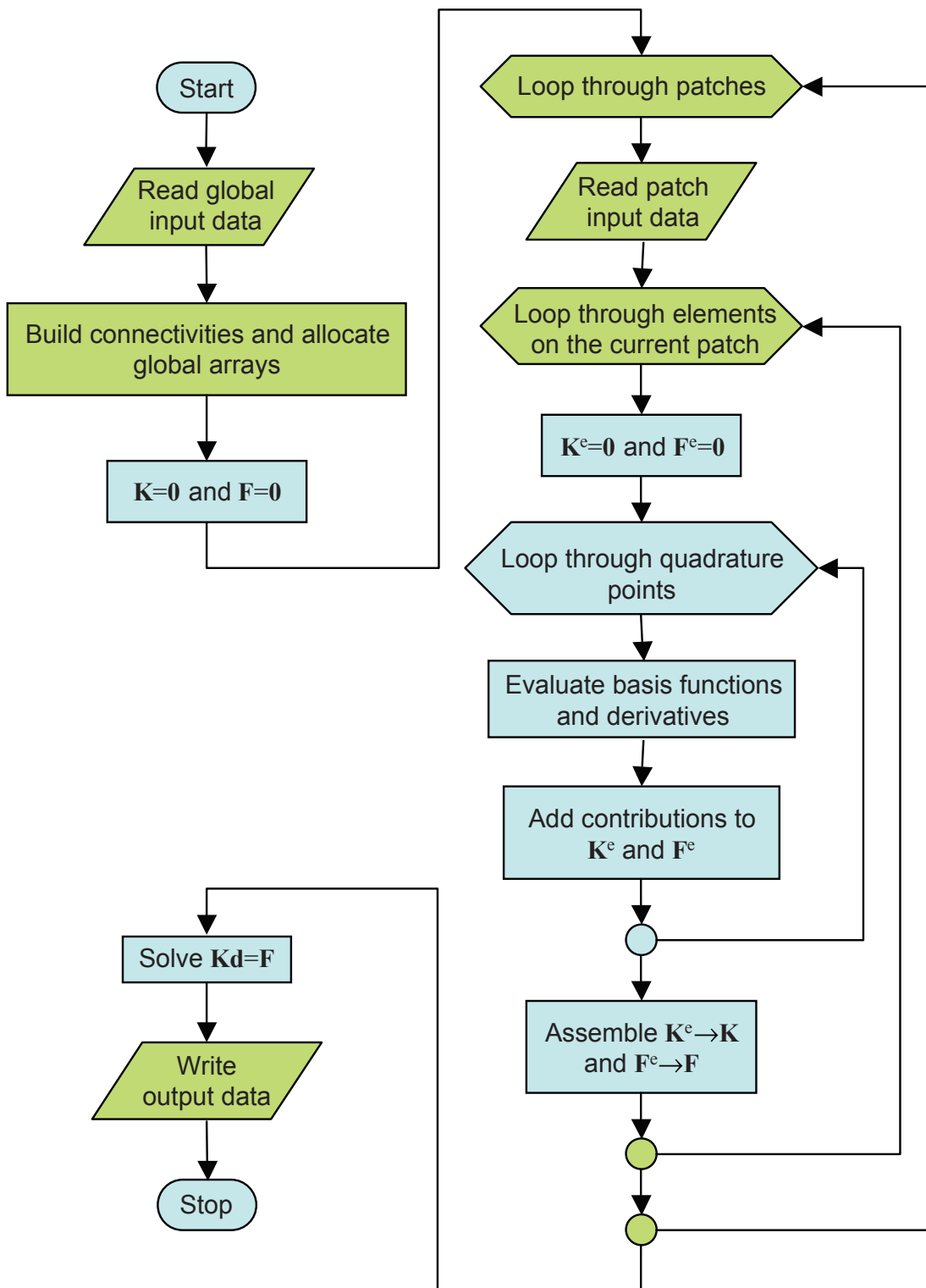


Figure 3.13: Flowchart of a multi-patch isogeometric analysis code. This figure is adopted in Prof. Hughes' book [74]

For an arbitrary $(\delta \mathbf{q})$, the above equation can be written as a simple form

$$\mathbf{K}\mathbf{q} = \mathbf{f} \quad (3.23)$$

where \mathbf{K} is global stiffness matrix and \mathbf{f} denotes global external load. Each of the components is the sum of their respective element contributions:

$$\mathbf{K} = \sum_{e=1}^n \mathbf{K}_e; \quad \mathbf{f} = \sum_{e=1}^n \mathbf{f}_e; \quad \mathbf{q} = \sum_{e=1}^n \mathbf{q}_e, \quad (3.24)$$

where \mathbf{K}_e is the element stiffness matrix,

$$\mathbf{K}_e = \int_{\Omega_e} \mathbf{B}^T \mathbf{D} \mathbf{B} d\Omega_e \quad (3.25)$$

and the external load is

$$\mathbf{f}_e = \int_{\Omega_e} \mathbf{R}^T \mathbf{g} d\Omega_e + \int_{\Gamma_{t,e}} \mathbf{R}^T \mathbf{f} d\Gamma_{t,e} \quad (3.26)$$

The computer implementation of IGA has many similarities with a standard FEM solver, but there are theoretic and technical differences one must be aware of when going from the classical FEM to IGA. The flowchart of FEM code is shown in Fig 3.12. The main differences in the code architecture from FEM to IGA are the input data, the evaluation of the basis functions and the postprocessing part. The code can be converted to an IGA code by replacing the routines that are shown in green. The flowchart of multi-patch isogeometric analysis code is also shown in Fig 3.13. The routines in green represent differences from the single-patch code.

3.3.1 Elements

As shown in Fig 3.4, every NURBS patch is defined over a parametric domain, which is divided into intervals by the knot vectors. Equivalently to finite elements, a NURBS element is defined by a set of nodes and corresponding basis functions. The nodes are the NURBS control points. They carry the degrees of freedom for the analysis and boundary conditions are applied to them. Since the element formulation in this thesis is displacement-based, the degrees of freedom are the displacements of the control points.

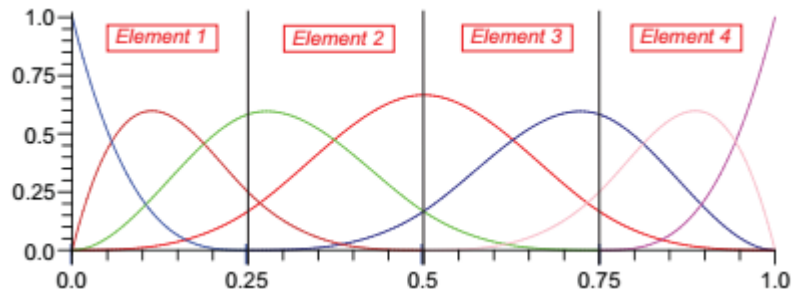


Figure 3.14: Isogeometric elements. The basis functions extend over a series of elements

It is important to note that with this definition of elements, the basis functions are not confined to one element but extend over a series of elements, as illustrated in Fig 3.14. This is a very important difference to classical finite elements because it allows higher continuities of shape functions over the element boundaries.

3.3.2 Mesh refinement

The methods of knot insertion and order elevation presented in Subsection 3.2.5, are used for mesh refinement in the analysis. Here, knot insertion corresponds to *h-refinement* of classical FEA since the number of elements is increased and order elevation corresponds to *p-refinement*. An important difference to refinement in classical FEA is that the refinement for NURBS does not change the geometry. This means that in each refinement step, the geometry is represented exactly and therefore a refined mesh can be further refined without the necessity of going back to the original model.

3.3.3 Stiffness matrix

Numerical integration of the stiffness matrix 1D for the patch is computed as:

$$K_{1D} = \sum_{i=1}^{NG_{\xi}} \left\{ \left[B(\xi_i) \right]^T [E] \left[B(\xi_i) \right] [A] \det[J] w_i^{NG} \right\} \quad (3.27)$$

Numerical integration of the stiffness matrix 2D for the patch is computed as:

$$K_{2D} = \sum_{i=1}^{NG_{\xi}} \sum_{j=1}^{NG_{\eta}} \left\{ \left[B(\xi_i, \eta_j) \right]^T [E] \left[B(\xi_i, \eta_j) \right] \det[J] w_i^{NG_{\xi}} w_j^{NG_{\eta}} \right\} \quad (3.28)$$

Numerical integration of the stiffness matrix 2D for the patch is evaluated as:

$$K_{3D} = \sum_{i=1}^{NG_{\xi}} \sum_{j=1}^{NG_{\eta}} \sum_{k=1}^{NG_{\zeta}} \left\{ \left[B(\xi_i, \eta_j, \zeta_k) \right]^T [E] \left[B(\xi_i, \eta_j, \zeta_k) \right] \det[J] w_i^{NG_{\xi}} w_j^{NG_{\eta}} w_k^{NG_{\zeta}} \right\} \quad (3.29)$$

Where notations in Eqs. 3.27, 3.28 and 3.29:

- $B(\xi_i)$, $B(\xi_i, \eta_j)$ and $B(\xi_i, \eta_j, \zeta_k)$: the deformation matrix or strain-displacement matrix in 1D, 2D and 3D, respectively.
- J : Jacobian matrix.
- E : Constitutive matrix of elastic stiffnesses.
- NG_ξ : the total number of Gaussian points per ξ for the specific patch.
- NG_η : the total number of Gaussian points per η for the specific patch.
- NG_ζ : the total number of Gauss Points per ζ for the specific patch.
- ξ_i , η_j and ζ_k : the coordinates of the tensor product Gaussian point i^{th} , j^{th} and k^{th} , respectively.
- $w_i^{NG_\xi}$, $w_j^{NG_\eta}$ and $w_k^{NG_\zeta}$: the corresponding weights of Gaussian point i^{th} , j^{th} and k^{th} , respectively.

3.4 A brief of NURBS based on Bézier extraction

As mentioned above, the IGA uses NURBS (or B-spline) functions for numerical analysis. An overview of these functions is presented in Section 3.2. In this section, the Bézier extraction operator for NURBS are discussed. Bézier extraction is a process in which the knots insertion algorithm is performed over the existing knots to p times. This process allows us to integrate IGA with existing FEM codes. Borden *et al.* [75] introduced these formulas, which are adopted in this section.

3.4.1 Bézier decomposition

We begin with the decomposition the curve of order p into its Bézier elements. We use the knot insertion algorithm for repeating all interior knots of a given knot vector to p times. This process subdivides the geometry into Bézier elements, leading to reducing the order of continuity of the NURBS but the continuity of curve is unchanged. It also means that NURBS basis functions have C^0 continuous between elements and become Bézier basis functions.

An example of a Bézier decomposition of the B-splines basis functions used with knot insertions with an original knot vector $\Xi = [0, 0, 0, 0.2, 0.4, 0.6, 0.8, 1, 1, 1]$

is shown in Fig 3.15. As a result, the number of control points and of basis functions increase equivalently.

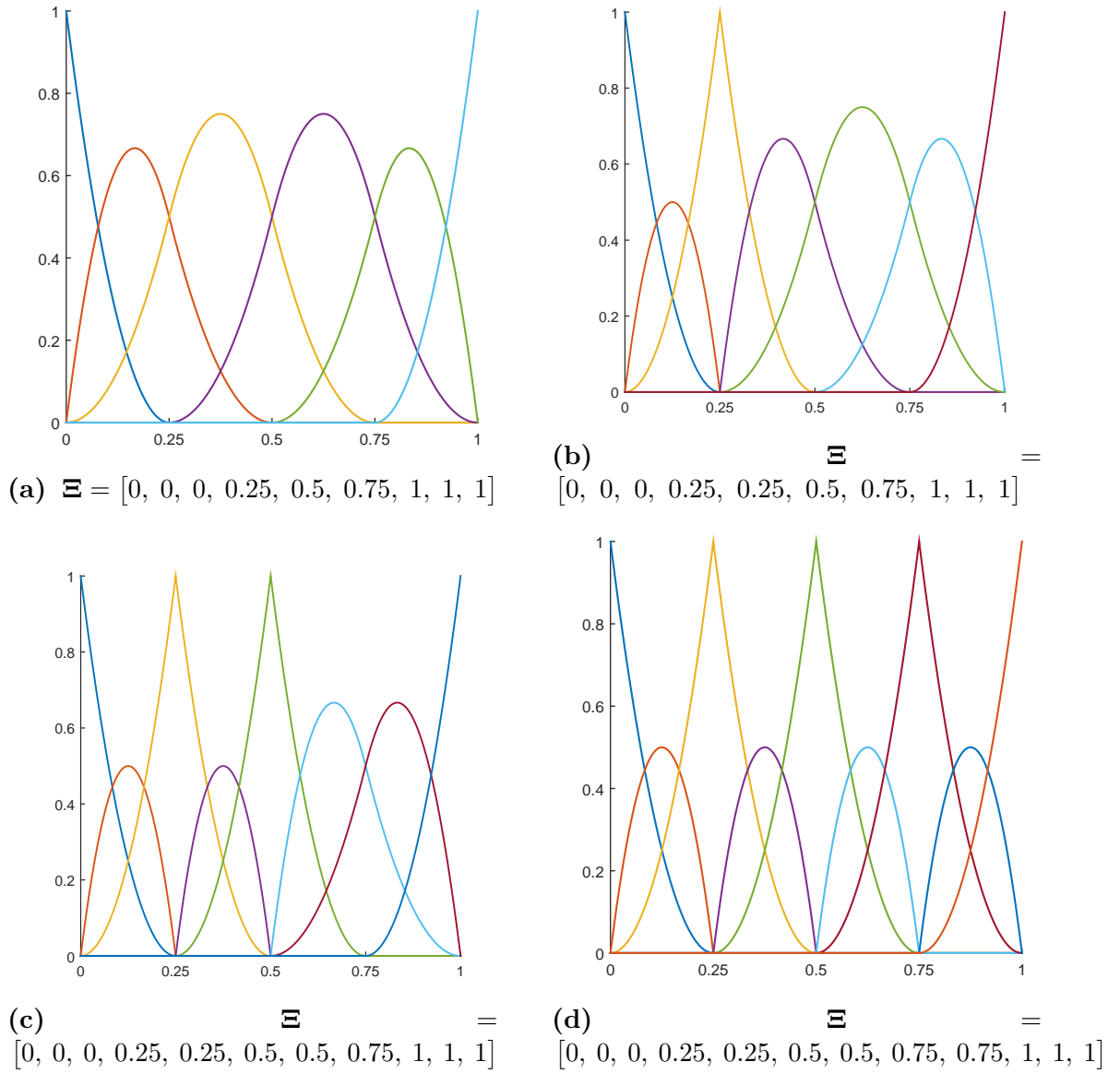


Figure 3.15: Bézier decomposition of $\Xi = [0, 0, 0, 0.25, 0.5, 0.75, 1, 1, 1]$

3.4.2 Bézier extraction [75; 76; 95] of NURBS

Supposedly, a B-spline curve has a knot vector $\Xi = [\xi_1, \xi_2, \dots, \xi_{n+p+1}]$ and a set of control points $\mathbf{P} = \{P_i\}_{i=1}^n$. It allows us to gain m new control $\mathbf{P} = \{\bar{P}_i\}_{i=1}^m$ from the

original control points $\mathbf{P} = \{P_i\}_{i=1}^n$ as

$$\bar{P}_i = \begin{cases} P_1 & i = 1 \\ \alpha_i P_i + (1 - \alpha_i) P_{i-1} & 1 \leq i \leq m \\ P_m & i = m \end{cases} \quad (3.30)$$

Let $\{\bar{\xi}_1, \bar{\xi}_2, \dots, \bar{\xi}_j, \bar{\xi}_m\}$ be a set of knots inserted in Bézier decomposition. Let α_i^j , $i = 1, 2, \dots, n + j$, be i^{th} component of α to j^{th} knot inserted for each new knot $\bar{\xi}_j$; $j = 1, 2, \dots, m$. α_i defined as

$$\alpha_i = \begin{cases} 1 & 1 \leq i \leq k - p \\ \frac{\bar{\xi} - \xi_i}{\xi_{i+p} - \xi_i} & k - p + 1 \leq i \leq k \\ 0 & i \geq k + 1 \end{cases} \quad (3.31)$$

Now, defining \mathbf{C}^j in [71].

$$\mathbf{C}^j = \begin{bmatrix} \alpha_1 & 1 - \alpha_2 & 0 & \dots & & 0 \\ 0 & \alpha_2 & 1 - \alpha_3 & 0 & \dots & 0 \\ 0 & 0 & \alpha_3 & 1 - \alpha_4 & 0 & \dots & 0 \\ \vdots & \vdots & & & \vdots & & \vdots \\ 0 & \dots & & & 0 & \alpha_{n+j-1} & 1 - \alpha_{n+j} \end{bmatrix} \quad (3.32)$$

In matrix form, Eq. 3.30 can be written by knot insertion process as

$$\bar{\mathbf{P}}^{j+1} = (\mathbf{C}^j)^T \bar{\mathbf{P}}^j \quad (3.33)$$

where $\bar{\mathbf{P}}^1 = \mathbf{P}$. The final set of control points is a new set of Bézier ones

$$\mathbf{C}^T = (\mathbf{C}^m)^T (\mathbf{C}^{m-1})^T (\mathbf{C}^1)^T \quad (3.34)$$

Consequently, the relation between new Bézier control points and original B-spline ones has the following form

$$\mathbf{P}^b = \mathbf{C}^T \mathbf{P} \quad (3.35)$$

where \mathbf{C} is called the Bézier extraction operator. The B-spline curve is from

$$x(\xi) = \mathbf{P}^T \mathbf{N}(\xi) \quad (3.36)$$

and after inserting knots, B-spline curve with Bézier points becomes:

$$x(\xi) = x(\mathbf{P}^b)^T \mathbf{B}(\xi) = \mathbf{P}^T \mathbf{C} \mathbf{B}(\xi) \quad (3.37)$$

From Eqs. 3.36 and 3.37 one obtains

$$\mathbf{N}^e(\xi) = \mathbf{C}^e \mathbf{B}(\xi) \quad (3.38)$$

In Eq. 3.38, the B-spline basis functions are equal to the Bernstein polynomials through \mathbf{C}^e ; where \mathbf{C}^e is a Bézier extraction operator, e denotes the element number and $\mathbf{B}(\xi)$ are Bernstein polynomials which is in bi-unit interval $[-1 \ 1]$ as follows:

$$B_{i,p}(\xi) = \frac{1}{2}(1 - \xi)B_{i,p-1}(\xi) + \frac{1}{2}(1 + \xi)B_{i-1,p-1}(\xi) \quad (3.39)$$

where

$$B_{1,0}(\xi) \equiv 1 \quad \text{and} \quad B_{i,p}(\xi) \equiv 0 \quad \text{if} \quad i < 1 \quad \text{or} \quad i > p + 1 \quad (3.40)$$

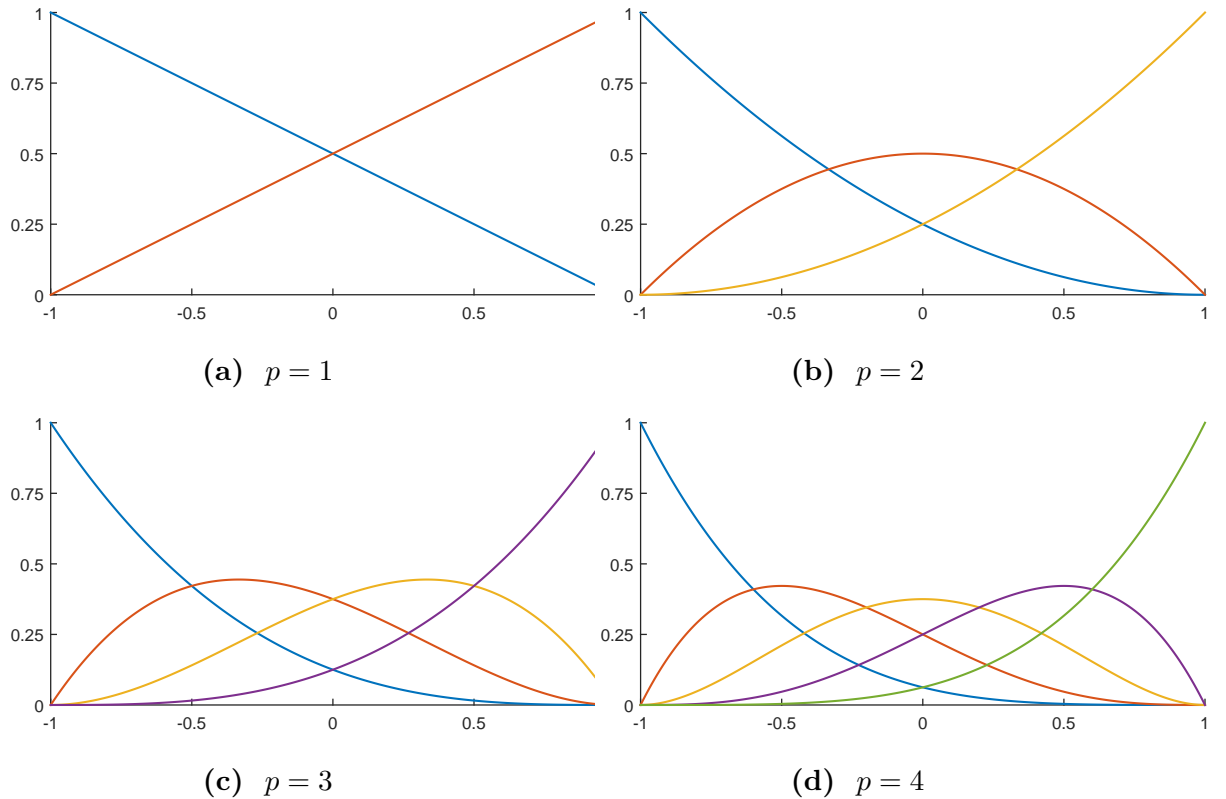


Figure 3.16: The Bernstein polynomials for polynomial degree $p = 1, 2, 3$ and 4 .

The Bernstein polynomials are also symmetric and interpolatory at the endpoints, similar to the Lagrange polynomials. The i^{th} derivative is

$$\frac{d}{d\xi} B_{i,p}(\xi) = \frac{p}{2} \{B_{i-1,p-1}(\xi) - B_{i,p-1}(\xi)\} \quad (3.41)$$

On the result in Eq. 3.36, a NURBS curve can be written as

$$x(\xi) = \frac{1}{W(\xi)} \mathbf{P}^T \mathbf{W} \mathbf{C} \mathbf{N}(\xi) = \frac{1}{W(\xi)} \mathbf{P}^T \mathbf{W} \mathbf{C} \mathbf{B}(\xi) = \frac{1}{W(\xi)} \left(\mathbf{C}^T \mathbf{W} \mathbf{P} \right)^T \mathbf{B}(\xi) \quad (3.42)$$

where \mathbf{W} are the NURBS weights. The weight function $W(\xi)$ is written as follows

$$W(\xi) = \mathbf{w}^T \mathbf{N}(\xi) = \mathbf{w}^T \mathbf{C} \mathbf{B}(\xi) = \left(\mathbf{w}^b \right)^T \mathbf{B}(\xi) = W^b(\xi) \quad (3.43)$$

where \mathbf{w}^b are the Bézier weights and are computed

$$\mathbf{w}^b = \mathbf{C}^T \mathbf{w} \quad (3.44)$$

Similar to Eq. 3.36, a NURBS curve in terms of Bézier points becomes

$$x(\xi) = \frac{1}{W^b(\xi)} \left(\mathbf{P}^b \right)^T \mathbf{W}^b \mathbf{B}(\xi), \quad (3.45)$$

where \mathbf{W}^b is the Bézier weights. Comparing Eqs. 3.42 and 3.45, the relation between the Bézier control points and the NUBRS control points are obtained as

$$\mathbf{P}^b = \left(\mathbf{W}^b \right)^{-1} \mathbf{C}^T \mathbf{W} \mathbf{P} \quad (3.46)$$

The NURBS basis functions for element e using the Bézier extraction operator become

$$\mathbf{R}^e(\xi) = \frac{\mathbf{W}^e \mathbf{N}^e(\xi)}{W^b(\xi)} = \frac{\mathbf{W}^e \mathbf{C}^e \mathbf{B}^e(\xi)}{W^b(\xi)} \quad (3.47)$$

Extraction operator of surface and solid works in the same manner as the NURBS curve as follows:

$$\mathbf{C}^e = \mathbf{C}^e(\xi) \otimes \mathbf{C}^e(\eta) \quad (3.48)$$

and

$$\mathbf{C}^e = \mathbf{C}^e(\xi) \otimes \mathbf{C}^e(\eta) \otimes \mathbf{C}^e(\zeta) \quad (3.49)$$

where $C^e(\xi)$, $C^e(\eta)$ and $C^e(\zeta)$ are the univariate elemental Bézier extractors in the ξ , η and ζ direction.

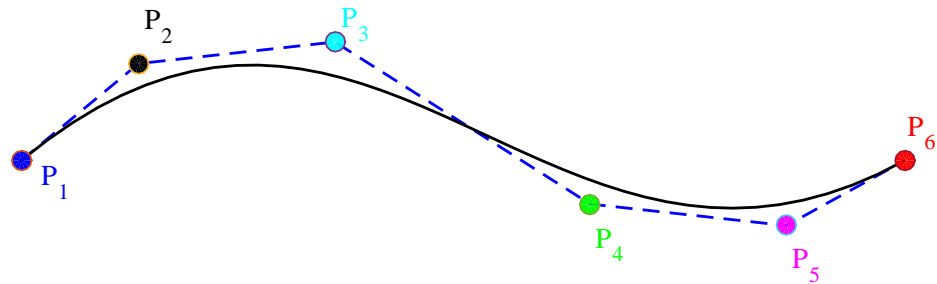
3.5 A brief review on Lagrange extraction of smooth splines

A detail of Lagrange extraction based on smooth splines is presented in the work of Dominik Schillinger *et al.* [77]. We present an overview of this process which decomposes a smooth piecewise polynomial B-spline basis into a C^0 nodal Lagrange basis.

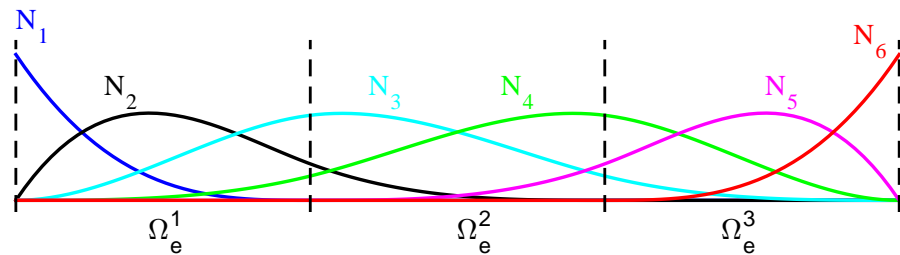
3.5.1 Lagrange decomposition

A B-spline curve $C(\xi)$ as shown in Fig 3.17 (a) is defined by a linear combination of B-spline basis functions $N_{i,p}$ and corresponding set of vector-valued control points P_i over the parametric space as follows:

$$C(\xi) = \sum_{i=1}^n N_{i,p}(\xi) P_i = \mathbf{P}^T \mathbf{N}(\xi) \quad (3.50)$$



(a) B-spline curve and B-spline control points.



(b) Corresponding cubic B-spline basis.

Figure 3.17: Smooth C^2 -continuous curve represented by a B-spline basis

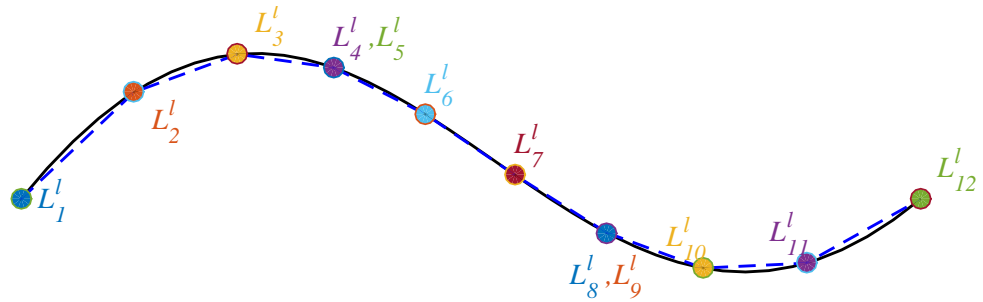
The parametric space which is used to define the B-spline basis function can be derived into knot spans as elements $\hat{\Omega}^e$ in the isogeometric analysis as depicted in Fig

3.17 (b). We now concentrate on a single element e and establish this element to a new parametric coordinate $\xi \in [-1, 1]$. The element is supported $(p + 1)$ B-spline basis functions created a linearly independent and complete polynomial basis up to degree p . We can represent the B-spline basis functions in another form which is based on a linear combination of the basis functions of any other polynomial basis and complete up to polynomial degree p . The nodal Lagrange basis functions satisfies these two properties. For each B-spline function, we can therefore write

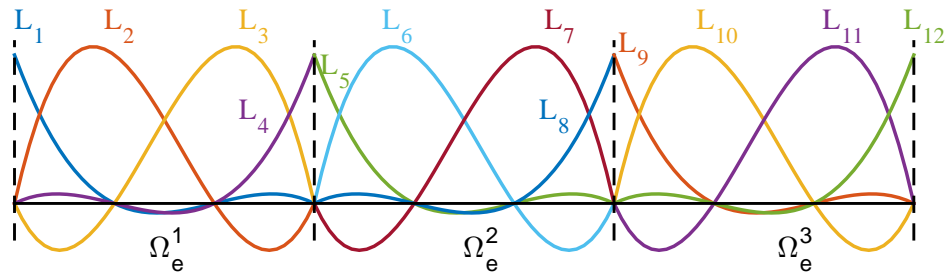
$$N_{a,p}^e(\xi) = \sum_{b=1}^{p+1} \alpha_{ab} L_{b,p}(\xi) \tag{3.51}$$

or in matrix form

$$\mathbf{N}^e(\xi) = \mathbf{D}^e \mathbf{L}(\xi) \tag{3.52}$$



(a) Lagrange curve and Lagrange control points.



(b) Corresponding cubic nodal basis.

Figure 3.18: Smooth C^2 -continuous curve represented by a nodal Lagrange basis

and after inserting Eq. (3.52) into Eq. (3.50), the B-spline curve segment with nodal Lagrange points in Eq. (3.50) becomes

$$C(\xi)^e = (\mathbf{P}^e)^T \mathbf{N}^e(\xi) = (\mathbf{P}^e)^T \mathbf{D}^e \mathbf{L}(\xi) = (\mathbf{P}^{l,e})^T \mathbf{L}(\xi) \tag{3.53}$$

where $\mathbf{L}(\xi) = \mathbf{L}_{a,p}(\xi)_{a=1}^{p+1}$ in Eqs. (3.52, 3.53) is a standard Lagrange basis functions which are identical in each element and associated nodal points $\hat{\xi}_a$ on the element e . Unlike B-splines basis functions which are required index e due to a difference in each element, the Lagrange basis functions are the same in each element. Therefore, they do not require an index e . \mathbf{D}^e , containing the coefficients α_{ab} , is a *Lagrange extraction operator* for element e . From Eq. (3.52), we can also see that the element B-splines functions are equal to the Lagrange basis function through \mathbf{D}^e . Eq. (3.53) also shows the relationship between the Lagrange and the smooth B-spline control points as follows:

$$\mathbf{P}^l = \mathbf{D}^T \mathbf{P} \quad (3.54)$$

Fig. 3.18 (a) shows the Lagrange control points and the new curve represented by Lagrange basis functions which is the same as the B-splines one as shown in Fig 3.17 (a). Fig 3.18 (a) also shows that this curve remains higher-order continuity between curve elements in spite of C^0 continuous Lagrange shape functions at element boundaries. The cubic Lagrange basis functions are shown in Fig 3.18 (b) over each element.

3.5.2 The Lagrange extraction operator

In this subsection, the computation of the Lagrange extraction operator is presented by using its interpolatory property at the nodal points $\hat{\xi}_a$ [96].

$$\mathbf{L}_{a,p}(\hat{\xi}_a) = \begin{cases} 1 & \text{if } a = b \\ 0 & \text{if } a \neq b \end{cases} \quad (3.55)$$

Fig. 3.18 (b) illustrates an examples of the interpolatory property at element nodes. An interpolation $\bar{u}(\xi)$ of a function $u(\xi)$ can be obtained by using Eq. (3.55) with nodal basis functions $\mathbf{L}_{a,p}$ as follow

$$\bar{u}(\xi) = \sum_{a=1}^{p+1} \mathbf{L}_{a,p} u(\hat{\xi}_a) \quad (3.56)$$

From Eq.(3.55) and (3.56), the coefficients of \mathbf{D}^e in the a^{th} row in Eq. (3.52) can be obtained by evaluating the corresponding $N_{a,p}^e$ at all element nodes $\{\hat{\xi}_b\}_{b=1}^{p+1}$. The full Lagrange extraction operator, \mathbf{D}^e , for 1D element can be expressed as

$$\mathbf{D}_{ab}^e = N_{a,p}^e(\hat{\xi}_b), \quad \{a, b\} = 1, \dots, p + 1 \quad (3.57)$$

or in matrix form

$$\mathbf{D}^e = \begin{bmatrix} N_{1,p}^e(\hat{\xi}_1) & N_{1,p}^e(\hat{\xi}_2) & \dots & N_{1,p}^e(\hat{\xi}_{p+1}) \\ N_{2,p}^e(\hat{\xi}_1) & N_{2,p}^e(\hat{\xi}_2) & \dots & N_{2,p}^e(\hat{\xi}_{p+1}) \\ \vdots & \vdots & & \vdots \\ N_{p+1,p}^e(\hat{\xi}_1) & N_{p+1,p}^e(\hat{\xi}_2) & \dots & N_{p+1,p}^e(\hat{\xi}_{p+1}) \end{bmatrix} \quad (3.58)$$

This subsection demonstrated the concept of one-dimensional Lagrange extraction operator. A multi-dimensional one can be constructed by evaluating tensor-product B-spline functions at nodal points. Summary of the element-level transformation connections between B-spline and Lagrange basis functions is shown in Fig 3.19. An example of the element-level transformation for 2D case is shown in Fig. 3.20.

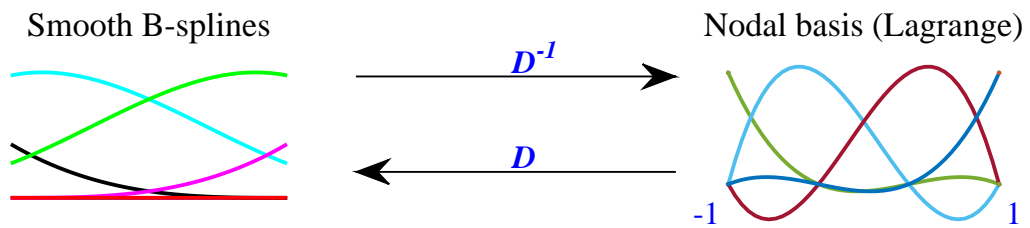


Figure 3.19: Demonstration of the Lagrange extraction operators in 1D case and their inverse for the transformation of B-spline, Lagrange on an element level. The second B-Splines element of the example curve is shown in Fig 3.17

3.5.3 Rational Lagrange basis functions and control points

NURBS can represent some conic shapes such as circles and ellipsoids exactly while B-Spline cannot represent these shapes. NURBS basis functions on each element e , $\mathbf{R}^e(\xi) = \{R_{a,p}^e(\xi)\}_{a=1}^{p+1}$, can be defined as

$$R_{a,p}^e(\xi) = \frac{w_a N_{a,p}^e(\xi)}{W(\xi)} \quad (3.59)$$

where w_a are weights of the a^{th} basis function. The weight function W is expressed as

$$W(\xi) = \sum_{b=1}^{p+1} w_b N_{b,p}^e(\xi) \quad (3.60)$$

We can rewrite Eq. (3.59) in matrix form

$$\mathbf{R}(\xi) = \frac{1}{W(\xi)} \mathbf{W} \mathbf{N}(\xi) \quad (3.61)$$

where \mathbf{W} is the diagonal matrix of weights defined as

$$\mathbf{W} = \begin{bmatrix} w_1 & & & \\ & w_2 & & \\ & & \ddots & \\ & & & w_{p+1} \end{bmatrix} \quad (3.62)$$

The NURBS curve in matrix form can be written as

$$C(\xi) = \mathbf{P}^T \mathbf{R}(\xi) = \frac{1}{W(\xi)} \mathbf{P}^T \mathbf{W} \mathbf{N}(\xi) \quad (3.63)$$

Substituting Eq. (3.52) into Eq. (3.63), the NURBS curve becomes NURBS curve in terms of the nodal Lagrange basis functions as follows

$$C(\xi) = \frac{1}{W(\xi)} \mathbf{P}^T \mathbf{W} \mathbf{D} \mathbf{L}(\xi) = \frac{1}{W(\xi)} (\mathbf{D}^T \mathbf{W} \mathbf{P})^T \mathbf{L}(\xi) \quad (3.64)$$

The weight function $W(\xi)$ in Eq. (3.68) is written in matrix form as

$$W(\xi) = \mathbf{w}^T \mathbf{N}(\xi) \quad (3.65)$$

In terms of the nodal Lagrange basis, the weight function becomes

$$W(\xi) = \mathbf{w}^T \mathbf{D} \mathbf{L}(\xi) = (\mathbf{D}^T \mathbf{w})^T \mathbf{L}(\xi) = (\mathbf{w}^l)^T \mathbf{L}(\xi) = W^l(\xi) \quad (3.66)$$

where $\mathbf{w} = \{w_a\}_{a=1}^{p+1}$ is a weight vector associated with NURBS basis function while $\mathbf{w}^l = \mathbf{D}^T \mathbf{w}$ is a weight vector associated with the Lagrange basis functions.

$$\mathbf{W}^l = \begin{bmatrix} w_1^l & & & \\ & w_2^l & & \\ & & \ddots & \\ & & & w_{p+1}^l \end{bmatrix} \quad (3.67)$$

By defining the diagonal matrix \mathbf{W}^l in Eq. (3.67), the Lagrange control points can be computed as

$$\mathbf{P}^l = (\mathbf{W}^l)^{-1} \mathbf{D}^T \mathbf{W} \mathbf{P} \quad (3.68)$$

This equation shows the connection between the Lagrange control points and the NURBS ones. We obtain the new form by multiplying \mathbf{W}^l to both sides in Eq. (3.68) as

$$\mathbf{D}^T \mathbf{W} \mathbf{P} = \mathbf{W}^l \mathbf{P}^l \quad (3.69)$$

Substituting Eq. (3.69) into Eq. (3.64), we finally obtain the Lagrange representation of a NURBS curve.

$$\begin{aligned} C(\xi) &= \mathbf{P}^T \mathbf{R}(\xi) = \frac{1}{W(\xi)} \mathbf{P}^T \mathbf{W} \mathbf{N}(\xi) = \frac{1}{W(\xi)} (\mathbf{D}^T \mathbf{W} \mathbf{P})^T \mathbf{L}(\xi) \\ &= \frac{1}{W^l(\xi)} (\mathbf{P}^l)^T \mathbf{W}^l \mathbf{D} \mathbf{L}(\xi) = \sum_{a=1}^n \frac{w_a^l L_{a,p}(\xi)}{W^l(\xi)} \mathbf{P}_a^l \end{aligned} \quad (3.70)$$

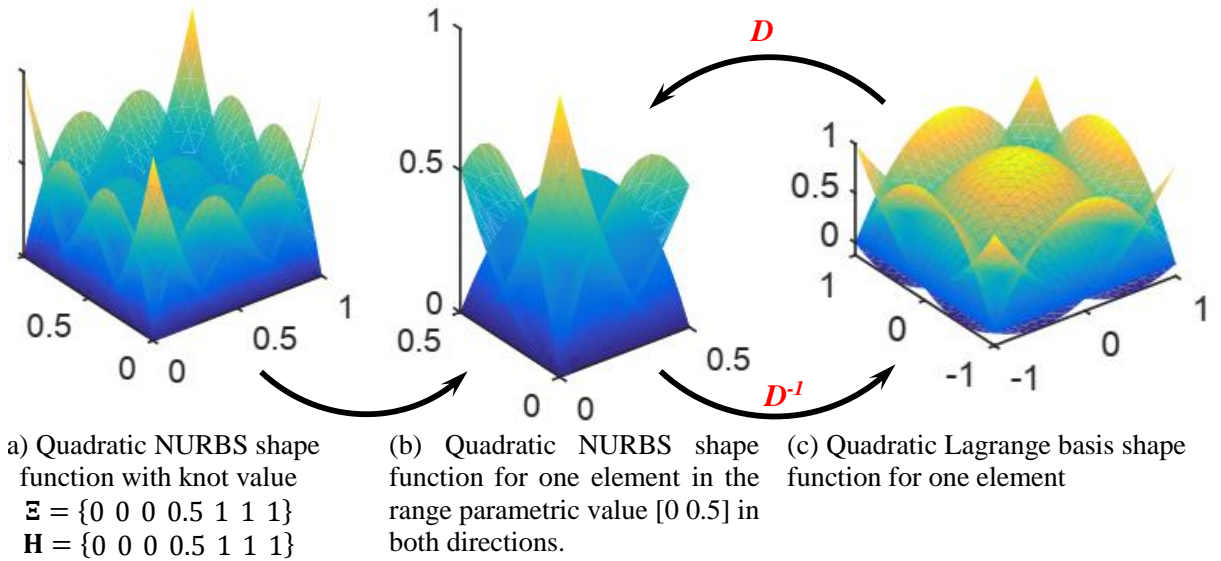


Figure 3.20: Demonstration of the Lagrange extraction operators in 2D case and their inverse for the transformation of NURBS and Lagrange on an element level. The first NURBS element of 2D case example is shown in Fig. 3.20(a)

In summary, each segment of a smooth NURBS curve can be equivalently represented by a set of C^0 nodal Lagrange elements. Note that the Lagrange representation of the NURBS curve still remains smoothness between curve segments in spite of the C^0 continuity of the nodal basis functions at element boundaries.

3.5.4 Using Lagrange extraction operators in a finite element code

After using a CAD tool to design the analyzed geometric object, we generate the data included Lagrange elements, control points \mathbf{P}^l , weights \mathbf{W}^l and extraction operators \mathbf{D} . These information are stored for each element separately. In element-level subroutines, we can use a standard nodal FEM code to compute the element stiffness matrix \mathbf{k}_{FEA}^e and the element load vector \mathbf{f}_{FEA}^e . Then, we use Lagrange extraction operator to compute the IGA element stiffness and load vector in Eqs. (3.71, 3.72) to transform the C^0 -continuous Lagrange to the NURBS element before assembly into the global arrays.

$$\mathbf{k}_{IGA}^e = (\mathbf{D}^e) \mathbf{k}_{FEA}^e (\mathbf{D}^e)^T \quad (3.71)$$

$$\mathbf{f}_{IGA}^e = (\mathbf{D}^e) \mathbf{f}_{FEA}^e \quad (3.72)$$

where \mathbf{k}_{IGA}^e and \mathbf{k}_{FEA}^e are the element stiffness matrices and \mathbf{f}_{IGA}^e and \mathbf{f}_{FEA}^e are the element force vectors for the smooth spline case and C^0 continuous Lagrange case, respectively.

4

THE ISOGEOMETRIC FINITE ELEMENT METHOD APPROACH TO LIMIT AND SHAKEDOWN ANALYSIS

4.1 Introduction

In general, the problem of limit and shakedown analysis can be transformed into an issue of mathematical nonlinear programming. In this chapter, the integrations in Eq. (2.53) is transformed into summation forms, which are based on two discretizations as follows:

- Load domain discretization: the integration over a certain time interval $t \in [0, T]$ is transformed into a summation form for $k = \overline{1, m}$, where k is a loading vertex and $m = 2^n$ is a number of vertices in the load space, n is the number of variable loads.
- Isogeometric finite element discretization: the integration over the entire structure Ω is transformed into the numerical integration for $i = \overline{1, NG}$, where i is a Gaussian point and NG is the number of Gaussian points in the structure.

With these discretizations, the limit and shakedown analysis is reduced to checking the restrictions only at all load vertices m and all Gaussian points NG instead of checking for the entire load domain L and the entire structure Ω .

Studying the lower bound theorem of Melan [16], Belystchko [19] showed that if the static shakedown condition is satisfied for all corners of the given convex polyhedral load domain then it will be satisfied for any load path within this domain. According

to the von Mises yield criterion and this remark, the shakedown limit load factor is introduced as a nonlinear optimization problem by Belytschko [19]. Based on the static theorem of Melan [16], Corradi *et al.* [97] improved Maier's work which analyzed the shakedown problem by linear programming with large number constraints to less linear inequality constraints, applied in numerical computations and obtained a primal static formulation as well as its dual kinematic version through duality properties. Dualities and convergence in limit and shakedown analysis were studied by Morelle [89; 90], Nguyen [98], Xue *et al.* [99], Xu *et al.* [100],...They focused two different kinds of duality in shakedown.

Discrete formulations of lower bound methods for perfectly plastic structures have been presented by some researchers such as: Hachemi *et al.* [101], Weichert [102], Le *et al.* [48] and so on. A primal dual approach to the discretization of the upper and lower bound method has been presented for perfectly plastic structures by some researchers: Vu. D. K [28], Yan [98], Do [54],.... A mainly extend Vu's discrete formulation of the upper bound method based on isogeometric analysis is investigated.

In this chapter, some problems are studied as below:

- The discretized formulations of limit and shakedown using isogeometric finite element method.
- The duality between upper bound and lower bound of shakedown limit load factor.
- The dual procedure for limit and shakedown analysis algorithm between the upper bound and lower bound.

4.2 Isogeometric FEM discretizations

4.2.1 Discretization formulation of lower bound

As we know in analysis of solids, by applying the principle of virtual work presented in Section 2.2.2 to the equilibrium equations we obtain their corresponding "weak form" and this "weak form" can be discretized by mean of the isogeometric finite element method.

First of all, the Eq. (2.24), the principle of virtual work equation, can be rewritten in matrix form:

$$\int_{\Omega} \boldsymbol{\sigma} \delta \boldsymbol{\varepsilon}^T d\Omega = \int_{\Omega} \mathbf{g} \delta \mathbf{u}^T d\Omega + \int_{\Gamma_t} \mathbf{q} \delta \mathbf{u}^T d\Gamma_t \quad (4.1)$$

The virtual displacement $\delta \mathbf{u}$ within an element e is approximated by interpolation of control point values:

$$\delta \mathbf{u} = \sum_{l=1}^{n_e} \mathbf{N}_l \delta \mathbf{u}_l^e \quad (4.2)$$

where \mathbf{N}_l and \mathbf{u}_l^e are the l^{th} shape function matrix and the vector of virtual displacements of the l^{th} control point of the IGA element e which has n_e control points. The virtual strain $\delta\boldsymbol{\varepsilon}$ is derived by:

$$\delta\boldsymbol{\varepsilon} = \partial\delta\mathbf{u} = \partial\mathbf{N}(\mathbf{x})\delta\mathbf{u}^e = \mathbf{B}(\mathbf{x})\delta\mathbf{u}^e \quad (4.3)$$

Note that $\mathbf{B}(\mathbf{x}) = \partial\mathbf{N}(\mathbf{x})$ is a deformation matrix. Eq.(4.3) is called strain-displacement relation or relation of upper bound and lower bound method.

By subdividing the whole volume Ω into ne elements Ω_e . By using Eqs.(4.2), (4.3) and some manipulations, the integration Eq.(4.1) has the following form:

$$\sum_{e=1}^{ne} \sum_{i=1}^{ng} w_i \mathbf{B}_i^{eT} \boldsymbol{\sigma}_i = \sum_{e=1}^{ne} \mathbf{f}^e \quad (4.4)$$

The Eq. (4.4) in elastic behaviour case becomes as follow

$$\sum_{e=1}^{ne} \sum_{i=1}^{ng} w_i \mathbf{B}_i^{eT} \boldsymbol{\sigma}_{ik}^E = \sum_{e=1}^{ne} \mathbf{f}_k^e \quad (4.5)$$

where

- \mathbf{B}_i^e is the deformation matrix $\mathbf{B}(\mathbf{x})$ at Gauss point \mathbf{x}_i of element Ω_e .
- \mathbf{f}^e is force vector of element e .
- w_i is the weight factor of the Gauss point i .
- n_e is the total number of elements in Ω
- ng is the total number of integration Gauss points in each element Ω_e .
- $\boldsymbol{\sigma}_{ik}^E$ defines the fictitious elastic stress vector at Gauss point i corresponding to the load domain vertex \hat{P}_k and is computed by $\boldsymbol{\sigma}_{ik}^E = \mathbf{E}^e \mathbf{B}_i^e \mathbf{u}_k^e$.
- \mathbf{f}_k^e is force vector of element e corresponding to the load domain vertex \hat{P}_k .
- \mathbf{E}^e is elastic modul matrix of the element e .

By integration on the whole elements using the Gauss-Legendre integration technique, the Eq.(4.5) can be expressed as follow:

$$\sum_{i=1}^{NG} w_i \mathbf{B}_i^{eT} \boldsymbol{\sigma}_{ik}^E = \sum_{e=1}^{ne} \mathbf{f}_k^e \quad (4.6)$$

where $NG = ne \times ng$ is total number of Gaussian point on whole domain. For residual stress, the Eq.(4.6) can be written as

$$\sum_{i=1}^{NG} w_i \mathbf{B}_i^{eT} \bar{\boldsymbol{\rho}}_i = \mathbf{B}^T \bar{\boldsymbol{\rho}} = \mathbf{0} \quad (4.7)$$

where \mathbf{B} is the global deformation matrix and $\bar{\boldsymbol{\rho}}$ denotes the global residual stress vector. They have the following form:

$$\mathbf{B} = \left[w_1 \mathbf{B}_1, w_2 \mathbf{B}_2, \dots, w_i \mathbf{B}_i, \dots, w_{NG-1} \mathbf{B}_{NG-1}, w_{NG} \mathbf{B}_{NG} \right] \quad (4.8)$$

$$\bar{\boldsymbol{\rho}}^T = \left[\bar{\boldsymbol{\rho}}_1^T, \bar{\boldsymbol{\rho}}_2^T, \dots, \bar{\boldsymbol{\rho}}_i^T, \dots, \bar{\boldsymbol{\rho}}_{NG-1}^T, \bar{\boldsymbol{\rho}}_{NG}^T \right] \quad (4.9)$$

Because the value of the residual stress $\bar{\boldsymbol{\rho}}$ is calculated at Gaussian point, the discretized necessary limit and shakedown conditions at Gaussian point i can be represented by:

$$f\left(\alpha \boldsymbol{\sigma}_{ik}^E + \bar{\boldsymbol{\rho}}_i\right) \leq 0 \quad \forall k = \overline{1, m} \quad \forall i = \overline{1, NG} \quad (4.10)$$

By using Eq.(2.24), the lower bound of the shakedown load multiplier presented in Eq.(2.37) may be written as:

$$\alpha^- = \max \alpha \quad (a)$$

subjected to: (4.11)

$$\left\{ \begin{array}{l} \int_{\Omega} \delta \varepsilon_{ij}(\mathbf{x}) \partial_j \bar{\rho}_{ij}(\mathbf{x}) d\Omega = 0 \quad \text{in } \Omega \quad (b) \\ \int_{\Omega} \delta \varepsilon_{ij}(\mathbf{x}) \sigma_{ij}^E(\mathbf{x}, \hat{P}_k) d\Omega = \int_{\Omega} f_i(\mathbf{x}, \hat{P}_k) \dot{u}_i d\Omega + \int_{\Gamma_t} \bar{t}_i(\mathbf{x}, \hat{P}_k) \dot{u}_i d\Gamma_t \quad \text{on } \Gamma_t \quad (c) \\ f\left(\alpha \sigma_{ij}^E(\mathbf{x}, \hat{P}_k) + \bar{\rho}_{ij}(\mathbf{x})\right) \leq 0 \quad \forall k = \overline{1, m} \quad (d) \end{array} \right.$$

Finally, the lower bound of limit and shakedown load factor which is based on Eq.(4.11), (4.7) and (4.10) becomes as

$$\alpha^- = \max \alpha \quad (a)$$

subjected to: (4.12)

$$\left\{ \begin{array}{l} \sum_{i=1}^{NG} w_i \mathbf{B}_i^{eT} \bar{\boldsymbol{\rho}}_i = \mathbf{B}^T \bar{\boldsymbol{\rho}} = \mathbf{0} \quad \text{in } \Omega \quad (b) \\ f\left(\alpha \boldsymbol{\sigma}_{ik}^E + \bar{\boldsymbol{\rho}}_i\right) \leq 0 \quad \forall k = \overline{1, m} \quad \forall i = \overline{1, NG} \quad (c) \end{array} \right.$$

The nonlinear mathematical optimization problem in Eq.(4.12) has $(NSC \times NG + 1)$ unknown variables: $NSC \times NG$ the residual stress $\bar{\rho}_i$ and load multiplier α , where NSC denotes number of stress components of each Gaussian point.

4.2.2 Discretization formulation of upper bound and upper bound algorithm

By subdividing the whole domain Ω into element Ω_e as the same way in the lower bound, the integration of the internal dissipation energy becomes

$$\sum_{k=1}^m \sum_{e=1}^{ne} \int_{\Omega_e} \mathbf{D}^p(\dot{\varepsilon}_{ij}^k) d\Omega \quad (4.13)$$

In case of using the von Mises yield criterion, the plastic dissipation function has a form as

$$\mathbf{D}^p(\dot{\varepsilon}_{ij}^k) = 2k_v \sqrt{J_2(\dot{\varepsilon}_{ij}^k)} = 2k_v \sqrt{\frac{1}{2} \dot{\varepsilon}_k^T \mathbf{D}_s \dot{\varepsilon}_k} \quad (4.14)$$

where $\dot{\varepsilon}_{ij}^k$ is plastic stain rate vector at load vertex k . \mathbf{D}_s is a diagonal square matrix and has a form as

$$\mathbf{D}_s = \text{diag} \left[1 \quad 1 \quad \frac{1}{2} \right] \quad \text{for plane stress or plane strain problems} \quad (4.15)$$

$$\mathbf{D}_s = \text{diag} \left[1 \quad 1 \quad 1 \quad \frac{1}{2} \right] \quad \text{for axisymmetric problems} \quad (4.16)$$

$$\mathbf{D}_s = \text{diag} \left[1 \quad 1 \quad 1 \quad \frac{1}{2} \quad \frac{1}{2} \quad \frac{1}{2} \right] \quad \text{for 3D problems} \quad (4.17)$$

and $\dot{\varepsilon}_k$ denotes the vector of strain rate at load vertex k .

$$\begin{aligned} \dot{\varepsilon}_k &= \left[\dot{\varepsilon}_{11}^k \quad \dot{\varepsilon}_{22}^k \quad \dot{\varepsilon}_{33}^k \quad 2\dot{\varepsilon}_{12}^k \quad 2\dot{\varepsilon}_{23}^k \quad 2\dot{\varepsilon}_{31}^k \right]^T \\ &= \left[\dot{\varepsilon}_{11}^k \quad \dot{\varepsilon}_{22}^k \quad \dot{\varepsilon}_{33}^k \quad \dot{\gamma}_{12}^k \quad \dot{\gamma}_{23}^k \quad \dot{\gamma}_{31}^k \right]^T \quad \text{for 3D problems} \end{aligned} \quad (4.18)$$

Substitution Eq.(4.14) into Eq.(4.13), the Eq.(4.13) becomes as

$$\sum_{k=1}^m \sum_{e=1}^{ne} \int_{\Omega_e} 2k_v \sqrt{\frac{1}{2} \dot{\varepsilon}_k^T \mathbf{D}_s \dot{\varepsilon}_k} d\Omega \quad (4.19)$$

The integration of the internal dissipation energy in Eq. (4.19) is calculated at Gaussian point i by using the Gauss-Legendre integration technique. The Eq. (4.19) becomes as

$$\begin{aligned} \sum_{k=1}^m \sum_{e=1}^{ne} \int_{\Omega_e} \mathbf{D}^p(\dot{\varepsilon}_{ij}^k) d\Omega &= \sum_{k=1}^m \sum_{e=1}^{ne} \sum_{i=1}^{ng} 2k_v \sqrt{\frac{1}{2} \dot{\varepsilon}_{ik}^T \mathbf{D}_s \dot{\varepsilon}_{ik}} \\ &= \sum_{k=1}^m \sum_{i=1}^{NG} \sqrt{2} k_v w_i \sqrt{\dot{\varepsilon}_{ik}^T \mathbf{D}_s \dot{\varepsilon}_{ik}} \end{aligned} \quad (4.20)$$

The difficulty of limit and shakedown analysis based on upper bound deals with singular dissipation function. In order to overcome this difficulty, many researchers such as Bui [103], Jospin and Nguyen [28], Yan [93],... utilized a technique called regularization of plastic dissipation function as an alternative plastic dissipation. The regularization method may be divided into three groups as viscous-plastic, separated-region and whole-region regularization method. Following the whole-region regularization technique, Anderson *et al.* [25; 26] modified the original dissipation function $\mathbf{D}^p(\dot{\varepsilon}_{ij}^k)$ by another one $\mathbf{D}^p(\dot{\varepsilon}_{ij}^k + \varepsilon_0^2)$. where ε_0 is a small value with condition $0 < \varepsilon_0^2 \ll 1$. We also follows this regularization in our analysis. Eq.(4.20) becomes

$$\sum_{k=1}^m \sum_{e=1}^{ne} \int_{\Omega_e} \mathbf{D}^p(\dot{\varepsilon}_{ij}^k + \varepsilon_0^2) d\Omega = \sum_{k=1}^m \sum_{i=1}^{NG} \sqrt{2} k_v w_i \sqrt{\dot{\varepsilon}_{ik}^T \mathbf{D}_s \dot{\varepsilon}_{ik} + \varepsilon_0^2} \quad (4.21)$$

By applying the same integration technique, the external energy calculated at Gaussian point i can be written as

$$\sum_{k=1}^m \int_{\Omega} \boldsymbol{\sigma}_k^E \dot{\varepsilon}^k d\Omega = \sum_{k=1}^m \sum_{i=1}^{NG} w_i \dot{\varepsilon}_{ik}^T \boldsymbol{\sigma}_{ik}^E \quad (4.22)$$

The incompressibility condition and compatible condition at each Gauss point i become as

$$\sum_{k=1}^m \boldsymbol{\varepsilon}_{ik} = \mathbf{B}_i \mathbf{u} \quad (4.23)$$

$$\dot{\varepsilon}_{11}^k + \dot{\varepsilon}_{22}^k + \dot{\varepsilon}_{33}^k = 0 \quad \text{for 3D problems} \quad (4.24)$$

Eq.(4.24) in general problem can be expressed in matrix form as

$$\mathbf{D}_v \dot{\varepsilon}_{ik} = \mathbf{0} \quad (4.25)$$

where \mathbf{D}_v is a square matrix and has a following form as

$$\mathbf{D}_v = \begin{bmatrix} 1 & 1 & 0 \\ 1 & 1 & 0 \\ 0 & 0 & 0 \end{bmatrix} \quad \text{for plane stress or plane strain problems} \quad (4.26)$$

$$\mathbf{D}_v = \begin{bmatrix} 1 & 1 & 1 & 0 \\ 1 & 1 & 1 & 0 \\ 1 & 1 & 1 & 0 \\ 0 & 0 & 0 & 0 \end{bmatrix} \quad \text{for axisymmetric problems} \quad (4.27)$$

$$\mathbf{D}_v = \begin{bmatrix} 1 & 1 & 1 & 0 & 0 & 0 \\ 1 & 1 & 1 & 0 & 0 & 0 \\ 1 & 1 & 1 & 0 & 0 & 0 \\ 0 & 0 & 0 & 0 & 0 & 0 \\ 0 & 0 & 0 & 0 & 0 & 0 \\ 0 & 0 & 0 & 0 & 0 & 0 \end{bmatrix} \quad \text{for 3D problems} \quad (4.28)$$

From Eq.(4.21) to Eq.(4.25), the optimization problem for shakedown limit load multiplier based on upper bound approach in Eq.(2.53) is formulated as

$$\alpha^+ = \min \sum_{k=1}^m \sum_{i=1}^{NG} \sqrt{2k_v w_i} \sqrt{\dot{\boldsymbol{\epsilon}}_{ik}^T \mathbf{D}_s \dot{\boldsymbol{\epsilon}}_{ik} + \varepsilon_0^2} \quad (\text{a})$$

subjected to: (4.29)

$$\begin{cases} \sum_{k=1}^m \dot{\boldsymbol{\epsilon}}_{ik} = \mathbf{B}_i \mathbf{u} & \forall i = \overline{1, NG} \end{cases} \quad (\text{b})$$

$$\begin{cases} \mathbf{D}_v \dot{\boldsymbol{\epsilon}}_{ik} = \mathbf{0} & \forall k = \overline{1, m} \quad \forall i = \overline{1, NG} \end{cases} \quad (\text{c})$$

$$\begin{cases} \sum_{k=1}^m \sum_{i=1}^{NG} w_i \dot{\boldsymbol{\epsilon}}_{ik}^T \boldsymbol{\sigma}_{ik}^E = 1 \end{cases} \quad (\text{d})$$

By reason of simplicity, we begin with rewriting the upper bound shakedown limit in Eq.(4.29) by defining some new definitions

+ The new strain rate vector \mathbf{e}_{ik}

$$\mathbf{e}_{ik} = w_i \mathbf{D}_s^{1/2} \dot{\boldsymbol{\epsilon}}_{ik} \quad (4.30)$$

+ The new fictitious elastic stress vector \mathbf{t}_{ik}

$$\mathbf{t}_{ik} = \mathbf{D}_s^{-1/2} \boldsymbol{\sigma}_{ik}^E \quad (4.31)$$

+ The new deformation matrix $\hat{\mathbf{B}}_{ik}$

$$\hat{\mathbf{B}}_{ik} = w_i \mathbf{D}_s^{1/2} \mathbf{B}_i \quad (4.32)$$

where $\mathbf{D}_s^{1/2}$ and $\mathbf{D}_s^{-1/2}$ are symmetric matrices such that: $\mathbf{D}_s^{-1/2} = (\mathbf{D}_s^{1/2})^{-1}$ and $\mathbf{D}_s = \mathbf{D}_s^{1/2} \mathbf{D}_s^{1/2}$. From Eq.(4.17), we have $\mathbf{D}_s^{-1/2}$, $\mathbf{D}_s^{1/2}$ for 3D problems as follow:

$$\mathbf{D}_s^{1/2} = \text{diag} \left[1 \quad 1 \quad 1 \quad \frac{1}{\sqrt{2}} \quad \frac{1}{\sqrt{2}} \quad \frac{1}{\sqrt{2}} \right] \quad (4.33)$$

$$\mathbf{D}_s^{-1/2} = \text{diag} \left[1 \quad 1 \quad 1 \quad \sqrt{2} \quad \sqrt{2} \quad \sqrt{2} \right] \quad (4.34)$$

Then the objective function in Eq.(4.29)a can be rewritten as

$$\begin{aligned} \alpha^+ &= \min \sum_{k=1}^m \sum_{i=1}^{NG} \sqrt{2} k_v w_i \sqrt{\dot{\mathbf{e}}_{ik}^T \mathbf{D}_s \dot{\mathbf{e}}_{ik} + \varepsilon_0^2} \\ &= \sqrt{2} k_v \sum_{k=1}^m \sum_{i=1}^{NG} \sqrt{w_i^2 \dot{\mathbf{e}}_{ik}^T \mathbf{D}_s \dot{\mathbf{e}}_{ik} + w_i^2 \varepsilon_0^2} = \sqrt{2} k_v \sum_{k=1}^m \sum_{i=1}^{NG} \sqrt{\dot{\mathbf{e}}_{ik}^T \dot{\mathbf{e}}_{ik} + \varepsilon_{0N}^2} \end{aligned} \quad (4.35)$$

As mentioned above, ε_0 , a small positive value, is chosen to overcome the singularity of the objective function. This leads to assume that ε_{0N} , a small positive number, is chosen to satisfy as

$$\varepsilon_{0N} = w_i \varepsilon_0 = \text{constant} \quad \forall i = \overline{1, NG} \quad (4.36)$$

Finally, a simplified form is obtained for the upper bound shakedown limit load as

$$\alpha^+ = \min \sum_{k=1}^m \sum_{i=1}^{NG} \sqrt{2} k_v \sqrt{\dot{\mathbf{e}}_{ik}^T \dot{\mathbf{e}}_{ik} + \varepsilon_{0N}^2} \quad (\text{a}) \quad (4.37)$$

subjected to:

$$\begin{cases} \sum_{k=1}^m \mathbf{e}_{ik} - \hat{\mathbf{B}}_i \mathbf{u} = \mathbf{0} & \forall i = \overline{1, NG} \end{cases} \quad (\text{b})$$

$$\begin{cases} \frac{1}{3} \mathbf{D}_v \mathbf{e}_{ik} = \mathbf{0} & \forall k = \overline{1, m} \quad \forall i = \overline{1, NG} \end{cases} \quad (\text{c})$$

$$\begin{cases} \sum_{k=1}^m \sum_{i=1}^{NG} \mathbf{e}_{ik}^T \mathbf{t}_{ik} - 1 = \mathbf{0} \end{cases} \quad (\text{d})$$

In order to solve optimization problem in Eq.(4.37), we use penalty method to modify the original objective function by adding the compatibility constraint in Eq. (4.37b) and incompressibility constraint (4.37c). The penalty function has a form as

$$\begin{aligned} F_P = \sum_{i=1}^{NG} \left\{ \sum_{k=1}^m \sqrt{2} k_v \sqrt{\mathbf{e}_{ik}^T \mathbf{e}_{ik} + \varepsilon_{0N}^2} + \frac{c}{2} \sum_{k=1}^m \mathbf{e}_{ik}^T \mathbf{D}_v \mathbf{e}_{ik} \right. \\ \left. + \frac{c}{2} \left(\sum_{k=1}^m \mathbf{e}_{ik} - \hat{\mathbf{B}}_i \mathbf{u} \right) \left(\sum_{k=1}^m \mathbf{e}_{ik} - \hat{\mathbf{B}}_i \mathbf{u} \right) \right\} \end{aligned} \quad (4.38)$$

where

- c is penalty parameter satisfied condition $c \gg 1$. The parameter c may be dependent on integration points or load vertices and c should be adjusted to fit different compatibility criteria. However, at this stage, for the sake of simplicity, c is let to be constant everywhere. Theoretically, when c goes to infinity we will recover related conditions.
- ε_{0N}^2 is a positive number and its value is reduced to zero as the procedure converges to solution. When ε_{0N}^2 goes to zero, the accurate solution may be expected provided that c is sufficiently large.

Based on the penalty function above, the upper bound problem in Eq.(4.37) converts into the modified form as:

$$\alpha^+ = \sqrt{2} k_v \left(\min F_P \right) \quad (\text{a})$$

subjected to: (4.39)

$$\sum_{k=1}^m \sum_{i=1}^{NG} \mathbf{e}_{ik}^T \mathbf{t}_{ik} - 1 = \mathbf{0} \quad (\text{b})$$

The problem in Eq.(4.39) can be solved by using Lagrange multiplier method. The Lagrange function of Eq.(4.39) has a form as

$$F_{PL} = F_P - \alpha \left(\sum_{k=1}^m \sum_{i=1}^{NG} \mathbf{e}_{ik}^T \mathbf{t}_{ik} - 1 \right) \quad (4.40)$$

In order to find the minimum of function F_{PL} , the first derivative of the variables in Eq.(4.40) must be equal to zero. The stationary condition called Karush-Kuhn-Tucker condition for the Lagrange function F_{PL} states that

$$\left\{ \begin{array}{l} \frac{\partial F_{PL}}{\partial \mathbf{e}_{ik}} = \frac{\mathbf{e}_{ik}}{\sqrt{\mathbf{e}_{ik}^T \mathbf{e}_{ik} + \varepsilon_{0N}^2}} + c \sum_{k=1}^m \mathbf{D}_v \mathbf{e}_{ik} \\ \quad + c \left(\sum_{k=1}^m \mathbf{e}_{ik} - \hat{\mathbf{B}}_i \mathbf{u} \right) - \alpha \mathbf{t}_{ik} = \mathbf{0} \quad \forall i, k \\ \frac{\partial F_{PL}}{\partial \mathbf{u}} = -c \sum_{i=1}^{NG} \hat{\mathbf{B}}_i^T \left(\sum_{k=1}^m \mathbf{e}_{ik} - \hat{\mathbf{B}}_i \mathbf{u} \right) = \mathbf{0} \\ \frac{\partial F_{PL}}{\partial \alpha} = \sum_{k=1}^m \sum_{i=1}^{NG} \mathbf{e}_{ik}^T \mathbf{t}_{ik} - 1 = 0 \end{array} \right. \quad \begin{array}{l} \text{(a)} \\ \text{(b)} \\ \text{(c)} \end{array} \quad (4.41)$$

In order to reduce numerical difficulty in singular situation when $\sqrt{\mathbf{e}_{ik}^T \mathbf{e}_{ik} + \varepsilon_{0N}^2} \rightarrow 0$, the equivalent of Eq.(4.41a) can be expressed as

$$\mathbf{e}_{ik} + c \sqrt{\mathbf{e}_{ik}^T \mathbf{e}_{ik} + \varepsilon_{0N}^2} \mathbf{D}_v \mathbf{e}_{ik} + c \sqrt{\mathbf{e}_{ik}^T \mathbf{e}_{ik} + \varepsilon_{0N}^2} \left(\sum_{k=1}^m \mathbf{e}_{ik} - \hat{\mathbf{B}}_i \mathbf{u} \right) - \alpha \sqrt{\mathbf{e}_{ik}^T \mathbf{e}_{ik} + \varepsilon_{0N}^2} \mathbf{t}_{ik} = \mathbf{0} \quad (4.42)$$

By reason of simplicity, we define some new functions as

$$\left\{ \begin{array}{l} \mathbf{f}_{ik} = \left(\mathbf{e}_{ik} + c \sqrt{\mathbf{e}_{ik}^T \mathbf{e}_{ik} + \varepsilon_{0N}^2} \mathbf{D}_v \mathbf{e}_{ik} \right. \\ \quad \left. + c \sqrt{\mathbf{e}_{ik}^T \mathbf{e}_{ik} + \varepsilon_{0N}^2} \left(\sum_{k=1}^m \mathbf{e}_{ik} - \hat{\mathbf{B}}_i \mathbf{u} \right) - \alpha \sqrt{\mathbf{e}_{ik}^T \mathbf{e}_{ik} + \varepsilon_{0N}^2} \mathbf{t}_{ik} \right) \\ \mathbf{h}_i = \hat{\mathbf{B}}_i^T \left(\sum_{k=1}^m \mathbf{e}_{ik} - \hat{\mathbf{B}}_i \mathbf{u} \right) \end{array} \right. \quad \begin{array}{l} \text{(a)} \\ \text{(b)} \end{array} \quad (4.43)$$

The Eq.(4.41) with new definitions in Eq.(4.43) becomes as

$$\begin{cases} \mathbf{f}_{ik} = \mathbf{0} \\ \sum_{i=1}^{NG} \mathbf{h}_i = \sum_{i=1}^{NG} \hat{\mathbf{B}}_i^T \left(\sum_{k=1}^m \mathbf{e}_{ik} - \hat{\mathbf{B}}_i \mathbf{u} \right) = \mathbf{0} \\ \sum_{k=1}^m \sum_{i=1}^{NG} \mathbf{e}_{ik}^T \mathbf{t}_{ik} - 1 = 0 \end{cases} \quad (4.44)$$

To solve Eqs.(4.44) by applying Newton-Raphson method, we get the following form as

$$\begin{cases} \mathbf{H}_{ik} d\mathbf{e}_{ik} + c\sqrt{\mathbf{e}_{ik}^T \mathbf{e}_{ik} + \varepsilon_{0N}^2} \left(\sum_{k=1}^m d\mathbf{e}_{ik} - \hat{\mathbf{B}}_i d\mathbf{u} \right) - d\alpha \sqrt{\mathbf{e}_{ik}^T \mathbf{e}_{ik} + \varepsilon_{0N}^2} \mathbf{t}_{ik} = -\mathbf{f}_{ik} & \text{(a)} \\ \sum_{i=1}^{NG} \hat{\mathbf{B}}_i^T \left(\sum_{k=1}^m d\mathbf{e}_{ik} - \hat{\mathbf{B}}_i d\mathbf{u} \right) = -\sum_{i=1}^{NG} \mathbf{h}_i & \text{(b)} \\ \sum_{k=1}^m \sum_{i=1}^{NG} \mathbf{t}_{ik}^T d\mathbf{e}_{ik} = -\sum_{k=1}^m \sum_{i=1}^{NG} \mathbf{t}_{ik}^T \mathbf{e}_{ik} + 1 & \text{(c)} \end{cases} \quad (4.45)$$

where

$$\begin{aligned} \mathbf{H}_{ik} = & \left(\left[\mathbf{I}_{ik} + c\sqrt{\mathbf{e}_{ik}^T \mathbf{e}_{ik} + \varepsilon_{0N}^2} \mathbf{D}_v \right] + \frac{1}{\sqrt{\mathbf{e}_{ik}^T \mathbf{e}_{ik} + \varepsilon_{0N}^2}} \left[c\mathbf{D}_v \mathbf{e}_{ik} \right. \right. \\ & \left. \left. + c \left(\sum_{k=1}^m \mathbf{e}_{ik} - \hat{\mathbf{B}}_i \mathbf{u} \right) - \alpha \mathbf{t}_{ik}^T \right] \mathbf{e}_{ik}^T \right) \end{aligned} \quad (4.46)$$

In Eq.(4.45), $d\mathbf{e}_{ik}$, $d\mathbf{u}$ are the incremental vectors of strain rate and displacement respectively while $d\alpha$ is the incremental value of α and \mathbf{I}_{ik} defines the identity matrix. The algorithm reaches convergence more stably if the first term of \mathbf{H}_{ik} is only kept in Eq.(4.46) and Eq.(4.46) approximates as

$$\mathbf{H}_{ik} \approx \left[\mathbf{I}_{ik} + c\sqrt{\mathbf{e}_{ik}^T \mathbf{e}_{ik} + \varepsilon_{0N}^2} \mathbf{D}_v \right] \quad (4.47)$$

The incremental vectors of strain rate, $d\mathbf{e}_{ik}$, can be computed from Eq.(4.45.a) as

$$d\mathbf{e}_{ik} = \left(-c\sqrt{\mathbf{e}_{ik}^T \mathbf{e}_{ik} + \varepsilon_{0N}^2} \mathbf{H}_{ik}^{-1} \left(\sum_{k=1}^m d\mathbf{e}_{ik} - \hat{\mathbf{B}}_i d\mathbf{u} \right) + d\alpha \sqrt{\mathbf{e}_{ik}^T \mathbf{e}_{ik} + \varepsilon_{0N}^2} \mathbf{H}_{ik}^{-1} \mathbf{t}_{ik} - \mathbf{H}_{ik}^{-1} \mathbf{f}_{ik} \right) \quad (4.48)$$

Writing Eq.(4.48) for $k = \overline{1, m}$, and then sum them up, we get

$$\begin{aligned} \sum_{k=1}^m d\mathbf{e}_{ik} = & \left(-c\mathbf{K}_i^{-1} \sum_{k=1}^m \sqrt{\mathbf{e}_{ik}^T \mathbf{e}_{ik} + \varepsilon_{0N}^2} \mathbf{H}_{ik}^{-1} \left(\sum_{k=1}^m d\mathbf{e}_{ik} - \hat{\mathbf{B}}_i d\mathbf{u} \right) \right. \\ & \left. + d\alpha \mathbf{K}_i^{-1} \sum_{k=1}^m \sqrt{\mathbf{e}_{ik}^T \mathbf{e}_{ik} + \varepsilon_{0N}^2} \mathbf{H}_{ik}^{-1} \mathbf{t}_{ik} - \mathbf{K}_i^{-1} \sum_{k=1}^m \mathbf{H}_{ik}^{-1} \mathbf{f}_{ik} \right) \end{aligned} \quad (4.49)$$

where

$$\mathbf{K}_i = \left[\mathbf{I}_i + c \sum_{k=1}^m \sqrt{\mathbf{e}_{ik}^T \mathbf{e}_{ik} + \varepsilon_{0N}^2} \mathbf{H}_{ik}^{-1} \right] \quad (4.50)$$

Computation of $d\mathbf{u}$

To compute the incremental displacement vector $d\mathbf{u}$, we substitute Eq.(4.48) into Eq.(4.45.b) and get

$$\begin{aligned} \sum_{i=1}^{NG} \hat{\mathbf{B}}_i^T \mathbf{C}_i \hat{\mathbf{B}}_i d\mathbf{u} = & - \sum_{i=1}^{NG} \hat{\mathbf{B}}_i^T \left(d\alpha \mathbf{K}_i^{-1} \sum_{k=1}^m \sqrt{\mathbf{e}_{ik}^T \mathbf{e}_{ik} + \varepsilon_{0N}^2} \mathbf{H}_{ik}^{-1} \mathbf{t}_{ik} \right. \\ & \left. + \mathbf{K}_i^{-1} \sum_{k=1}^m \mathbf{H}_{ik}^{-1} \mathbf{f}_{ik} \right) + \sum_{i=1}^{NG} \mathbf{h}_i \end{aligned} \quad (4.51)$$

where

$$\mathbf{C}_i = \mathbf{I}_i - c \left[\sum_{k=1}^m \sqrt{\mathbf{e}_{ik}^T \mathbf{e}_{ik} + \varepsilon_{0N}^2} \mathbf{H}_{ik}^{-1} \right] \quad (4.52)$$

From definition of Eq.(4.50), we have Eq.(4.52) in new form as

$$\mathbf{C}_i = \mathbf{I}_i - c \left[\sum_{k=1}^m \sqrt{\mathbf{e}_{ik}^T \mathbf{e}_{ik} + \varepsilon_{0N}^2} \mathbf{H}_{ik}^{-1} \right] = \mathbf{I}_i - \mathbf{K}_i^{-1} [\mathbf{K}_i - \mathbf{I}_i] = \mathbf{K}_i^{-1} \quad (4.53)$$

If we define some new notations as

$$\left\{ \begin{array}{l} \mathbf{S} = \sum_{i=1}^{NG} \hat{\mathbf{B}}_i^T \mathbf{K}_i^{-1} \hat{\mathbf{B}}_i \quad (\text{a}) \\ \mathbf{f}_1 = -\sum_{i=1}^{NG} \hat{\mathbf{B}}_i^T \mathbf{K}_i^{-1} \sum_{k=1}^m \sqrt{\mathbf{e}_{ik}^T \mathbf{e}_{ik} + \varepsilon_{0N}^2} \mathbf{H}_{ik}^{-1} \mathbf{t}_{ik} \quad (\text{b}) \\ \mathbf{f}_2 = -\sum_{i=1}^{NG} \hat{\mathbf{B}}_i^T \mathbf{K}_i^{-1} \sum_{k=1}^m \mathbf{H}_{ik}^{-1} \mathbf{f}_{ik} + \sum_{i=1}^{NG} \mathbf{h}_i \quad (\text{c}) \end{array} \right. \quad (4.54)$$

then Eq.(4.51) can be rewritten as

$$\mathbf{S} d\mathbf{u} = d\alpha \mathbf{f}_1 + \mathbf{f}_2 \quad (4.55)$$

By substituting \mathbf{f}_{ik} and $\sum_{i=1}^{NG} \mathbf{h}_i$ from Eq.(4.43) into Eq.(4.44.c), then solving Eq.(4.55), we obtain the incremental displacement vector as

$$d\mathbf{u} = (\alpha + d\alpha) \mathbf{S}^{-1} \mathbf{f}_1 - \mathbf{u} \quad (4.56)$$

Computation of $d\mathbf{e}_{ik}$

The increment of the strain vector can be obtained by substituting \mathbf{f}_{ik} in Eq.(4.43.a) and $\sum_{k=1}^m d\mathbf{e}_{ik}$ in Eq.(4.49) into Eq.(4.48)

$$d\mathbf{e}_{ik} = \left(d\mathbf{e}_{ik} \right)_1 + (\alpha + d\alpha) \left(d\mathbf{e}_{ik} \right)_2 \quad (4.57)$$

where

$$\left\{ \begin{array}{l} \left(d\mathbf{e}_{ik} \right)_1 = -\mathbf{e}_{ik} \quad (\text{a}) \\ \left(d\mathbf{e}_{ik} \right)_2 = c\sqrt{\mathbf{e}_{ik}^T \mathbf{e}_{ik} + \varepsilon_{0N}^2} \mathbf{H}_{ik}^{-1} \mathbf{K}_i^{-1} \hat{\mathbf{B}}_i \mathbf{S}^{-1} \mathbf{f}_1 + \sqrt{\mathbf{e}_{ik}^T \mathbf{e}_{ik} + \varepsilon_{0N}^2} \mathbf{H}_{ik}^{-1} \mathbf{t}_{ik} \quad (\text{b}) \\ \quad -c\sqrt{\mathbf{e}_{ik}^T \mathbf{e}_{ik} + \varepsilon_{0N}^2} \mathbf{H}_{ik}^{-1} \mathbf{K}_i^{-1} \sum_{k=1}^m \left(\sqrt{\mathbf{e}_{ik}^T \mathbf{e}_{ik} + \varepsilon_{0N}^2} \mathbf{H}_{ik}^{-1} \mathbf{t}_{ik} \right) \end{array} \right. \quad (4.58)$$

Computation of $(\alpha + d\alpha)$

We can get $(\alpha + d\alpha)$ from Eq.(4.57), then insert $d\mathbf{e}_{ik}$ from Eq.(4.45.b) as

$$\alpha + d\alpha = \frac{d\mathbf{e}_{ik} - \left(d\mathbf{e}_{ik}\right)_1}{\left(d\mathbf{e}_{ik}\right)_2} = \frac{1 - \sum_{k=1}^m \sum_{i=1}^{NG} \mathbf{t}_{ik}^T \left(\mathbf{e}_{ik} + \left(d\mathbf{e}_{ik}\right)_1\right)}{\sum_{k=1}^m \sum_{i=1}^{NG} \mathbf{t}_{ik}^T \left(d\mathbf{e}_{ik}\right)_2} \quad (4.59)$$

Based on Eq.(4.56 & 4.57), we can update the displacement vector \mathbf{u} and the global strain rate vector \mathbf{e} :

$$\mathbf{e} = \left[\mathbf{e}_{11} \quad \dots \quad \mathbf{e}_{ik} \quad \dots \quad \mathbf{e}_{NG.m} \right] \quad (4.60)$$

The new vectors of \mathbf{u} and \mathbf{e} tend to satisfy Eq.(4.41.b & 4.42) simultaneously. By forcing them to fulfil Eqs.(4.41.c), we obtain Lagrange multiplier α updated as $(\alpha + d\alpha)$ in Eq.(4.59). Iterating these steps may drive us to a stable set of \mathbf{u} , \mathbf{e} & α satisfying all conditions Eqs.(4.41.b, 4.41.c & 4.42). Details of the iterative algorithm are presented hereafter and also illustrated in Fig 4.1.

- Step 01: Initialize displacement and strain rate vectors: \mathbf{u}^0 and \mathbf{e}^0 such that the normalized condition Eq.(4.41.c) is satisfied:

$$\sum_{k=1}^m \sum_{i=1}^{NG} \mathbf{t}_{ik}^T \mathbf{e}_{ik}^0 = 1. \quad (4.61)$$

Normally the fictitious elastic solution must be computed first in order to define the load domain \mathbf{L} in terms of the fictitious elastic generalized stress σ_{ik}^E . Hence, \mathbf{u}^0 and \mathbf{e}^0 may assume fictitious values (after being normalized) for their initialization. Set up initial values for the penalty parameter c and for ε_{0N} . Set up convergence criteria and maximum number of iterations.

- Step 02: Calculate \mathbf{S} , \mathbf{f}_1 , \mathbf{f}_2 from (4.54) at the current values of \mathbf{u} and \mathbf{e} .
- Step 03: Calculate $(\alpha + d\alpha)$, $d\mathbf{u}$ and $d\mathbf{e}_{ik}$ from Eqs.(4.59, 4.56 and 4.57), respectively.
- Step 04: Perform a line search to find λ_k such that:

$$\lambda_s = \min F_P(\mathbf{u} + \lambda d\mathbf{u}, \mathbf{e} + \lambda d\mathbf{e}) \quad (4.62)$$

Update displacement \mathbf{u} , strain \mathbf{e}_{ik} and λ as:

$$\mathbf{u} = \mathbf{u} + \lambda_s d\mathbf{u} \quad (\text{a})$$

$$\mathbf{e}_{ik} = \mathbf{e}_{ik} + \lambda_s d\mathbf{e}_{ik} \quad (\text{b}) \quad (4.63)$$

$$\alpha = \alpha + d\alpha \quad (\text{c})$$

- **Step 05**: Check convergence criteria ($|\alpha_p^k - \alpha_p^{k-1}| \leq tol$ or $\alpha_d^k > \alpha_p^k$): if they are all satisfied, then go to step **06**, otherwise go to step **02**.
- **Step 06**: Stop.

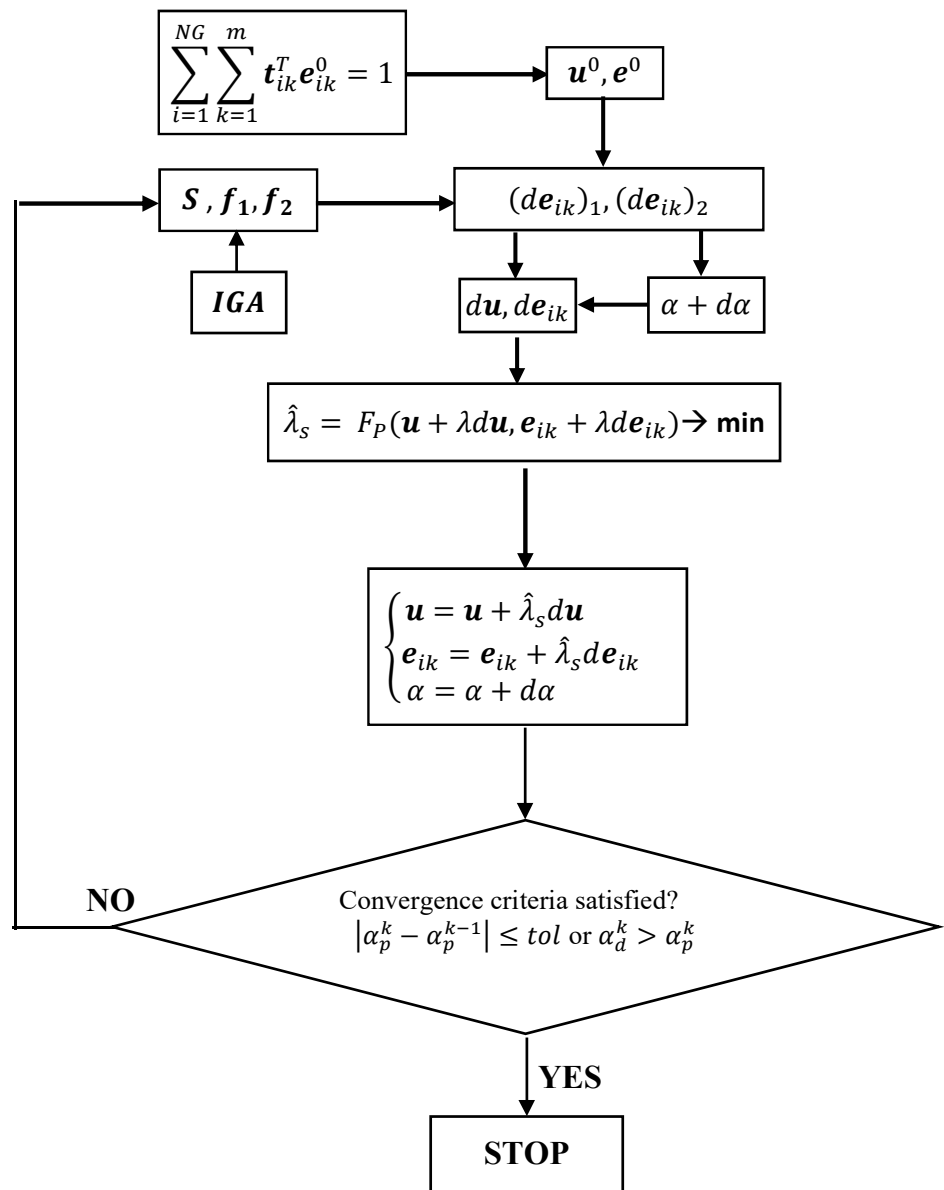


Figure 4.1: Flow chart for the upper bound algorithm for shakedown analysis

4.3 Dual relationship between lower bound and upper bound and dual algorithm

Based on the research of Bazaraa *et al.* [104], the Lagrange dual function of Eq.(4.37) with $\varepsilon_{0N} = 0$ has form as follow:

$$F_L = \sum_{i=1}^{NG} \left\{ \sum_{k=1}^m \sqrt{2}k_v \sqrt{\mathbf{e}_{ik}^T \mathbf{e}_{ik}} - \sum_{k=1}^m \frac{\boldsymbol{\gamma}_{ik}^T \mathbf{D}_v \mathbf{e}_{ik}}{3} - \boldsymbol{\beta}_i^T \left(\sum_{k=1}^m \mathbf{e}_{ik} - \hat{\mathbf{B}}_i \mathbf{u} \right) \right\} - \alpha \left(\sum_{k=1}^m \sum_{i=1}^{NG} \mathbf{e}_{ik}^T \mathbf{t}_{ik} - 1 \right) \quad (4.64)$$

where $\boldsymbol{\gamma}_{ik}, \boldsymbol{\beta}_i$ denote Lagrange multipliers vectors at Gauss point i and load vertex k and α is a scalar Lagrange multiplier. Based on \mathbf{D}_v in Eq.(4.28), the $\boldsymbol{\gamma}_{ik}$ has a special form

$$\boldsymbol{\gamma}_{ik} = [\gamma_{ik} \quad \gamma_{ik} \quad \gamma_{ik} \quad 0 \quad 0 \quad 0] \quad (4.65)$$

The special vector $\boldsymbol{\gamma}_{ik}$ in Eq.(4.65) shows that only one incompressibility coressponding to only one Lagrange multiplier at each Gauss point i and load vertex k . The dual problem in Eq.(4.37) becomes

$$\max_{\boldsymbol{\gamma}_{ik}, \boldsymbol{\beta}_i, \alpha} \left(\min_{\mathbf{e}_{ik}, \mathbf{u}} F_L \right) \quad (4.66)$$

According to the strong duality theorem presented by Bazaraa *et al.* [104], no dual gap exists between dual and primal solutions:

$$\min_{\mathbf{h}(\mathbf{e}_{ik}, \mathbf{u}) = \mathbf{0}} \sum_{i=1}^{NG} \sum_{k=1}^m \sqrt{2}k_v \sqrt{\mathbf{e}_{ik}^T \mathbf{e}_{ik}} = \max_{\boldsymbol{\gamma}_{ik}, \boldsymbol{\beta}_i, \alpha} \left(\min_{\mathbf{e}_{ik}, \mathbf{u}} F_L \right) \quad (4.67)$$

Another form of the Lagrange dual function in Eq.(4.64) can be rewritten as

$$F_L = \sum_{i=1}^{NG} \sum_{k=1}^m \left(\frac{\sqrt{2}k_v \mathbf{e}_{ik}}{\sqrt{\mathbf{e}_{ik}^T \mathbf{e}_{ik}}} - \boldsymbol{\gamma}_{ik} - \boldsymbol{\beta}_i - \mathbf{t}_{ik} \alpha \right)^T \mathbf{e}_{ik} + \sum_{i=1}^{NG} \boldsymbol{\beta}_i^T \hat{\mathbf{B}}_i \mathbf{u} + \alpha \quad (4.68)$$

We accept in Eq.(4.68) that if $\sqrt{\mathbf{e}_{ik}^T \mathbf{e}_{ik}}$ is equal to zero then $\sqrt{2k_v} \mathbf{e}_{ik} / \sqrt{\mathbf{e}_{ik}^T \mathbf{e}_{ik}} = \mathbf{0}$. The stationarity conditions of the dual form in Eq.(4.68) are presented hereafter

$$\left\{ \begin{array}{l} \frac{\partial F_L}{\partial \mathbf{e}_{ik}} = \frac{\mathbf{e}_{ik}}{\sqrt{\mathbf{e}_{ik}^T \mathbf{e}_{ik}}} - \left(\gamma_{ik} + \beta_i + \alpha \mathbf{t}_{ik} \right) = \mathbf{0} \quad (\text{a}) \\ \frac{\partial F_L}{\partial \gamma_{ik}} = \mathbf{D}_v \mathbf{e}_{ik} = \mathbf{0} \quad (\text{b}) \\ \frac{\partial F_L}{\partial \beta_{ik}} = \sum_{k=1}^m \mathbf{e}_{ik} - \hat{\mathbf{B}}_i \mathbf{u} = \mathbf{0} \quad (\text{c}) \\ \frac{\partial F_L}{\partial \mathbf{u}} = \sum_{i=1}^{NG} \hat{\mathbf{B}}_i^T \beta_i = \mathbf{0} \quad (\text{d}) \\ \frac{\partial F_L}{\partial \alpha} = \sum_{k=1}^m \sum_{i=1}^{NG} \mathbf{e}_{ik}^T \mathbf{t}_{ik} - 1 = \mathbf{0} \quad (\text{e}) \end{array} \right. \quad (4.69)$$

In Section 4.2.2, a penalty function is written as

$$F_P = \sum_{i=1}^{NG} \left\{ \sum_{k=1}^m \sqrt{2k_v} \sqrt{\mathbf{e}_{ik}^T \mathbf{e}_{ik}} + \varepsilon_{0N}^2 + \frac{c}{2} \sum_{k=1}^m \mathbf{e}_{ik}^T \mathbf{D}_v \mathbf{e}_{ik} + \frac{c}{2} \left(\sum_{k=1}^m \mathbf{e}_{ik} - \hat{\mathbf{B}}_i \mathbf{u} \right) \left(\sum_{k=1}^m \mathbf{e}_{ik} - \hat{\mathbf{B}}_i \mathbf{u} \right) \right\}$$

and its stationarity conditions:

$$\left\{ \begin{array}{l} \frac{\partial F_{PL}}{\partial \mathbf{e}_{ik}} = \frac{\mathbf{e}_{ik}}{\sqrt{\mathbf{e}_{ik}^T \mathbf{e}_{ik}} + \varepsilon_{0N}^2} + c \sum_{k=1}^m \mathbf{D}_v \mathbf{e}_{ik} + c \left(\sum_{k=1}^m \mathbf{e}_{ik} - \hat{\mathbf{B}}_i \mathbf{u} \right) - \alpha \mathbf{t}_{ik} = \mathbf{0} \quad \forall i, k \quad (\text{a}) \\ \frac{\partial F_{PL}}{\partial \mathbf{u}} = -c \sum_{i=1}^{NG} \hat{\mathbf{B}}_i^T \left(\sum_{k=1}^m \mathbf{e}_{ik} - \hat{\mathbf{B}}_i \mathbf{u} \right) = \mathbf{0} \quad (\text{b}) \\ \frac{\partial F_{PL}}{\partial \alpha} = \sum_{k=1}^m \sum_{i=1}^{NG} \mathbf{e}_{ik}^T \mathbf{t}_{ik} - 1 = \mathbf{0} \quad (\text{c}) \end{array} \right.$$

If γ_{ik} and β_{ik} are defined as:

$$\left\{ \begin{array}{l} \gamma_{ik} = -c \mathbf{D}_v \mathbf{e}_{ik} \quad (\text{a}) \\ \beta_{ik} = -c \left(\sum_{k=1}^m \mathbf{e}_{ik} - \hat{\mathbf{B}}_i \mathbf{u} \right) \quad (\text{b}) \end{array} \right. \quad (4.70)$$

the the Penalty-Lagrange function in Eq.(4.40) becomes similar to Eq.(4.64)

$$F_{PL} = \sum_{i=1}^{NG} \left\{ \sum_{k=1}^m \sqrt{2k_v} \sqrt{\mathbf{e}_{ik}^T \mathbf{e}_{ik}} - \frac{1}{6} \sum_{k=1}^m \gamma_{ik}^T \mathbf{D}_v \mathbf{e}_{ik} - \frac{1}{2} \beta_i^T \left(\sum_{k=1}^m \mathbf{e}_{ik} - \hat{\mathbf{B}}_i \mathbf{u} \right) \right\} - \alpha \left(\sum_{k=1}^m \sum_{i=1}^{NG} \mathbf{e}_{ik}^T \mathbf{t}_{ik} - 1 \right) \quad (4.71)$$

while the stationarity conditions become similar to Eqs.(4.69)

$$\begin{cases} \frac{\mathbf{e}_{ik}}{\sqrt{\mathbf{e}_{ik}^T \mathbf{e}_{ik} + \varepsilon_{0N}^2}} - (\gamma_{ik} + \beta_{ik} + \alpha \mathbf{t}_{ik}) = \mathbf{0} \\ \sum_{i=1}^{NG} \hat{\mathbf{B}}_i^T \beta_{ik}^T = \mathbf{0} \\ \sum_{k=1}^m \sum_{i=1}^{NG} \mathbf{e}_{ik}^T \mathbf{t}_{ik} - 1 = \mathbf{0} \end{cases}$$

or

$$\begin{cases} \mathbf{e}_{ik} - \sqrt{\mathbf{e}_{ik}^T \mathbf{e}_{ik} + \varepsilon_{0N}^2} (\gamma_{ik} + \beta_{ik} + \alpha \mathbf{t}_{ik}) = \mathbf{0} & \text{(a)} \\ \sum_{i=1}^{NG} \hat{\mathbf{B}}_i^T \beta_{ik}^T = \mathbf{0} & \text{(b)} \\ \sum_{k=1}^m \sum_{i=1}^{NG} \mathbf{e}_{ik}^T \mathbf{t}_{ik} - 1 = \mathbf{0} & \text{(c)} \end{cases} \quad (4.72)$$

For reason of simplicity, we define some new notations as

$$\begin{cases} \mathbf{f}_{ik} = \mathbf{e}_{ik} - \sqrt{\mathbf{e}_{ik}^T \mathbf{e}_{ik} + \varepsilon_{0N}^2} (\gamma_{ik} + \beta_i + \alpha \mathbf{t}_{ik}) = \mathbf{0} & \text{(a)} \\ \mathbf{g}_{ik} = \gamma_{ik} + c \mathbf{D}_v \mathbf{e}_{ik} & \text{(b)} \\ \mathbf{h}_{ik} = \beta_i + c \left(\sum_{k=1}^m \mathbf{e}_{ik} - \hat{\mathbf{B}}_i \mathbf{u} \right) & \text{(c)} \end{cases} \quad (4.73)$$

In order to solve the Eqs.(4.70 & 4.72), we use the Newton Raphson method and obtain as

$$\left\{ \begin{array}{l}
 \mathbf{M}_{ik} d\mathbf{e}_{ik} - \sqrt{\mathbf{e}_{ik}^T \mathbf{e}_{ik} + \varepsilon_{0N}^2} \left(d\boldsymbol{\gamma}_i + d\boldsymbol{\beta}_i + d\boldsymbol{\alpha} \mathbf{t}_{ik} \right) = -\mathbf{f}_{ik} \quad (\text{a}) \\
 \sum_{i=1}^{NG} \hat{\mathbf{B}}_i^T d\boldsymbol{\beta}_i^T = -\sum_{i=1}^{NG} \hat{\mathbf{B}}_i^T \boldsymbol{\beta}_i^T \quad (\text{b}) \\
 \sum_{k=1}^m \sum_{i=1}^{NG} d\mathbf{e}_{ik}^T \mathbf{t}_{ik} = -\sum_{k=1}^m \sum_{i=1}^{NG} \mathbf{e}_{ik}^T \mathbf{t}_{ik} + 1 \quad (\text{c}) \\
 d\boldsymbol{\gamma}_{ik} + c\mathbf{D}_v d\mathbf{e}_{ik} = -\mathbf{g}_{ik} \quad (\text{d}) \\
 d\boldsymbol{\beta}_i + c \left(\sum_{k=1}^m d\mathbf{e}_{ik} - \hat{\mathbf{B}}_i d\mathbf{u} \right) = -\mathbf{h}_{ik} \quad (\text{e}) \\
 \left\| \boldsymbol{\gamma}_i + \boldsymbol{\beta}_i + \boldsymbol{\alpha} \mathbf{t}_{ik} \right\| \leq 1 \quad (\text{f})
 \end{array} \right. \quad (4.74)$$

where

$$\mathbf{M}_{ik} = \left[\mathbf{I}_{ik} - \left(\boldsymbol{\gamma}_i + \boldsymbol{\beta}_i + \boldsymbol{\alpha} \mathbf{t}_{ik} \right) \frac{\mathbf{e}_{ik}^T}{\sqrt{\mathbf{e}_{ik}^T \mathbf{e}_{ik} + \varepsilon_{0N}^2}} \right] \quad (4.75)$$

Substituting Eq.(4.74.d) into Eq.(4.74.a) we have:

$$\hat{\mathbf{M}}_{ik} d\mathbf{e}_{ik} - \sqrt{\mathbf{e}_{ik}^T \mathbf{e}_{ik} + \varepsilon_{0N}^2} \left(-\mathbf{g}_{ik} + d\boldsymbol{\beta}_i + d\boldsymbol{\alpha} \mathbf{t}_{ik} \right) = -\mathbf{f}_{ik} \quad (4.76)$$

where the new matrix $\hat{\mathbf{M}}_{ik}$ is defined as

$$\hat{\mathbf{M}}_{ik} = \left[\mathbf{M}_{ik} + \sqrt{\mathbf{e}_{ik}^T \mathbf{e}_{ik} + \varepsilon_{0N}^2} c \hat{\mathbf{D}}_v \right] \quad (4.77)$$

Now we can compute the incremental vector $d\mathbf{e}_{ik}$ of the strain from

$$d\mathbf{e}_{ik} = \sqrt{\mathbf{e}_{ik}^T \mathbf{e}_{ik} + \varepsilon_{0N}^2} \hat{\mathbf{M}}_{ik}^{-1} \left(-\mathbf{g}_{ik} + d\boldsymbol{\beta}_i + d\boldsymbol{\alpha} \mathbf{t}_{ik} \right) - \hat{\mathbf{M}}_{ik}^{-1} \mathbf{f}_{ik} \quad (4.78)$$

By writing Eq.(4.78) for all $\overline{1, k}$ and then sum of them, we obtain as

$$\sum_{k=1}^m d\mathbf{e}_{ik} = \sum_{k=1}^m \sqrt{\mathbf{e}_{ik}^T \mathbf{e}_{ik} + \varepsilon_{0N}^2} \hat{\mathbf{M}}_{ik}^{-1} \left(-\mathbf{g}_{ik} + d\boldsymbol{\beta}_i + d\boldsymbol{\alpha} \mathbf{t}_{ik} \right) - \sum_{k=1}^m \hat{\mathbf{M}}_{ik}^{-1} \mathbf{f}_{ik} \quad (4.79)$$

Substituting \mathbf{f}_{ik} from Eq.(4.73.a), \mathbf{g}_{ik} from Eq.(4.73.b), $d\beta_i$ from Eq.(4.74.e) into Eq.(4.79), after some manipulations, we obtain

$$\begin{aligned} \sum_{k=1}^m d\mathbf{e}_{ik} &= c\hat{\mathbf{K}}_i^{-1} \sum_{k=1}^m \sqrt{\mathbf{e}_{ik}^T \mathbf{e}_{ik} + \varepsilon_{0N}^2 \hat{\mathbf{M}}_{ik}^{-1} \hat{\mathbf{B}}_i} d\mathbf{u} - \hat{\mathbf{K}}_i^{-1} \sum_{k=1}^m \sqrt{\mathbf{e}_{ik}^T \mathbf{e}_{ik} + \varepsilon_{0N}^2 \hat{\mathbf{M}}_{ik}^{-1}} \mathbf{g}_{ik} \\ &\quad - \hat{\mathbf{K}}_i^{-1} \sum_{k=1}^m \sqrt{\mathbf{e}_{ik}^T \mathbf{e}_{ik} + \varepsilon_{0N}^2 \hat{\mathbf{M}}_{ik}^{-1}} \hat{\mathbf{M}}_{ik}^{-1} \mathbf{h}_i \\ &\quad + (d\alpha) \hat{\mathbf{K}}_i^{-1} \sum_{k=1}^m \sqrt{\mathbf{e}_{ik}^T \mathbf{e}_{ik} + \varepsilon_{0N}^2 \hat{\mathbf{M}}_{ik}^{-1}} \hat{\mathbf{M}}_{ik}^{-1} \mathbf{t}_{ik} - \hat{\mathbf{K}}_i^{-1} \sum_{k=1}^m \hat{\mathbf{M}}_{ik}^{-1} \mathbf{f}_{ik} \end{aligned} \quad (4.80)$$

where

$$\hat{\mathbf{K}}_i = \left[\mathbf{I}_i + c \sum_{k=1}^m \sqrt{\mathbf{e}_{ik}^T \mathbf{e}_{ik} + \varepsilon_{0N}^2 \hat{\mathbf{M}}_{ik}^{-1}} \right] \quad (4.81)$$

Computation of $d\mathbf{u}$

We substitute Eq.(4.74.e) into Eq.(4.74.b) with consideration Eqs.(4.73) and (4.80) leading to:

$$d\mathbf{u} = -\mathbf{u} + \hat{\mathbf{S}}^{-1} \hat{\mathbf{f}}_1 + (\alpha + d\alpha) \hat{\mathbf{S}}^{-1} \hat{\mathbf{f}}_2 \quad (4.82)$$

where:

$$\left\{ \begin{array}{l} \hat{\mathbf{S}} = \sum_{i=1}^{NG} \hat{\mathbf{B}}_i^T \hat{\mathbf{K}}_i^{-1} \hat{\mathbf{B}}_i \quad (a) \\ \hat{\mathbf{f}}_1 = - \sum_{i=1}^{NG} \hat{\mathbf{B}}_i^T \hat{\mathbf{K}}_i^{-1} \left(\sum_{k=1}^m \mathbf{e}_{ik} - \sum_{k=1}^m \hat{\mathbf{M}}_{ik}^{-1} \mathbf{e}_{ik} \right. \\ \quad \left. - c \sum_{k=1}^m \sqrt{\mathbf{e}_{ik}^T \mathbf{e}_{ik} + \varepsilon_{0N}^2 \hat{\mathbf{M}}_{ik}^{-1}} \mathbf{D}_v \mathbf{e}_{ik} \right) \quad (b) \\ \hat{\mathbf{f}}_2 = - \sum_{i=1}^{NG} \hat{\mathbf{B}}_i^T \hat{\mathbf{K}}_i^{-1} \sum_{k=1}^m \sqrt{\mathbf{e}_{ik}^T \mathbf{e}_{ik} + \varepsilon_{0N}^2 \hat{\mathbf{M}}_{ik}^{-1}} \mathbf{e}_{ik} \quad (c) \end{array} \right. \quad (4.83)$$

Computation of $d\mathbf{e}_{ik}$

$$d\mathbf{e}_{ik} = [d\mathbf{e}_{ik}]_a + [d\mathbf{e}_{ik}]_b + (\alpha + d\alpha) [d\mathbf{e}_{ik}]_c \quad (4.84)$$

where $[de_{ik}]_a$, $[de_{ik}]_b$ and $[de_{ik}]_c$ are defined as

$$\begin{aligned}
 [de_{ik}]_a &= c \sum_{k=1}^m \sqrt{e_{ik}^T e_{ik} + \varepsilon_{0N}^2} \hat{M}_{ik}^{-1} \hat{K}_i^{-1} \hat{B}_i \hat{S}^{-1} \sum_{i=1}^{NG} \hat{B}_i^T \hat{K}_i^{-1} \sum_{k=1}^m e_{ik} \\
 &\quad - c \sqrt{e_{ik}^T e_{ik} + \varepsilon_{0N}^2} \hat{M}_{ik}^{-1} \hat{K}_i^{-1} \sum_{k=1}^m e_{ik}
 \end{aligned} \tag{4.85}$$

$$\begin{aligned}
 [de_{ik}]_b &= -c \sum_{k=1}^m \sqrt{e_{ik}^T e_{ik} + \varepsilon_{0N}^2} \hat{M}_{ik}^{-1} \hat{K}_i^{-1} \hat{B}_i \hat{S}^{-1} \sum_{i=1}^{NG} \hat{B}_i^T \hat{K}_i^{-1} \sum_{k=1}^m \hat{M}_{ik}^{-1} \left(\mathbf{I}_{ik} \right. \\
 &\quad \left. + \sqrt{e_{ik}^T e_{ik} + \varepsilon_{0N}^2} c \mathbf{D}_v \right) e_{ik} + c \sqrt{e_{ik}^T e_{ik} + \varepsilon_{0N}^2} \hat{M}_{ik}^{-1} \hat{K}_i^{-1} \sum_{k=1}^m \hat{M}_{ik}^{-1} \left(\mathbf{I}_{ik} \right. \\
 &\quad \left. + \sqrt{e_{ik}^T e_{ik} + \varepsilon_{0N}^2} c \mathbf{D}_v \right) e_{ik} - \hat{M}_{ik}^{-1} \left(\mathbf{I} + \sqrt{e_{ik}^T e_{ik} + \varepsilon_{0N}^2} c \mathbf{D}_v \right) e_{ik}
 \end{aligned} \tag{4.86}$$

$$\begin{aligned}
 [de_{ik}]_c &= c \sum_{k=1}^m \sqrt{e_{ik}^T e_{ik} + \varepsilon_{0N}^2} \hat{M}_{ik}^{-1} \hat{K}_i^{-1} \hat{B}_i \hat{S}^{-1} \sum_{i=1}^{NG} \hat{B}_i^T \hat{K}_i^{-1} \sum_{k=1}^m \sqrt{e_{ik}^T e_{ik} + \varepsilon_{0N}^2} \hat{M}_{ik}^{-1} t_{ik} \\
 &\quad - c \sum_{k=1}^m \sqrt{e_{ik}^T e_{ik} + \varepsilon_{0N}^2} \hat{M}_{ik}^{-1} \hat{K}_i^{-1} \sum_{k=1}^m \sqrt{e_{ik}^T e_{ik} + \varepsilon_{0N}^2} \hat{M}_{ik}^{-1} t_{ik} \\
 &\quad + \sqrt{e_{ik}^T e_{ik} + \varepsilon_{0N}^2} \hat{M}_{ik}^{-1} t_{ik}
 \end{aligned} \tag{4.87}$$

Computation of $(\alpha + d\alpha)$

We obtain $(\alpha + d\alpha)$ by substituting Eq.(4.84) into Eq.(4.74.c) then solving for unknown $(\alpha + d\alpha)$ as

$$\alpha + d\alpha = \frac{1 - \sum_{i=1}^{NG} \sum_{k=1}^m t_{ik}^T \left(e_{ik} + [de_{ik}]_a + [de_{ik}]_b \right)}{\sum_{i=1}^{NG} \sum_{k=1}^m t_{ik}^T [de_{ik}]_c} \tag{4.88}$$

If the existing value of e_{ik} is already normalized, that is

$$\sum_{i=1}^{NG} \sum_{k=1}^m t_{ik}^T e_{ik} = 1 \tag{4.89}$$

The Eq.(4.88) becomes as follow:

$$\alpha + d\alpha = \frac{\sum_{i=1}^{NG} \sum_{k=1}^m \mathbf{t}_{ik}^T \left([\mathbf{d}\mathbf{e}_{ik}]_a + [\mathbf{d}\mathbf{e}_{ik}]_b \right)}{\sum_{i=1}^{NG} \sum_{k=1}^m \mathbf{t}_{ik}^T [\mathbf{d}\mathbf{e}_{ik}]_c} \quad (4.90)$$

The details of the iterative dual algorithm are presented as follow:

- **Step 01**: Initialize displacement and strain vectors: \mathbf{u}^0 and \mathbf{e}^0 such that the normalized condition in Eq.(4.89) is satisfied:

$$\sum_{i=1}^{NG} \sum_{k=1}^m \mathbf{t}_{ik}^T \mathbf{e}_{ik}^0 = 1$$

Set the stress vectors equal to zero vectors

$$\begin{cases} \gamma_{ik}^0 = \mathbf{0} \\ \beta_i^0 = \mathbf{0} \end{cases} \quad \forall k = \overline{1, m}, \quad \forall i = \overline{1, NG} \quad (4.91)$$

Set up initial values for the penalty parameter c and ε_{0N} . Set up convergence criteria, maximum number of iterations.

- **Step 02**: Calculate $[\mathbf{d}\mathbf{e}_{ik}]_a$, $[\mathbf{d}\mathbf{e}_{ik}]_b$ from Eqs.(4.85, 4.86) and $\hat{\mathbf{S}}$, $\hat{\mathbf{f}}_1$, $\hat{\mathbf{f}}_2$ from Eq.(4.83) at current value \mathbf{e} , \mathbf{u}
- **Step 03**: Compute $(\alpha + d\alpha)$, $d\mathbf{u}$ and $d\mathbf{e}_{ik}$ from Eqs.(4.90, 4.82, & 4.84), respectively.
- **Step 04**: Perform a line search to find $\hat{\lambda}_k$ such that:

$$\hat{\lambda}_k = \min F_P(\mathbf{u} + \lambda d\mathbf{u}, \mathbf{e} + \lambda d\mathbf{e}) \quad (4.92)$$

where F_P is the Penalty function in Eq.(4.38) Update displacement and strain rate as:

$$\begin{aligned} \mathbf{u} &= \mathbf{u} + \hat{\lambda}_k d\mathbf{u} & (a) \\ \mathbf{e}_{ik} &= \mathbf{e}_{ik} + \hat{\lambda}_k d\mathbf{e}_{ik} & (b) \end{aligned} \quad (4.93)$$

- Step 05: Calculate the vectors of incremental stresses $d\boldsymbol{\gamma}_{ik}, d\boldsymbol{\beta}_i$ from Eq.(4.74.d & e)

$$\begin{cases} d\boldsymbol{\gamma}_{ik} = -c\mathbf{D}_v d\mathbf{e}_{ik} - \mathbf{g}_{ik} & \text{(a)} \\ d\boldsymbol{\beta}_i = -c\left(\sum_{k=1}^m d\mathbf{e}_{ik} - \hat{\mathbf{B}}_i d\mathbf{u}\right) - \mathbf{h}_{ik} & \text{(b)} \end{cases} \quad (4.94)$$

- Step 06: Perform linesearch to find λ_s such that:

$$\begin{aligned} \lambda_s &= \max \lambda \\ \text{Subjected to :} & \quad \quad \quad (4.95) \\ & \left\| \left(\boldsymbol{\gamma}_i + \boldsymbol{\beta}_i + \alpha \mathbf{t}_{ik} \right) + \lambda \left(d\boldsymbol{\gamma}_i + d\boldsymbol{\beta}_i + d\alpha \mathbf{t}_{ik} \right) \right\| \leq \mathbf{1} \end{aligned}$$

Update stresses $\boldsymbol{\gamma}_{ik}, \boldsymbol{\beta}_i$ and scalar α with a chosen parameter τ : $0 \leq \tau \leq 1$

$$\begin{cases} \boldsymbol{\gamma}_{ik} = \boldsymbol{\gamma}_{ik} + \tau \lambda_s d\boldsymbol{\gamma}_{ik} & \text{(a)} \\ \boldsymbol{\beta}_i = \boldsymbol{\beta}_i + \tau \lambda_s d\boldsymbol{\beta}_i & \text{(b)} \\ \alpha = \alpha + \tau \lambda_s d\alpha & \text{(c)} \end{cases} \quad (4.96)$$

- Step 07: Check convergence criteria ($\text{abs}(\alpha_p^k - \alpha_p^{k-1}) \leq \text{tol}$ or $\alpha_d^k > \alpha_p^k$): if they are all satisfied then go to step **08**, otherwise go to steps **02**.
- Step 08: Stop.

Details of the primal-dual algorithm are presented hereafter and also illustrated in Fig.4.2.

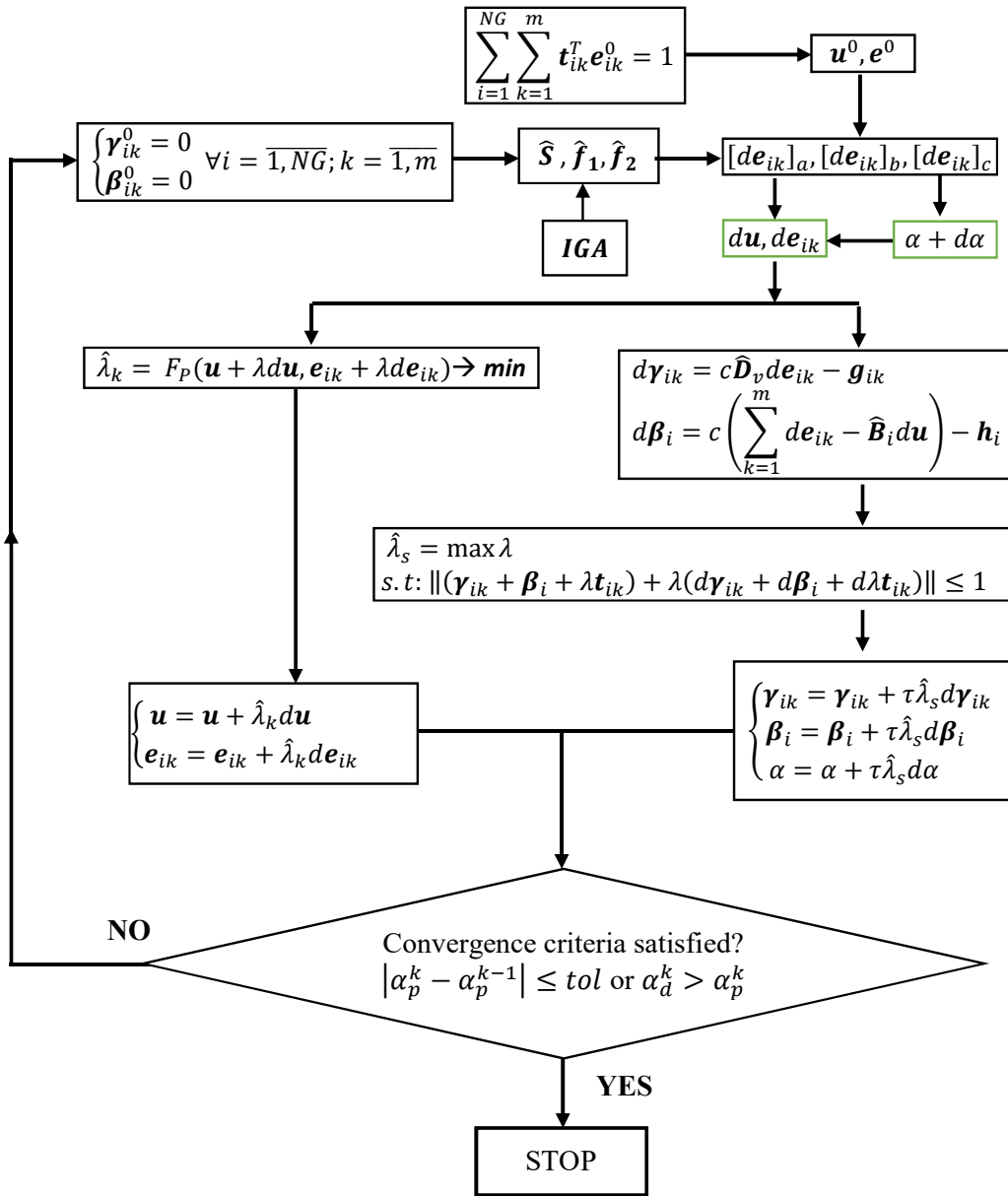


Figure 4.2: Flow chart for the primal-dual algorithm for shakedown analysis

5

NUMERICAL APPLICATIONS

5.1 Introduction

Our theory and algorithms are validated through a series of examples in this chapter. Example problems considered in this chapter are divided into four sections:

- (1) Limit and shakedown analysis of two dimensional structures.
- (2) Limit and shakedown analysis of three dimensional structures.
- (3) Limit and shakedown analysis of pressure vessel components.
- (4) Limit analysis of crack structures.

Note that von Mises yield conditions and elastic perfectly plastic material are assumed in all examples. The load factors obtained by averaging its lower and upper bound values at the final iteration are compared with some analytical solutions or other solutions found in the literature. The different choices of the optimization parameters which may have different effects on behaviour of the dual algorithm are also investigated in this chapter.

5.2 Limit and shakedown analysis of two dimensional structures

5.2.1 Square plate with a central circular hole

The first example considered in limit and shakedown analysis of 2D structures is a square plate with a central circular hole subjected to different load cases P_1 and

P_2 , which has been found very frequently in literature. The full model of this problem is shown as in Fig 5.1(a). Due to the symmetry of geometry and applied loads, one fourth of the plate is described with length L , height L and radius $R/L = 0.2$ and apply boundary conditions as shown in Fig 5.1(b).

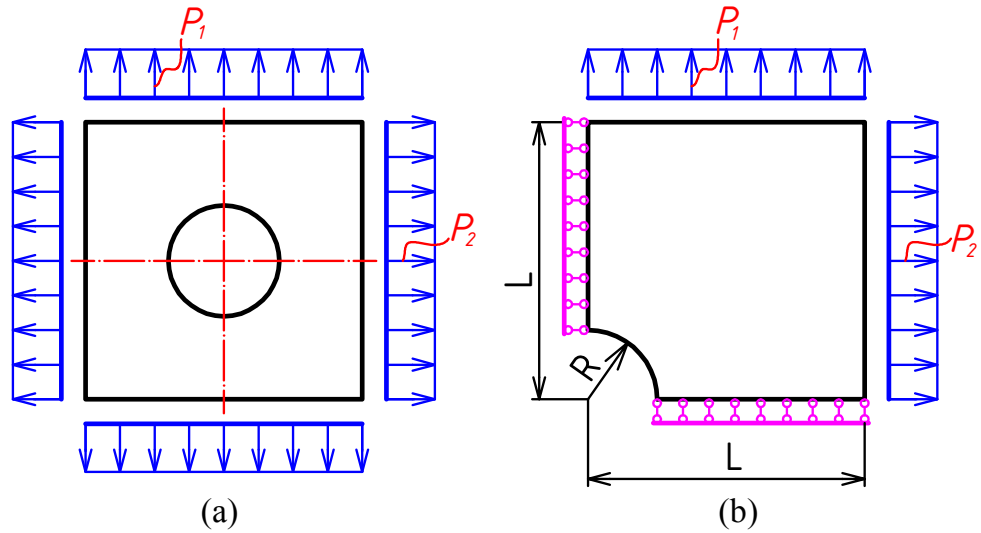


Figure 5.1: Square plate with a central hole: Full (a) and symmetric geometry (b).

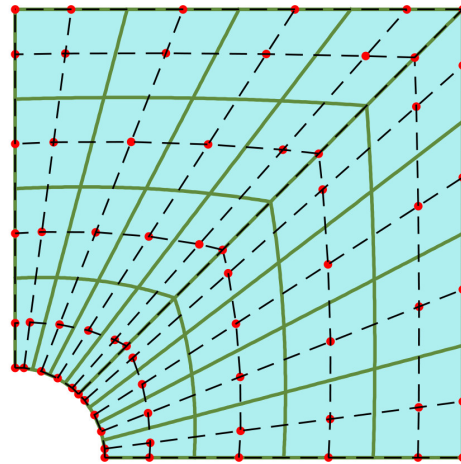


Figure 5.2: Square plate with central circular hole: Quadratic NURBS mesh with 32 elements and control net.

The given data is used as follows: Young's modulus $E = 2.1e^5$ MPa, Poisson's ratio $\nu = 0.3$ and yield stress $\sigma_y = 116.2$ MPa. This problem is studied by many researchers in Refs [17; 32; 33; 50; 105]. In this study, the mesh is discretized by multi-patch of

NURBS with polynomial order $p = 2$ to 4 using 288 NURBS elements with 756 degrees of freedom (DOF), 200 NURBS elements with 650 DOF and 162 NURBS elements with 650 DOF, respectively. An example of IGA mesh is illustrated in Fig 5.2.

Gaydon and McCrum [17] presented the exact solution of the limit load multiplier for plane stress case applying von Mises yield criterion in their work. In case of $P_2 = 0, P_1 \in [0, \sigma_y]$ and $R/L = 0.2$, the exact collapse limit load is as

$$p_{lim} = (1 - R/L)\sigma_y = 0.8\sigma_y \quad (5.1)$$

The varying loads for shakedown analysis are $0 \leq P_1 \leq \sigma_0$ & $0 \leq P_2 \leq \sigma_0$. Both limit and shakedown analysis are studied for different load cases shown in Table 5.1.

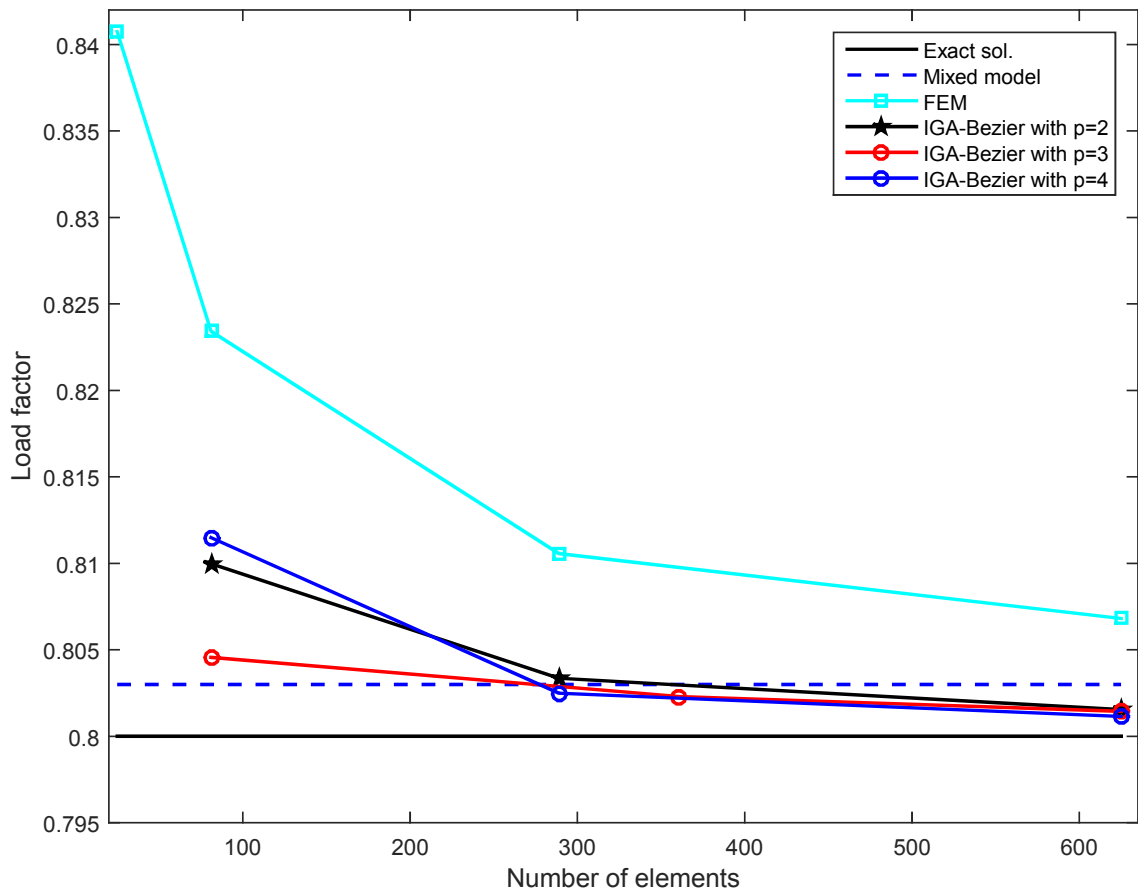


Figure 5.3: The convergence of the IGA compared with those of different methods for limit analysis (with $P_2 = 0$) of the square plate with a central circular hole.

Fig 5.3 shows numerical solutions gained for FEM-Q4 and IGA based on Bézier extraction versus to the increasing variation of degrees of freedom. From Fig. 5.3, it can

be seen that the limit load factors converge rapidly to the analytical solution and the present solution agrees very well with those of the other existing methods such as FEM, mixed model [23] and NS-FEM [106], dual algorithm [28]. It can be observed that IGA method yield the best convergent behaviour of the plastic limit load factor. The results confirm that the IGA methods can be applied for plastic limit analysis problems.

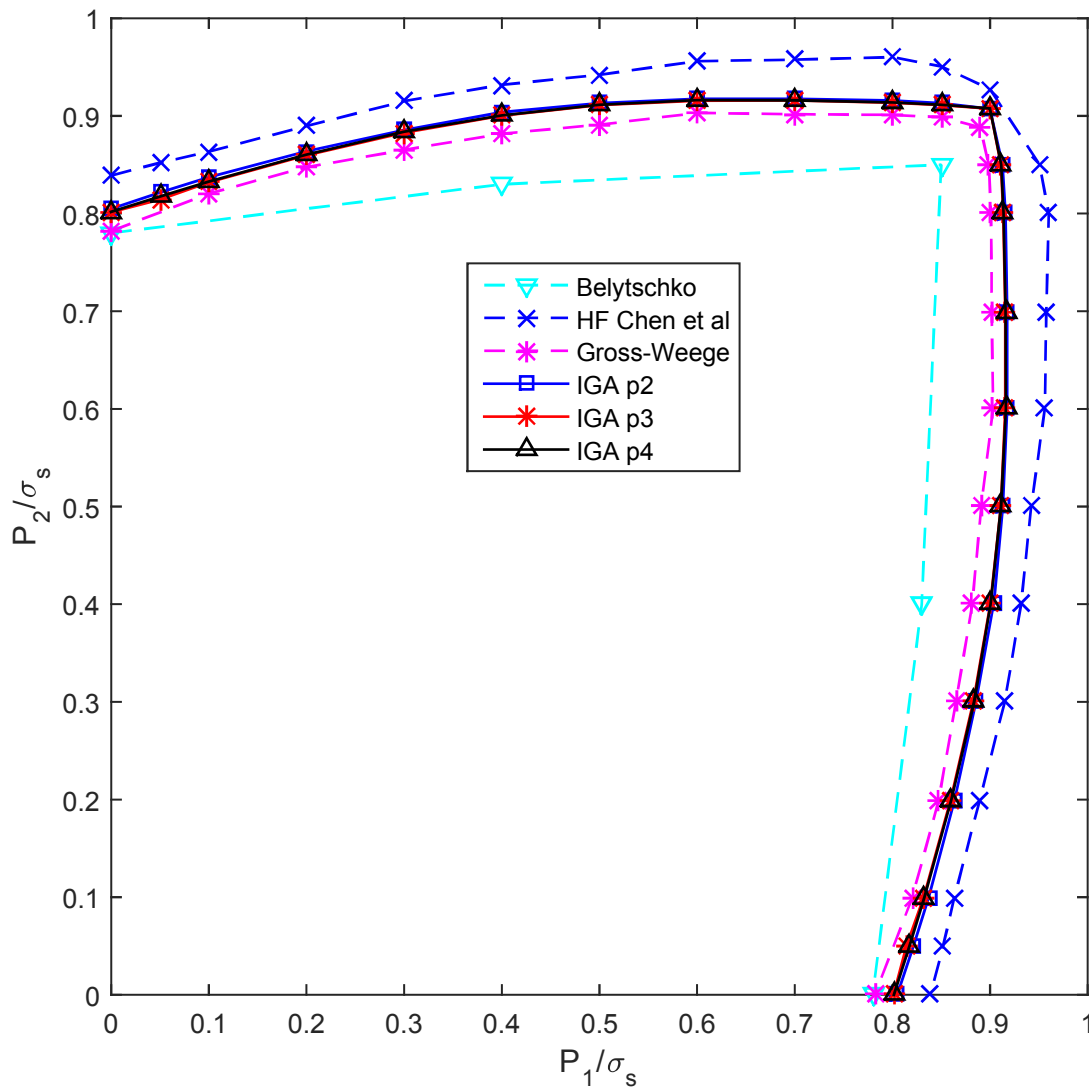
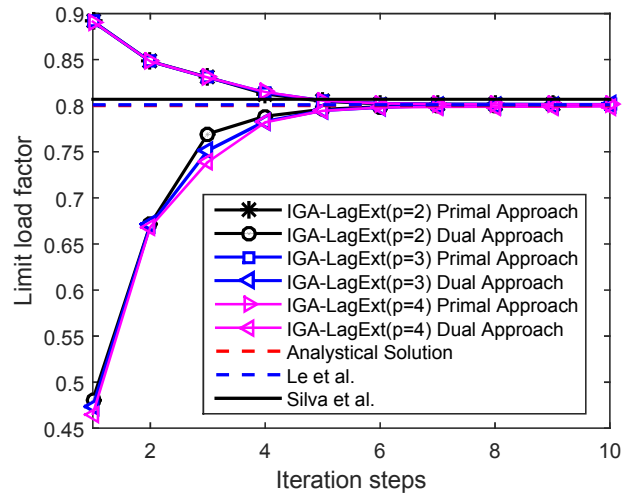
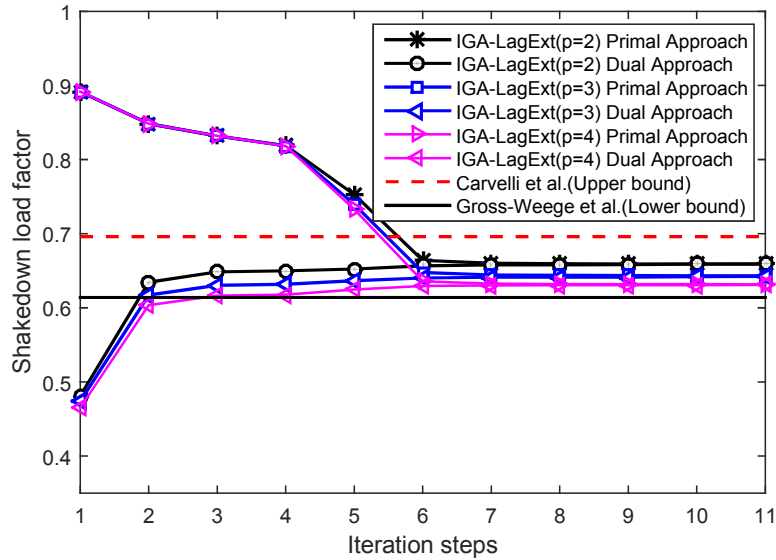


Figure 5.4: The limit load domain of the square plate with a central circular hole using the IGA compared with those of other numerical methods.

Fig 5.4 shows the limit load domains, which use the IGA based on Bézier extraction and some other methods. IGA solutions are seen to agree very well with those of lower bound method in [50; 107] and the upper bound method in [33; 107].



(a) Limit analysis



(b) Shakedown analysis

Figure 5.5: Limit and shakedown load factors for square plate with a central hole subjected to tension load $P_1 = \sigma_0$; $P_2 = 0$.

Our results compared with other solutions are illustrated in Fig 5.5. Reasonable agreement can be shown in Fig 5.5 and Table 5.1. It can be seen that our limit factor results is close to the results using cell-based smooth FEM by Le *et al.* [33]. It can be clearly seen that our results are greater than available literature values obtained by lower bound method and smaller than available literature values obtained by upper bound method.

Table 5.1: Collapse load multiplier for square plate with a circular hole with different loading cases compared with available solutions

| Authors and Approaches | | $P_2 = P_1$ | $P_2 = P_1/2$ | $P_2 = 0$ |
|--|-------------------------|-------------|---------------|-----------|
| Limit Analysis | | | | |
| Silva and Antao[108], Upper bound | | 0.899 | 0.915 | 0.807 |
| Le <i>et al.</i> [33], Upper bound | | 0.895 | 0.911 | 0.801 |
| Zouain <i>et al.</i> [23], Mixed formulation | | 0.894 | 0.911 | 0.803 |
| Analytical solution[17] | | - - - | - - - | 0.8 |
| Chen <i>et al.</i> [50], Lower bound | | 0.874 | 0.899 | 0.798 |
| Gross-Weege[107], Lower bound | | 0.882 | 0.891 | 0.782 |
| Tran <i>et al.</i> [105], Dual Algorithm | | 0.896 | 0.912 | 0.805 |
| IGA-Bezier-Ext, Dual Algorithm | $p = 2$, $ndofs = 578$ | 0.8961 | 0.9124 | 0.8033 |
| | $p = 3$, $ndofs = 722$ | 0.8954 | 0.9116 | 0.8023 |
| | $p = 4$, $ndofs = 578$ | 0.8956 | 0.9120 | 0.8025 |
| IGA-Lag-Ext, Dual Algorithm | $p = 2$, $ndofs = 756$ | 0.8954 | 0.9115 | 0.8012 |
| | $p = 3$, $ndofs = 650$ | 0.8947 | 0.9114 | 0.8013 |
| | $p = 4$, $ndofs = 650$ | 0.8944 | 0.9112 | 0.8004 |
| Shakedown Analysis | | | | |
| Carvelli <i>et al.</i> [109], Upper bound | | 0.518 | 0.605 | 0.696 |
| Zouain <i>et al.</i> [23], Mixed formulation | | 0.429 | 0.500 | 0.594 |
| Gross-Weege[107], Lower bound | | 0.446 | 0.524 | 0.614 |
| Tran <i>et al.</i> [105], Dual Algorithm | | 0.444 | 0.514 | 0.610 |
| IGA-Bezier-Ext, Dual Algorithm | $p = 2$, $ndofs = 578$ | 0.4529 | 0.5238 | 0.6209 |
| | $p = 3$, $ndofs = 722$ | 0.4481 | 0.5186 | 0.6155 |
| | $p = 4$, $ndofs = 578$ | 0.4483 | 0.5188 | 0.6157 |
| IGA-Lag-Ext, Dual Algorithm | $p = 2$, $ndofs = 756$ | 0.4866 | 0.599 | 0.6590 |
| | $p = 3$, $ndofs = 650$ | 0.4728 | 0.5450 | 0.6433 |
| | $p = 4$, $ndofs = 650$ | 0.4624 | 0.5339 | 0.6315 |

For example of limit analysis case with load case $P_1 = \sigma_y$ & $P_2 = 0$ and with load case $P_1 = P_2 = \sigma_y$ (results are in parentheses), comparisons with other available works in detail are as follows: $\alpha = 0.8012$, 08013 & 0.80004 (0.8954, 0.8947 & 0.8944) are obtained through the analysis corresponding with polynomial order $p = 2, 3, 4$ respectively; $\alpha = 0.807$ (0.899) in Ref [108] and $\alpha = 0.801$ (0.895) in Ref [33] obtained by upper bound approach; $\alpha = 0.798$ (0.874) in Ref [50] and $\alpha = 0.782$ (0.882) in Ref [107] obtained by lower bound approach.

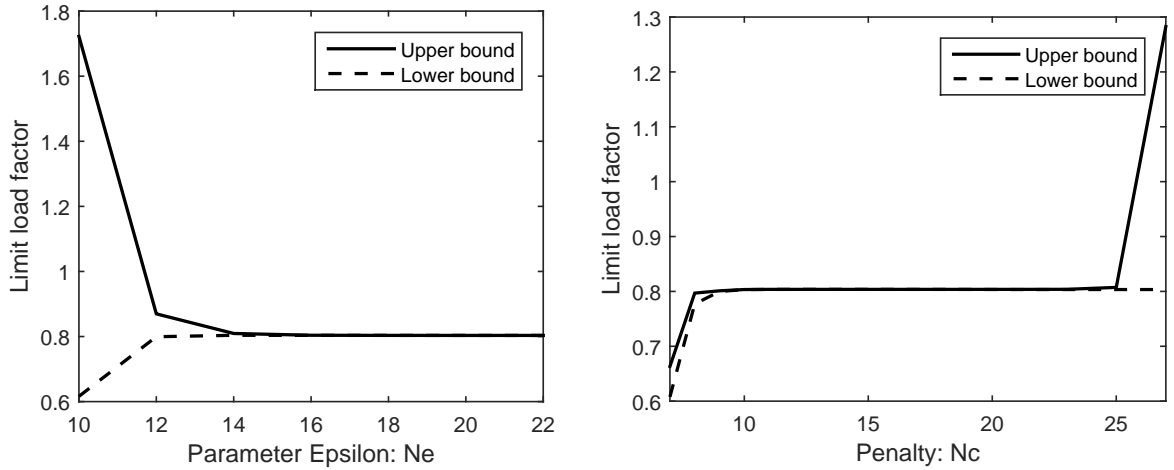
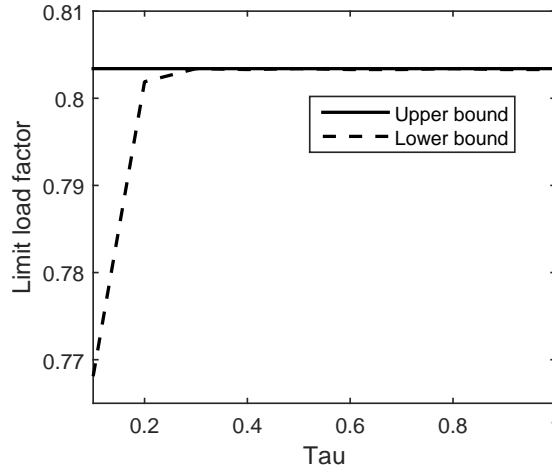
Table 5.2: Influence of parameter ε , ($c = 10^{10}$ and $\tau = 0.9$)

| Total Iterations | Upper bound | Lower bound | $\varepsilon^2 = 10^{-N_e}$ |
|------------------|-------------|-------------|-----------------------------|
| 9 | 1.7225 | 0.6162 | 1.0e-10 |
| 13 | 0.8697 | 0.7994 | 1.0e-12 |
| 16 | 0.8093 | 0.8038 | 1.0e-14 |
| 17 | 0.8039 | 0.8036 | 1.0e-16 |
| 15 | 0.8035 | 0.8035 | 1.0e-18 |
| 16 | 0.8034 | 0.8034 | 1.0e-20 |
| 22 | 0.8034 | 0.8033 | 1.0e-24 |
| 19 | 0.8034 | 0.8034 | 1.0e-28 |

Table 5.3: Influence of parameter c , ($\varepsilon = 10^{-10}$ and $\tau = 0.9$).

| Total Iterations | Upper bound | Lower bound | $c = 10^{N_C}$ |
|------------------|-------------|-------------|----------------|
| 3 | 0.6634 | 0.6078 | 1.0e+07 |
| 4 | 0.7969 | 0.7771 | 1.0e+08 |
| 9 | 0.8011 | 0.7998 | 1.0e+09 |
| 15 | 0.8034 | 0.8033 | 1.0e+10 |
| 24 | 0.8037 | 0.8036 | 1.0e+11 |
| 22 | 0.8037 | 0.80369 | 1.0e+12 |
| 22 | 0.8037 | 0.80369 | 1.0e+13 |
| 23 | 0.8037 | 0.80369 | 1.0e+14 |
| 18 | 0.8037 | 0.80368 | 1.0e+15 |
| 19 | 0.8037 | 0.80366 | 1.0e+16 |
| 34 | 0.8037 | 0.80361 | 1.0e+18 |
| 28 | 0.8037 | 0.80358 | 1.0e+19 |
| 13 | 0.8037 | 0.8034 | 1.0e+21 |
| 20 | 0.8038 | 0.8034 | 1.0e+23 |
| 23 | 0.8073 | 0.8034 | 1.0e+25 |
| 24 | 1.2828 | 0.8034 | 1.0e+27 |

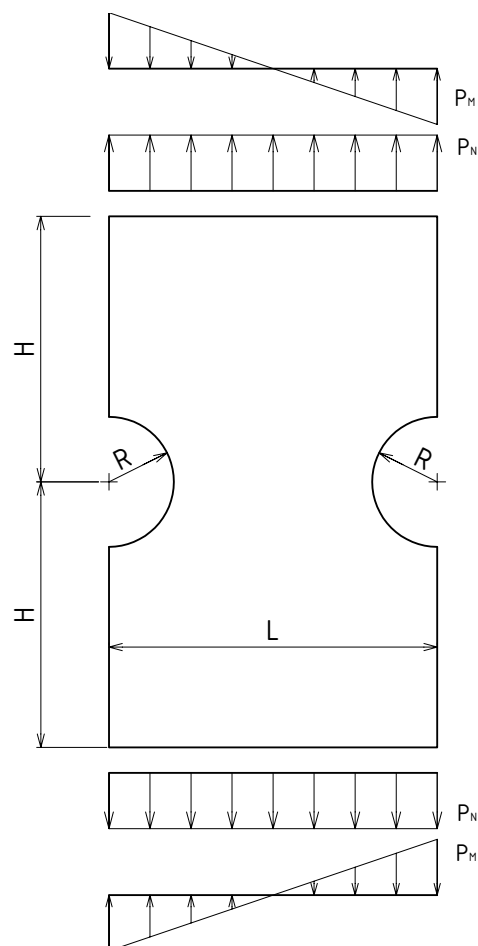
The influences of optimization parameters (ε , c and τ) are investigated independently of each other and the numerical results are shown in Fig. (5.6) and Tables (5.2, 5.3 and 5.4). It can be observed that:

(a) $\epsilon^2 = 10^{-Ne}$, ($c = 10^{10}$ and $\tau = 0.9$)(b) $c = 10^{Nc}$, ($\epsilon = 10^{-10}$ and $\tau = 0.9$)(c) τ , ($\epsilon = 10^{-10}$ and $c = 10^{10}$)**Figure 5.6:** Influence parameter of ϵ , c and τ

- The parameter ϵ has very little influence on the computational results in the range of $\epsilon^2 = 10^{-14} \div 10^{-22}$. Both lower and upper bound limit load factors keep stationary (all results are found by using parameters $c = 10^{10}$ and $\tau = 0.9$).
- In the range of penalty parameter $c = 10^9 \div 10^{20}$, number error is less than 1% for both upper bound and lower bound shown in Fig. 5.6(b).
- The parameter τ has no influence of lower and upper limit load factor, except for the case $\tau \leq 0.1$. The Table 5.4 shown that small τ leads to slow convergence of problem.

Table 5.4: Influence of parameter τ , ($\varepsilon = 10^{-10}$ and $c = 10^{10}$)

| Total Iterations | Upper bound | Lower bound | τ |
|------------------|-------------|-------------|--------|
| 34 | 0.8034 | 0.7681 | 0.1 |
| 34 | 0.8034 | 0.8019 | 0.2 |
| 30 | 0.8034 | 0.8034 | 0.3 |
| 25 | 0.8034 | 0.8033 | 0.4 |
| 21 | 0.8034 | 0.8034 | 0.5 |
| 17 | 0.8034 | 0.8033 | 0.6 |
| 17 | 0.8034 | 0.8033 | 0.7 |
| 25 | 0.8034 | 0.8034 | 0.8 |
| 15 | 0.8034 | 0.8033 | 0.9 |
| 12 | 0.8034 | 0.8033 | 1.0 |

**Figure 5.7:** Full geometry and applied load of grooved rectangular plate.

5.2.2 Grooved rectangular plate subjected to varying tension

This example is well-known benchmark under plane stress and plane strain states subjected to tension p_N as shown in Fig 5.7 (a). Taking advantage of symmetry of geometry and applied load, only a half of the problem with length L , height L and radius $R = 0.25L = 250 \text{ mm}$ of two semi-circular notches as shown in Fig 5.7 (b). This benchmark was introduced by Prager and Hodge [110] under Tresca yield criterion. However, von Mises yield condition is used in our research. This problem is also studied by some authors for von Mises yield criterion such as Casciaro *et al.* [111], Yan [93], Nguyen *et al.* [55; 106], Tran *et al.* [105] and more recently Do *et al.* [54]. The following material properties are chosen: Young's modulus $E = 2.1e^5 \text{ MPa}$, Poisson's ratio $\nu = 0.3$ and yield stress $\sigma_y = 116.2 \text{ MPa}$.

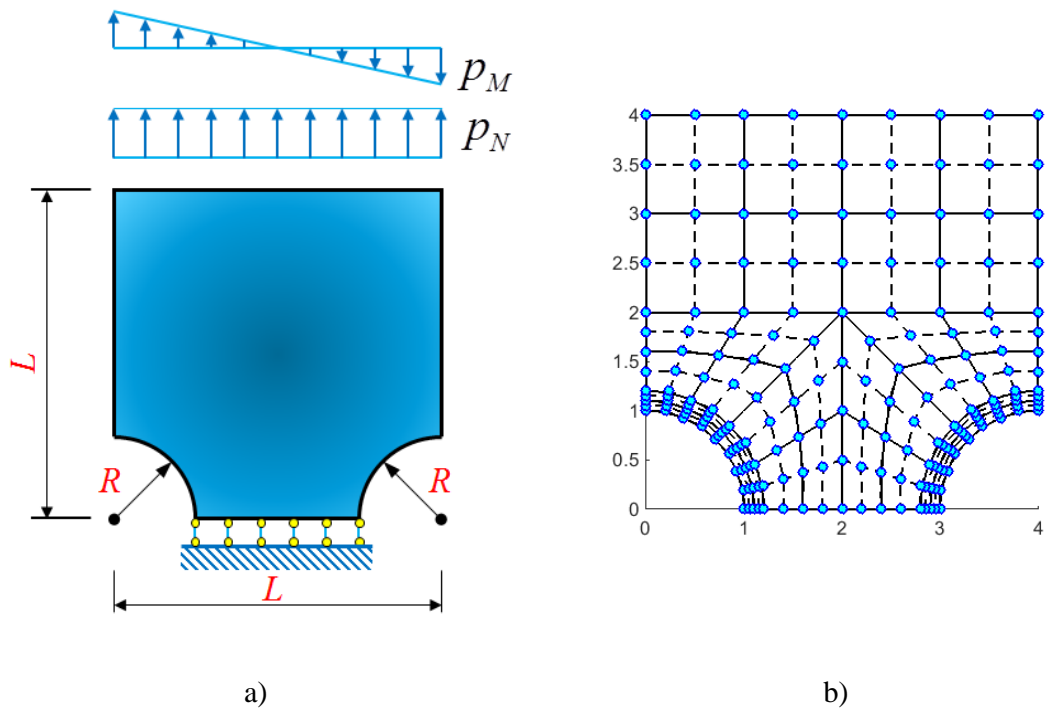
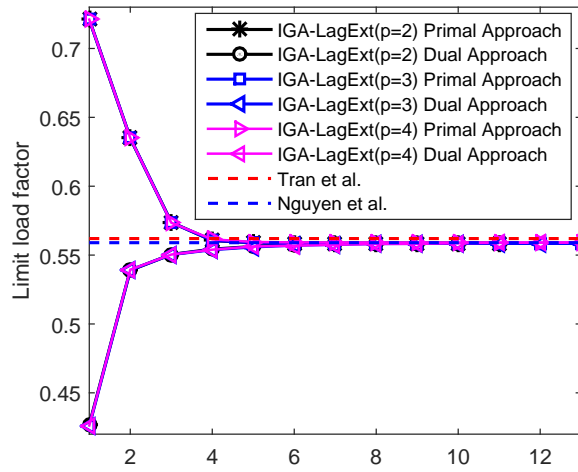
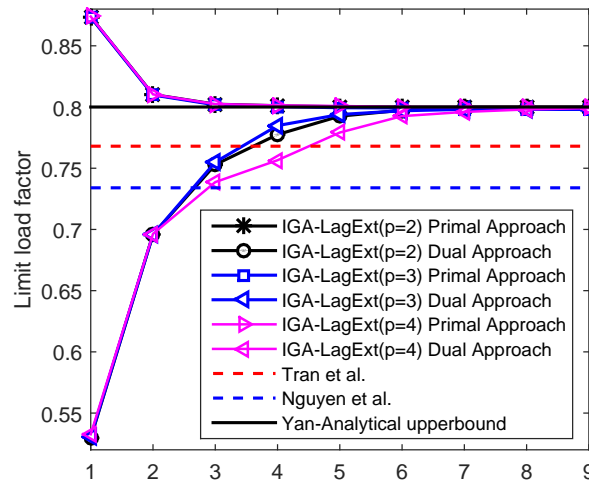


Figure 5.8: A symmetry of the grooved rectangular plate: a) A symmetric model including applied loads and boundary conditions; b) 2D control point net and 40 NURBS quadratic elements.

In this study, the mesh is discretized by multi-patch of NURBS with polynomial order $p = 2$ to 4 using 384 NURBS elements with 1082 degrees of freedom (DOF), 216 NURBS elements with 866 DOF and 96 NURBS elements with 674 DOF, respectively. The IGA mesh example for order $p = 2$ using 96 NURBS elements is illustrated in Fig 5.8.



(a) Plane stress state



(b) Plane strain state

Figure 5.9: Limit load factors of the plate with tension of a strip with semi-circular notches.

The numerical results of the present approach are listed in Table 5.5 and compared with those of other available methods. It is obviously clear that our numerical result is well accordant with result of other methods for both plane stress and plane strain states. In case of plane stress condition, the limit collapse multipliers of the current method for three meshes mentioned above are respectively 0.558, 0.559 and 0.559 which is equal to 0.559 in Ref [54; 106] and belong to the range of the analytical solution $0.500 \div 0.577$ in Ref [93]. In case of plane strain state, the limit load factors respectively obtain 0.798, 0.799 and 0.799 which is quite close to 0.769 in Ref [93], 0.768 in Ref [105], 0.797 in Ref [54] and slightly lower than analytical upper bound 0.80 reported in [93]. Table 5.5 also shows that the present approach gives high accuracy with fewer

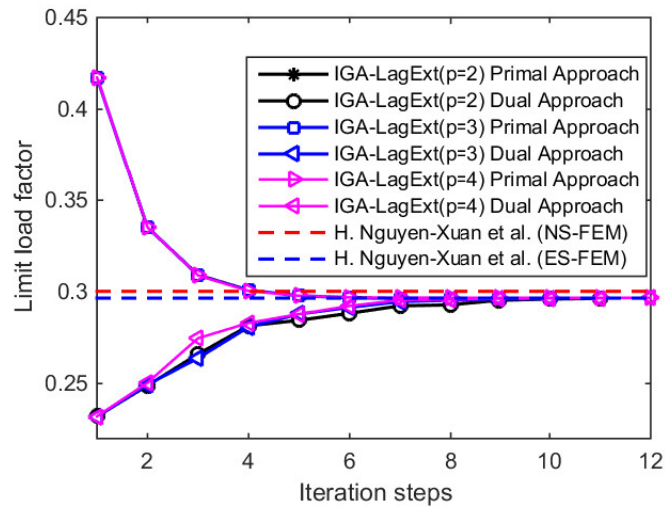
degrees of freedom compared with the results in Ref [54]. Fig 5.9 shows the limit load factors of upper bound and quasi-lower bound of this problem. We also study the limit and shakedown analysis for complicated loads (subjected to both tension and bending loads). The load domain for the shakedown problem is defined by $p_N \in [0 \ \sigma_y]$ and $p_M \in [0 \ \sigma_y]$. The results of this problem under complicated loads are listed in Table 5.6. The convergence of limit and shakedown load factors are demonstrated in Fig 5.10.

Table 5.5: Collapse multiplier for the grooved rectangular plate subjected to constant pure tension: Comparison of limit load multipliers for different approaches.

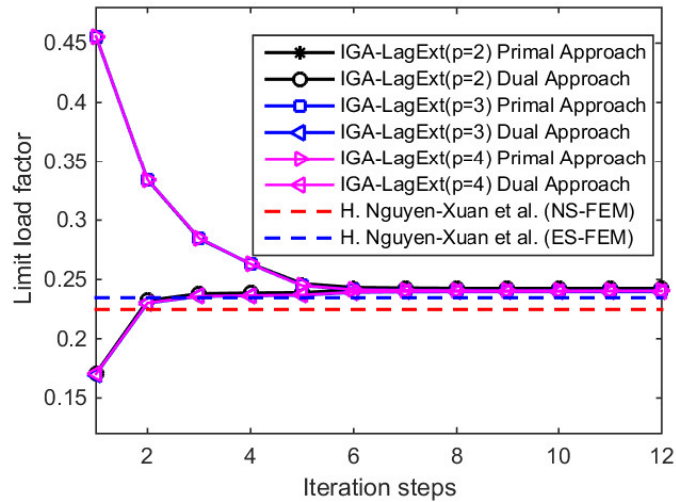
| Authors and Methods | | Plane stress | Plane strain | Yield criterion |
|---|-----------------------|--------------|--------------|-----------------|
| Prager [110], Analytical | | 0,5 | 0.63÷0.695 | Tresca |
| Yan [93], Analytical | | 0.5÷0.577 | 0.727÷0.8 | von Mises |
| Casciaro <i>et al.</i> [111], Numerical | | 0,568 | 0,699 | von Mises |
| Yan [93], Numerical | | 0,588 | 0,769 | von Mises |
| Tran <i>et al.</i> [105], Numerical | | 0,562 | 0,768 | von Mises |
| H. Nguyen-Xuan <i>et al.</i> [106], Numerical | | 0,559 | 0,734 | von Mises |
| IGA-Bézier-Ext Numerical [54] | $p = 2, ndofs = 1410$ | 0,56 | 0,799 | von Mises |
| | $p = 3, ndofs = 1766$ | 0,558 | 0,797 | von Mises |
| | $p = 4, ndofs = 1410$ | 0,559 | 0,798 | von Mises |
| IGA-Lag-Ext Numerical | $p = 2, ndofs = 1082$ | 0,558 | 0,798 | von Mises |
| | $p = 3, ndofs = 866$ | 0,559 | 0,799 | von Mises |
| | $p = 4, ndofs = 674$ | 0,559 | 0,799 | von Mises |

Table 5.6: Elastic shakedown analysis load multiplier for the grooved rectangular plate subjected to both tension p_N and bending p_M with the defined load domains $p_N \in [0 \ \sigma_y]$ and $p_M \in [0 \ \sigma_y]$

| Authors & Methods | | Limit analysis | Shakedown analysis |
|---------------------------------|-----------------------|----------------|--------------------|
| Nguyen-Xuan <i>et al.</i> [106] | NS-FEM | 0.3003 | 0.2247 |
| | ES-FEM | 0.2966 | 0.2346 |
| IGA-LagExt | $p = 2, ndofs = 1082$ | 0.2965 | 0.2423 |
| | $p = 3, ndofs = 866$ | 0.2964 | 0.2403 |
| | $p = 4, ndofs = 674$ | 0.2968 | 0.2404 |



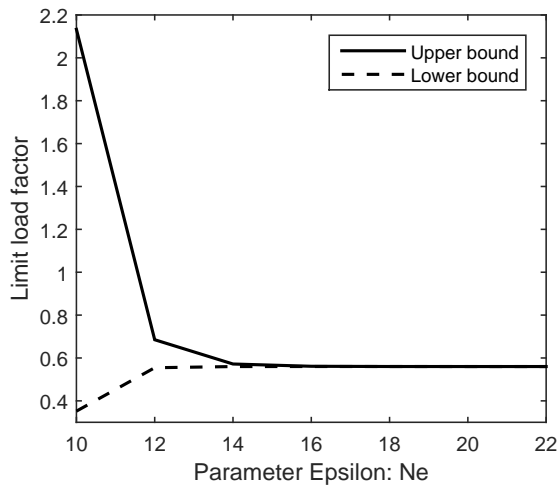
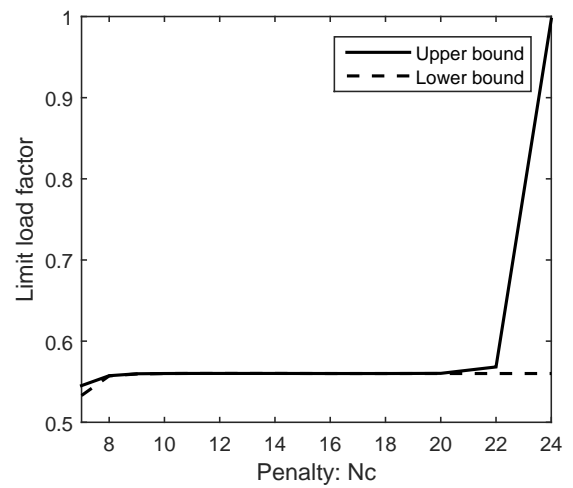
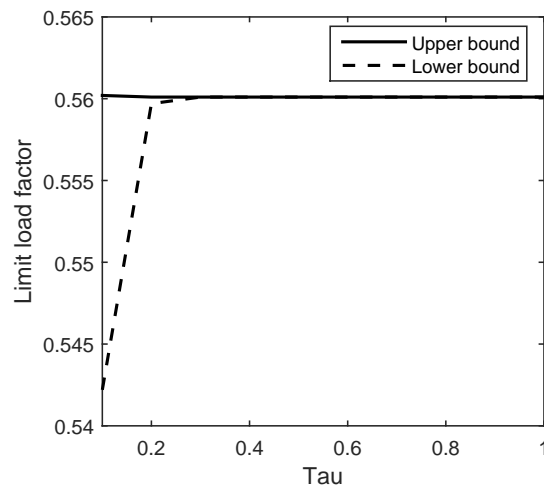
(a) Limit analysis



(b) Shakedown analysis

Figure 5.10: Limit and shakedown load factors for the grooved rectangular plate subjected to both tension and bending loads.

From Fig (5.11) and Tables (5.7, 5.8 and 5.9), it can be seen that algorithm gives the stable results when ε parameter $\varepsilon \geq 10^{-7}$, penalty parameter $c \in [10^7, 10^{12}]$ and $\tau \geq 0.2$. The higher value of τ paramter, the faster convergence of limit load factor.

(a) $\varepsilon^2 = 10^{-Ne}$, ($c = 10^{10}$ and $\tau = 0.9$)(b) $c = 10^{Nc}$, ($\varepsilon = 10^{-10}$ and $\tau = 0.9$)(c) τ , ($\varepsilon = 10^{-10}$ and $c = 10^{10}$)**Figure 5.11:** Influence parameter of ε , c and τ **Table 5.7:** Influence of parameter ε , ($c = 10^{10}$ and $\tau = 0.9$)

| Total Iterations | Upper bound | Lower bound | $\varepsilon^2 = 10^{-Ne}$ |
|------------------|-------------|-------------|----------------------------|
| 07 | 2.133 | 0.3520 | 1.0e-10 |
| 11 | 0.6851 | 0.5545 | 1.0e-12 |
| 11 | 0.5719 | 0.5600 | 1.0e-14 |
| 22 | 0.5613 | 0.5602 | 1.0e-16 |
| 14 | 0.5602 | 0.5602 | 1.0e-18 |
| 10 | 0.5601 | 0.5601 | 1.0e-20 |
| 08 | 0.5601 | 0.5601 | 1.0e-22 |

Table 5.8: Influence of parameter c , ($\varepsilon = 10^{-10}$ and $\tau = 0.9$)

| Total Iterations | Upper bound | Lower bound | $c = 10^{NC}$ |
|------------------|-------------|-------------|---------------|
| 3 | 0.5452 | 0.5330 | 1.0e+07 |
| 5 | 0.5574 | 0.5572 | 1.0e+08 |
| 6 | 0.5598 | 0.5595 | 1.0e+09 |
| 8 | 0.5601 | 0.5601 | 1.0e+10 |
| 19 | 0.5602 | 0.5602 | 1.0e+11 |
| 18 | 0.5602 | 0.5602 | 1.0e+12 |
| 15 | 0.5602 | 0.5602 | 1.0e+14 |
| 14 | 0.5601 | 0.5601 | 1.0e+16 |
| 29 | 0.5601 | 0.5601 | 1.0e+18 |
| 26 | 0.5603 | 0.5601 | 1.0e+20 |
| 20 | 0.5682 | 0.5601 | 1.0e+22 |
| 24 | 0.9966 | 0.5601 | 1.0e+24 |

Table 5.9: Influence of parameter τ , ($\varepsilon = 10^{-10}$ and $c = 10^{10}$)

| Total Iterations | Upper bound | Lower bound | τ |
|------------------|-------------|-------------|--------|
| 34 | 0.5602 | 0.5422 | 0.1 |
| 34 | 0.5601 | 0.5597 | 0.2 |
| 29 | 0.5601 | 0.5601 | 0.3 |
| 21 | 0.5601 | 0.5601 | 0.4 |
| 17 | 0.5601 | 0.5601 | 0.5 |
| 14 | 0.5601 | 0.5601 | 0.6 |
| 12 | 0.5601 | 0.5601 | 0.7 |
| 11 | 0.5601 | 0.5601 | 0.8 |
| 8 | 0.5601 | 0.5601 | 0.9 |
| 17 | 0.5601 | 0.5601 | 1.0 |

5.3 Limit and shakedown analysis of 3D structures

5.3.1 Thin square slabs with two different cutout subjected to tension

The first 3D problem that we assess the performance of the IGA via the limit analysis is the thin square slab with two different cutouts subjected to tension as shown in Fig 5.13 [106]. The given data is selected as in Section 3.2.5. This problem is studied by many researchers such as Chen *et al.*[21], Nguyen *et al.*[106].The geometry of 3D holed plate is shown in Fig 5.13.

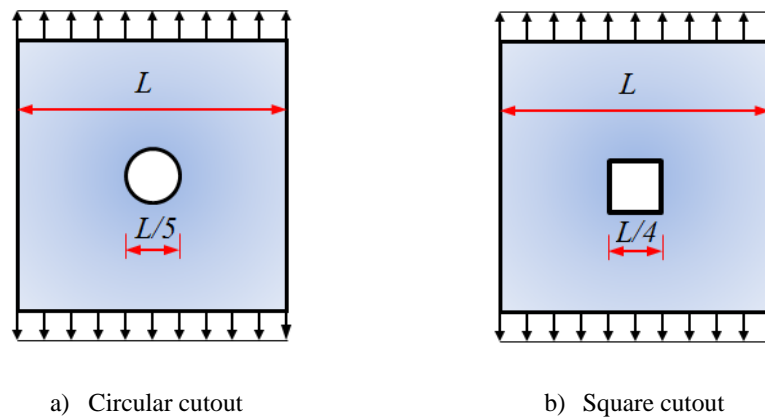


Figure 5.12: The 2D view geometry of thin square slabs with two different cutouts subjected to biaxial loading.

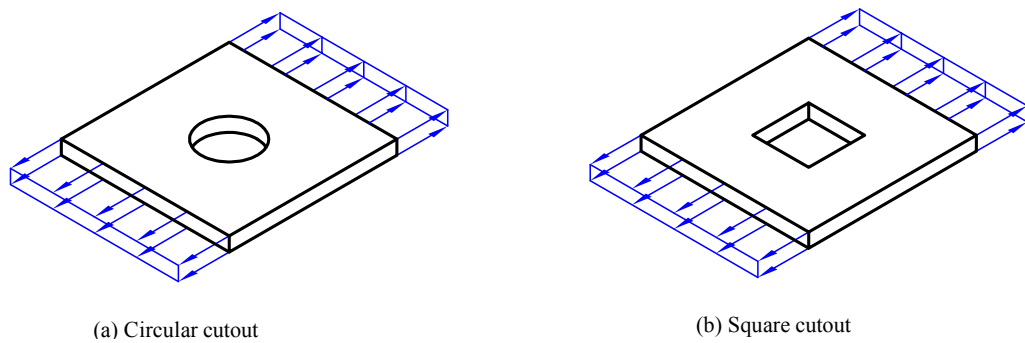


Figure 5.13: The 3D geometry of thin square slabs with two different cutouts subjected to biaxial loading.

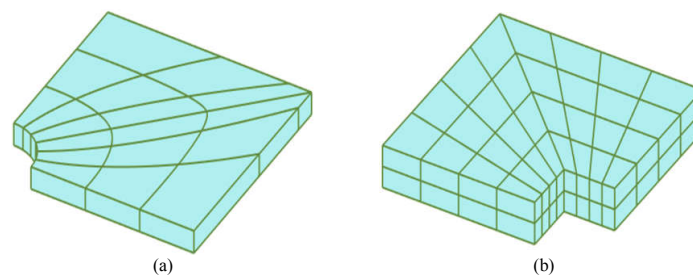


Figure 5.14: The 3D quadrant NURBS meshes of thin square slabs with two different cutouts: (a)-Circular cutout and (b)-Square cutout

Due to the symmetry of the structure and the loading, only the quadrants of two slabs are modeled and their discretizations using NURBS elements are illustrated in Fig. 5.14 and Fig. 5.15. The ratio between the diameter of the hole and the length of the plate is 0.2. The ratio between the depth of the plate and the length of the plate is

0.05. The yield stress of the material is 360 MPa. In this study $L = 20$ cm has been chosen.

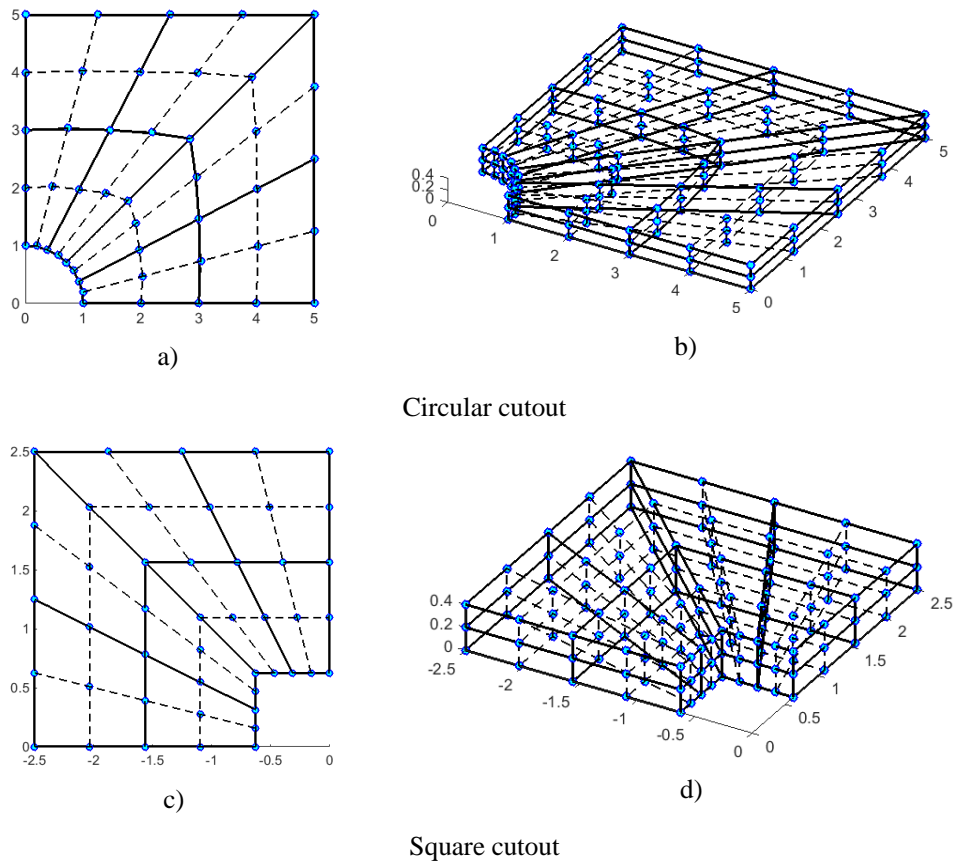
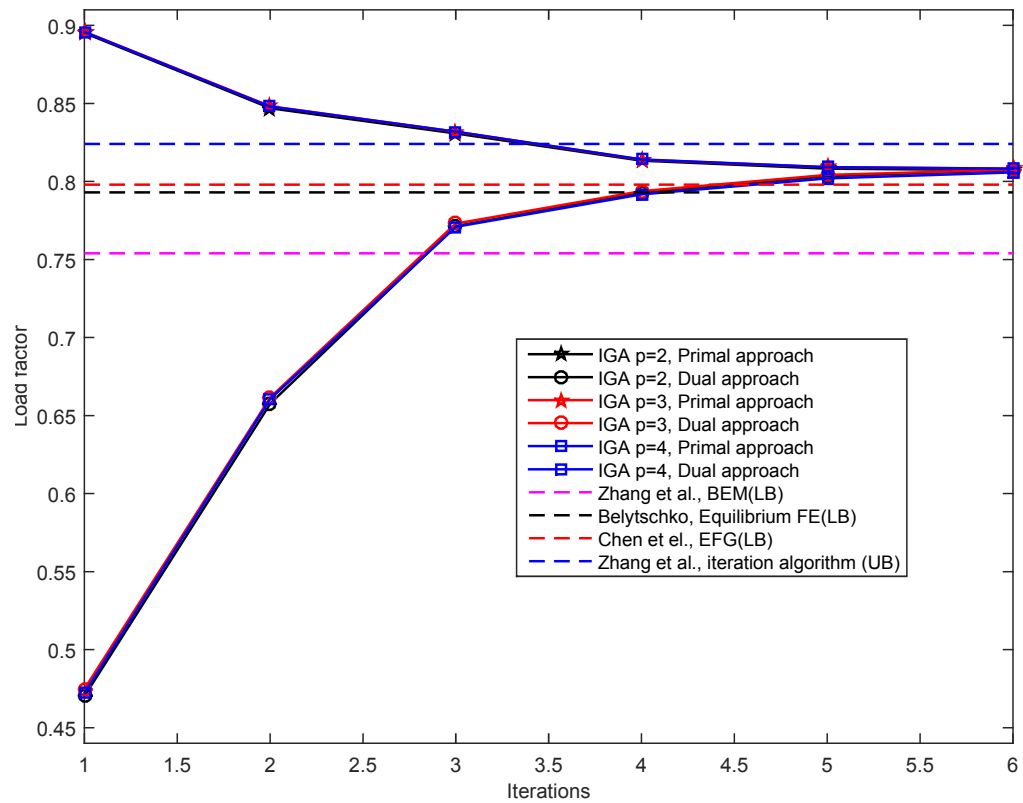


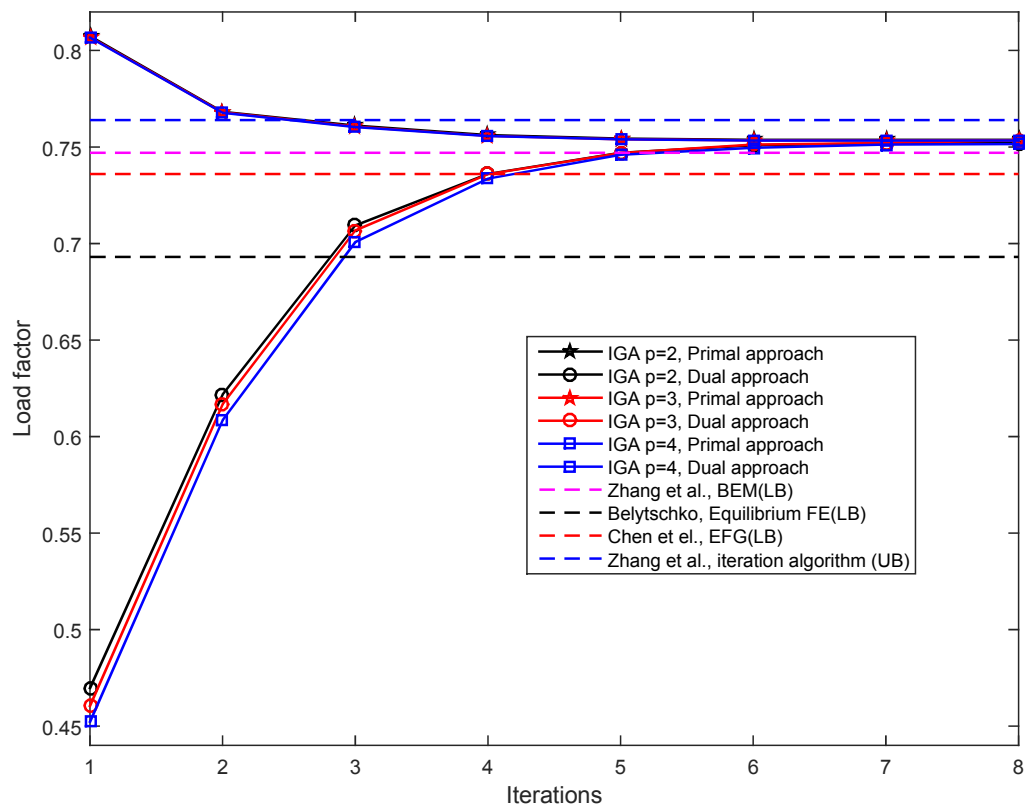
Figure 5.15: Finite element discretization using quartic NURBS elements for thin square slabs with two different cutouts.

Table 5.10: The limit load factor of the IGA in comparison with those of other methods for thin square slabs with two different cutouts.

| Authors & Methods | a) Circular cutout | b) Square cutout |
|--|--------------------|------------------|
| Zhang <i>et al.</i> [38], BEM (LB) | 0.754 | 0.747 |
| Belytschko [19], equilibrium FE (LB) | 0.793 | 0.693 |
| Chen <i>et al.</i> [50], EFG (LB) | 0.798 | 0.736 |
| Zhang <i>et al.</i> [20], iteration algorithm (UB) | 0.824 | 0.764 |
| Tran <i>et al.</i> [47], dual algorithm | 0.805 | 0.748 |
| IGA ($p = 2$, $nel = 144$, $ndofs = 2925$) | 0.807 | 0.752 |
| IGA ($p = 3$, $nel = 36$, $ndofs = 1710$) | 0.807 | 0.752 |
| IGA ($p = 4$, $nel = 16$, $ndofs = 1377$) | 0.807 | 0.752 |



(a) Circular



(b) Square

Figure 5.16: Convergence of limit load factors using the IGA solution in comparison with those of other methods for thin square slabs with two different cutouts: a) circular; b) square.

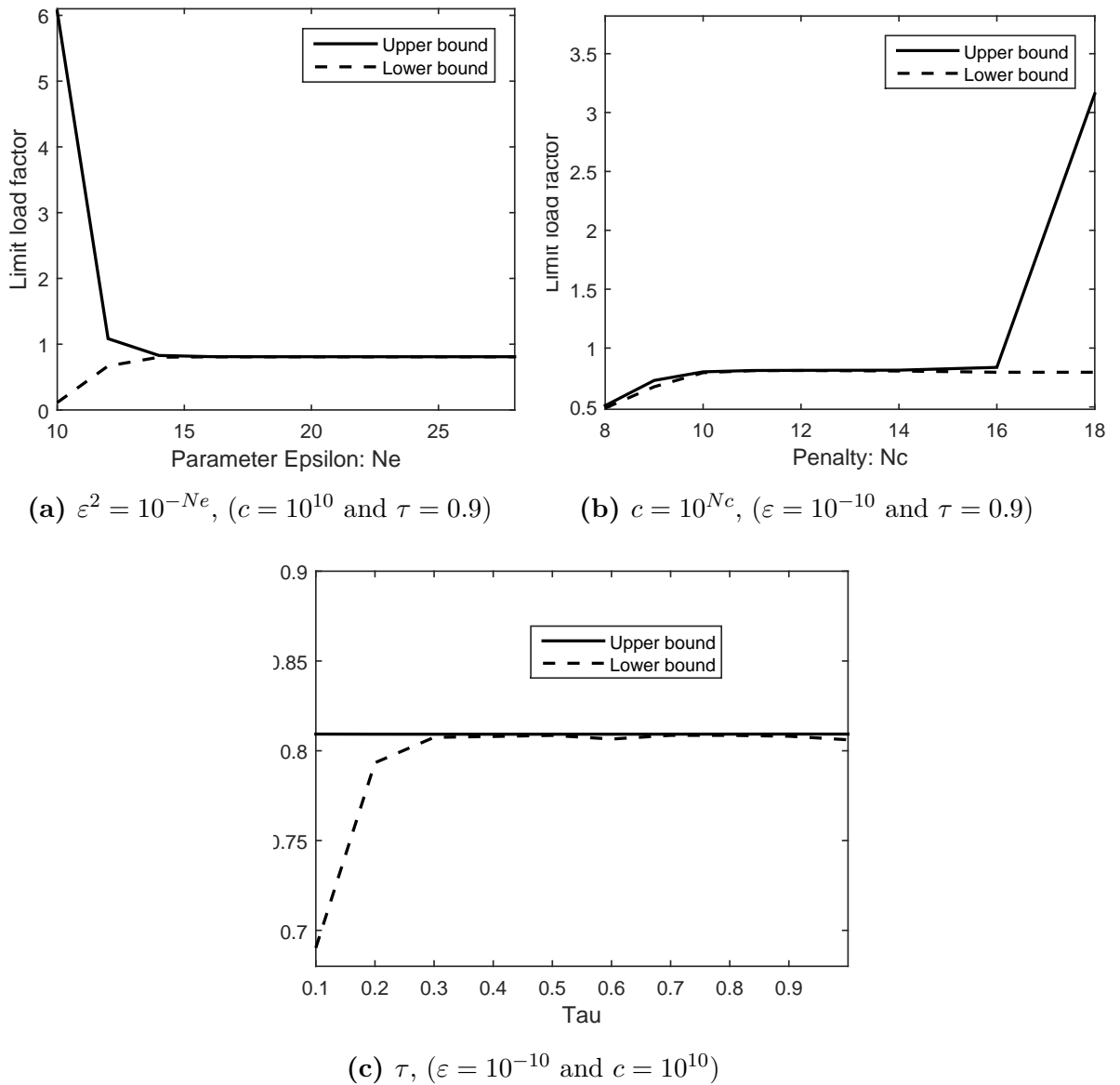


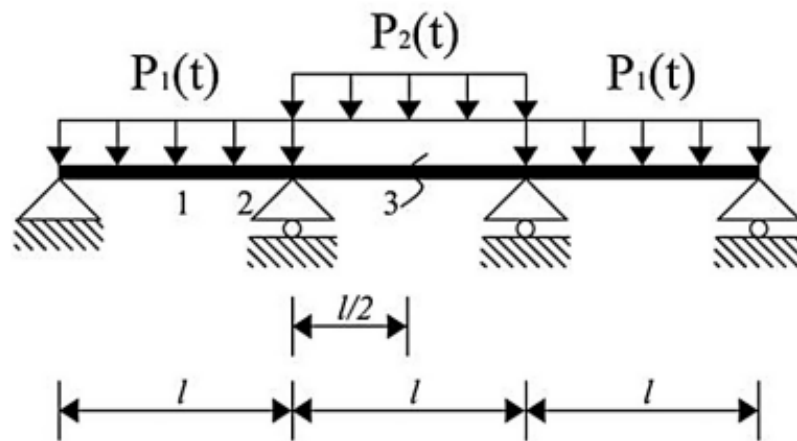
Figure 5.17: Influence parameter of ε , c and τ for 3D circular cutout.

This plane stress problem has been solved numerically by finite element [106], by boundary element method (BEM) [38] and recently by the element-free Galerkin (EFG) method [50]. Table 5.10 shows the limit load factors of the IGA in comparison with those of several different limit analysis approaches, and Fig 5.16 illustrates simultaneously convergence of the limit load factors for both the upper and lower bounds. Using the primal-dual algorithm, all the upper and lower bounds for two case of slabs in Fig 5.16 converge rapidly to the solutions in Table 5.10. Also from Fig 5.16 and Table 5.10, it can be seen that the solutions of the IGA are lower than those of the upper bound models and higher than those of the lower bound approaches. This implies that the

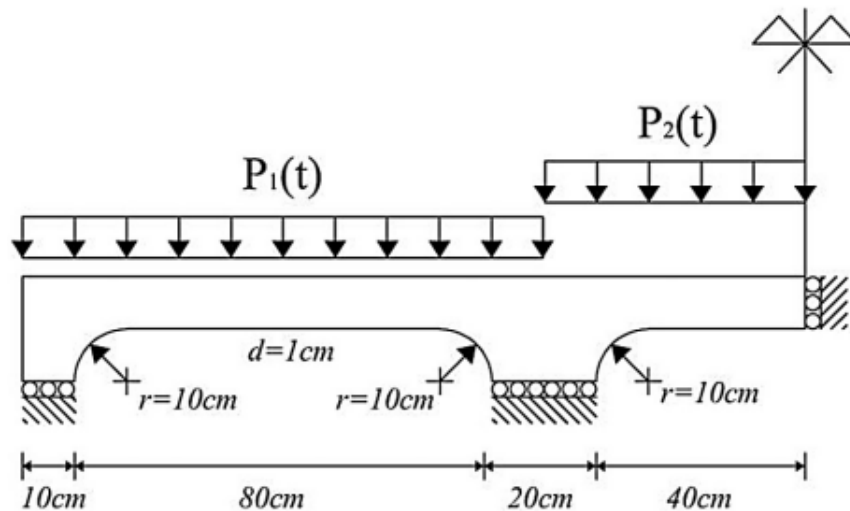
IGA can produce the results closer to the exact value than several other methods in the literature.

The influence of parameters ε , c and τ are investigated independently. The results are shown in Fig 5.17. It can be clear seen that the numerical results are obtained the stable when ε parameter $\varepsilon \geq 10^{-7}$, penalty parameter $c \in [10^9, 10^{16}]$ and $\tau \geq 0.3$.

5.3.2 2D and 3D symmetric continuous beam



(a) Full model of the continuous beam



(b) Full model of the continuous beam

Figure 5.18: Geometry and loading of the continuous beam [50].

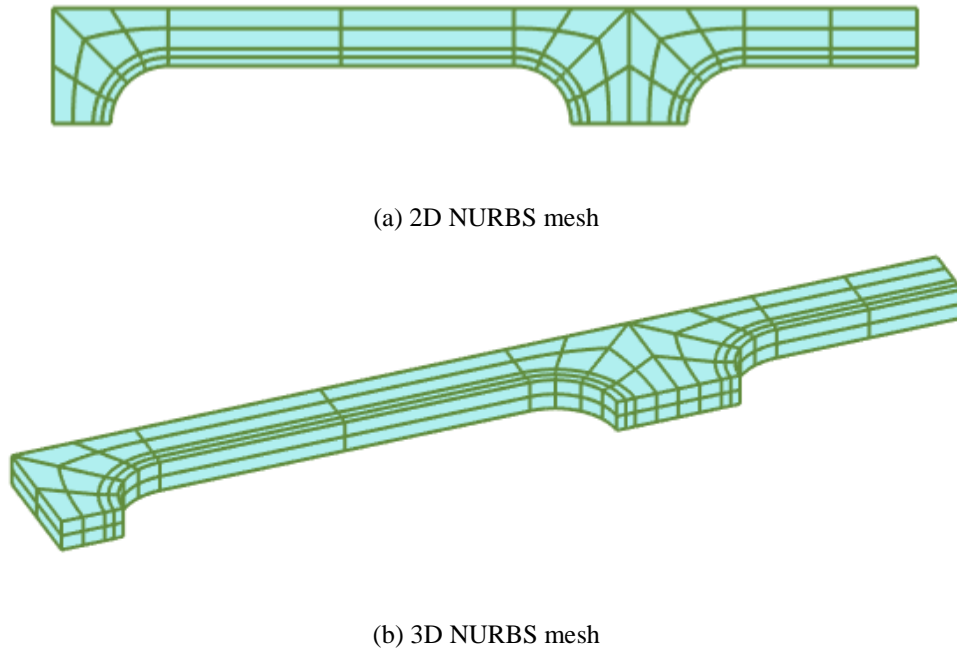


Figure 5.19: Continuous beam: (a) 2D NURBS mesh and (b) 3D NURBS mesh.

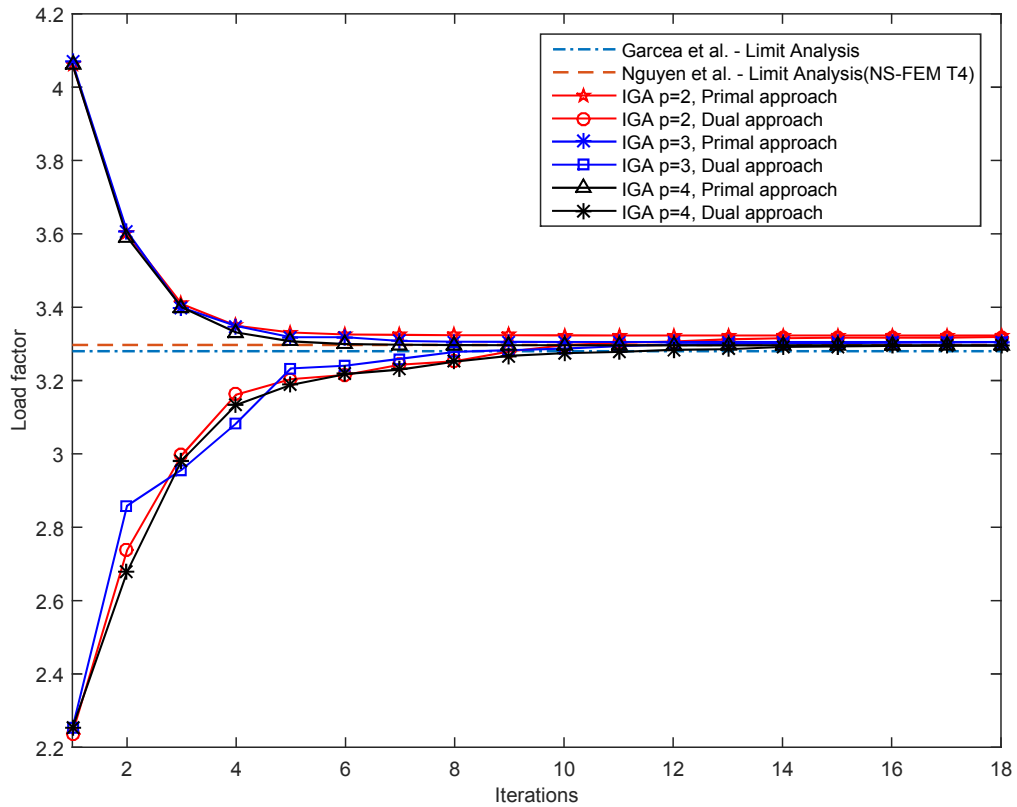
Table 5.11: Shakedown load factor of the symmetric continuous beam with various load domains

| Case | Load domain (MPa) | Shakedown load factor | | | | |
|-----------|-------------------------|-----------------------|-------|-------------------|-------------------|-------------------|
| | | Ref[112] | [50] | <i>IGA, p = 2</i> | <i>IGA, p = 3</i> | <i>IGA, p = 4</i> |
| 2D | | | | | | |
| 1 | $1.2 \leq p_1 \leq 2.0$ | 3.244 | 3.297 | 3.285 | 3.267 | 3.258 |
| | $0 \leq p_2 \leq 1.0$ | | | | | |
| 2 | $0 \leq p_1 \leq 2.0$ | - | 2.174 | 2.187 | 2.169 | 2.170 |
| | $0.6 \leq p_2 \leq 1.0$ | | | | | |
| 3 | $0 \leq p_1 \leq 2.0$ | - | 2.152 | 2.164 | 2.147 | 2.148 |
| | $0 \leq p_2 \leq 1.0$ | | | | | |
| 3D | | | | | | |
| 1 | $1.2 \leq p_1 \leq 2.0$ | - | - | 3.361 | 3.316 | 3.396 |
| | $0 \leq p_2 \leq 1.0$ | | | | | |
| 2 | $0 \leq p_1 \leq 2.0$ | - | - | 2.221 | 2.218 | 2.227 |
| | $0.6 \leq p_2 \leq 1.0$ | | | | | |
| 3 | $0 \leq p_1 \leq 2.0$ | - | - | 2.191 | 2.166 | 2.184 |
| | $0 \leq p_2 \leq 1.0$ | | | | | |

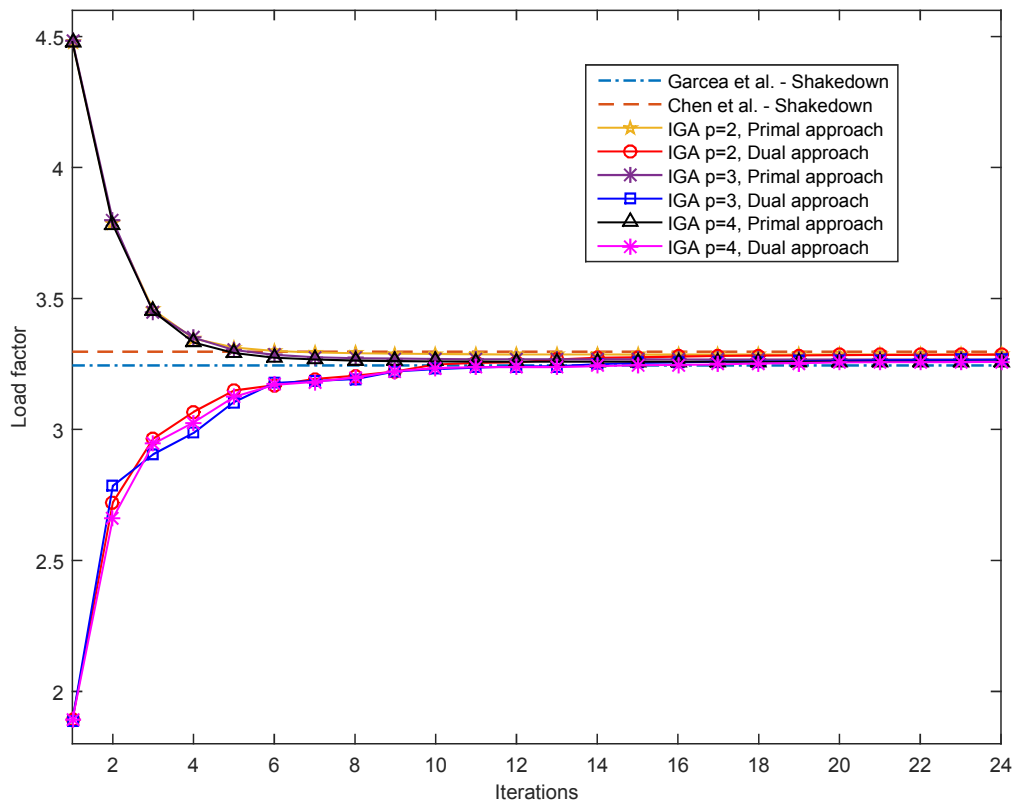
A symmetric continuous steel beam subjected to two independent loads is described in Fig 5.18. The material parameters are: $E = 1.8 \times 10^5 MPa$, $\nu = 0.3$, $\sigma_y = 100 MPa$. The load domain is chosen analogously as in Ref [112]: $1.2 MPa \leq p_1 \leq 2.0 MPa$, $0 \leq p_2 \leq 1.0 MPa$. The IGA discretization using quadratic mesh with 352 NURBS elements and 1521 numbers of control points is described in Fig 5.19. Limit and shakedown values are reported in Table 5.11. The convergence of limit and shakedown load factors in comparison with those of two other methods are described in Fig 5.20. The obtained solutions are suitable to the published results in Ref [50], [112]. Finally, Table 5.11 closes shakedown solutions of this problem with various load domains.

Table 5.12: Influence of parameter ε^2 , ($c = 10^{10}$ and $\tau = 0.9$)

| Total Iterations | Upper bound | Lower bound | $\varepsilon = 10^{-N_e}$ |
|------------------|-------------|-------------|---------------------------|
| 08 | 15.889 | 2.149 | 10 |
| 09 | 6.927 | 3.094 | 11 |
| 11 | 4.411 | 3.296 | 12 |
| 13 | 3.659 | 3.317 | 13 |
| 15 | 3.427 | 3.321 | 14 |
| 16 | 3.355 | 3.322 | 15 |
| 19 | 3.332 | 3.322 | 16 |
| 19 | 3.325 | 3.323 | 17 |
| 26 | 3.323 | 3.322 | 18 |
| 21 | 3.323 | 3.323 | 19 |
| 25 | 3.322 | 3.322 | 20 |
| 34 | 3.322 | 3.322 | 22 |
| 34 | 3.322 | 3.315 | 24 |



(a) Limit analysis



(b) Shakedown analysis

Figure 5.20: 2D Continuous beam: Convergence of limit and shakedown load factors in comparison with those of two other methods.

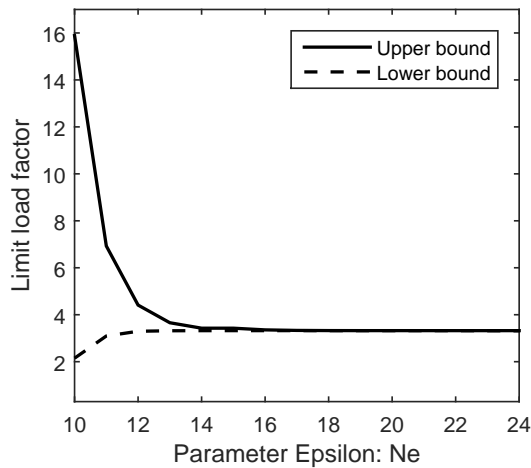
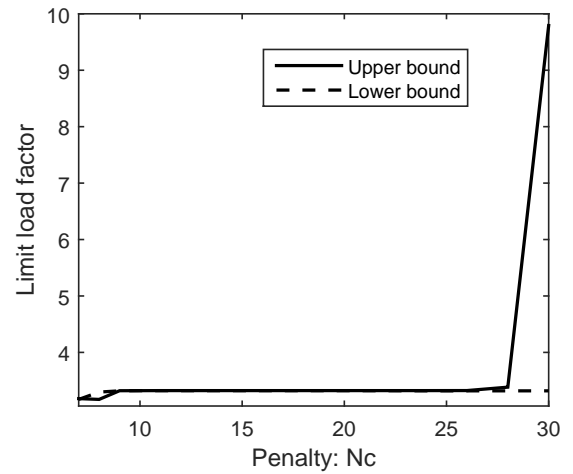
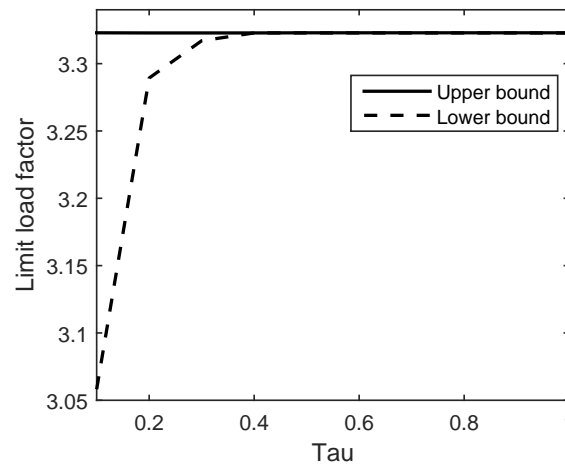
The influence of parameters ε , c and τ are investigated independently and shown in Tables (5.12, 5.13 and 5.14). The results are also shown in Fig 5.21. It is clear that the numerical results are obtained the stable when ε parameter $\varepsilon \geq 10^{-7}$, penalty parameter $c \in [10^9, 10^{26}]$ and $\tau \geq 0.3$.

Table 5.13: Influence of parameter c , ($\varepsilon = 10^{-10}$ and $\tau = 0.9$).

| Total Iterations | Upper bound | Lower bound | $c = 10^{NC}$ |
|------------------|-------------|-------------|---------------|
| 5 | 3.181 | 3.167 | 7 |
| 11 | 3.167 | 3.297 | 8 |
| 19 | 3.321 | 3.319 | 9 |
| 25 | 3.322 | 3.322 | 10 |
| 25 | 3.323 | 3.322 | 11 |
| 25 | 3.323 | 3.322 | 12 |
| 27 | 3.323 | 3.322 | 14 |
| 26 | 3.323 | 3.322 | 16 |
| 34 | 3.323 | 3.322 | 18 |
| 34 | 3.323 | 3.322 | 20 |
| 29 | 3.323 | 3.321 | 22 |
| 34 | 3.323 | 3.319 | 24 |
| 25 | 3.3238 | 3.3184 | 26 |
| 34 | 3.3840 | 3.3187 | 28 |
| 34 | 9.7917 | 3.3187 | 30 |

Table 5.14: Influence of parameter τ , ($\varepsilon = 10^{-10}$ and $c = 10^{10}$)

| Total Iterations | Upper bound | Lower bound | τ |
|------------------|-------------|-------------|--------|
| 34 | 3.3229 | 3.0582 | 0.1 |
| 34 | 3.3228 | 3.2893 | 0.2 |
| 34 | 3.3228 | 3.2170 | 0.3 |
| 34 | 3.3228 | 3.3228 | 0.4 |
| 32 | 3.3229 | 3.3228 | 0.5 |
| 28 | 3.3229 | 3.3228 | 0.6 |
| 26 | 3.3229 | 3.3228 | 0.7 |
| 28 | 3.3229 | 3.3228 | 0.8 |
| 25 | 3.3229 | 3.3228 | 0.9 |
| 24 | 3.3229 | 3.3227 | 1.0 |

(a) $\varepsilon^2 = 10^{-Ne}$, ($c = 10^{10}$ and $\tau = 0.9$)(b) $c = 10^{Nc}$, ($\varepsilon = 10^{-10}$ and $\tau = 0.9$)(c) τ , ($\varepsilon = 10^{-10}$ and $c = 10^{10}$)**Figure 5.21:** Influence parameter of ε , c and τ

5.3.3 Thin-walled pipe subjected to internal pressure and axial force

The last problem is a thin-walled pipe with radius R and thickness t considered in Fig 5.22. The pipe is subjected to axial force F together with internal pressure p . Cocks and Leckie [113] studied the problem analytically, using the Tresca yield criterion and Yan [93] using the Von Mises yield criterion.

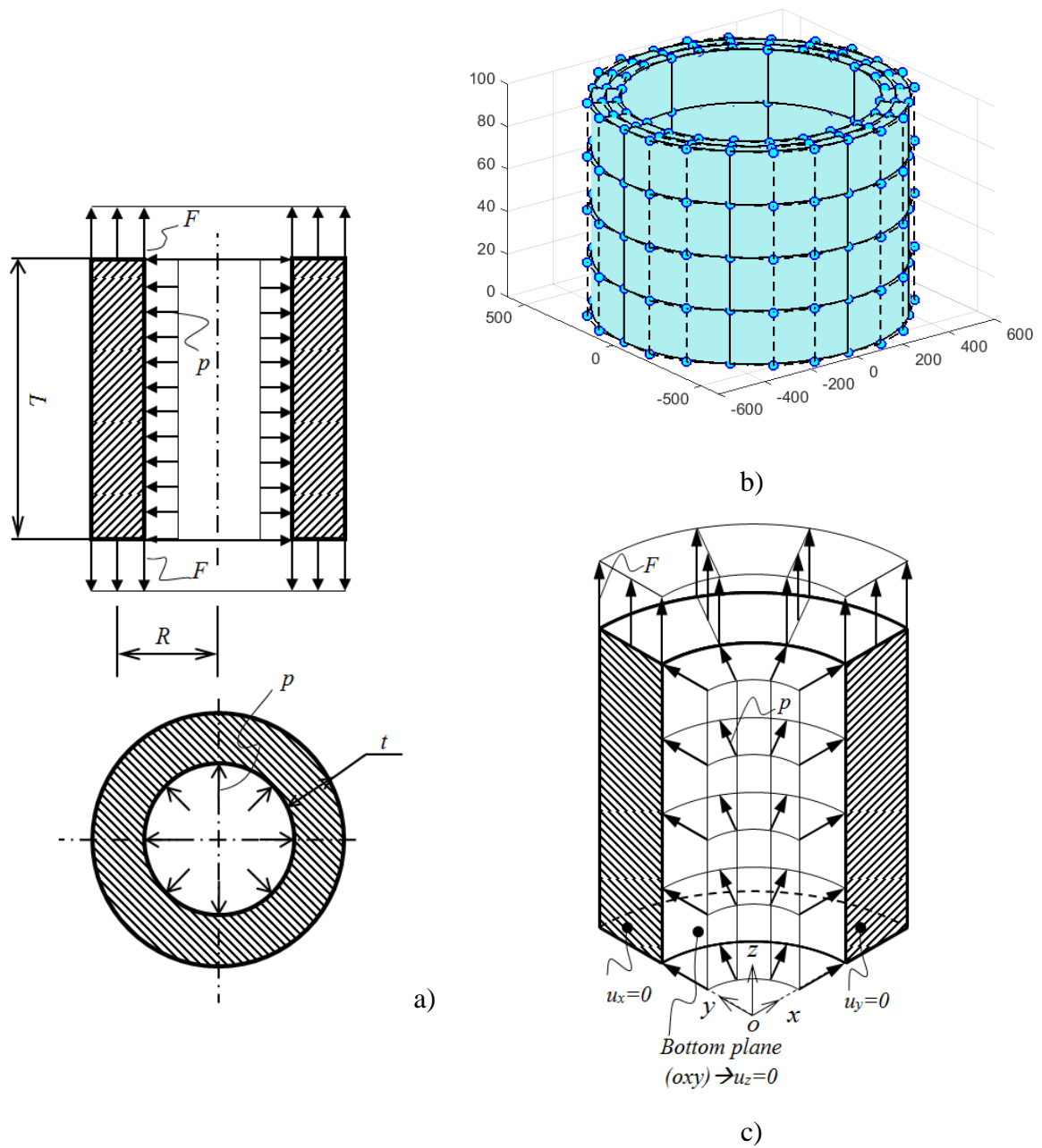


Figure 5.22: A thin-walled pipe subjected to internal pressure and axial force: a) Full model subjected to internal pressure and axial uniform loads; b) Cubic mesh and control net; c) a quarter of the model with symmetric conditions imposed on the oxz , oyz and oxy surface.

The plastic collapse limit can be calculated by using the condition in Ref [93] if internal pressure and axial force increase monotonically and proportionally as follows:

$$\frac{p^2}{p_l^2} + \frac{F^2}{F_l^2} - \frac{p}{p_l} \frac{F}{F_l} = 1 \quad (5.2)$$

where $p_l = \beta \frac{\sigma_0 t}{R}$, $F = \sigma_0$ with $\beta = 1$ for a long pipe without the end constraining effect. In case that internal pressure remains constant, and axial force varies within the range $[-F, F]$, we can compute the shakedown limit by using the following condition:

$$\frac{p^2}{p_l^2} + \frac{F^2}{F_l^2} + \frac{p}{p_l} \frac{F}{F_l} = 1 \quad (5.3)$$

Note that we could have Eq. 5.2 and 5.3 by using the Von Mises yield criterion (Yan [93]). If we use the Tresca yield criterion, the shakedown range is limited by the condition (Cocks and Leckie [113]):

$$\frac{p}{p_l} = 1 - \frac{F}{F_l} \quad (5.4)$$

Due to their symmetry, only the quadrant of the whole pipe is discretized by 3D NURBS elements with quadratic, cubic and quartic mesh. The given data for this problem: $R = 500mm, t = 10mm, L = 100mm, \sigma_0 = 116.2MPa$.

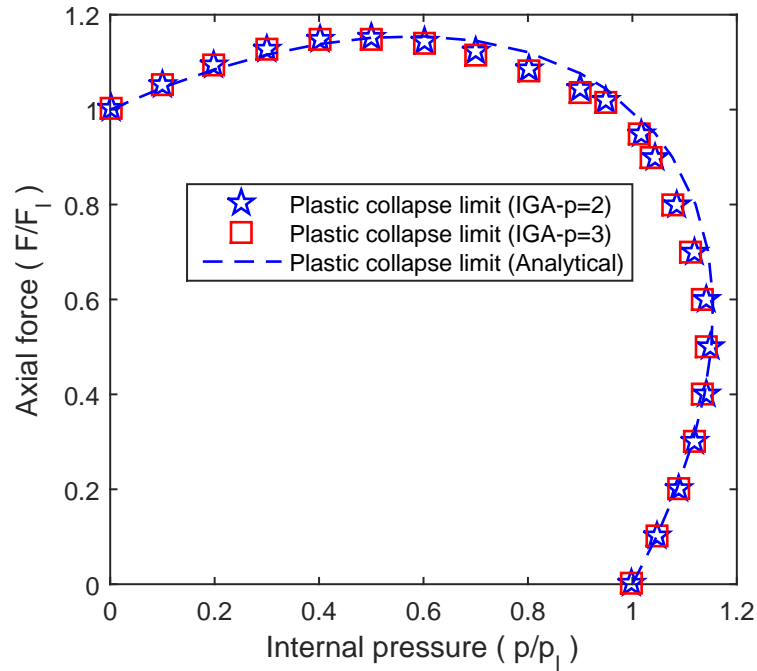


Figure 5.23: The limit load domain of the IGA compared with exact solution for thin-walled pipe problem.

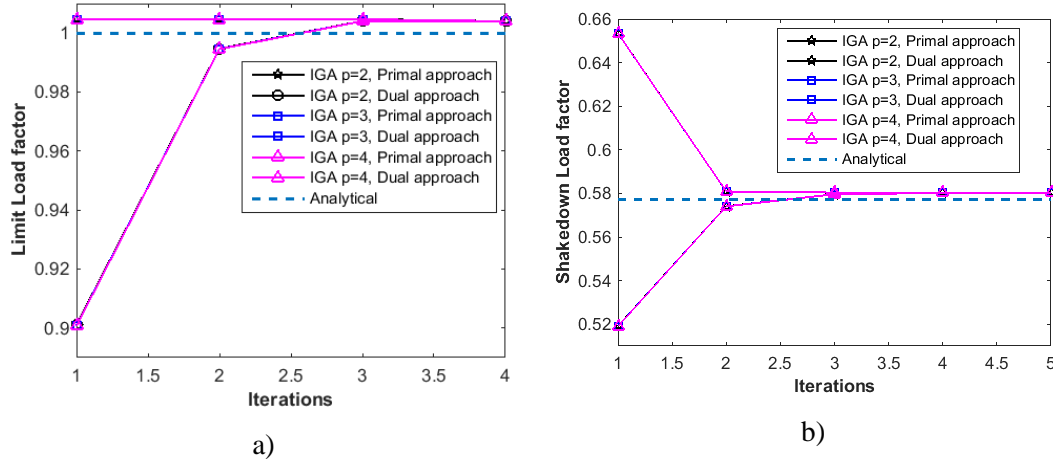
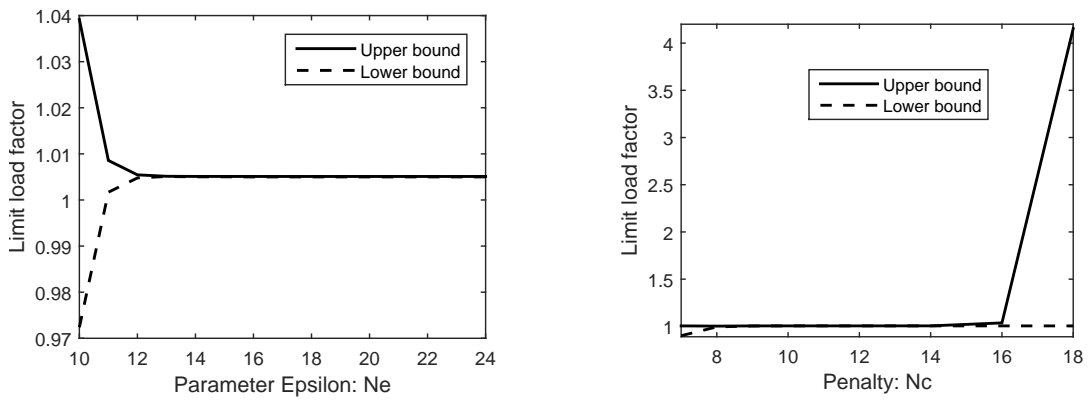
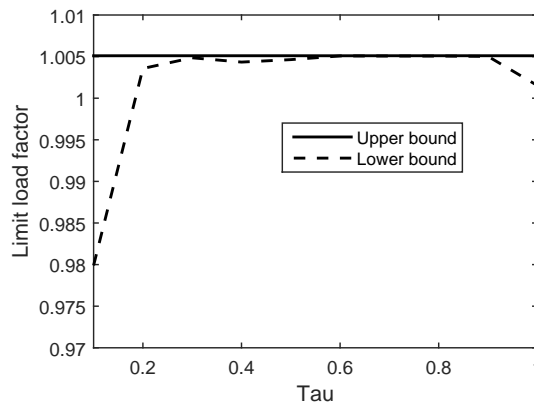


Figure 5.24: The limit load domain of the IGA compared with exact solution for thin-walled pipe problem: a) Limit Analysis; b) Shakedown analysis.



(a) $\varepsilon^2 = 10^{-Ne}$, ($c = 10^{10}$ and $\tau = 0.9$)

(b) $c = 10^{Nc}$, ($\varepsilon = 10^{-10}$ and $\tau = 0.9$)



(c) τ , ($\varepsilon = 10^{-10}$ and $c = 10^{10}$)

Figure 5.25: Influence parameter of ε , c and τ

The interaction diagram for limit analysis is plotted in Fig 5.23. In this diagram, collapse limit load factors are the averages of the upper and lower bounds. Analytical solutions are calculated by applying the formulation from Eq. 5.2. The diagram shows that numerical solutions agree very well with analytical solutions. The computational results for limit and shakedown analyses are present in Fig 5.24. In the limit analysis case, the upper bound of the limit load factor is $\alpha^+ = 0.9978$ while the lower bound is $\alpha^- = 0.99899$ compared with analytical factor $\alpha = 1.0$ obtained by Eq. 5.2. In the shakedown analysis case, the upper bound of the shakedown gives $\alpha^+ = 0.58026$, the lower bound gives $\alpha^- = 0.580258$ compared with analytical load factor $\alpha = 0.57735$ by using the formula from Eq. 5.3. In both case, the numerical errors are less than 1%. The upper bound and lower bound values converge rapidly to solution.

Algorithm gives the stable results when $\varepsilon \geq 10^{-7}$, $c \in [10^9 \div 10^{16}]$ and $0.2 \leq \tau \leq 0.9$. The influence of these parameters are shown in Fig 5.25.

5.4 Limit and shakedown analysis of pressure vessel components

5.4.1 Pressure vessel support skirt

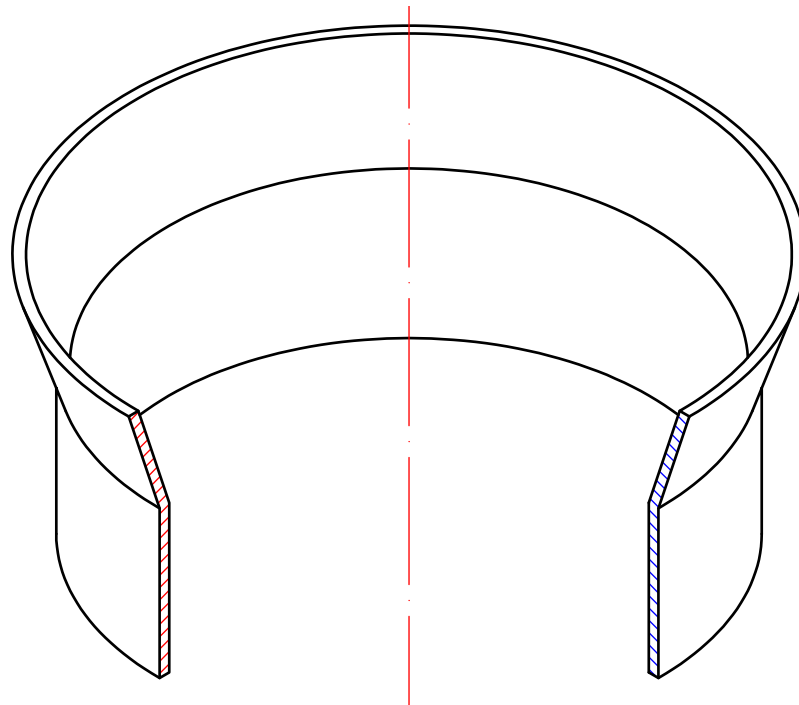
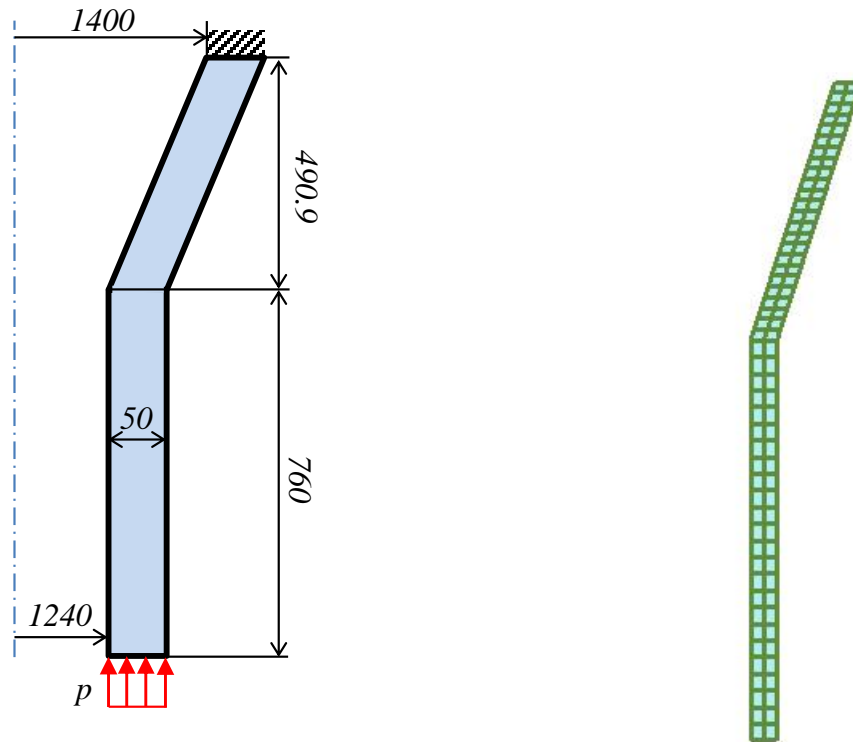


Figure 5.26: The pressure vessel skirt: Three quarter of full 3D model.

This problem is interested in pressure vessel and piping engineering technology since it serves as a benchmark problem for developing stress classification procedures [114]. This problem is investigated by Seshadri *et al.* [115] and Simha *et al.* [116].



(a) Axisymmetric model with boundary condition and applied load

(b) NURBS mesh with 96 elements

Figure 5.27: Axisymmetric model of the pressure vessel skirt

The geometry of this problem is displayed in Fig 5.26 and 5.27(a). Following the material properties utilized in [116], the material properties are used in our analysis: Young's modulus $E = 211$ GPa, Poisson's ratio $\nu = 0.3$ and yield stress $\sigma_y = 250$ MPa. The applied load is $p = 77.3$ MPa as shown in Fig 5.27 (a). The IGA mesh is discretized by multi-patch of NURBS with polynomial order $p = 2$ to 4 using 4704 NURBS elements with 10848 DOF, 1944 NURBS elements with 5304 DOF and 1176 NURBS elements with 3850 DOF, respectively. The IGA mesh for order $p = 2$ using 64 NURBS elements is illustrated in Fig 5.27 (b).

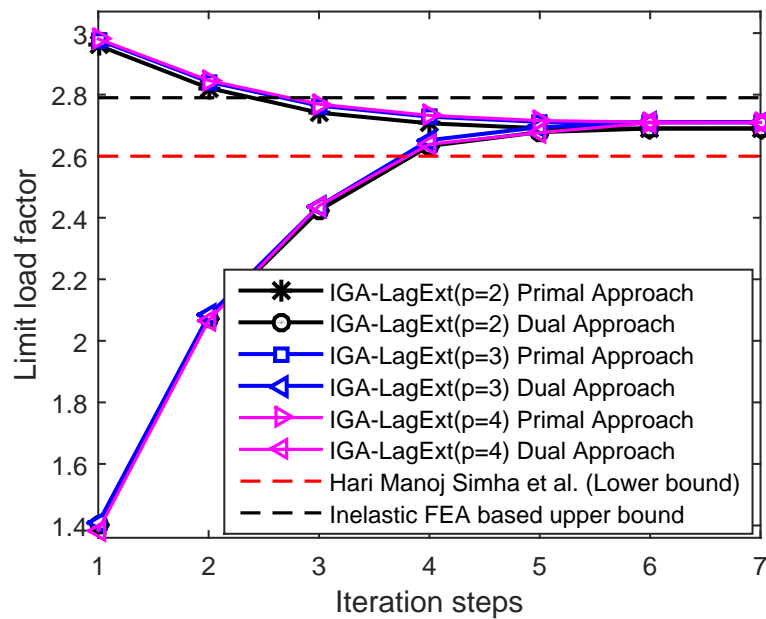


Figure 5.28: Limit analysis: Convergence of limit load factors for the pressure vessel skirt.

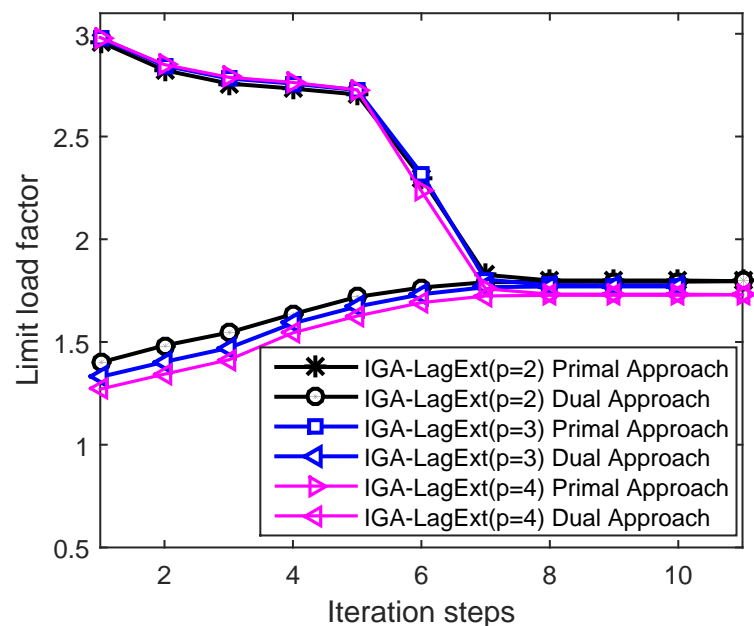
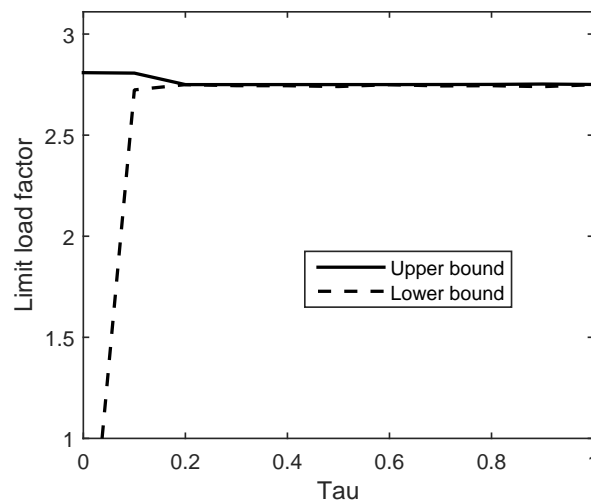
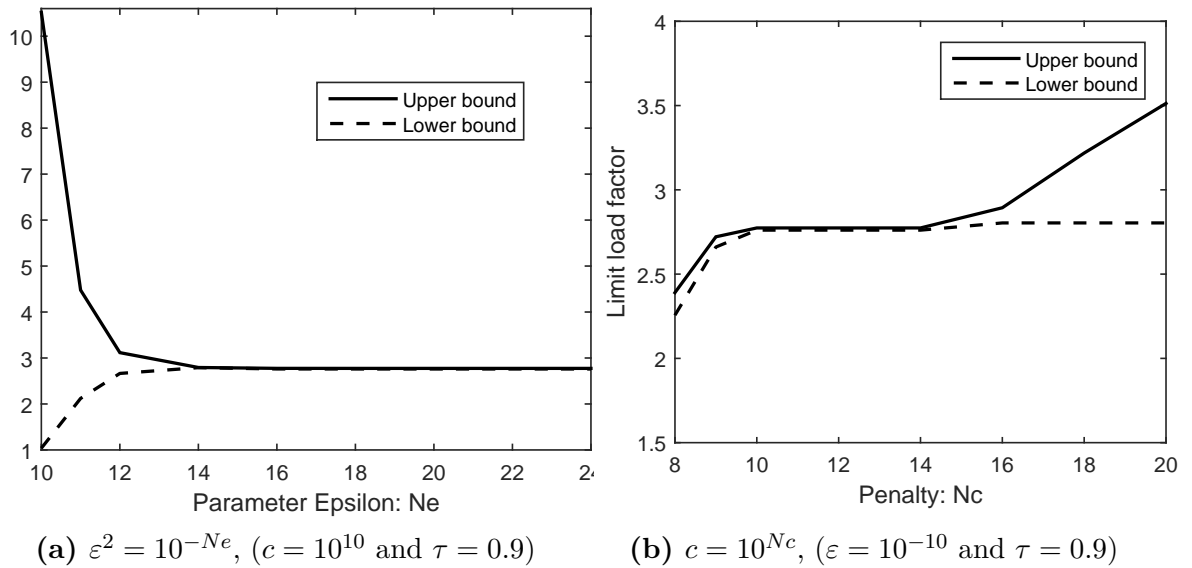


Figure 5.29: Shakedown analysis: Convergence of shakedown load factors for the pressure vessel skirt.

The results for both limit and shakedown analysis are presented in Table 5.15 together with the limit analysis results investigated by Simha *et al.* in Ref [116]. It

can be clearly seen that the current results for limit analysis case are in very good agreement with the limit load factors obtained by Simha *et al* [116]. Fig 5.28 shows the limit collapse multipliers and compared with the other methods. The convergence of the shakedown load factors is shown in Fig 5.29.

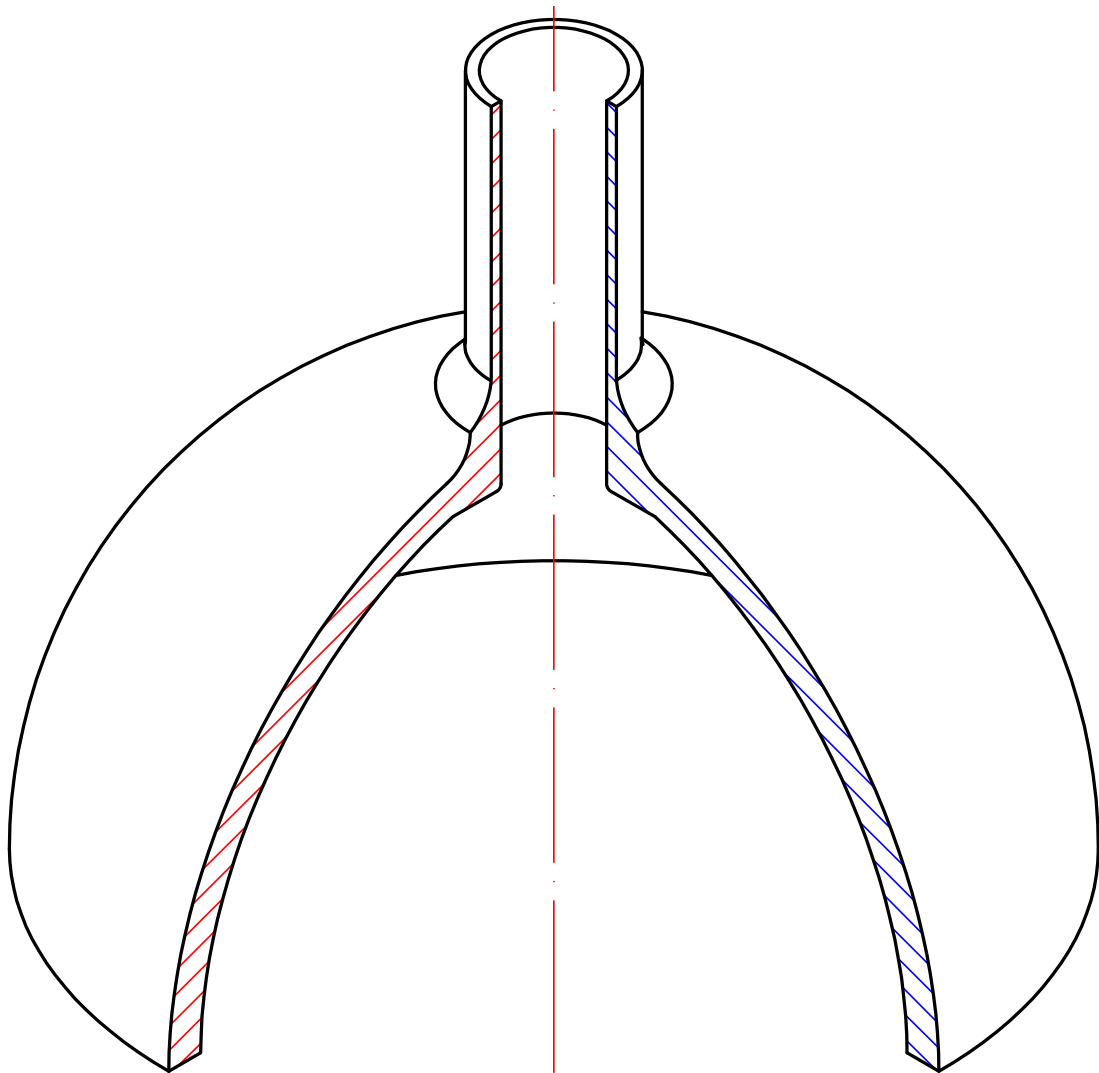


(c) τ , ($\epsilon = 10^{-10}$ and $c = 10^{10}$)

Figure 5.30: Influence parameter of ϵ , c and τ

Table 5.15: Collapse multiplier for the vessel pressure skirt: Comparison of limit load multipliers for different approaches

| Author | Method | LA | SA |
|---------------------------|---|-------|-------|
| | Lower bound | 2.600 | - - - |
| Simha <i>et al.</i> [116] | Inelastic FEM-Upper bound | 2.790 | - - - |
| | $p = 2, ndofs = 10848$ IGA-LagExt, Dual algorithm | 2.690 | 1.796 |
| | $p = 3, ndofs = 5304$ IGA-LagExt, Dual algorithm | 2.703 | 1.773 |
| IGA-LagExt | $p = 4, ndofs = 3850$ IGA-LagExt, Dual algorithm | 2.709 | 1.730 |

**Figure 5.31:** The reinforced nozzle model and geometry: Three quarter of full 3D model.

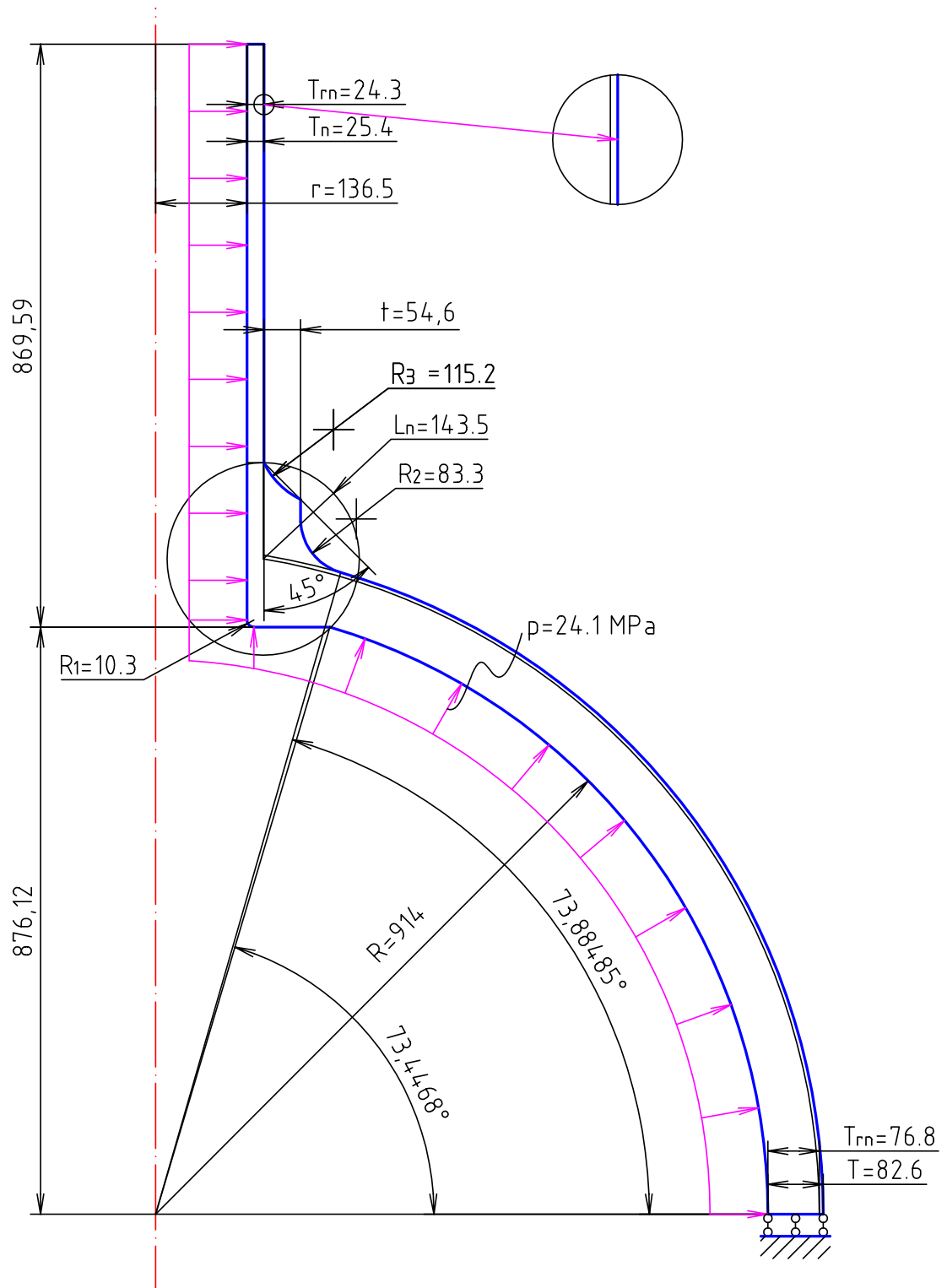


Figure 5.32: The reinforced nozzle model and geometry: Geometry of the axisymmetric model [117; 118]

5.4.2 Reinforced Axisymmetric Nozzle

Reinforced axisymmetric nozzle is an example of a well-designed pressure component with smooth geometric transitions. This problem is studied for limit analysis by Seshadri *et al.* [117] using m_α -tangent method and Mahmood *et al.* [118] using the m_α -tangent multiplier in conjunction with elastic modulus adjustment procedure. The 3D model is illustrated in Fig 5.31. A reinforced axisymmetric cylindrical nozzle on a hemispherical head as shown in Fig 5.32, which is subjected to an internal pressure of $p = 24.1$ MPa is analyzed here.

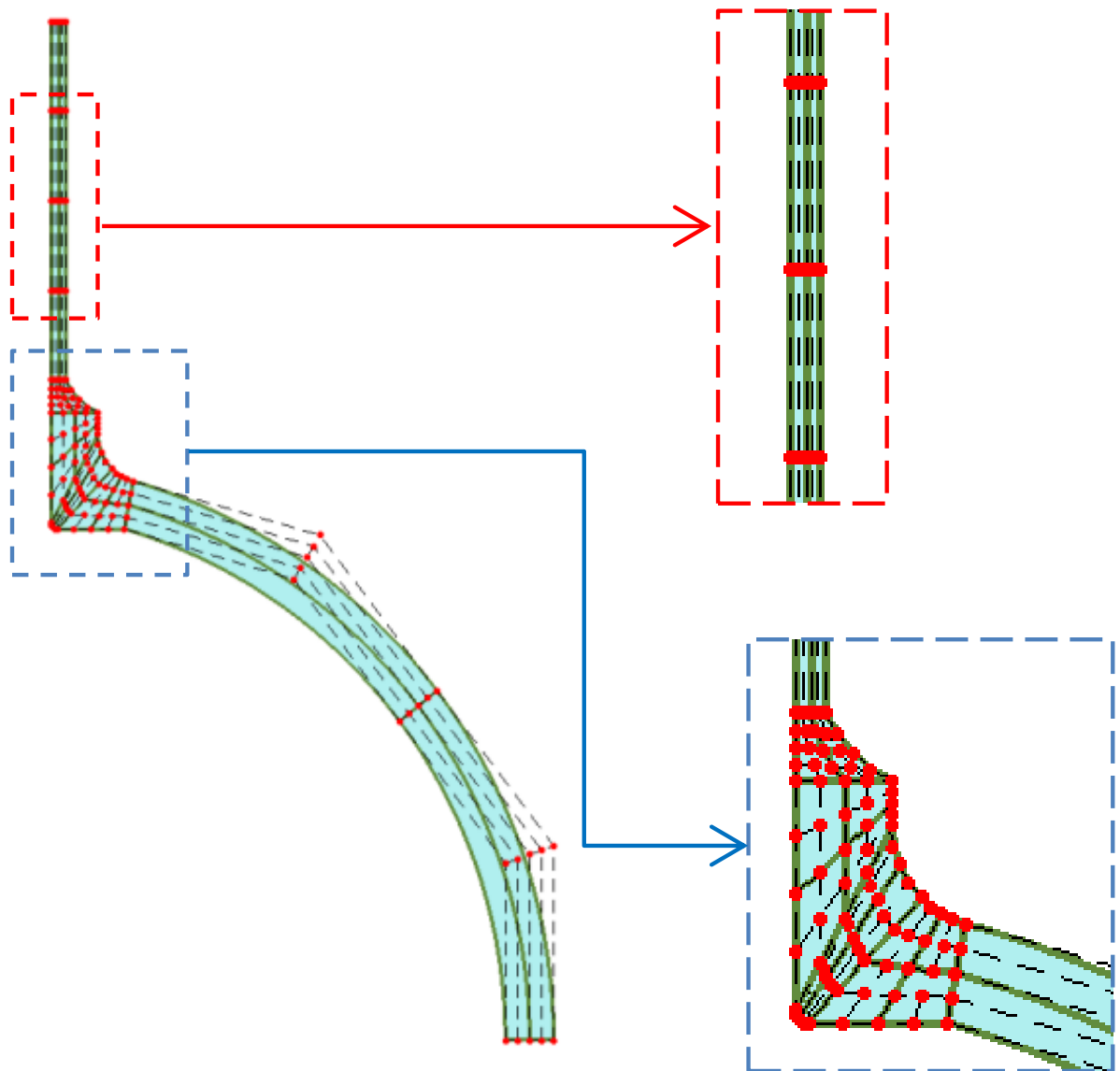


Figure 5.33: The NURBS mesh of the reinforced axisymmetric nozzle

The detail of dimensions can be listed as: the inner radius of the head $R = 914.4$ mm; the nominal wall thickness $T = 82.6$ mm; Inside radius of the nozzle $r = 136.5$ mm; the nominal wall thickness $T_n = 25.4$ mm; the required minimum wall thickness of the head $T_{rn} = 76.8$ mm and of the nozzle $T_{rn} = 24.3$ mm, respectively. The geometric transitions of the reinforcement are modeled with fillet radius, $R_1 = 10.3$ mm, $R_2 = 83.3$ mm and $R_3 = 115.2$ mm. Other dimensions include reinforcement thickness $t = 54.6$ mm and the angle of reinforcement, $\theta = 45^\circ$. The reinforcement is bounded by the reinforcement-zone boundary, specified by circle of radius $L_n = 143.5$ mm. The modulus of elasticity is specified as 262 GPa, and the yield strength is assumed to be 262 MPa. The geometry is modeled using NURBS elements with axisymmetric consideration.

Table 5.16: Collapse multiplier for the reinforced axisymmetric nozzle: Comparison of limit load multipliers for different approaches

| Author | Method | LA | SA |
|------------------------------|---------------------------------|----------------------------|-------------|
| Mahmood <i>et al.</i> [118] | m_α tangent, Upper bound | 1.850 | - - - |
| | Inelastic FEM, Upper bound | 1.874 | - - - |
| Seshadri <i>et al.</i> [117] | m_α tangent, Lower bound | 1.605 | - - - |
| | m_α tangent, Upper bound | 1.891 | - - - |
| | Inelastic FEM-Upper bound | 1.874 | - - - |
| IGA-LagExt | $p = 2, ndofs = 4620$ | IGA-LagExt, Dual algorithm | 1.785 0.669 |
| | $p = 3, ndofs = 4100$ | IGA-LagExt, Dual algorithm | 1.769 0.659 |
| | $p = 4, ndofs = 3376$ | IGA-LagExt, Dual algorithm | 1.707 0.567 |

The IGA mesh is discretized by multi-patch of NURBS with polynomial order $p = 2$ to 4 using 1792 NURBS elements with 4620 DOF, 1344 NURBS elements with 4100 DOF and 768 NURBS elements with 3376 DOF, respectively. The NURBS mesh and control net for order $p = 2$ are illustrated in Fig. 5.33. The results for both limit and shakedown analysis are summarized in Table 5.16 and also listed some other methods such as inelastic finite element analysis is performed, which gives a limit load multiplier of $\alpha_{NFEA} = 1.874$. The convergence of the limit load factors is shown in Fig 5.34 and shakedown load factors is demonstrated in Fig 5.35.

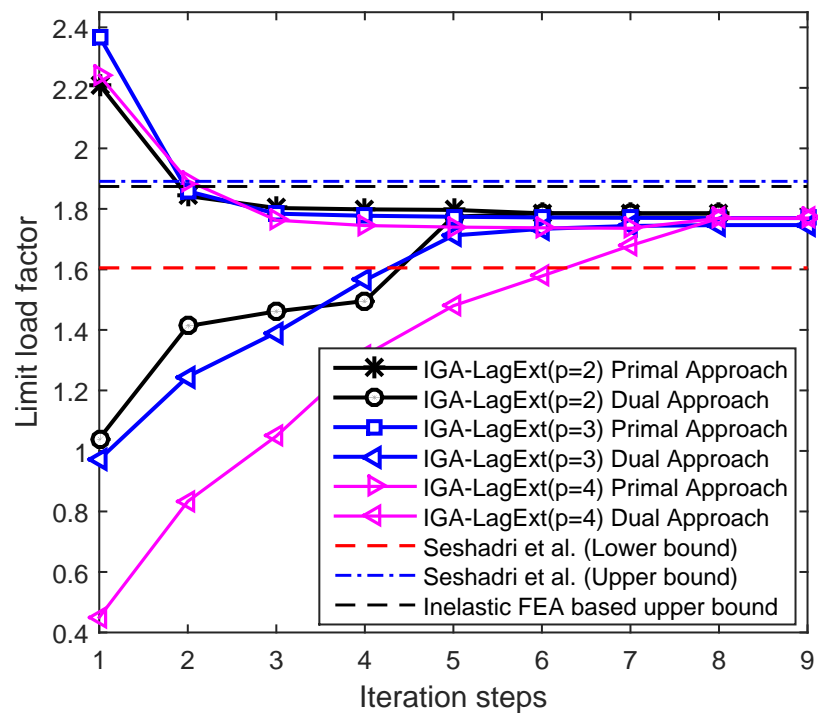


Figure 5.34: Convergence of limit load factors for the reinforced axisymmetric nozzle.

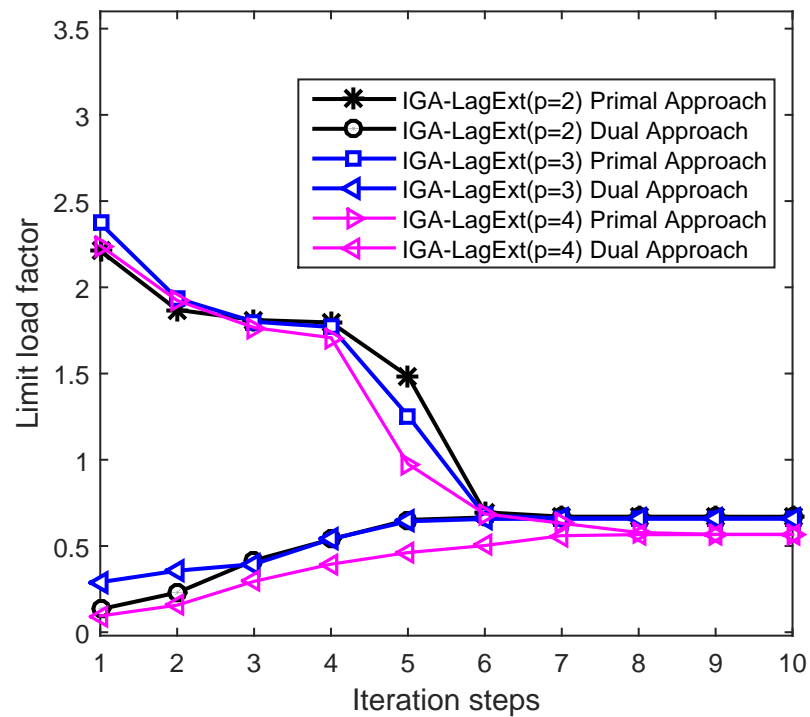
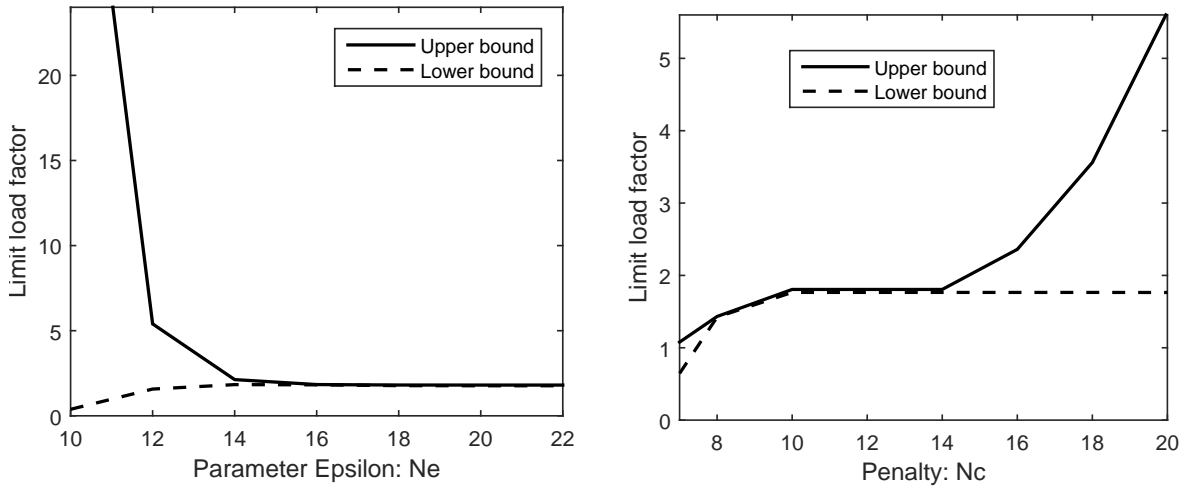
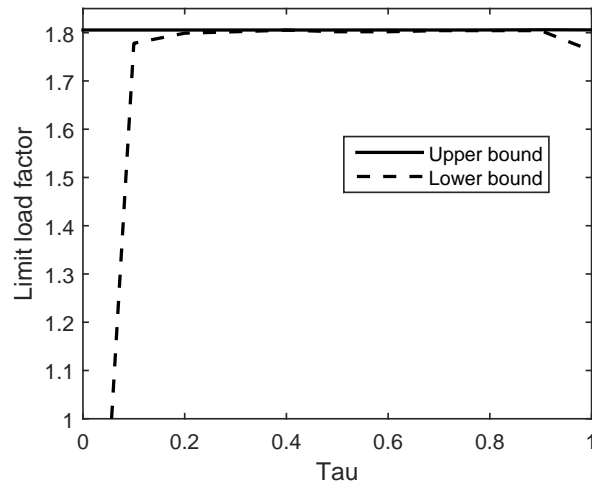


Figure 5.35: Convergence of shakedown load factors for the reinforced axisymmetric nozzle.

(a) $\varepsilon^2 = 10^{-Ne}$, ($c = 10^{10}$ and $\tau = 0.9$)(b) $c = 10^{Nc}$, ($\varepsilon = 10^{-10}$ and $\tau = 0.9$)(c) τ , ($\varepsilon = 10^{-10}$ and $c = 10^{10}$)**Figure 5.36:** Influence parameter of ε , c and τ

The numerical results shown in Fig (5.36) are obtained by independently studying the influences of optimization parameters (ε , c and τ). It is clear that:

- The parameter ε has very little influence on the computational results in the range of $\varepsilon = 10^{-7} \div 10^{-12}$. The errors of the lower and upper limit load factors are less than 1% (all results are found by using parameters $c = 10^{10}$ and $\tau = 0.9$).
- The penalty parameter $c \in [10^9 \div 10^{14}]$, number error is less than 1% for both upper bound and lower bound shown in Fig. 5.6(b).

- The parameter τ in the range of $\tau \in [0.2 \div 0.9]$ has no influence of lower and upper limit load factor. The larger τ value, the faster convergence of algorithm.

5.5 Limit analysis of crack structures

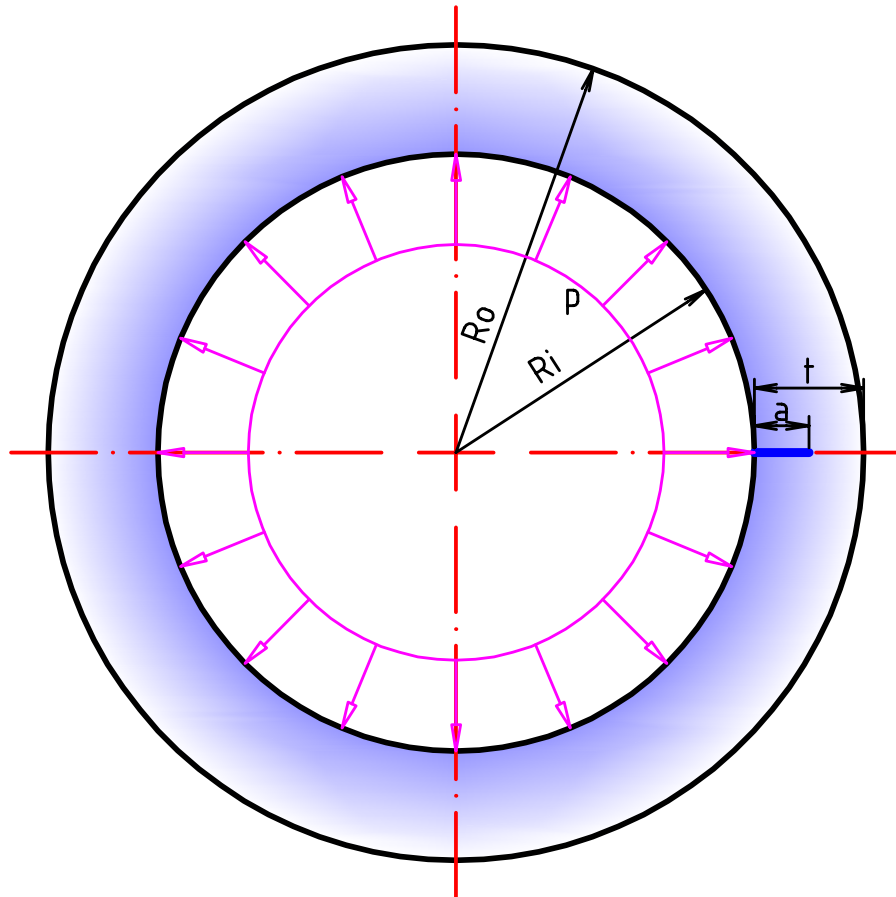


Figure 5.37: Full geometrical and dimensional model

Pressure vessel which is designed to hold liquids or gases contains various parts such as thin walled vessels, thick walled cylinders, nozzle, head, nozzle head, skirt support and so on. Two types of defects, axial and circumferential cracks, are commonly found in pressure vessel and piping. The limit analyses of the pressure vessel components were successfully studied by many researchers such as Zhang *et al.* [37], Abou *et al.* [119], Ngo *et al.* [120], Staat *et al.* [121], Simha *et al.* [116], Mohmood *et al.* [118], Seshadri *et al.* [115; 117] and so on. The limit load of structures with cracks is also important parameters on one hand for fracture safety evaluation of structural failure [35; 44; 122], and on the other hand for direct estimation of fracture toughness [98]. This topic can be found in many studies [55; 98; 123–128].

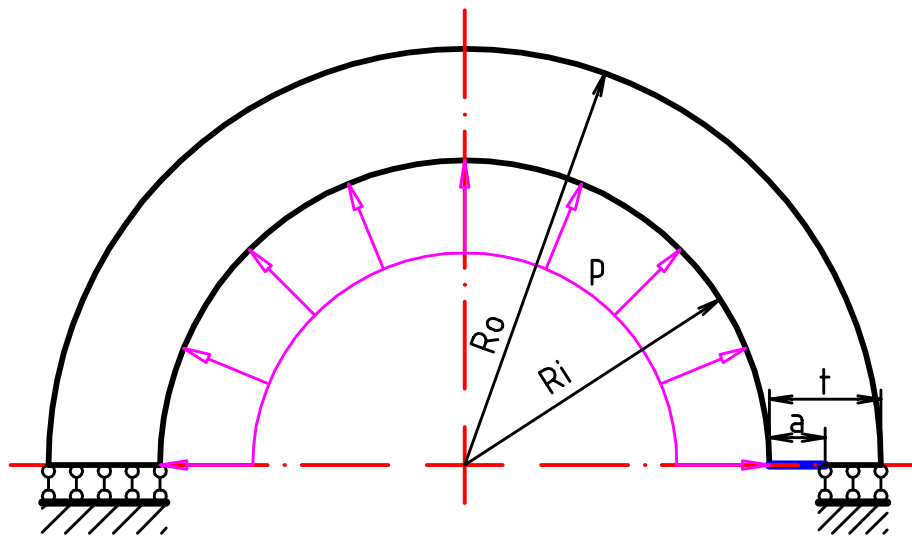


Figure 5.38: The half model of the cylinder with longitudinal crack subjected to internal pressure

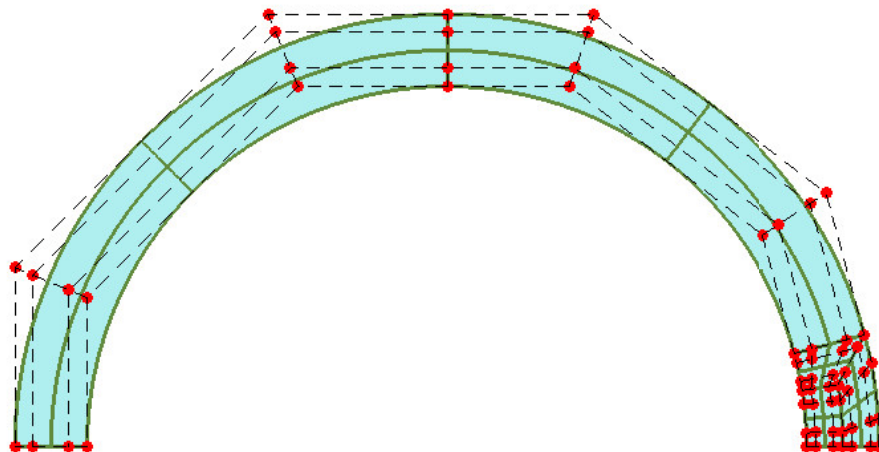


Figure 5.39: NURBS mesh of the half model for the cylinder subjected to internal pressure with a longitudinal crack

In this section, we present a cracked cylinder subjected to internal pressure. The geometrical and dimensional model are displayed in Fig 5.37. Due to symmetry, only a half of the model is considered in our numerical analysis as shown in Fig 5.38. Three cases are considered with different crack length a included: $a = 0.25t$, $a = 0.5t$ and $a = 0.75t$, respectively. Fig 5.39 shows an example of NURBS mesh. The analytical solutions of this problem are investigated by Chell [124], Miller [123] and Yan *et al.* [98]. The numerical solutions of this problem are also studied by Yan *et al.* [98] using

Q8 elements, Kim *et al.* [129] and, more recently, Nguyen-Xuan *et al.* [79]. The approximately available solutions in literature are summarized as:

- Chell's analytical solution [124].

$$\alpha = \frac{t - a}{(R_i + a) \ln \left(\frac{R_0}{R_i} \right)} \quad (5.5)$$

- Miller's lower bound analytical solution [123].

$$\alpha = \ln \left(\frac{R_0}{R_i + a} \right) / \ln \left(\frac{R_0}{R_i} \right) \quad (5.6)$$

- Yan *et al.* analytical solution [98].

$$\alpha = \frac{R_0^2 - (R_i + a)^2}{2R_0R_i \ln \frac{R_0}{R_i}} \quad (5.7)$$

- Yan *et al.* numerical solution [98].

$$\alpha = 1 - 0.7716 \left(\frac{a}{t} \right) - 0.2267 \left(\frac{a}{t} \right)^2 \quad (5.8)$$

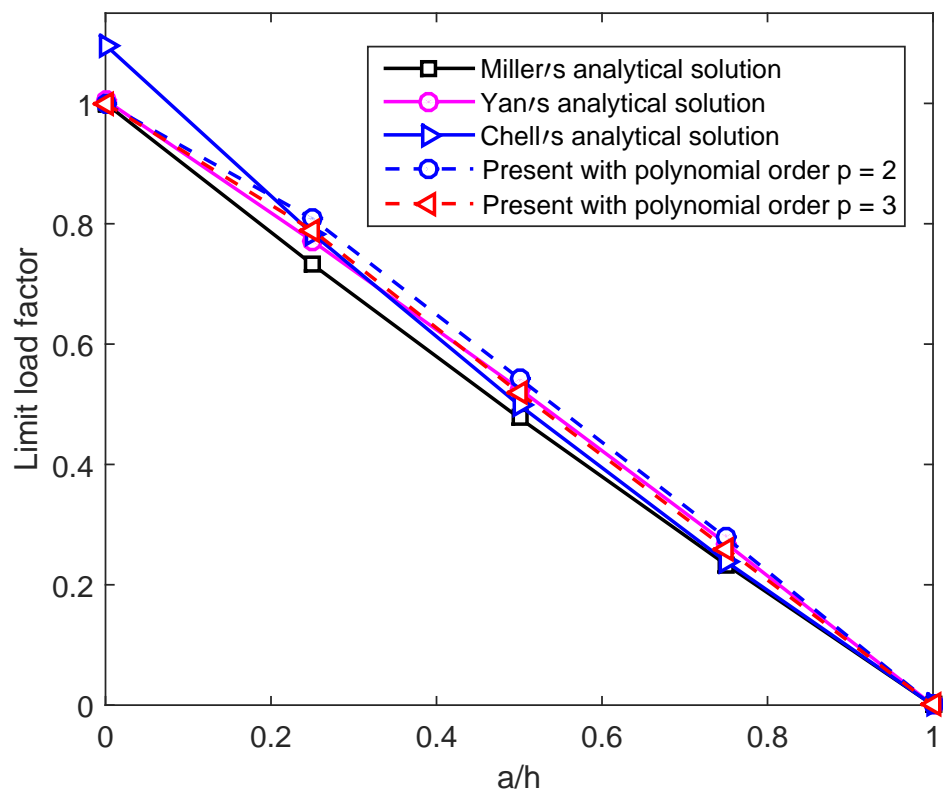
- Kim *et al.* numerical solution [129].

$$\alpha = \frac{2t \left(1 - 0.356 \left(\frac{a}{t} \right) - 1.6882 \left(\frac{a}{t} \right)^2 + 1.0442 \left(\frac{a}{t} \right)^3 \right)}{(R_i + a) \ln \frac{R_0}{R_i}} \quad (5.9)$$

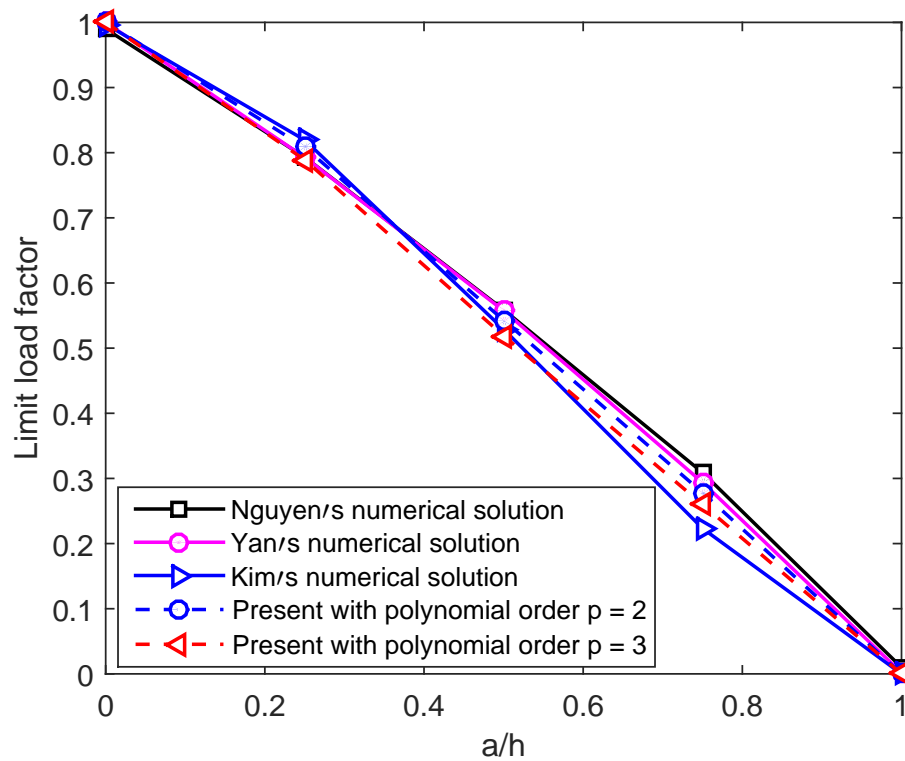
Table 5.17: Collapse multiplier for the cracked cylinder subjected to internal pressure: Comparison of limit load multipliers for different approaches

| Authors | Methods | Limit load factor |
|-----------------------------------|-----------------------|-------------------|
| $a = 0.25t$ | | |
| IGA-LagExt | $p = 2, ndofs = 5474$ | 0.8083 |
| | $p = 3, ndofs = 4304$ | 0.7890 |
| Yan <i>et al.</i> [98] | Numerical | 0.7929 |
| Kim <i>et al.</i> [129] | | 0.8195 |
| H. Nguyen-Xuan <i>et al.</i> [79] | | 0.7932 |
| Miller [123] | Analytical | 0.7324 |
| $a = 0.5t$ | | |
| IGA-LagExt | $p = 2, ndofs = 5474$ | 0.5429 |
| | $p = 3, ndofs = 4304$ | 0.5189 |
| Yan <i>et al.</i> [98] | Numerical | 0.5575 |
| Kim <i>et al.</i> [129] | | 0.5290 |
| H. Nguyen-Xuan <i>et al.</i> [79] | | 0.5589 |
| Miller [123] | Analytical | 0.4772 |
| $a = 0.75t$ | | |
| IGA-LagExt | $p = 2, ndofs = 5474$ | 0.2781 |
| | $p = 3, ndofs = 4304$ | 0.2599 |
| Yan <i>et al.</i> [98] | Numerical | 0.2938 |
| Kim <i>et al.</i> [129] | | 0.2233 |
| H. Nguyen-Xuan <i>et al.</i> [79] | | 0.3089 |
| Miller [123] | Analytical | 0.2334 |

The results are listed in Table 5.17. The limit load factors are compared with analytically approximate and numerical solution as shown in Fig5.40. It is obviously observed from Table and Figures that the present results are good agreement with other available solutions.



(a) Present collapse multiplier compared with the analytical solutions



(b) Present collapse multiplier compared with the numerical solutions

Figure 5.40: Limit load factors of the cylinder with a longitudinal crack under internal pressure

6

CONCLUSIONS AND FURTHER STUDIES

6.1 Conclusions

The aims of this research, which are (i) to develop the isogeometric finite element method, which have been developed in recent years to contribute a new procedure in the field of computation of limit and shakedown analysis, and (ii) to increase the efficiency of solving large size problems efficiently, have successfully achieved through the development of a number of procedures presented in this thesis. The main contributions in this thesis can be outlined as follows:

- Investigation of the isogeometric analysis based on Bézier extraction which can integrate IGA into the existing FEM codes in combination with primal-dual algorithm in computation of limit and shakedown load factors.
- Investigation of the Lagrange extraction which can direct link between IGA and the standard nodal finite element formulation in combination with primal-dual algorithm in computation of limit and shakedown load factors.
- A novel numerical approach for evaluating limit and shakedown load factors of pressure vessel components.
- By using the primal-dual algorithm, the problem size is reduced to the size of the linear elastic analysis. Thus, it can be more readily applied in practical engineering. Moreover, the actual Newton directions updated at each iteration automatically ensures the kinematical conditions of the displacements.

- Numerical results demonstrate high accuracy of present method with moderate number of degrees of freedom.
- The present approach showed some advantages of the IGA in terms of flexibility in refinement, exact geometry and connection the smooth spline basis to the C^0 Lagrange polynomials basis that lead the more accurate solutions in comparison with other numerical available ones.
- The method is not susceptible to the volumetric locking since the kinematical conditions are automatically ensured by using Newton directions updated every iteration.
- The present approach allows us determinate simultaneously both upper and lower bounds of the actual load value. It means that this approach can provide an accurate and effective tool to estimate the limit load in terms of solution accuracy and computational cost.
- The results obtained in this study show a good agreement with the reference solutions and compared very well with other available ones.

In summary, the combination of the IGA and the primal-dual algorithm results in an effective and robust numerical tools for limit and shakedown analysis in practical engineering problems with lesser computational cost.

6.2 Limitations and Further studies

Although IGA has been successfully applied in a wide variety of applications, the method has some drawbacks with respect to FEM. The first drawbacks is the difficulty of the implementation of adaptive IGA mesh refinement due to a tensor-product structure. Mesh refinement in IGA has global effects, which include an unwanted ripples on the surface, a large percentage of superfluous control points, etc. The second drawback of IGA is the non-interpolatory characteristic of the basis functions, which adds a difficulty in handling essential boundary conditions. These limitation of IGA can be extended research in future.

The current study was also concerned on the performance of the present method for the computation of 2D, 3D and axisymmetric structures. However, the limitation of geometry is still simple. The complicated geometry for the limit and shakedown problem can be considered in the future research.

The method presented can be extended in many ways. The following tasks may be recommended for future research.

- Computational effect with adaptive local refinement for structures subjected to complex loads. The adaptive local refinement problem based on conforming quadtree meshes is investigated in our work [80]. This work will be extended to IGA in the future.
- Enhance computational effect with adaptive local refinement based on T-splines.
- Basic standard limit and shakedown analysis is investigated in this research. Other special effects such as hardening, geometric, temperature, etc. will be taken into account in future.

References

- [1] G. Kazinczy. Experiments with clamped beams (in hungarian). *Betonszemle* 2, 68:83–101, 1914.
- [2] Kist. N. C. Does a stress analysis based on the proportionality of force and deformation lead to a good design of steel bridges and buildings? (in dutch). *DegenInieur*, 4:743, 1917.
- [3] W. Prager and P.G.Jr. Hodge. *Theory of perfectly plastic solids*. Wiley: New York, USA, 1951.
- [4] W. Prager. *Limit Analysis: The development of a concept. Foundation of plasticity 2*(edited by Sawczuk). Noordhoff, 1972.
- [5] Martin. J. B. *Plasticity*. MIT Press, 1975.
- [6] Hodge. P. G. *Plastic analysis of structures*. Mc Graw Hill, 1959.
- [7] Hodge. P. G. The mises yield condition for rotationally symmetric shells. *Quarterly of Applied Mathematics*, 18:305–311, 1961.
- [8] Hodge. P. G. *Limit analysis of Rotationally symmetric plates and shells*. Prentice Hall, New Jersey, 1963.
- [9] Chakrabarty. *Theory of Plasticity*. Mc Graw Hill, 1988.
- [10] Lubliner .J. *Plasticity theory*. Mac Millan, 1990.
- [11] Pham DucChinh. Shakedown theory for elastic-perfectly plastic bodies revisited. *International Journal of Mechanical Sciences*, 3:1011–1027, 2003.
- [12] Pham DucChinh. Shakedown theory for elastic plastic kinematic hardening bodies. *International Journal of Plasticity*, 23:1240–1259, 2007.
- [13] Pham Duc Chinh. Reduced shakedown formulation in plane stress problems. *International Journal of Computational Methods*, 11:1343009, 2014.

-
- [14] Pham Duc Chinh. Consistent limited kinematic hardening plasticity theory and path-independent shake-down theorems. *International Journal of Mechanical Sciences*, 130:11–18, 2017.
- [15] W.T. Koiter. *General theorems for elastic plastic solids*. Proceedings of Solid Mechanics (edited by Sneddon I. N. and Hill R.) Nord-Holland, 1960.
- [16] E. Melan. Theorie statisch unbestimmter systeme aus ideal plastischem baustoff. *Sitzber. Akad. Wiss. Wien*, 145:195–218, 1960.
- [17] F.A Gaydon and A.W McCrum. A theoretical investigation of the yield point loading of a square plate with a central circular hole. *Journal of Mechanics and Physics Solids*, 2:156–169, 1951.
- [18] R Casciaro and L Cascini. A mixed formulation and mixed finite elements for limit analysis. *International Journal for Numerical Methods in Engineering*, 18:211–243, 1982.
- [19] T Belytschko and P. G Hodge. Plane stress limit analysis by finite element. *Journal of Engineering Mechanics Division*, 96:931–944, 1970.
- [20] P Zhang, M. W Lu, and K. C Hwang. A mathematical programming algorithm for limit analysis. *Acta Mechanica Sinica*, 7:267–274, 1991.
- [21] H. F Chen, Y. H Liu, Z. Z Cen, and B. Y Xu. On the solution of limit load and reference stress of 3-d structures under multi-loading systems. *Engineering Structures*, 21:530–537, 1999.
- [22] H Huh and W. H Yang. A general algorithm for limit solutions of plane stress problems. *Journal of Solids and Structures*, 28:727–738, 1991.
- [23] N Zouain, J Herskovits, L. A Borges, and R. A Feijoo. An iterative algorithm for limit analysis with nonlinear yield functions. *Journal of Solids and Structures*, 30:1397–1417, 1993.
- [24] M Heitzer and M Staat. Fem-computation of load carrying capacity of highly loaded passive components by direct methods. *Nuclear Engineering and Design*, 193(3):349–358, 1999.
- [25] K. D Andersen, E Christiansen, A. R Conn, and M. L Overton. An efficient primal-dual interior-point method for minimizing a sum of euclidean norms. *SIAM Journal of Science Computation*, 22:243–262, 2000.

-
- [26] E. D. Andersen, C. Roos, and T. Terlaky. On implementing a primal-dual interior-point method for conic quadratic programming. *Mathematical Programming*, 95:249–277, 2003.
- [27] J Pastor, T. H Thai, and P Francescato. Interior point optimization and limit analysis: an application. *Communications in Numerical Methods in Engineering*, 19:779–785, 2003.
- [28] Duc Khoi Vu, A. M Yan, and H. Nguyen-Dang. A primal-dual algorithm for shakedown analysis of structure. *Computer Methods in Applied Mechanics and Engineering*, 193:4663–4674, 2004.
- [29] Z. Zouain, L. Borges, and J. L. Silveira. An algorithm for shakedown analysis with nonlinear yield functions. *Computer Methods in Applied Mechanics and Engineering*, 191:2463, 2002.
- [30] J. C. Nagtegaal, D. M. Parks, and J. R. Rice. On numerically accurate finite element solutions in the fully plastic range. *Computer Methods in Applied Mechanics and Engineering*, 4:153–177, 1974.
- [31] J. Pastor S. Turgeman A. Bottero, R. Negre. Finite element method and limit analysis theory for soil mechanics problems. *Computer Methods in Applied Mechanics and Engineering*, 22:131–149, 1980.
- [32] A. Capsoni and L. Corradi. A finite element formulation of the rigid-plastic limit analysis problem. *International Journal for Numerical Methods in Engineering*, 40:2063–2086, 1997.
- [33] Canh V. Le, H. Nguyen-Xuan, H. Askes, Stéphane P. A. Bordas, T. Rabczuk, and H. Nguyen-Vinh. A cell-based smoothed finite element method for kinematic limit analysis. *International Journal for Numerical Methods in Engineering*, 83:1651–1674, 2010.
- [34] Mohammed Mournassi, Salim Belouettar, Éric Béchet, Stéphane P.A.Bordas, Didier Quoirin, and Michel Potier-Ferry. Finite element analysis on implicitly defined domains: An accurate representation based on arbitrary parametric surfaces. *Computer Methods in Applied Mechanics and Engineering*, 200:774–796, 2011.
- [35] G.Legrain, C.Geuzaine, J.F.Remacle, N.Moës, P.Cresta, and J.Gaudin. Numerical simulation of cad thin structures using the extended finite element method and level sets. *Finite Elements in Analysis and Design*, 77:40–58, 2013.

-
- [36] G.Legrain, N.Chevaugéon, and K.Dréau. High order x-fem and levelsets for complex microstructures: Uncoupling geometry and approximation. *Computer Methods in Applied Mechanics and Engineering*, 241:172–189, 2012.
- [37] X. F Zhang, Y. H Liu, Y. N Zhao, and Z Cen. Lower bound limit analysis by the symmetric galerkin boundary element method and the complex method. *Computer Methods in Applied Mechanics and Engineering*, 191:1967–1982, 2002.
- [38] X. F Zhang, Y. H Liu, and Z Cen. Boundary element methods for lower bound limit and shakedown analysis. *Engineering Analysis with Boundary Elements*, 28:905–917, 2004.
- [39] Y Liu, X. Z Zhang, and Z Cen. Lower bound shakedown analysis by the symmetric galerkin boundary element method. *International Journal of Plasticity*, 21:21–42, 2005.
- [40] R.N.Simpson, S.P.A.Bordas, J.Trevelyan, and T.Rabczuk. A two-dimensional isogeometric boundary element method for elastostatic analysis. *Computer Methods in Applied Mechanics and Engineering*, 209:87–100, 2014.
- [41] R.N.Simpson, S.P.A.Bordas, H.Lian, and J.Trevelyan. An isogeometric boundary element method for elastostatic analysis: 2d implementation aspects. *Computers and Structures*, 118:2–12, 2013.
- [42] M.A.Scott, R.N.Simpson, J.A.Evans, S.Lipton, S.P.A.Bordas, T.J.R.Hughes, and T.W.Sederberg. Isogeometric boundary element analysis using unstructured t-splines. *Computer Methods in Applied Mechanics and Engineering*, 254:197–221, 2013.
- [43] Haojie Lian, R.N.Simpson, and S.P.A.Bordas. Stress analysis without meshing: isogeometric boundary-element method. *Proceedings of the Institution of Civil Engineers-Engineering and Computational Mechanics*, 166:88–99, 2013.
- [44] X.Peng, E.Atroshchenko, P.Kerfriden, and S.P.A.Bordas. Isogeometric boundary element methods for three dimensional static fracture and fatigue crack growth. *Computer Methods in Applied Mechanics and Engineering*, 316:151–185, 2017.
- [45] Haojie Lian, Pierre Kerfriden, and Stéphane P. A. Bordas. Implementation of regularized isogeometric boundary element methods for gradient-based shape optimization in two-dimensional linear elasticity. *International Journal for Numerical Methods in Engineering*, 106:972–1017, 2016.

-
- [46] Haojie Lian, Pierre Kerfriden, and Stéphane P. A. Bordas. Shape optimization directly from cad: An isogeometric boundary element approach using t-splines. *Computer Methods in Applied Mechanics and Engineering*, 317:1–41, 2017.
- [47] R.N.Simpson, M.A.Scott, M.Taus, D.C.Thomas, and H.Lian. Acoustic isogeometric boundary element analysis. *Computer Methods in Applied Mechanics and Engineering*, 269:265–290, 2014.
- [48] C. V. Le, H. Askes, and M. Gilbert. A locking-free stabilized kinematic efg model for plane strain limit analysis. *Computers and Structures*, 106-107:1–8, 2012.
- [49] J. S. Chen, C. T. Wu, S. Yoon, and Y. You. A stabilized conforming nodal integration for galerkin mesh-free methods. *International Journal for Numerical Methods in Engineering*, 50:435–466, 2001.
- [50] S Chen, Y Liu, and Z Cen. Lower-bound limit analysis by using the efg method and non-linear programming. *International Journal for Numerical Methods in Engineering*, 74(3):391–4157, 2008.
- [51] C. V. Le, M Gilbert, and H Askes. Limit analysis of plates using the efg method and second-order cone programming. *International Journal for Numerical Methods in Engineering*, 78:1532–1552, 2009.
- [52] T Tran-Cong PLH Ho, Canh V Le. Limit state analysis of reinforced concrete slabs using an integrated radial basis function based mesh-free method. *Applied Mathematical Modelling*, 53:1–11, 2018.
- [53] T Tran-Cong PLH Ho, Canh V Le. Displacement and equilibrium mesh-free formulation based on integrated radial basis functions for dual yield design. *Engineering Analysis with Boundary Elements*, 71:92–100, 2016.
- [54] Hien. V. Do and H. Nguyen-Xuan. Limit and shakedown isogeometric analysis of structures based on bézier extraction. *European Journal of Mechanics - A/Solids*, 63:149–164, 2017.
- [55] H. Nguyen-Xuan, Loc V. Tran, Chien H.Thai, and Canh. V. Le. Plastic collapse analysis of cracked structures using extended isogeometric elements and second-order cone programming. *Theoretical and Applied Fracture Mechanics*, 72:13–27, 2014.

-
- [56] Chiozzi Andrea, Milani Gabriele, and Tralli Antonio. A genetic algorithm nurbs-based new approach for fast kinematic limit analysis of masonry vaults. *Computers and Structures*, 182:187–204, 2017.
- [57] Gang Xua, Bernard Mourrain, Régis Duvigneau, and André Galligo. Parameterization of computational domain in isogeometric analysis: Methods and comparison. *Computer Methods in Applied Mechanics and Engineering*, 200:2021–2031, 2011.
- [58] Gang Xua, Bernard Mourrain, Régis Duvigneau, and André Galligo. Optimal analysis-aware parameterization of computational domain in 3d isogeometric analysis. *Computer-Aided Design*, 45:812–821, 2013.
- [59] Gang Xua, Bernard Mourrain, Régis Duvigneau, and André Galligo. Analysis-suitable volume parameterization of multi-block computational domain in isogeometric applications. *Computer-Aided Design*, 45:395–404, 2013.
- [60] Elisabeth Pilgerstorfer and Bert Jüttler. Bounding the influence of domain parameterization and knot spacing on numerical stability in isogeometric analysis. *Computer Methods in Applied Mechanics and Engineering*, 268:589–613, 2014.
- [61] Elena Atroshchenko, Satyendra Tomar, Gang Xu, and Stéphane P.A. Bordas. Weakening the tight coupling between geometry and simulation in isogeometric analysis: From sub- and super-geometric analysis to geometry-independent field approximation (gift). *International Journal for Numerical Methods in Engineering*, 114:1131–1159, 2018.
- [62] Grégory Legrain. A nurbs enhanced extended finite element approach for unfitted cad analysis. *Computational Mechanics*, 52:913–929, 2013.
- [63] N.Nguyen-Thanh, H.Nguyen-Xuan, S.P.A.Bordas, and T.Rabczuk. Isogeometric analysis using polynomial splines over hierarchical t-meshes for two-dimensional elastic solids. *Computer Methods in Applied Mechanics and Engineering*, 200:1892–1908, 2011.
- [64] Dominik Schillinger, John A.Evans, Alessandro Reali, Michael A.Scott, and Thomas J.R.Hughes. Isogeometric collocation: Cost comparison with galerkin methods and extension to adaptive hierarchical nurbs discretizations. *Computer Methods in Applied Mechanics and Engineering*, 267:170–232, 2013.
- [65] Gang Xu, Ming Li, Bernard Mourrain, Timon Rabczuk, Jinlan Xu, and Stéphane P.A.Bordas. Constructing iga-suitable planar parameterization from complex cad

- boundary by domain partition and global/local optimization. *Computer Methods in Applied Mechanics and Engineering*, 328:175–200, 2018.
- [66] N.Vu-Bac, T.X.Duong, T.Lahmer, X.Zhuang, R.A.Sauer, H.S.Park, and T.Rabczuk. A nurbs-based inverse analysis for reconstruction of nonlinear deformations of thin shell structures. *Computer Methods in Applied Mechanics and Engineering*, 331:427–455, 2018.
- [67] C. Anitescu, M.N. Hossain, and T. Rabczuk. Recovery-based error estimation and adaptivity using high-order splines over hierarchical t-meshes. *Computer Methods in Applied Mechanics and Engineering*, 328:638–662, 2018.
- [68] J.W. Simon and D. Weichert. *Interior-Point Method for Lower Bound Shakedown Analysis of von Mises-Type Materials. Limit State of Materials and Structures*(Editors by Géry de Saxcé, Abdelbacet Oueslati, Eric Charkaluk and Jean-Bernard Tritsch). Springer, 2013.
- [69] Alan R.S.Ponter, Paolo. Fuschi, and Markus. Engelhardt. Limit analysis for a general class of yield conditions. *European Journal of Mechanics - A/Solids*, 19(3):401–421, 2000.
- [70] H. F. Chen, A.R.S. Ponter, and R.A Ainsworth. The linear matching method applied to the high temperature life assessment of structures, part 1. assessments involving constant residual stress fields. *International Journal of Pressure Vessels and Piping*, 83:123–135, 2006.
- [71] H. F. Chen, A.R.S. Ponter, and R.A Ainsworth. The linear matching method applied to the high temperature life assessment of structures, part 2. assessments beyond shakedown involving changing residual stress fields. *International Journal of Pressure Vessels and Piping*, 83:136–147, 2006.
- [72] D. K. Vu. *Dual Limit and Shakedown analysis of structures*. PhD Dissertation, Université de Liège, Belgium, 2001.
- [73] T. J. R Hughes., J. A. Cottrell., and Y. Bazilevs. Isogeometric analysis: Cad, finite elements, nurbs, exact geometry and mesh refinement. *Computer Methods in Applied Mechanics and Engineering*, 194:4135–4195, 2005.
- [74] J. A. Cottrell., T. J. R Hughes., and Y. Bazilevs. *Isogeometric analysis: Towards Integration of CAD and FEA*. John Wiley and Sons, 2009.

- [75] Evans J.A Borden M.J, Scott M.A and Hughes T.J.R. Isogeometric finite element data structures based on bézier extraction of nurbs. *International Journal for Numerical Methods in Engineering*, 88:126–156, 2011.
- [76] D. C. Thomas, M. A. Scott, J. A. Evans, K. Tew, and E. J. Evans. Bézier projection: a unified approach for local projection and quadrature-free refinement and coarsening of nurbs and t-splines with particular application to isogeometric design and analysis. *Computer Methods in Applied Mechanics and Engineering*, 284:55–105, 2014.
- [77] Dominik Schillinger, Praneeth K. Ruthal, and Lam H. Nguyen. Lagrange extraction and projection for nurbs basis functions: A direct link between isogeometric and standard nodal finite element formulations. *International Journal for Numerical Methods in Engineering*, 108(6):515–534, 2016.
- [78] C. Costa R. Feijoo L.A. Borges, N. Zouain. An adaptive approach to limit analysis. *International Journal of Solids and Structures*, 38:1707–1720, 2001.
- [79] H. Nguyen-Xuan, Son Nguyen-Hoang, T.Rabczuk, and K.Hackl. A polytree-based adaptive approach to limit analysis of cracked structures. *Computer Methods in Applied Mechanics and Engineering*, 313:1006–1039, 2017.
- [80] H Nguyen-Xuan and Khanh N Chau Hien. V. Do. An adaptive strategy based on conforming quadtree meshes for kinematic limit analysis. *Computer Methods in Applied Mechanics and Engineering*, 341:485–516, 2018.
- [81] TQ Chu PLH Ho, Canh V Le. The equilibrium cell-based smooth finite element method for shakedown analysis of structures. *International Journal of Computational Methods*, 71:1840013, 2017.
- [82] Canh V Le. Estimation of bearing capacity factors of cohesive-frictional soil using the cell-based smoothed finite element method. *Computers and Geotechnics*, 83:178–183, 2017.
- [83] Gang Xua, Bernard Mourrain, Régis Duvigneau, and André Galligo. Constructing analysis-suitable parameterization of computational domain from cad boundary by variational harmonic method. *Journal of Computational Physics*, 252:275–289, 2013.
- [84] M. Kleiber J.A. König. On a new method of shakedown analysis. *Bull. Acad. Polonaise Sci. XXVI*, 4:165–171, 1978.

-
- [85] Bree J. Elastic-plastic behaviour of thin tubes subjected to internal pressure and intermittent high heat fluxes with application to fast nuclear reactor fuel elements. *Journal of Strain Analysis*, 2:226–238, 1967.
- [86] Cherniavsky O. F Gokhfeld D. A. *Limit analysis of structures at thermal cycling*. Sijthoff and Noordhoff, The Netherlands, 1980.
- [87] Sawczuk A. Shakedown analysis of elastic-plastic structures. *Nuclear engineering and design*, 28:121–136, 1974.
- [88] M.Kleiber A.Borkowski. On a numerical approach to shakedown analysis of structures. *Computer Methods in Applied Mechanics and Engineering*, 2:101–119, 1980.
- [89] P. Morelle. Structural shakedown analysis by dual finite-element formulations. *Engineering Structures*, 6:70–79, 1984.
- [90] Nguyen-Dang Hung P. Morelle. Etude numérique de l’adaptation plastique des plaques et des coques de révolution par les éléments finis d’équilibre. *J. Méc. Théor. Appl.*, 2:567–599, 1983.
- [91] Polizzotto C. Upper bounds on plastic strains elastic-perfectly plastic solids subjected to variable loads. *International Journal of Mechanical Sciences*, 21:317–327, 1979.
- [92] Jospin J.R. Displacement estimates of pipe elbows prior to plastic collapse loads. *Nuclear Engineering and Design*, 97:165–178, 1978.
- [93] A. M. Yan. *Contribution to direct limit state analysis of plastified and cracked structures*. PhD Dissertation, Université de Liège, Belgium, 1999.
- [94] L. Piegl and W. Tiller. *The NURBS Book*. Springer, 1997.
- [95] Verhoosel C.V Sederberg T.W Scott M.A, Borden M.J and Hughes T.J.R. Iso-geometric finite element data structures based on bézier extraction of t-splines. *International Journal for Numerical Methods in Engineering*, 88:126 – 156, 2011.
- [96] E. Suli and D.F. Mayers. *An introduction to numerical analysis*. Cambridge University Press, 2003.
- [97] A. Zavelani L. Corradi. A linear programming approach to shakedown analysis of structures. *Computer Methods in Applied Mechanics and Engineering*, 3:37–53, 1974.

-
- [98] A. M. Yan and H. Nguyen-Dang. Limit analysis of cracked structures by mathematical programming and finite element technique. *Computational Mechanics*, 24:319–333, 1999.
- [99] F. W. Williams B. Y. Xu M. D. Xue, X. F. Wang. Lower-bound shakedown analysis of axisymmetric structures subjected to variable mechanical and thermal loads. *International Journal of Mechanical Sciences*, 39:965–976, 1997.
- [100] Haiyuan Yang Yueheng Xu. Subdomain bounding technique for large scale shakedown analysis. *Computers and Structures*, 30:883–886, 1988.
- [101] Dieter Weichert A. Hachemi. Numerical shakedown analysis of damaged structures. *Computer Methods in Applied Mechanics and Engineering*, 160:57–70, 1998.
- [102] Dieter Weichert. On the influence of geometrical nonlinearities on the shakedown of elastic-plastic structures. *International Journal of Plasticity*, 2:135–148, 1986.
- [103] Bui Cong Thanh. *Analyses directe des états limites plastiques des structures par programmation mathématique et discretisation en éléments finis*. PhD Dissertation, Université de Liège, Belgium, 1998.
- [104] Bazaraa M. S, Sherali H. D, and Shetty C. M. *Nonlinear programming. Theory and algorithms*. John Wiley and Sons, 1993.
- [105] T. N. Tran, G. R Liu, H. Nguyen-Xuan, and T. Nguyen-Thoi. An edge-based smoothed finite element method for primal-dual shakedown analysis of structures. *International Journal for Numerical Methods in Engineering*, 82:917–938, 2010.
- [106] H. Nguyen-Xuan, T. Rabczuk, T. Nguyen-Thoi, T. N. Tran, and N. Nguyen-Thanh. Computation of limit and shakedown loads using a node-based smoothed finite element method. *International Journal for Numerical Methods in Engineering*, 90:287–310, 2012.
- [107] Johannes Gross-Weege. On the numerical assessment of the safety factor of elastic-plastic structures under variable loading. *International Journal of Mechanical Sciences*, 39:417–433, 1997.
- [108] M. Vicente da Silva and A. N. Antão. A non-linear programming method approach for upper bound limit analysis. *International Journal for Numerical Methods in Engineering*, 72:1192–1218, 2007.

-
- [109] V. Carvelli, Z.Z. Cen, Y. Liu, and G. Maier. Shakedown analysis of defective pressure vessels by a kinematic approach. *Archive of Applied Mechanics*, 69:751–764, 1999.
- [110] W. Prager and P. G Hodge. *Theory of Perfectly Plastic Solids*. John Wiley and Sons, 1951.
- [111] R Casciaro and L Cascini. A mixed formulation and mixed finite elements for limit analysis. *International Journal for Numerical Methods in Engineering*, 18:211–243, 1982.
- [112] Petrolo S Garcea G, Armentano G and Casciaro R. Finite element shakedown analysis of two-dimensional structures. *International Journal for Numerical Methods in Engineering*, 63:1174–1202, 2005.
- [113] Cocks A. C. F. and Leckie F. A. Deformation bounds for cyclically loaded shell structures operating under creep condition. *Journal of Applied Mechanics, Transactions of the ASME*, 55:509–516, 1988.
- [114] G. L. Hollinger and John L. Hechmer. Three dimensional stress evaluation guidelines progress report. *Recertification and Stress Classification Issues, ASME PVP*, 277:95–102, 1994.
- [115] Seshadri R. and S. P. Mangalaramanan. Lower bound limit loads using variational concepts: The m_α method. *International Journal of Pressure Vessels and Piping*, 71:93–106, 1997.
- [116] C. Hari Manoj Simha and R. Adibi-Asl. Lower bound limit load estimation using a linear elastic analysis. *Journal of Pressure Vessel Technology*, 134:021207.1–021207.10, 2012.
- [117] R. Seshadri and M. M. Hossain. Simplified limit load determination using the m_α -tangent method. *Journal of Pressure Vessel Technology*, 131:021213.1–021213.6, 2009.
- [118] S. L. Mahmood and R. Seshadri. Limit load evaluation using the m_α -tangent multiplier in conjunction with elastic modulus adjustment procedure. *Journal of Pressure Vessel Technology*, 135:051203.1–051203.9, 2013.
- [119] Jeries Abou-Hanna and Timothy E. McGreevy. A simplified ratcheting limit method based on limit analysis using modified yield surface. *International Journal of Pressure Vessels and Piping*, 88:11–18, 2011.

-
- [120] N.S Ngo and F. Tin-Loi. Shakedown analysis using the p-adaptive finite element method and linear programming. *Engineering Structures*, 29(1):46–56, 2007.
- [121] M. Staat and M. Heitzer. Lisa — a european project for fem-based limit and shakedown analysis. *Nuclear Engineering and Design*, 201:151–166, 2006.
- [122] X.Peng, E.Atroshchenko, P.Kerfriden, and S.P.A.Bordas. Linear elastic fracture simulation directly from cad: 2d nurbs-based implementation and role of tip enrichment. *International Journal of Fracture*, 204:55–78, 2017.
- [123] A. G. Miller. Review of limit loading of structures containing defects. *International Journal of Pressure Vessels and Piping*, 32:197–327, 1988.
- [124] G. G. Chell. *Elastic-plastic fracture mechanics*. in Developments in Fracture Mechanics-1 (Edit by Chell G. G.), Applied Science Publishers, London, 1979.
- [125] T. D. Tran and C. V. Le. Extended finite element method for plastic limit load computation of cracked structures. *International Journal for Numerical Methods in Engineering*, 104:2–17, 2015.
- [126] M. Staat and Duc Khoi Vu. Limit analysis of flaws in pressurized pipes and cylindrical vessels. part i: Axial defects. *Engineering Fracture Mechanics*, 74:431–450, 2007.
- [127] M. Staat and Duc Khoi Vu. Limit analysis of flaws in pressurized pipes and cylindrical vessels. part ii: Circumferential defects. *Engineering Fracture Mechanics*, 97:314–333, 2013.
- [128] Y. Lei. A review of limit load solutions for cylinders with axial cracks and development of new solutions. *International Journal of Pressure Vessels and Piping*, 85:825–850, 2008.
- [129] Yun-Jae Kim, Do-Jun Shim, Nam-Su Huh, and Young-Jin Kim. Plastic limit pressures for cracked pipes using finite element limit analyses. *International Journal of Pressure Vessels and Piping*, 79:321–330, 2002.